PARYLENE MICROCOLUMN FOR MINIATURE GAS CHROMATOGRAPH

A Thesis
Presented to
The Academic Faculty

By

Hongseok "Moses" Noh

In Partial Fulfillment of the Requirements for
the Degree Doctor of Philosophy
in Mechanical Engineering

Georgia Institute of Technology

April 26, 2004

PARYLENE MICROCOLUMN FOR MINIATURE GAS CHROMATOGRAPH

Approved:

Peter J. Hesketh, Chairman

Wenjing Ye

Yogendra Joshi

Bruno Frazier

Boris Mizaikoff

Date approved by chairman: April 26, 2004

ACKNOWLEDGEMENT

"But seek first his kingdom and his righteousness,

and all these things will be given to you as well" (Matthew 6:33)"

I thank God for his abundant blessings on my life. He has saved me and made me his child. He has called me and gave me a great vision to be a prophet to the nations. He granted me this precious Ph.D. training and helped me to achieve it. I did not do anything but he did everything for me. Praise be to the Lord. I pray that I may seek his kingdom and his righteousness first throughout all my life.

There are so many people to whom I would like to give my sincere thanks. Without their advice, assistance, encouragement, understanding, love, and prayer, I could not have completed this dissertation. I would like to dedicate this dissertation to all of them.

Dr. Peter J. Hesketh (my advisor)

MEMS group alumni and current members

ME/ECE MEMS people and other cleanroom users

Committee members and other professors

Colleagues and friends

UBF members

My parents, brother and relatives

My wife and two children

TABLE OF CONTENTS

LIST OF TABLES

LIST OF FIGURES

x

SUMMARY

This research contributes to worldwide efforts to miniaturize one of the most powerful and versatile analytical tools, gas chromatography (GC). If a rapid, sensitive and selective hand-held GC system is realized, it would have a wide range of applications in many industries and research areas. As a part of developing a hand-held GC system, this research focuses on the separation column, which is the most important component of a GC system. This thesis describes the development of a miniature separation column that has low thermal mass and an embedded heating element for rapid thermal cycling. The world's first thin polymer film (parylene) GC column has been successfully developed. This thesis includes: first, a study of theoretical column performance of rectangular GC column; second, the design optimization of parylene column and embedded heating element; third, the development of new processes such as parylene micromolding and stationary phase coating technique for parylene column; fourth, the fabrication of parylene GC column with an embedded heating element; and lastly, the testing and evaluation of parylene GC column through GC analysis.

CHAPTER 1

INTRODUCTION

Until recently, a hand-held chemical analytical system has only been a dream. Now through current research efforts this is no longer just a science fiction. Nowadays many miniature analytic systems, so called 'Lab-on-a-chip' are being realized through the use of microfabrication technologies. Although not many commercial products exist at present, eventually miniature analytical systems will become a part of our daily life.

This research contributes to worldwide efforts to miniaturize one of the most powerful and versatile analytical tools, gas chromatography (GC). This thesis describes the development of a miniature separation column that has low thermal mass and an embedded heating element for rapid thermal cycling. This work includes new process development for parylene microcolumn fabrication, theoretical analysis of column performance, design optimization and fabrication of a miniature parylene GC column with an embedded heating element, and the evaluation of the GC column.

1.1 STATEMENT OF THE PROBLEMB

Gas chromatography is a technique most widely used for the separation and analysis of volatile chemicals. A typical GC is a bulky system that contains a sample

1

injection unit, a separation column, a temperature-programmable oven, an output detector

and a data processing unit as shown in Figure 1-1. There has been tremendous interest in

the miniaturization of a GC system because of its potential capabilities: portability, rapid

analysis time, low dead volume, low power consumption and low cost. If a rapid,

sensitive, and selective hand-held GC system can be realized, it would have a wide range

of applications in biomedical and environmental research, food and health industry, and

anti-terrorism efforts by replacing the conventional bench-top systems. For example, this

system can be used for the field detection of chemical, biological, and chemical warfare

agents and explosives.
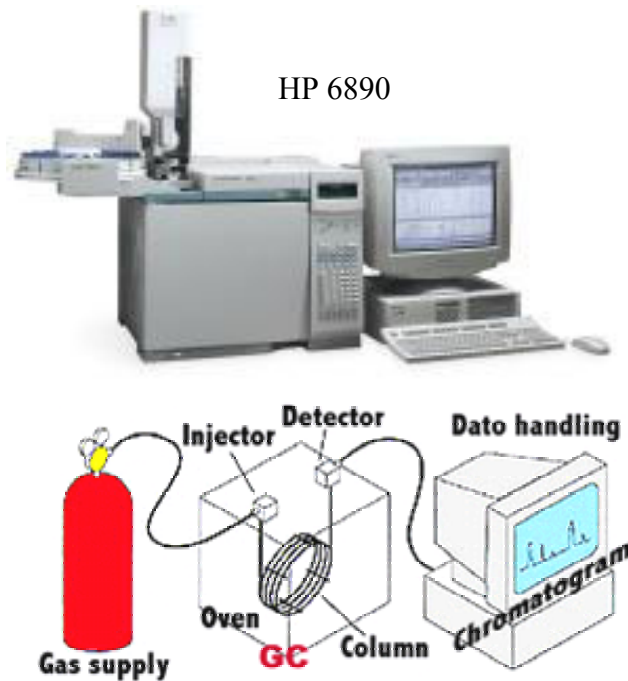
Figure 1-1. A typical gas chromatograph (HP 6890, Agilent Technologies Inc.) and its schematic diagram [www.chem.agilent.com].

In order to build a feasible hand-held GC system, every part of the system needs to be miniaturized without a loss in performance compared to current systems. The most important part of a GC system is the separation column because the separation of the analytes is achieved via their differential migration through the column. The analysis time and resolution of a GC system highly depend on the performance of the separation column. Therefore, the separation column is often called 'the heart of GC.'

Conventional separation columns are made of fused-silica capillary tubes that are fabricated by high temperature drawing method. The fused-silica capillary column (Figure 1-2) generally has the polyimide film on the outer surface to provide flexibility and a thin layer, a so called 'stationary phase', inside the column. During the mobile phase, carrier gas containing analytes sweeps the stationary phase, the analytes are separated depending on their unique partition coefficients between the two phases. The stationary phase can be either liquid or solid and usually coated through a dynamic (injection) or static (withdrawal) coating method. Since the separation is based on the partitioning of the analytes between two phases, column temperature is a very important parameter for column performance. Generally, the fused-silica column is installed in a temperature-programmable oven for thermal cycling during the GC analysis. The conventional temperature-programmable oven is a bulky convection oven. Therefore, when the miniaturization of a GC separation column is considered, the heating device for the column must be considered as well.
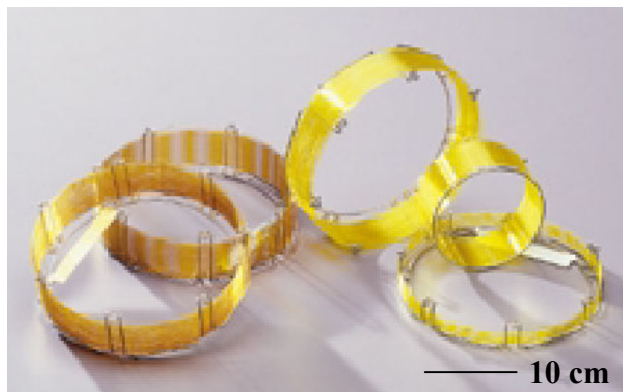
Figure 1-2. Fused-silica gas chromatographic columns [www.chem.agilent.com].

This work focuses on the development of a miniature separation column for the hand-held GC system. The requirements for the miniature separation column of a hand-held GC system are listed below.

- Small size

- Short retention time and good column efficiency

- Embedded heating element

- Low thermal mass for a rapid thermal cycling

- Capability to be coated with various stationary phases

- Capability to be integrated with other components of the GC system.

The first miniature separation column for GC was a micromachined silicon/glass column that was quite revolutionary at that time [1, 2]. Terry et al. etched a spiral microchannel on silicon wafer and anodically bonded it to a Pyrex glass substrate. Since then, a micromachined silicon/glass column has become standard for miniature GC. No other type of miniature GC column has since been developed. What has been done by other research groups was basically a modification of the silicon/glass column using new

silicon etching techniques, such as deep reactive ion etching (RIE) [3-5]. Figure 1-3

shows an example of a micromachined silicon/glass column [5].

However, the micromachined silicon/glass column is not the best solution for a

hand-held GC system, because it does not satisfy all of the requirements listed above.

While the silicon/glass column can be built in a small area and also be integrated with

other components on the same chip, it has several drawbacks: First, the power

consumption for heating still remains too high to use commercial batteries. Also, the

cooling time is fairly long unless there is an external cooling device. This is due to

comparatively large thermal mass of the silicon/glass column and the ineffective heating

by an external source. Second, the micromachined silicon/glass has considerable surface

roughness due to the silicon etching process. This roughness causes non-uniformity with

coating of the stationary phase, and therefore lowers the column performance. Third, it is

difficult to take advantage of the open structure of the silicon microchannel for stationary

phase coating because of the requirement of anodic bonding process. Apart from

conventional silica column, the micromachined silicon/glass column has more options in

terms of stationary phase coating. For example, stationary phase can be deposited directly

on silicon microchannel by chemical vapor deposition or plasma coating. However, the

anodic bonding process following deposition or coating limits this freedom because it

requires high temperature and specific materials.
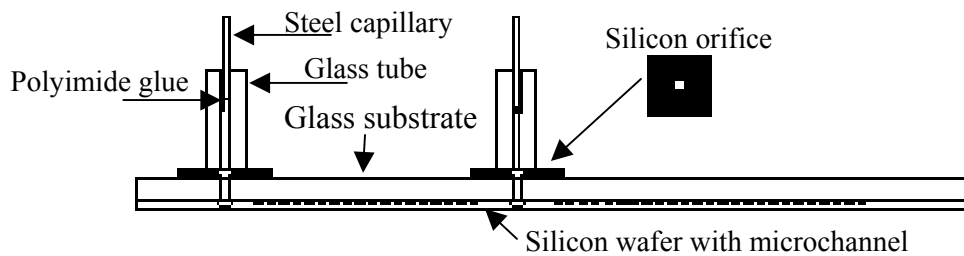
(a)

(b)

Figure 1-3. An example of micromachined silicon/glass column (a) cross-sectional view, (b) natural view [5].

Can there be a better separation column for a miniature GC that has lower thermal mass, less surface roughness and embedded heating element? Can we make a low-cost thin polymer GC column that provides a good performance? Can we take advantage of the open structure of the micromachined channel for stationary phase coating? This research was motivated by these questions.

This thesis describes the development of a new miniature separation column that has low thermal mass and an embedded heating element for rapid thermal cycling. The new column is made of a thin film polymer, parylene (poly paraxylylene). Figure 1-4 shows parylene columns with and without gold heating element. The miniature parylene GC column provides a faster thermal cycling of the column for rapid and frequent GC

analysis. Moreover, the embedded heating element maximizes the advantage with lower power consumption. In addition, this column has reduced surface roughness and can take advantage of the open structure of the micromachined channel for stationary phase coating.

The scope of this work includes:

(1) Investigation of theoretical column performance for rectangular columns.

(2) Design of parylene column with embedded heating element considering the separation performance, thermal cycling, integration, deformation, and permeation.

(3) Development of a new fabrication process for long, enclosed parylene columns.

(4) Investigation of diverse stationary phase coating methods

(5) Fabrication of parylene columns with stationary phase and embedded heating element.

(6) Testing and evaluation of the parylene GC columns.
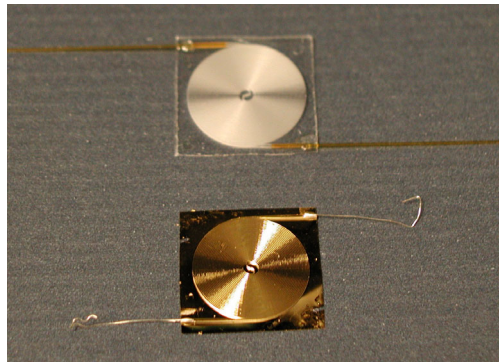
Figure 1-4. Parylene gas chromatographic columns with (bottom) and without (top) heating element.

1.2 RESEARCH OBJECTIVES

(1) Development of a new fabrication method, 'parylene micromolding' – The conventional fabrication method for parylene devices is not appropriate for fabricating a long parylene microcolumn because it is a diffusion-limited process and therefore it takes considerable amount of time for the fabrication. A new method using a molding concept is proposed in this research. This new method consists of the fabrication of silicon molds, parylene deposition, parylene/parylene thermal lamination, and the release of parylene columns from the silicon mold. The process parameters especially for parylene/parylene bonding are thoroughly examined and the bonding strength is evaluated to investigate the feasibility of fabricating parylene GC column. This new fabrication method is further explored for other applications such as wafer bonding and the fabrication of diverse microchannels.

(2) Investigation of theoretical column performance for rectangular GC columns – Two important things that must be addressed regarding column performance are retention time and band broadening. They are the main parameters of the analysis time and resolution of a GC. Conventional fused-silica columns with circular cross-section have been well researched concerning these issues. In this thesis, the column performance analysis is performed for the micromachined columns which have narrow rectangular cross-section. The performance of a narrow rectangular column is compared with that of a conventional circular column. In addition, the effect of design and operation parameters on the column performance will be thoroughly investigated for the micromachined columns.

(3) Optimization of the design of a parylene GC column – The most important thing in GC column design is the performance of the column. The target performance in this research is that the retention time should be less than 1 minute and the number of theoretical plate should be more than 10,000. Other things that need to be considered in designing parylene GC column include the integration with other components, the deformation by inner pressure, and the gas permeation through the column wall. The design of a parylene GC column is optimized considering the above aspects.

(3) Investigation of the thermal cycling of parylene microcolumn – Column temperature is very important in GC analysis because the separation of the analytes is based on their partitioning between stationary and mobile phases. Parylene GC column has low thermal mass because it is made of thin polymer film. As a result, it can be heated and cooled very fast, enabling rapid and frequent analysis. ANSYS heat transfer modeling is performed to investigate the heating and cooling rate, power consumption, and temperature distribution of both the parylene column and the silicon/glass column. The actual thermal cycling is also measured for the parylene column with an embedded heating element. A thin film metal wire is formed for joule heating by evaporating metal on the corrugated surface of parylene column.

(4) Investigation of the stationary phase coating method for parylene GC column – A GC column without a stationary phase cannot function. There are more than 200 stationary phases that are commercially available for conventional packed or open tubular columns. The question is 'can we still use these stationary phases for parylene GC column?' The conventional injection coating method with common stationary phase is investigated for this purpose. Another important issue is whether we can take advantage

of the open structure of the micromachined channel for stationary phase coating. Dry coating methods such as plasma polymerization and chemical vapor deposition are investigated for this purpose.

(5) The complete fabrication of a parylene GC column that has stationary phase and embedded heating element – All partially investigated parts are combined together and a complete fabrication flow is proposed to build a parylene GC column that contains stationary phase and an embedded heating element. The parylene GC column is then fabricated according to the proposed fabrication flow. The completed parylene GC column includes proper tubing and packaging, and is literally 'ready for use'.

(6) Evaluation of parylene GC column – The completed parylene GC column can be installed in a conventional GC for evaluation. Retention time and the number of theoretical plates are measured for some volatile organic chemicals (VOC) and compared with the theoretically calculated values. The separation of some VOC mixture by parylene GC column is demonstrated and compared with that by conventional fused-silica column.

1.3 STRUCTURE OF THE THESIS

Chapter 2 provides background information regarding this research. The information includes approaches for field chemical detection, fundamentals of gas chromatography, previous research on miniature gas chromatography, and the application of parylene in MEMS.

Chapter 3 describes the theoretical column performance for both circular and rectangular columns. This chapter provides analytical tools to deal with gas flow in microchannel, retention time, column efficiency, and resolution. The effects of design and operation parameters on column performance will be thoroughly investigated.

Chapter 4 presents the design of parylene GC column. In the first part of this chapter, the optimization of column geometry will be discussed considering column performance, integration, gas permeation, and mechanical strength. In the second part, the design of the heating element and heat spreader will be modeled using finite element analysis.

Chapter 5 describes the development of two processes that are crucial in fabricating the parylene GC column. They are parylene micromolding and stationary phase coating for parylene column. The parameters and strength of parylene/parylene bonding are thoroughly investigated. Diverse technique will be investigated for stationary phase coating.

Chapter 6 describes the fabrication of a parylene GC column with embedded heating element. Details of problems encountered in fabrication process will be discussed and some prototypes will be presented.

Chapter 7 presents the evaluation of the parylene GC column. Results from flow test, heating element tests and GC tests will be presented and compared with analytical results.

Chapter 8 presents the conclusions from this research and provides suggestions for the next generation of parylene GC column. Finally, recommendations for future work will be presented.

C H A P T E R   2

B A C K G R O U N D

Miniature gas chromatography is one of the most versatile approaches for field chemical detection. In this chapter, other approaches are reviewed before we take a closer look at GC. Then some fundamentals of GC will be provided. Most of all, previous work by other research groups in the miniaturization of GC system will be thoroughly reviewed. Additionally, in-depth information about parylene, the main material used in this research, will be provided for the further discussion in the following chapters.

2.1 APPROACHES FOR FIELD CHEMICAL DETECTION

Field chemical detection is crucial in many areas such as environmental and food industries, health and biomedical sciences, and anti-terrorism efforts. The requirements for field chemical detection system include portability, fast response time, low power consumption, robustness, and low cost, as well as the general requirements for chemical sensing systems which are good sensitivity, selectivity, and reproducibility. Of course, there is no system that meets all requirements. Many chemical sensors and sensing systems are commercially available or under development. They can be categorized into four general groups based on the principal physics and operating mechanisms; (1)

chromatography and spectrometry; (2) mass sensors, (3) electrochemical sensors; and (4) optical sensors. Most of the contents in this section are based on a report (SAND2001-0643) from Sandia National Laboratories [6].

2.1.1 CHROMATOGRAPHY AND SPECTROMETRY

Gas chromatography is a method for the separation and analysis of complex mixtures of volatile organic and inorganic compounds. This is a powerful apparatus for separating a complex mixture into individual components. A gas chromatograph consists of sample injection unit, separation column, detector, and data handling unit. Generally, GC is a bench-top system, but there are commercially available portable GC systems. Moreover, hand-held GC systems are being developed currently by several different groups. Detail information about GC will be given in section 2.2 and 2.3.

The ion mobility spectrometer (IMS) can be considered a sub-class of chromatographic separators. The principle of every IMS is a time-of-flight measurement. After a gaseous sample has entered the spectrometer it will be ionized by a radioactive source, the resulting positive and negative charged species will be accelerated over a short distance and the time-of-flight will be determined. Commercially available detection systems for chemical warfare agents are mostly based on ion mobility spectrometry. IMS is often interfaced with GC for better performance, forming GC/IMS. Figure 2-1 shows portable IMS systems for chemical agent detection. It is suited for the screening of traces in gas and for the detection of toxic industrial compounds and chemical warfare agents down to the ppb-range.

Some of the mass spectrometers are portable enough to carry into the field. The principle of the mass spectrometer is similar to the ion mobility spectrometer, except a vacuum is required. Sampled gas mixtures are ionized, and charged molecular fragments are produced. These fragments are sorted in a mass filter according to their mass to charge ratio. The ions are detected as electrical signals with an electron multiplier or a Faraday plate.
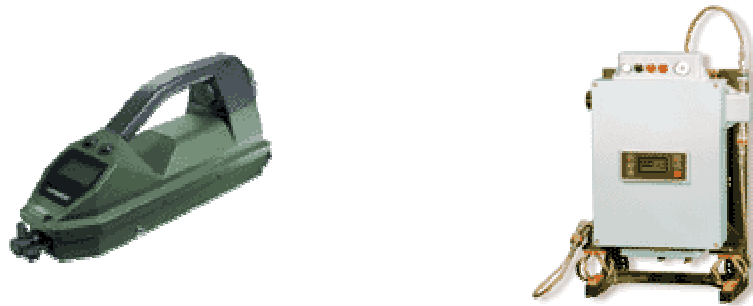
Figure 2-1. Portable ion mobility spectrometer for the detection of chemical warfare agents (RAID-M and RAID-S, *Bruker-Daltonics, Inc.*).

2.1.2 MASS SENSORS

The most common and sensitive mass sensors is surface acoustic wave (SAW) sensors. SAW sensors consist of an input transducer, a chemical adsorbent film, and an output transducer on a piezoelectric substrate as shown in Figure 2-2. The input transducer launches an acoustic wave which travels through the chemical film and is detected by the output transducer. The velocity and attenuation of the signal are sensitive to the viscoelasticity as well as the mass of the thin film which can allow for the identification of the contaminant.

Sandia National Laboratories has developed and tested a six-SAW device array [http://www.sandia.gov/media/factsheets/99_sm_saw.htm]. Using the array, they have been able to identify 14 different individual organic compounds over a wide range of concentrations with 98% accuracy. Naval Research Laboratory has also developed SAW sensor systems to monitor hazardous chemical vapors such as chemical warfare agents [http://www.nrl.navy.mil/content.php?P=CHEMVAPORSENSOR]. The detection limits of the devices are in the parts per trillion range. In this system, individual devices generate SAW in piezoelectric quartz, with frequencies in the MHz range. A selective chemical absorbent, coated on the SAW devices, allows gas detection by changes in SAW frequency. Arrays of polymer-coated SAW devices detect different gases, and pattern-recognition techniques interpret data and identify unknown(s). SAW devices are very sensitive but it is difficult to discriminate among unknown mixture of chemicals. In addition, some polymer absorbents react strongly to water vapor.
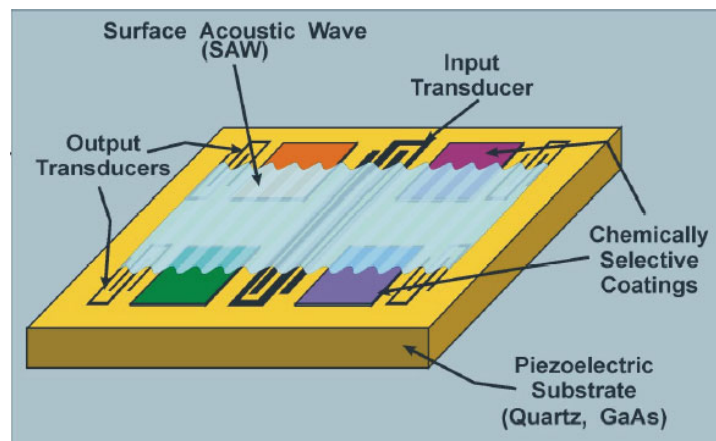
Figure 2-2. Schematic of Sandia's SAW device [http://www.sandia.gov/media/factsheets/99_sm_saw.htm].

The other major type of mass sensor is microcantilevers. Theses cantilevers respond to changes in mass by bending. Appropriate coatings are applied to the cantilevers to absorb chemicals of interest. Active research in this area is being performed by Oak Ridge National Laboratory [http://bio.lsd.ornl.gov/highlights/2000mar3.htmlx].

2.1.3 ELECTROCHEMICAL SENSORS

Electrochemical sensors can be classified into three groups: potentiometric (measurement of voltage); amperometric (measurement of current); and conductometric (measurement of conductivity). Potentiometric and amperometric sensors employ an electrochemical cell consisting of a casting that contains a collection of chemical reactants in contact with the surroundings through two terminals (an anode and a cathode) of identical composition. These are commonly used for water analysis such as pH sensing. For gas detection, the top of the casing has a membrane which can be permeated by the gas sample. Gases such as oxygen, nitrogen oxide, and chlorine, which are electrochemically reducible, are sensed at the cathode while electrochemically oxidizable gases such as carbon monoxide, nitrogen dioxide, and hydrogen sulfide are sensed at the anode. However, there is no commercial potentiometric cell for volatile organic chemicals; most are used for toxic gases and oxygen.

On the other hand, conductometric sensors are commonly used for the detection of volatile organic chemicals. Commercial conductometric sensors can be classified into three types: polymer-absorption chemiresistors; catalytic bead sensors; and metal-oxide semiconductor sensors.

Polymer-Absorption chemiresistors consist of a chemically sensitive absorbent deposited on an electrode. When chemical vapors come into contact with the absorbent, the chemicals absorb into the polymers, causing them to swell. The swelling changes the resistance of the electrode, which can be measured. Often, an array of chemiresistors is used to increase analytic discrimination. However, the unit must be "trained" for each analyte of interest. Figure 2-3 shows a hand-held chemiresistor system manufactured by Cyrano Sciences[TM]. This device includes an array of 32 chemiresistors, each of which consists of a pair of electrical contacts that are bridged by a composite film. This composite film is made of non-conducting polymer and conductive carbon black particles. Sandia National Laboratories has developed chemiresistors using polymer films deposited on microelectrodes [http://www.sandia.gov/media/NewsRel/NR2001/watsniff.htm]. Chemiresistors are small, low power devices and have good sensitivity to various chemicals. But they may not be able to discriminate among unknown mixtures of chemicals. Some polymer absorbents react strongly to water vapor. Although reversible, signal may experience hysteresis and a shift in the baseline when exposed to chemicals.

Catalytic bead sensors are low-power (50-300mW) devices that have been used for many years in the detection of combustible gases, particularly methane in air. They are used widely in portable gas detection instruments. This sensor consists of a passive and active element, both made from an embedded coiled platinum wire in a porous ceramic. The active element is coated with a catalyst such as platinum, and the passive element is coated with an inert glass to act as a reference element to compensate for environmental conditions. Both elements are heated and when a combustible gas contacts the elements, the vapor combusts on the active element and the active element increases

in temperature. As a result, the resistance of the platinum coil changes and it is measured using a wheatstone bridge. Thermo Electron Corporation has a portable soil vapor monitor that uses the catalytic bead sensor for detecting combustible hydrocarbon gases (Figure 2-4 left).

(a)

(b)
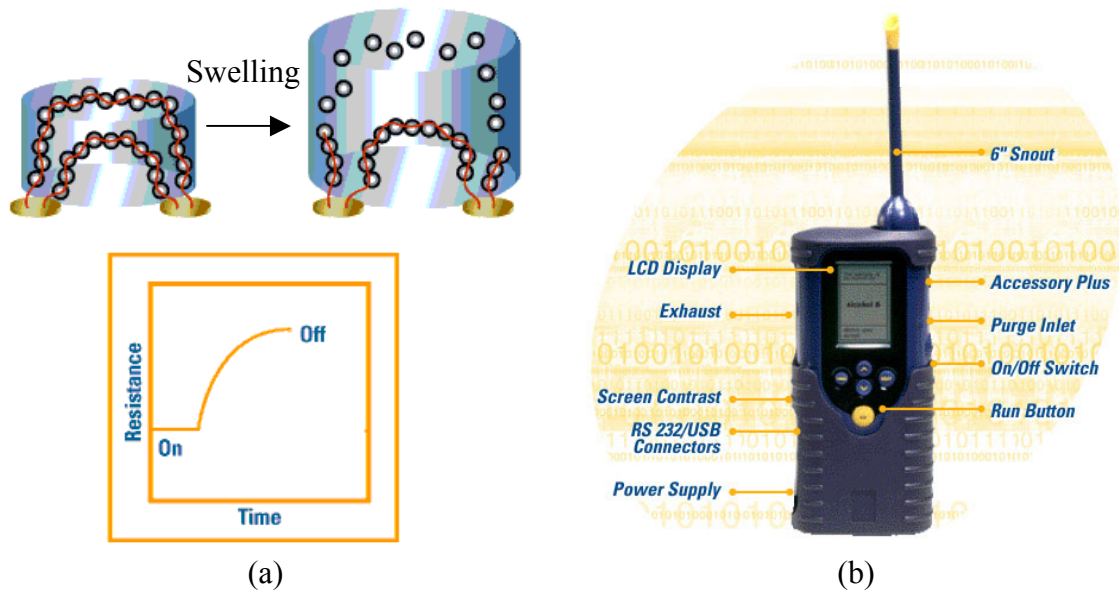
Figure 2-3. Chemiresistor, (a) working principle, (b) commercial product (cyranose[TM] 320).

Figure 2-4 Commercial catalytic bead sensor (Innova-SV, Thermo Electron Corporation) and metal-oxide semiconductor sensor (TGS813, Figaro) [https://www.thermo.com and https://www.figarosensor.com].

18

The metal oxide semiconductor (MOS) sensor is comprised of a tin oxide that is sintered on a small ceramic tube. A coiled wire is placed through the center of the ceramic tube to act as the sensor heater. Metal wires provide electrical contact between the tin oxide and the rest of the electronics. The combination of the sensor operating temperature and the composition of the metal oxide yields different responses to various combustible gases. When the metal oxide is heated, oxygen is adsorbed on the surface with a negative charge. Donor electrons are transferred to the adsorbed oxygen, leaving a positive charge in the layer. Inside the sensor, electrical current flows through the grain boundary of metal oxide microcrystals. Resistance to this electrical current is caused by negatively charged oxygen at grain boundaries. In the presence of a reducing gas, a surface catalyzed combustion occurs and the surface density of negatively charged oxygen decreases, thereby decreasing the resistance of the sensor. Figaro has developed MOS sensors for detection of solvent vapors (Figure 2-4 right). This sensor has high sensitivity to combustible gases such as hydrogen and reducing gases such as NO, H_2S, etc. However the sensitivity to aromatic and halogenated hydrocarbons is questionable.

2.1.4 OPTICAL SENSORS

Two types of optical sensors are used for chemical detection: colorimetry and fiber-optic sensors. Colorimetry works by analyzing the color of contaminated water that has been mixed with a particular chemical reagent. There are commercially available pocket colorimeter test kits and strips for the detection of petroleum hydrocarbons and

toxic gases [https://www.lamotte.com]. This is very simple to use, but chemical sensitivity is limited to individual VOCs and requires actual water samples.

Fiber-optic sensors are again classified into three groups. The first group involves sending a light source directly through the optical fiber and analyzing the light reflected or emitted by the contaminants. The second group uses optical fiber with a chemically interacting thin film attached to the tip. This film is formulated to bind with certain types of chemicals. Contaminant concentration can be found by measuring the color of the thin film, the change of refractive index, or by measuring the fluorescing of the film. The third group of optical fiber sensors involves injecting a reagent near the sensor. This reagent reacts with the contaminant and the reaction products are detected to give an estimate of the contaminant concentration. Fiber optic sensors require low power and can detect various chemicals at very low concentrations, but some organic pollutants are not easily differentiated using UV-visible spectroscopy.

2.2 FUNDAMENTALS OF GAS CHROMATOGRAPHY

2.2.1 ELUTION GAS CHROMATOGRAPHY

Gas chromatography is a method for separating and analyzing components of mixtures of volatile compounds [7]. The most common technique for GC is the elution technique. A stream of inert gas, the carrier gas, passes continuously through the column, and the mixture to be separated is introduced instantaneously at the beginning of the

column as a sample either of a gas or a volatile liquid. The sample is transported in a

mobile phase and the mobile phase is then forced through a stationary phase which is

fixed in a column. Some solutes are more strongly retained by the stationary phase than

others and as a result, a mixture sample can be separated as illustrated in Figure 2-5.
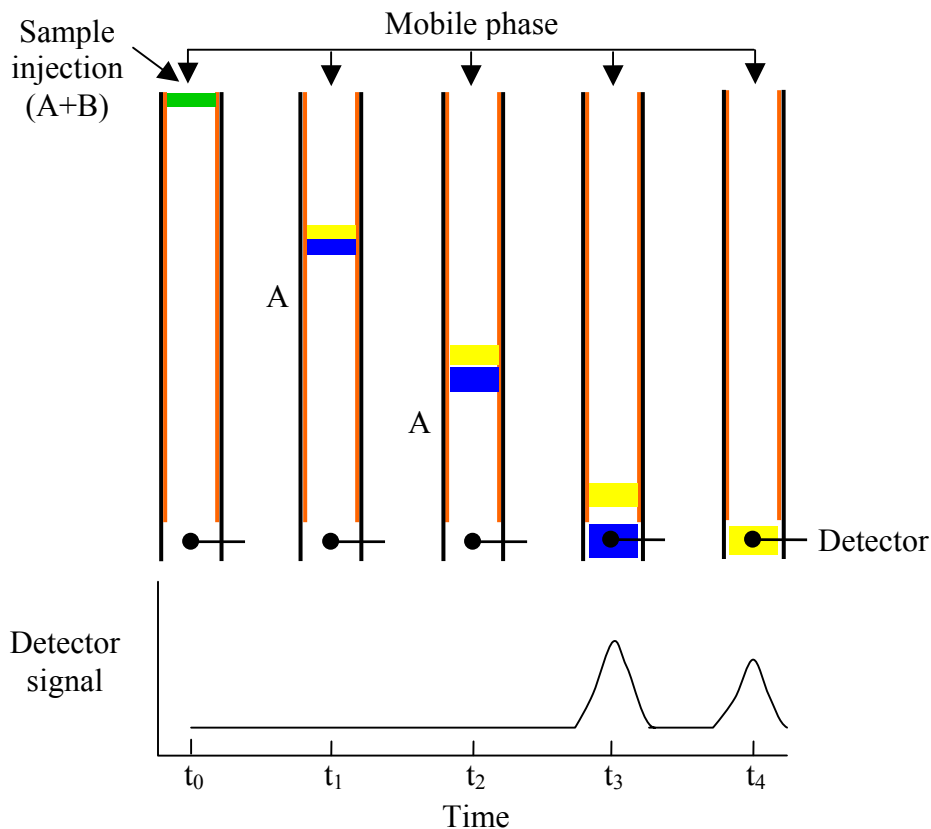
Figure 2-5. Principle of elution chromatography.

The stationary phase can be either liquid or solid. As a result, the retention

chromatography is categorized into 'gas-liquid chromatography' and 'gas-solid

chromatography.' In gas-solid chromatography, the retention of analytes is the

consequence of the physical adsorption of an analyte on the solid stationary phase. In

gas-liquid chromatography, the retention of an analyte is based upon the partition of the

analyte between a gaseous mobile phase and a liquid phase immobilized on the surface of an inert solid in gas-liquid chromatography. Gas-liquid chromatography has greater general utility and is more widely used, while gas-solid chromatography is especially useful for the separation of highly volatile compounds, including gas samples.

When the sample is introduced to the inlet end of the column in gas-liquid chromatography, each solute in that sample engages in a highly dynamic equilibrated partitioning between the stationary phase and the mobile phase in accordance with its distribution constant. The distribution constant is defined as

$$K_C = \frac{c_S}{c_M}$$

Equation 2-1

where c_S and c_M are the concentrations of solute in stationary and mobile phase respectively. The flow of carrier gas disrupts the equilibrium distribution at the front and rear of the band, causing continuous evaporation at the rear and reestablishment at the front as the sample passes through the column as shown in Figure 2-6. Because all solutes are injected simultaneously, separation is obviously contingent on differences between the K_C values of the individual solutes.

Because solute movement can only occur in the mobile phase, the average rate at which a solute zone migrates down the column depends on the fraction of time it spends in that phase. The proportion of a solute that is in the mobile phase at any given time is a function of the "net" vapor pressure of that solute. Therefore, the less volatile solutes or those components that are strongly retained by the stationary phase move slowly with the flow of mobile phase. Hence, separation is achieved while the solutes are passing through the column. Then, the separated solutes are swept toward the detector and a certain

physical property change is detected at the detector. The detected signal is then plotted as a function of time. This plot is called a 'chromatogram'. Figure 2-7 shows an example chromatogram for a solvent mixture. A thermal conductivity detector was used in this example. The position of peaks serves to identify the components, and the area under the peaks represents the amount of each component.

Mobile phase

Solute concentration in mobile phase

Partitioning from stationary phase into mobile phase

Partitioning from mobile phase into stationary phase

Stationary phase

Solute concentration in stationary phase
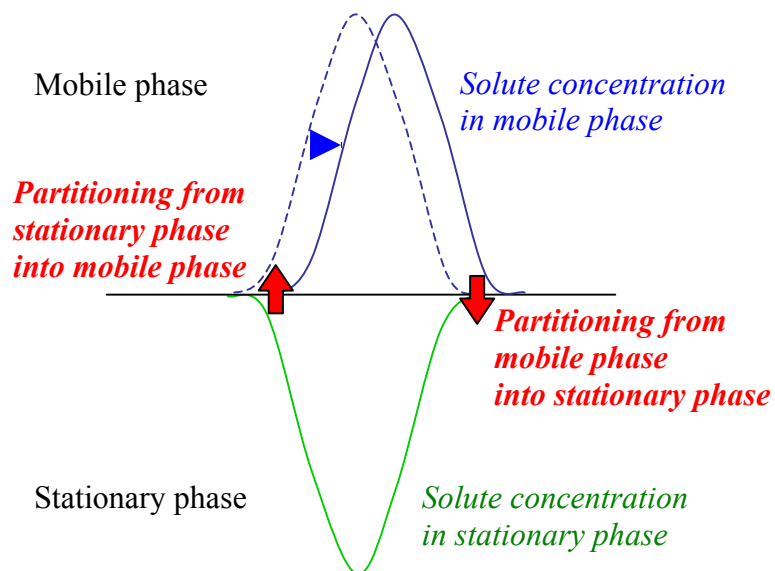
Figure 2-6. Principle of elution chromatography

Two things must be noted in terms of elution chromatography. First, analytes are diluted due to diffusion while they are traveling through the column. In another words, the bandwidth of each analyte peak is broadened with time. This is related to column efficiency and will be discussed more in Chapter 3. Second, column temperature is critical to the analysis because the vapor pressure and consequently the distribution constant, K_C, highly depends on the temperature as shown in Equation 2-2. If the column temperature is too low, K_C becomes too high and as a result the solutes remain largely in the stationary phase. They neither separate from each other nor elute from the column. If

the column temperature is too high, K_C becomes too low and the solute spends most of their time in the mobile phase. As a result, the solutes will elute from the column as an non-separated mixture.

Solvents

1. Isopropanol
2. Unknown
3. Methyl ethyl ketone
4. Ethyl acetate
5. n-Butyl alcohol
6. Ethyl cellosolve
7. Methyl isobutyl ketone
8. Toluene

9. n-Butyl acetate
10. Diacetone alcohol
11. p-Xylene
12. Cellosolve acetate
13. o-Xylene
14. Butyl cellosolve
15. Butyl cellosolve acetate

200°C (2 min)

5°C/min

70°C

25 min

Carrier:	Helium, 30 psi
Column:	HP-1 (Cross-Linked Methyl Silicone), 50 m x 0.2 mm x 0.52 µm (Part No. 19091Z-205)
Injection:	Split, 1 µl
Oven:	Temperature program listed above
Detector:	TCD

Figure 2-7. Example chromatogram.

.

$$\log K_C = \frac{A}{T_C} + B$$

Equation 2-2

Therefore, column temperature is an important variable that must be controlled to a few tenths of a degree for precise work. The optimum column temperature depends

upon the boiling point of the sample and the degree of separation required. Roughly, a temperature equal to or slightly above the average boiling point of a sample is ideal to obtain a reasonable elution time. For a sample with a broad boiling range, it is often desirable to employ temperature programming, where the column temperature is increased either continuously or in steps as the separation proceeds. Figure 2-8 shows the improvement in a chromatogram brought about by temperature programming.
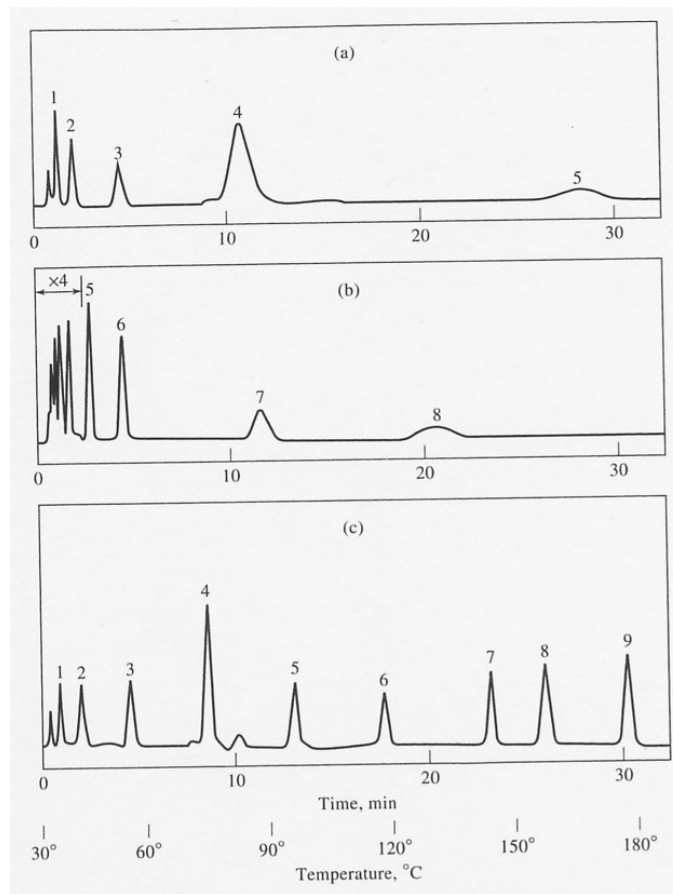
Figure 2-8. Effect of temperature on gas chromatogram: (a) isothermal at 45 $^{\circ}$C; (b) isothermal at 145 $^{\circ}$C; (c) programmed at 30 $^{\circ}$C to 180 $^{\circ}$C. [8]

2.2.2 PACKED COLUMN AND OPEN TUBULAR COLUMN

In elution gas chromatography, the function of the column is to expose the stationary phase to the mobile phase in order to guarantee an optimum separation through maximum repeated partition steps between these two phases. GC columns can be classified into two big categories – packed columns and open tubular (or "capillary") columns. Packed columns are densely packed with a uniform packing material, which is coated with a thin liquid stationary phase. Open tubular columns have a thin stationary phase coating on the wall surface.

The open tubular column is capable of separations that are vastly superior to those obtained on packed columns. The short capillary analysis deliver separation equivalent to that obtained in the much longer packed column analysis as shown in Figure 2-9. The capillary resolution is superior. Integrated peak areas from the packed column analysis will include appreciable solvent contributions. The solute peaks are well removed from the solvent in the capillary analysis, and quantification will be enhanced.

(a)   (b)
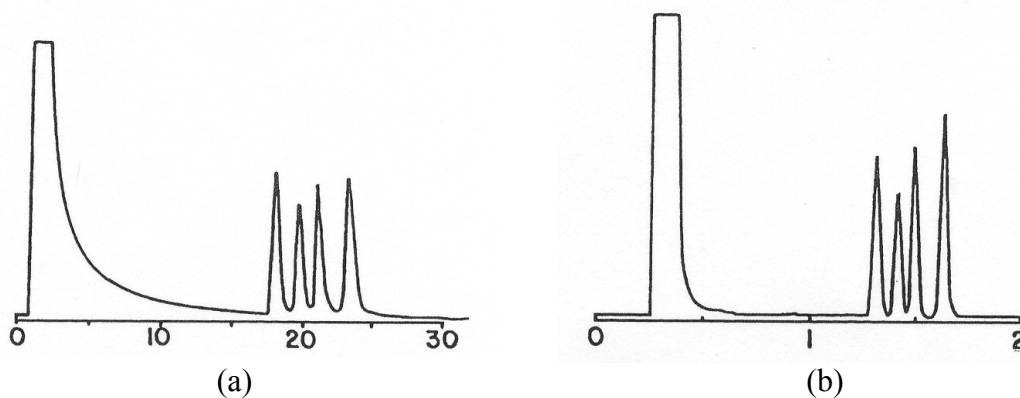
Figure 2-9. Chromatograms of a mixture of methyl benzoates: (a) packed column analysis (25 min); (b) 1.7 m x 0.25 mm glass capillary analysis (1.7 min). [7]

The striking difference between the two sets of chromatographic results is best attributed in the degree of randomness exhibited by identical molecules of each individual solute. These behavioral differences between identical molecules can be attributed to three factors [7].

First, the packed column offers solute molecules a multiplicity of flow paths but the open tubular column has a single flow path and molecules would be expected to exhibit mobile phase residence times that were much more nearly identical.

Second, there is much more stationary phase in the packed column, and the film thickness is not uniform. As a result, the times that identical molecules of a given solute spent in the stationary phase would be quite diverse. But in the open tubular column, the stationary phase is in a thinner and much more uniform film. Hence, the range of times that identical molecules spent in the stationary phase would be expected to be much narrower.

Third, packed column support materials are poor heat conductors and a temperature range must exist across any transverse section of the packed column. As a result, the solute molecules whose flow path is down the center of the packed column will be at a lower temperature, exhibit lower vapor pressures, and spend more of their time in the stationary phase than will identical molecules whose flow path are closer to the column wall. However in the fused silica column, the stationary phase exists as a thin film of very low thermal mass. There should be no temperature variation across any transverse section of the column.

2.2.3 STATIONARY PHASE

Clearly, to be useful in gas-liquid chromatography, the stationary phase must generate different distribution constants for different solutes. In addition, these constants must not be extremely large or extremely small because the former lead to prohibitively long retention times and the latter result in such short retention times that separation are incomplete. To have a reasonable residence time in the column, a species must show some degree of solubility with the stationary phase. Here, the principle of "like dissolves like" applies, where "like" refers to the polarities of the solute and the stationary phase. Hydrocarbon-type stationary phases and dialkyl siloxanes are nonpolar, whereas polyester phases are highly polar. Polar stationary phases contain functional groups such as -CN, -CO, and -OH. Polar solutes include alcohols, acids, and amines; solutes of medium polarity include ethers, ketones, and aldehydes. Saturated hydrocarbons are nonpolar. Generally, the polarity of the stationary phase should match that of the sample components. When the match is good, the order of elution is determined by the boiling point of eluents.

Table 2-1 lists the most widely used stationary phases for both packed and open tubular column GC in order of increasing polarity. Five of the stationary phases listed in Table 2-1 are polydimethyl siloxanes that have the general structure:
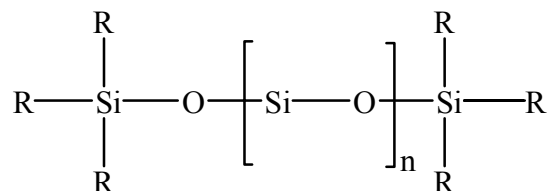
In polydimethyl siloxane, the –R groups are all –CH$_3$, resulting in nonpolar stationary phase. In the other polysiloxanes a fraction of methyl groups are replaced by functional groups such as phenyl (-C$_6$H$_5$), cyanopropyl (-C$_3$H$_6$CN), and trifluoropropyl (-C$_3$H$_6$CF$_3$). The fifth entry in Table 2-1 is a polyethylene glycol that finds widespread use for separating polar species. The molecular structure of polyethylene glycol is shown below.

$$HO—CH_2—CH_2 \left(O—CH_2—CH_2 \right)_n OH$$
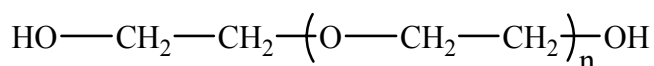
Table 2-1. Some common stationary phases for gas-liquid chromatography. [9]

Stationary Phase	Trade Name	Common Application
Polydimethyl siloxane	OV-1, SE-30	Hydrocarbon; polynuclear aromatics; drugs; steroids; PCBs
Poly(phenylmethyldimethyl) siloxane (10% phenyl)	OV-3, SE-52	Fatty acid methyl esters; alkaloids; drugs; halogenated compounds
Poly(phenylmethyl) siloxane (50% phenyl)	OV-17	Drugs; steroids; pesticides; glycols
Poly(trifluoropropyldimethyl) siloxane	OV-210	Chlorinated aromatics; nitroaromatics; alkyl-substituted benzenes
Polyethylene glycol	Carbowax 20M	Free acids; alcohols; ethers; essential oils; glycols
Poly(dicyanolallyldimethyl) siloxane	OV-275	Polyunsaturated fatty acids; rosin acids; free acids; alcohols

With use, columns slowly lose their stationary phase due to "bleeding", in which small amount of stationary phase is carried out of the column during the elution process. Therefore commercial columns generally have bonded and/or cross-linked stationary phases. The purpose of bonding and cross-linking is to provide a longer-lasting stationary phase that can be rinsed with a solvent when the film becomes contaminated.

Commercial columns are available having stationary phases that vary in thickness from 0.1 to 5 μm. Film thickness primarily affects the retentive character and the capacity of a column. Thick films are used with highly volatile analytes because such films retain solutes for a longer time.

2.2.4 OTHER COMPONENTS OF GAS CHROMATOGRAPH

2.2.4.1 INJECTION SYSTEMS

Column efficiency requires that the sample be of suitable size and be introduced as a "plug" of vapor; slow injection of oversized samples causes band spreading and poor resolution. The most common method of sample injection involves the use of a microsyringe to inject a liquid or gaseous sample through a septum into a flash vaporizer port located at the head of the column. For ordinary analytical columns, sample sizes vary from a few tenths of a microliter to 20 μL. Capillary columns require much smaller samples ($\sim 10^{-3}$ μL); here, a sample splitter system is employed to deliver only a small fraction of the injected sample to the column head, with the remainder going to waste. For quantitative work, more reproducible sample sizes for both liquids and gases are obtained by means of a rotary sample valve which has a sample loop of a certain volume.

2.2.4.2 DETECTORS

The ideal detector for GC has adequate sensitivity, reproducibility, linear response to solutes, short response time, reliability, and nondestructive detection. The sensitivity of present-day detectors lies in the range of 10^{-8} to 10^{-15} g solute/s. The most popular detectors are flame ionization detectors, thermal conductivity detectors, and electron capture detectors.

The flame ionization detector (FID) is the most widely used for GC. With a burner, the effluent from the column is mixed with hydrogen and air and then ignited electrically. Most organic compounds produce ions and electrons when pyrolyzed at the flame. A potential of a few hundred volts is applied across the burner tip and a collector electrode located above the flame. The number of ions produced is roughly proportional to the number of reduced carbon atoms in the flame. Functional groups, such as carbonyl, alcohol, halogen, and amine, yield fewer ions or none at all in a flame. In addition, the detector is insensitive toward noncombustible gases such as H_2O, CO_2, SO_2, and NO_x. These properties make the FID a most useful detector for the analysis of most organic samples, including those that are contaminated with water and the oxides of nitrogen and sulfur. The FID exhibits a high sensitivity ($\sim 10^{-13}$ g/s), large linear response range ($\sim 10^7$) and low noise. A disadvantage of the FID is that it destroys the sample.

A thermal conductivity detector (TCD), sometime called a katharometer, is based upon changes in the thermal conductivity of the gas stream brought about by the presence of analyte molecules. The sensing element of a TCD is an electrically heated element whose temperature depends on the thermal conductivity of the surrounding gas. The thermal conductivities of helium and hydrogen are roughly six to ten times greater than

31

those of most organic compounds. Thus, in the presence of even small amount of organic materials, a relatively large decrease in the thermal conductivity of the column effluent takes place; consequently, the detector undergoes a marked rise in temperature. The advantage of the TCD is its simplicity, its large linear response range ($\sim 10^5$), its general response to both organic and inorganic species, and its nondestructive character. A limitation of the TCD is its relatively low sensitivity ($\sim 10^{-8}$ g solute/mL carrier gas).

The electron-capture detector (ECD) has become one of the most widely used detectors for environmental samples because this detector selectivity detects halogen containing compounds, such as pesticides and polychlorinated biphenyls. An electron from an emitter causes ionization of the carrier gas and the production of a burst of electrons. In the absence of organic species, a constant standing current between a pair of electrodes results from this ionization process. The current decreases markedly, however, in the presence of those organic molecules that tend to capture electrons. The ECD is highly sensitive to molecules containing electronegative functional groups such as halogens, peroxides, quinines, and nitro groups. It is insensitive to functional groups such as amines, alcohols, and hydrocarbons.

There are other commercially available detectors such as atomic emission detector (AED), sulfur chemiluminescence detector (SCD), thermionic detector (TID), flame photometric detector (FPD), and photoionization detector (PID). The SCD is particularly useful for the determination of pollutants such as mercaptans and the TID is selective toward organic compounds containing phosphorous and nitrogen. GC is often coupled with the selective techniques of spectroscopy and electrochemistry, thus giving so-called hyphenated methods that provide the chemist with powerful tools for identifying the

components of complex mixtures. For example, GC can be directly interfaced with mass spectrometer (GC-MS), Fourier transform infrared spectrometers (GC-FTIR), or ion mobility spectrometers (GC-IMS).

2.3 OVERVIEW OF MINIATURE GAS CHROMATOGRAPHY

2.3.1 HISTORY AND TRENDS

Table 2-2 shows the history of the miniature GC. The first miniature GC was reported by Terry in 1970's [1, 2]. The first miniature GC system consisted of a sample injection valve and a 1.5 m long separation column fabricated on a 2 inch dia silicon wafer. The separation column was etched by isotropic wet etching and anodically bonded to a pyrex glass plate. The cross section of the column was U-shape, with a width of 200 μm and a typical depth of 30 μm. The completed silicon/glass column was then lined with a commercial stationary phase (OV-101). A thermal conductivity detector (TCD) was separately batch fabricated and mechanically clamped to the column wafer. The separation of a hydrocarbon mixture with this GC system was reported and the number of theoretical plates for the peaks ranged from 385 to 2300.

Table 2-2. History of micro GC.

Author	Column	Dimension	Stationary phase	Injector/Detector	Test
Terry, 1979 Stanford Univ.	Silicon/glass (wet etching)	200 μm x 30 μm x 1.5 m	OV-101	Solenoid- actuated diaphragm valve/ Micromachined TCD	Hydrocarbons in 10s
Bruns, 1992 Microsensor Technology, Inc.	Silica column	150 μm x 4 ~10 m	OV-1 DB-5	Pneumatically actuated diaphragm/ Micromachined TCD	Solvents, pollutants in 1 min
Reston & Kolesar, 1994 Air Force Institute of Tech.	Silicon/glass (wet etching)	300 μm x 10 μm x 0.9 m	CuPc (Evaporation)	Commercial gas sample valve/ micromachined thermoresistor & TCD	NH_3 and NO_2 in 30 min
Hannoe & Sugimoto, 1997 NTT Lab., Japan	Silicon/glass (wet etching)	100 μm x 10 μm x 2 m	Fluorocarbon (Sputtering)	Mass spectrometer (GC/MS)	N/A
Wiranto, 1999 Univ. of South Australia	Silicon/glass (wet etching)	100 μm x 20 μm x 1.25m	PDMS	FID (HP5890)	Hydrocarbon mixture in 1.25 min
Frishman & Amirav, 2000 Tel Aviv Univ., Israel	Silica column	320 μm x12cm	OV-1	Pulsed flame photometric detector (PFPD)	CWA simulants in 1.5 min
Nieradko & Malecki, 2000 Wroclaw Univ., Poland	Silicon/glass (wet etching)	35 μm x 11 μm x 30 m	Squalan	FID (HP5890) or Pneumatic injection valve/ coil katharometer	Hydrocarbon mixture in 20 min
Lehmann, 2000 SLS MicroTech, Germany	Silicon/glass (wet etching)	N/A 0.86 m	PDMS (PECVD)	Electromagnetically driven injector/ micromachined TCD	N/A
Frye-Mason, 1998-2001 Sandia National Lab.	Silicon/glass (dry etching)	40 μm x 250 μm x 1 m	OV-1	Preconcentrator SAW array	Hydrocarbon mixture DMMP in 1 min
Najafi, 2003 Univ. of Michigan	Silicon/glass (dry etching)	150 μm x 260 μm x 3m	OV-1	Preconcentrator-focuser Chemiresistor array	Hydrocarbon mixture in 1.5 min

This first miniature GC system has improved on for 20 years [10], creating a new family of portable and fast GC. In 1995-96 a series of portable GC's, manufactured by MTI Analytical Instruments was introduced onto the market. The portable GC was equipped with micromachined diaphragm valves and thermal conductivity detectors. However, narrow-bore fused silica capillary columns were used in these systems instead of a micromachined silicon/glass column. The performance was fairly good and they demonstrated the separations of solvent mixture, pollutant mixture, permanent gas mixture and hydrocarbon mixture by using different narrow-bore fused silica capillary columns that had different stationary phases. Although it was not a completely micromachined system, this first portable GC enabled innovative applications; for example, the analysis of astronomical objects in laboratories on the Earth orbit. The Columbia space shuttle was equipped with very fast micro GC MTI Quad analyzer and the data was transmitted to the Earth by microcomputer [11]. MTI Analytical Instruments was later merged to HP-Agilent Technologies and still manufactures portable GC systems as shown below. However, it must be noted that the commercial portable GC systems are still equipped with glass capillary columns.
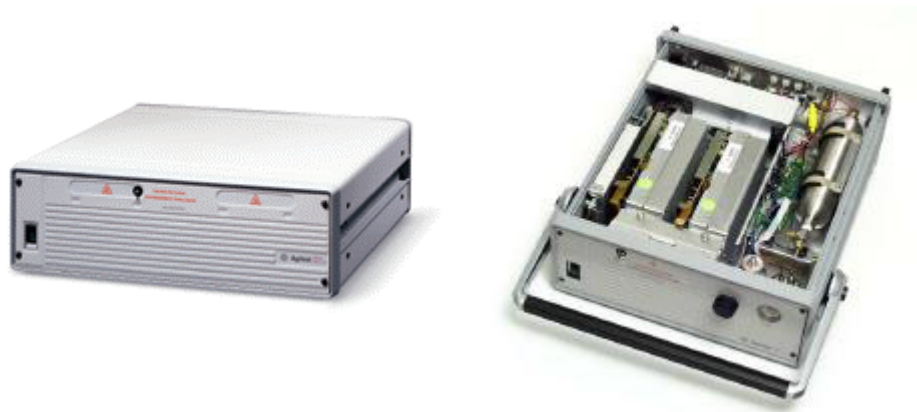
Figure 2-10. Commercial portable GC (3000 Micro GC, Agilent Technologies).

Reston and Kolesar [12, 13] reported another micromachined GC system for the separation and detection of ammonia and nitrogen dioxide. The 0.9 m long rectangular column with a width of 300 μm and a height of 10 μm was fabricated by isotropic wet etching and anodic bonding. A 0.2 μm thick copper phthalocyanine (CuPc) was deposited from gas phase and it was used as a stationary phase. The advantage of the vapor deposited solid stationary phase is its better thickness uniformity. In addition, stationary phase deposition can be completed in much more convenient way before anodic bonding. However, the solid stationary phase limits the application of the GC system because of its high selectivity. A commercial gas sample valve and a dual detector (a CuPc coated chemiresistor and a thermal conductivity detector) were employed for nitrogen dioxide detection. They demonstrated the separation of ammonia and nitrogen dioxide in less than 30 min.

Hannoe and Sugimoto [14] introduced a micromachined silicon/glass column that had a sputtered fluorocarbon film as a stationary phase. The silicon channel was etched using a mixture of hydrofluoric, nitric, and acetic acid and had very smooth surface. Simple and small dead-volume joint between silica tube and column end was achieved using ultrasonic machining. This column was installed in conventional GC-MS and a sharp methane peak was obtained.

Wiranto [4] also reported a micromachined silicon/glass column which is 100 μm wide, 20 μm deep and 125 cm long column. A commercial stationary phase was coated inside the silicon/glass column by conventional dynamic coating method and then the column was installed in a commercial GC system (HP 5890), replacing fused silica capillary column. Performances of the micromachined silicon/glass columns have been

36

demonstrated by their ability to completely separate a series of hydrocarbon mixture (C_{11}

to C_{16}) in less than 1.25 min under the isothermal condition of 150 ^{o}C

Frishman and Amirav [15] reported a hand-held GC for field analysis of chemical

warfare agents (CWA) for the first time. The GC was equipped with a pulsed-flame

photometric detector (PFPD). The GC had both fast repetitive analysis mode and

continuous sampling "sniff" mode. Fast repetitive analysis was demonstrated with a

cycle time of 30 seconds, combined with very low detection limits of 20 ng/m^3 for

organophosphorus CWA simulants and 200 ng/m^3 for organosulfur compounds. The

system inlet was heated and the sample path was inert without any metal, enabling fast

response time and low detection limits for a low volatility agent such as VX. They used a

short (1.5 m) silica capillary column, which was inserted into a metal tube and arranged

in four circular loops with 13 cm diameter on a structural support. The other components

were not made by micromachining, either.

Nieradko and Malecki [5] have been developing a multi-chip, integrated GC

system. The multi-chip module consists of isotropically etched silicon/glass column,

pneumatic injection valve with floating Teflon foil, and thermoelectric katharometric

detector for microflow analysis. The katharometric detector consists of microchannel and

platinum wire and the resistance change of the platinum wire is monitored. The

prototype of each part was fabricated separately and integrated into a multi-chip module.

The column was fabricated on 3" wafer with dimensions of minimum 35x11 μm^2 to

maximum 300x150 μm^2. The length ranges from 12 to 30 m. This long micromachined

column was tested in a conventional GC (HP 5890) and showed the separation of

aliphatic and aromatic hydrocarbon mixture in 20 min.

Lehmann *et al*. [16, 17] in SLS Micro Technology GmbH, Germany recently presented a hand-held GC system which consists of micro TCD detector, electromagnetically driven sliding injector, and a micromachined silicon/glass column. Their column has a plasma polymerized polydimethylsiloxane (PDMS) like layer as a stationary phase. Three major units: detector, injector, and column, were integrated on a credit card sized mother board as shown below. However, they have not reported any separation results yet.
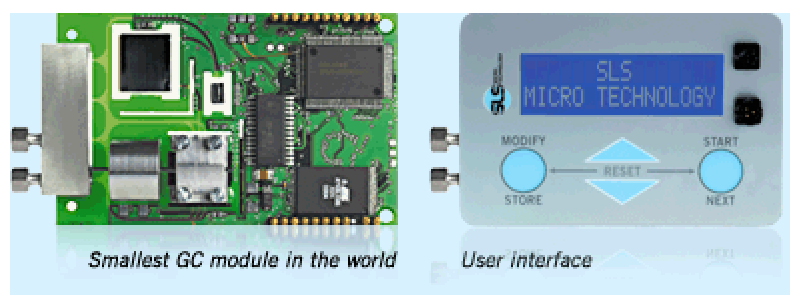
Figure 2-11. A hand held GC system from SLS Micro Technology GmbH.

Sandia National Laboratories has also been developing a miniature, integrated chemical laboratory (μChemLab) that can provide faster response, smaller size, and an ability to utilize multiple columns for enhanced versatility and chemical discrimination [3, 18-20] The main application of this system is the trace detection of selected target analytes such as CWA and explosives. In this application, rapid analysis can be critical to provide early warning. Therefore the μChemLab program has a goal to develop small (palm-top computer-sized), lightweight, and autonomous systems that provides rapid (1 min), sensitive (1-10 ppb), and selective detection of target analytes. To achieve this goal,

they have developed a micromachined sample collector/concentrator, a silicon/glass

column, and a chemically selective surface acoustic wave (SAW) array detector.
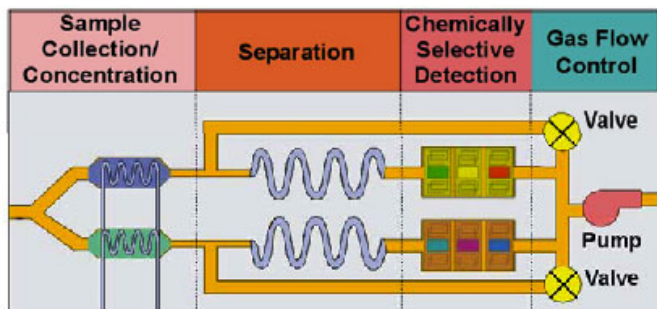
Figure 2-12. µChemLab of Sandia National Laboratories.

Their GC columns were fabricated using high aspect ratio silicon etching

(HARSE) to have narrow and deep cross-section (40 µm wide and 250 µm deep). With

only 4 psi of pressure, separation of dimethyl methyl phosphonate (DMMP: a nerve agent

simulant) from toluene and xylene was demonstrated. It was also reported that using a

slightly higher temperature (80 $^{\circ}$C), the same separation could be achieved in less than 30

seconds. They have developed an analytical tool that models the transport and surface

interaction process to achieve an optimized design of the GC column. They also have

investigated gas flow in long capillary tubes to characterize the flow behavior.

Another research group developing a miniature GC is the Engineering Research

Center for Wireless Integrated MicroSystems at the University of Michigan [21]. Their

goal is developing a microsystem that can monitor temperature, pressure, humidity, and

gas composition with part-per-billion sensitivity. The system consists of a pre-concentrator, separation column, a chemiresistive sensing array, a vacuum pump, and integrated microvalves. Figure 2-13 shows the conceptual drawing of the microGC of the University of Michigan. The final system is targeted to be able to analyize 30+ VOC's in less than 10 min.
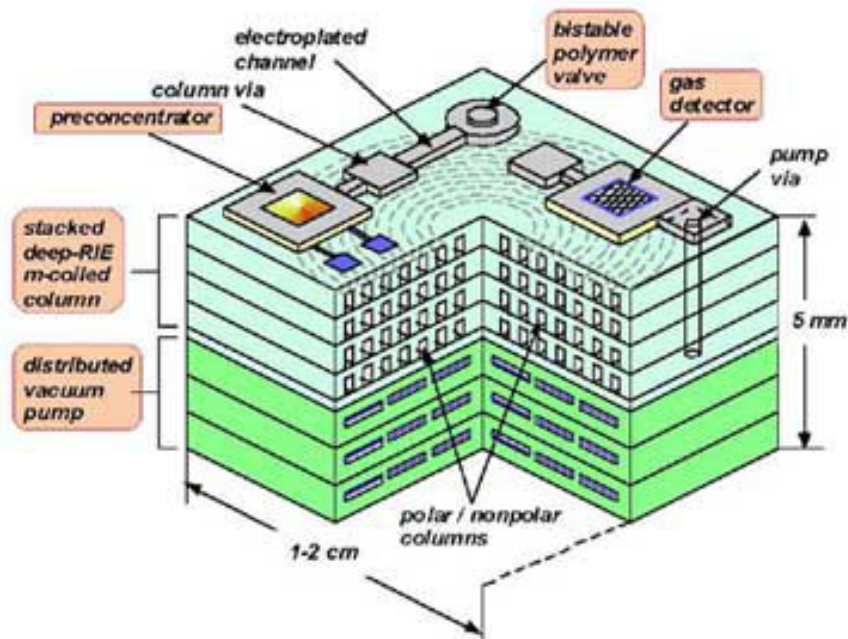
Figure 2-13. Conceptual drawing of the 10-yr microGC of the University of Michigan [http://www.eng.nsf.gov/eec/erc/directory/erc_r.htm].

2.3.2 SEPARATION COLUMN

Although each component is important in a GC system, the efficiency of a GC system depends primarily on the separation column efficiency. Conventional bench-top

GC systems use fused silica capillary columns, and even some commercial portable GC systems have short versions of fused silica capillary columns. However, for a miniature GC system, micromachined silicon/glass columns have been used because they can provide smaller sizes, lower power consumption for heating, and an ability to integrate other components on a single chip.

The micromachined silicon/glass columns are fabricated by etching microchannel on silicon wafer followed by anodic bonding with a Pyrex glass substrate. Silicon microchannels can be fabricated by either isotropic wet etching or anisotropic plasma etching. Figure 2-14 (a) shows examples of each case. Wet etching generally produces a wide and shallow channel but the surface is very smooth. On the contrary, deep RIE etched silicon microchannel provides improved ruggedness but worse surface roughness as shown in Figure 2-14. Recently, a thin walled silicon/glass column was also reported [21]. They diffused boron to the deep RIE etched silicon microchannel to form p++ etch stop about 10 μm deep. A pyrex glass was then bonded to the silicon substrate followed by ethylene diamine pyrocatechol (EDP) etching.

Can a micro GC column work better than a conventional GC column? This is an important question that needs to be addressed. The classical Golay's equation can be used with some modifications to investigate the separation efficiency of micromachined columns. Spangler [22-24] also developed a theory for the height equivalent to a theoretical plate (HETP) of a micromachined rectangular GC column. According to this theory, rectangular columns can have lower HETPs and higher volumetric flow than conventional capillary columns for a given column length. A good rule of thumb is that the resolution can be adjusted by selecting the column height (provided it is much less

41

than the column width), and the volumetric flow of carrier gas can be adjusted by selecting the column width (or cross-sectional area).

(a)   (b)
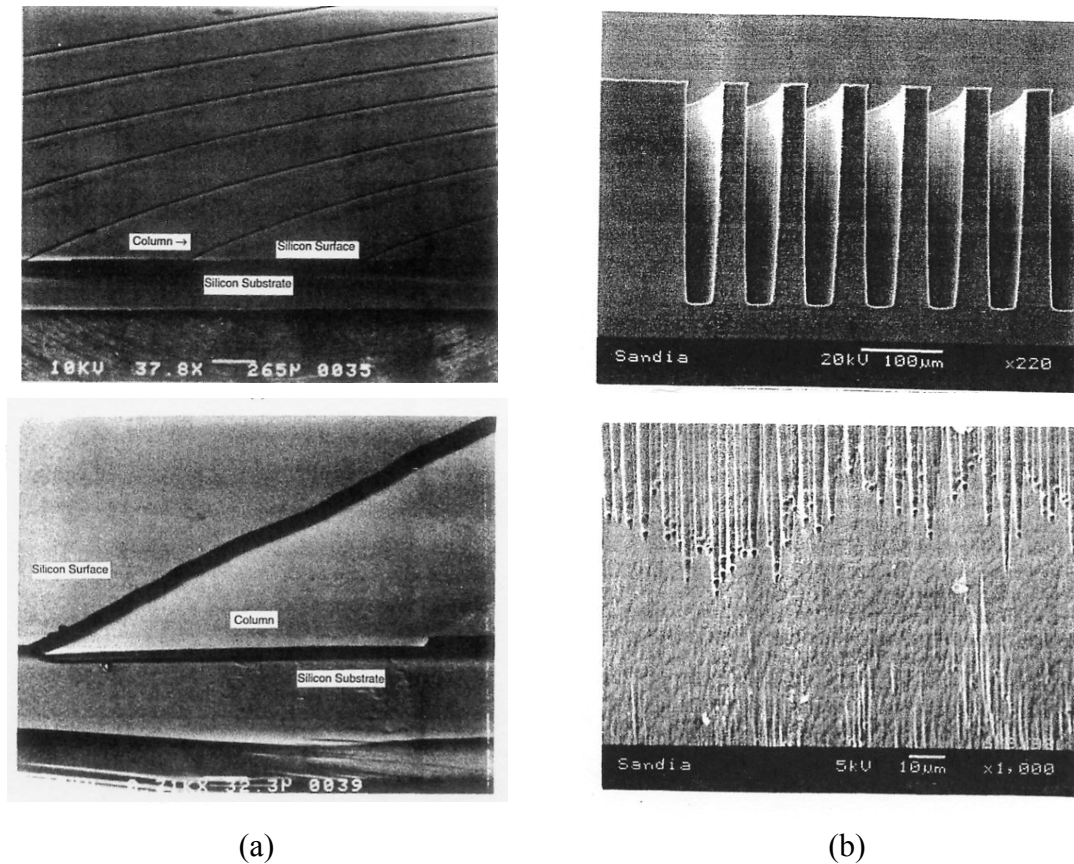
Figure 2-14. Micromachined silicon microchannel, (a) wet etched channel [12], (b) dry etched channel [3].

Sandia National Laboratories developed an analytical model and a computer simulation tool for this purpose [19]. The analytical model consists of a flow module and a separation module. The flow module models compressibility and slip flow effects, which are significant in gas flow in a long and narrow column. The separation module predicts column performance based on the modified Golay equation. Both models have performed well against experimental data. Computational simulations have been performed to investigate the geometric effect on analyte transport, which the analytical

models fail to capture. Simulation flow could capture the complex flow and transport dynamics better than the analytical models. However, if the condition changes, a wider column and/or a larger flow velocity, complex flow structure can be generated from the curvature of the column, leading to a substantial band spreading, which will degrade the chromatographic performance. According to Sandia's analytic model, the performance of GC depends on the ratio of length-to-width of the column. As the size of the column decreases, one can achieve a similar performance (same number of theoretical plates) with a shorter column [19]. Three characteristics in micromachined GC column are: a high-aspect-ratio rectangular channel, to achieve the desired volumetric flow rate and also to maximize the surface area-to-volume ratio; a length-to-width ratio of about 20,000 to obtain an efficient separation; a tight spiral configuration in order to fit the long column onto a small area.

The stationary phase is the key element of GC column. The general methods of coating stationary phase in conventional fused silica glass column are pumping or withdrawing a solution through the column. The former is called the 'dynamic method' and the latter 'static method'. The solution contains certain solutes that can be used as stationary phase. While the solution passes through the column, the solute is deposited on the column wall, forming the stationary layer. These conventional methods have been used in micromachined silicon/glass column. However, the coating quality is not as good as in fused silica column. The micromachined silicon/glass columns usually have rectangular cross section and rough surface, resulting in non-uniform coating. This issue has been addressed and some surface treatment has been investigated to improve the coating uniformity [3]. The better solution for coating uniformity is the direct deposition

43

from a gaseous phase. Kolesar *et al.* deposited a solid stationary phase, CuPc (Copper Phthalocyanine), in silicon microchannel using thermal evaporation [12]. As other solid adsorbent phases, CuPc has the inherent selectivity of detecting some gases such as nitrogen dioxide and ammonia. Sugimoto *et al.* reported another solid stationary phase, plasma-polymerized fluoropolymer deposited by RF sputtering [25]. This film exhibits swelling in VOCs but little response to water vapor. This discriminatory character makes it attractive for environmental sensing applications. Lehmann *et al.* used PECVD to deposit PDMS-like film on their micromachined silicon microchannel [17]. This method is very promising because the structure of final film resembles that of polydimethylsiloxane (PDMS), which is the standard in gas chromatography. Also, good step coverage on the side wall was obtained by the PECVD process.

2.4 PARYLENE IN MICROELECTROMECHANICAL SYSTEMS

2.4.1 INTRODUCTION TO PARYLENE

Parylene conformal coating technology, originally developed by Union Carbide, has been in commercial use for more than 25 years. Parylene (poly(p-xylylene)) is an insulating thermoplastic polymer film that has a high degree of chemical inertness, absence of pinholes and perfect conformity to the topography of the surface applied. This class of polymer has been used for decades on a variety of applications – especially those involving the protection of electronic devices and circuitry.

Parylene coating process is best described as a vapor deposition polymerization (VDP) (Figure 2-15). The dimer obtained by the direct pyrolysis of p-xylene is very stable compound. This dimer can be evaporized into vapor phase at around 170 $^{\circ}$C. Then the dimers are pyrolyzed into monomers at around 650 ~ 700 $^{\circ}$C. The monomer molecule is thermally stable, but kinetically very reactive toward polymerization with other molecules of its kind. On condensation it polymerizes spontaneously to produce a coating of high molecular weight, linear poly(p-xylylene).
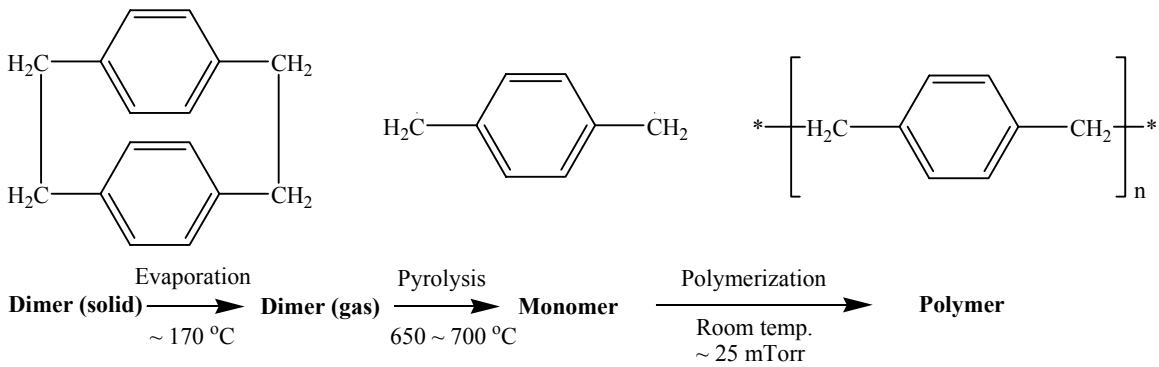
Figure 2-15. Parylene deposition process.
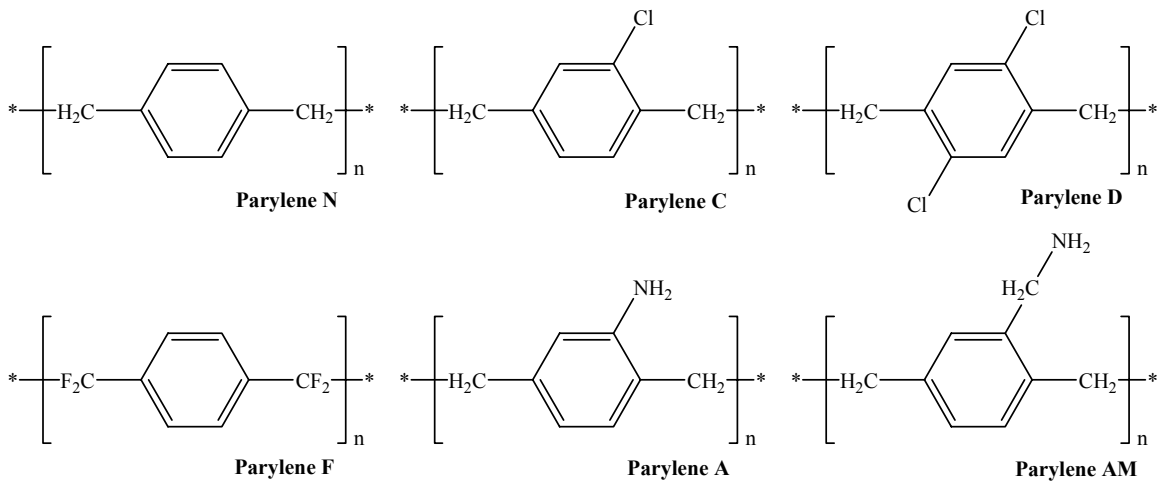
Figure 2-16. Molecular structures of parylenes.

45

Substitutes can be attached to the ring positions of the dimer, di-p-xylylene (DPX). Although a variety of substituted dimers are known in the literature, at present only, DPXN, DPXC, and DPXD are commercially available, which give rise to Parylene N, Parylene C, and Parylene D, respectively. Parylene A, Parylene AM, and Parylene F will be also commercially available in a near future. Different functional groups produce different material properties. Figure 2-16 shows the molecular structures of different parylenes.

The physical processes of condensation and diffusion must be considered along with the p-xylylene polymerization chemistry for a proper understanding of what happens microscopically during vapor deposition polymerization. A gaseous monomer is transported to the location within the coating where it is to be consumed to produce polymer by an initial condensation, followed by diffusion. The monomer is consumed by initiation and propagation, in which existing polymer molecules are extended to a higher molecular weight. In steady-state VDP, both reactions proceed continuously inside polymeric coating, in the reaction zone just behind the growth interface. The concentration of monomer within the coating decreases approximately exponentially with distance from the growth interface. With this decrease in monomer concentration, the rates of initiation and propagation reactions also decrease. Under conditions prevailing during a typical deposition, the characteristic depth of the reaction zone is a few hundred nanometers, and the maximum concentration of monomer, ie., the concentration at the growth interface, is of the order of a few tenths percent by weight [26]. During the vapor deposition process, the polymer chain ends remain truly alive, ceasing to grow only when they are so far from the growth interface that fresh monomer can no longer reach them.

2.4.2 MATERIAL PROPERTIES OF PARYLENE

The engineering properties of commercial parylenes are summarized in Table 2-3. As crystalline polymers, the parylenes retain useful physical integrity up to temperatures approaching their crystalline melting points. However, their glass transition temperature (T_g), the temperature over which the amorphous phase changes from a rigid condition to a more flexible, rubbery condition, are known to be $60 \sim 150\,^{\circ}C$ [27, 28].

During formation, the motions of the parylene polymer chains in the vitreous medium are restricted. The properties of freshly deposited parylenes, therefore, generally differ from those that have been aged or annealed. Restricted polymer chain motion during VDP severely limits their ability to organize into crystallites, and consequently, freshly deposited parylenes are metastable. With the passage of time, and sooner if heated, they will reorganize into a thermodynamically more satisfactory configuration, increasing crystallinity. Certain physical properties of freshly deposited parylenes therefore can be expected to change upon aging or annealing. In general, an increase in crystallinity with aging or annealing results in a lowering of elongation to break and an increase in modulus and strength.

The as-deposited stress of parylene C was found to be compressive. The stress is about -6 MPa [28, 29]. As it is heated, the stress becomes more compressive initially from the as-deposited value of -6 to -15 MPa. Above $100\,^{\circ}C$ the stress remains practically the same at -14 MPa. This is due to the flow above T_g. Upon cooling, the stress becomes more tensile and increases to about +21 MPa when the cooling rate is slow. If it is rapidly cooled, the polymer does not have enough time to flow and thus higher stress results.

Table 2-3. Properties of commercial parylenes [27].

Property	Parylene N	Parylene C	Parylene D
General			
Density [g/cm^3]	1.110	1.289	1.418
Refractive index	1.661	1.639	1.669
Mechanical			
Tensile modulus [GPa]	2.4	3.2	2.8
Tensile strength [MPa]	45	70	75
Yield strength [MPa]	42	55	60
Elongation to break [%]	30	200	10
Coefficient of friction, static/dynamic	0.25/0.25	0.29/0.29	0.35/0.31
Thermal			
Melting point [^{o}C]	420	290	380
Glass transition point [^{o}C]	< 90	< 90	< 90
Coefficient of expansion at 25 ^{o}C [K^{-1}]	6.9 x 10^{-5}	3.5 x 10^{-5}	
Heat capacity at 25 ^{o}C [J/(g·K)]	1.3	1.0	
Thermal conductivity at 25 ^{o}C [W/(m·K)]	0.12	0.082	
Electrical			
Dielectric constant at 60 Hz	2.65	3.15	2.84
at 1 kHz	2.65	3.10	2.82
at 1 MHz	2.65	2.95	2.80
Dissipation factor at 60 Hz	0.0002	0.020	0.004
at 1kHz	0.0002	0.019	0.003
at 1MHz	0.0006	0.013	0.002
Dielectric strength at 25 μm [MV/m]	235 – 275	185 - 220	215
Volume resistivity at 23 ^{o}C, 50% RH [Ω·cm]	1.4 x 10^{17}	8.8 x 10^{16}	2 x 10^{16}
Surface resistivity at 23 ^{o}C, 50% RH [Ω·cm]	1 x 10^{13}	1 x 10^{14}	5 x 10^{16}
Barrier			
Water absorption [%]	< 0.1	< 0.1	< 0.1
Water vapor transmission at 37 ^{o}C [ng/(Pa·s·m)]	0.0012	0.0004	0.0002
Gas permeability at 25 ^{o}C [amol/(Pa·s·m)]			
N_2	15.4	2.0	9.0
O_2	78.4	14.4	64.0
CO_2	429	15.4	26.0

Figure 2-17 shows the life-time of parylene N, C, and D as a function of temperature both in air and in vacuum. The failure criterion means a 50% loss in tensile strength. In the degradation of many polymers, tensile strength is maintained until chain scission has reduced molecular weight to the point at which entanglement is no longer a factor in determining physical properties. Beyond that point it drops abruptly. The most important mode of degradation for parylenes is oxidative chain scission. Oxidative degradation limits the use of parylenes at elevated temperatures in many common applications. This data suggest that parylene C performs in air without significant loss of physical properties for 10 yr at the temperature below 100 $^{\circ}$C. For applications where oxygen can be excluded, Figure 2-17(b) shows that 10 year use projections exceed 200 $^{\circ}$C.
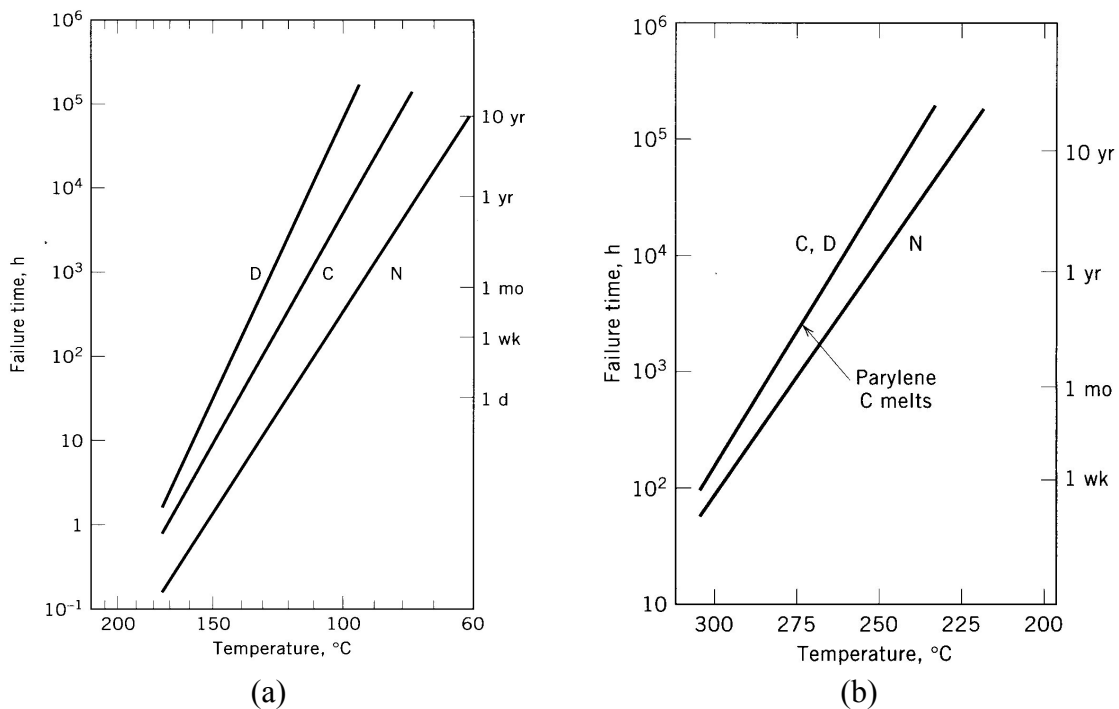
Figure 2-17 Life time of parylene N, C, and D as a function of temperature, (a) in air, (b) in vacuum.

The bulk electrical properties of the parylenes make them excellent candidates for use in electronic construction. The dielectric constants and dielectric losses are low and unaffected by absorption of atmostpheric water. The parylenes do not absorb visible light, and absorb only at the shorter wavelength, high energy end of the ultraviolet range. Films and coatings are colorless in the visible, becoming opaque to sufficiently short wavelength UV light. The surface energies of parylene were approximately 45 mJ/m^2. Plasma treatments using reactive gases (N_2, O_2) as well as inert gases (Ar, He) generate a carbonyl group on the surface and as a result, lower the contact angle for water.

The bulk barrier properties of parylenes are among the best of organic polymeric coatings. One of the most important parameter to decide solvent resistance is crystallinity. Because the crystalline domains are much more resistant to permeation than the amorphous phase, they retain their reinforcing structural role even in the presence of permeants in the amorphous phase. When a parylene film is exposed to a solvent, a slight swelling is observed as the solvent invades the amorphous phase. Table 2-4 shows the amount of swelling of parylene N, C, and D in various solvents.

Table 2-4. Swelling on immersion in various solvents for the commercial parylenes at room temperature [27].

Solvent	Volume change, %		
	Parylene N	Parylene C	Parylene D
Dichlorobenzene	0.2	3.0	1.8
Mixed xylenes	1.4	2.3	1.1
Monochlorobenzene	1.1	1.5	1.5
Trichloroethylene	0.5	0.8	0.8
Acetone	0.3	0.9	0.4
Pyridine	0.2	0.5	0.5
Isopropyl alcohol	0.3	0.1	0.1
Deionized water	0.0	0.0	0.0

2.4.3 APPLICATIONS OF PARYLENE IN MEMS

Traditionally parylene has been used as a coating material for many products such as electronics because of its conformal coating and low gas permeability. Also there was an effort to investigate parylene as a dielectric material for an interlayer connection [30, 31] . Yeh and Callahan pioneered patterning parylene using oxygen plasma etching. Recently, parylene has been drawing lots of attentions in MEMS because it is conformally deposited at room temperature. Parylene can be used as a structural material in MEMS as well as coating material. Particularly, it has been used to develop microfluidic devices that require thin membranes as a crucial part. Table 2-5 lists some of the representative devices made of parylene and the related techniques.

Y. C. Tai group at Caltech has developed various parylene microfluidic devices such as check valves [32, 33], nozzles [34], heat exchanger [35], a valved-skin for a micro-butterfly [36, 37], and neuro-cages [38]. These combine silicon bulk micromachining and parylene deposition/patterning to fabricate these devices. For free-standing structures, they also developed a method using photoresist as a sacrificial material. Positive photoresist is patterned on the parylene layer that has been deposited onto a substrate, and then another layer of parylene is deposited onto the photoresist pattern. The sacrificial photoresist can be removed in acetone leaving free-standing parylene structures.

Other groups also have been utilizing parylene in their MEMS devices. C. P. Wong group at Georgia Tech investigated parylene for MEMS device encapsulation [39]. E. S. Kim group at University of Hawaii applied a parylene membrane to acoustic devices. They reported a parylene-diaphragm piezoelectric acoustic transducers [40]. Our

group (Hesketh group) at Georgia Tech also has been working with parylene for last several years. A parylene/metal/parylene corrugated membrane was developed for electrochemical actuation [41] and ultra low pressure sensing [42]. A rapid and low-cost parylene micromolding technique was developed and applied to several applications such as a micro GC column [43, 44], microfluidic channels [45, 46], and wafer bonding [47, 48].

Table 2-5. Parylene in MEMS.

Authors	Application	Related Technique
Wang & Tai, 1999 Cal. Tech.	Micro check valve	Sacrificial photoresist
Grosjean & Tai, 1999 Cal. Tech.	Thermopneumatic valve	Silicone on parylene membrane heater
Wang & Tai, 1999 Cal. Tech.	Nozzle for electrospray	Overhanging parylene microcapillary
Wu & Tai, 1999 Cal. Tech.	Micro heat exchanger	Thermal insulation by parylene coating
Pornsin-Sirirak & Tai, 2000 Cal. Tech.	Flapping wing	Ti-alloy wing frame + parylene wing membrane
Wu & Wong, 2000 Georgia Tech.	MEMS device encapsulation	Material property investigation
Han & Kim, 2000 Univ. Hawaii	Piezoelectric acoustic transducer	Parylene diaphragm with electrode and piezoelectric film
Stanczyk & Hesketh, 2000 Univ. Illinois	Electrochemical actuator	Corrugated parylene/Pt/parylene membrane
Noh & Hesketh, 2002 Georgia Tech.	Miniature GC column	Parylene/parylene thermal bonding
He & Tai, 2003 Cal. Tech.	Parylene neuro-cages	Parylene anchors
Xie & Tai, 2003 Cal. Tech.	Mass flow controller	Electrostatic microvalve + thermal flow sensor
Noh & Hesketh, 2003 Georgia Tech.	Diaphragm pressure sensor	Parylene corrugated diaphragm with SU-8 rim
Noh & Hesketh, 2003 Georgia Tech.	Electrophoretic/dielectro-phoretic microchannel	Parylene micromolding
Noh & Hesketh, 2004 Georgia Tech.	Wafer bonding, MEMS packaging	Parylene bonding using microwave heating

CHAPTER 3

THEORETICAL COLUMN PERFORMANCE

Column performance is generally quantified by two terms, retention time and column efficiency (band broadening). These two terms decide the separation capability (resolution) of a GC column. Therefore, understanding the effects of parameters on the retention time and column efficiency is very important and must be done before designing a GC column. This involves the fluid mechanics of a gas flow in a microchannel and diffusion theory. In this chapter, the derivation of the formula for retention time and column efficiency for a rectangular GC column will be discussed, starting with the investigation of gas flow in a microchannel. Then, the effect of diverse parameters will be examined using the derived formula.

3.1 GAS FLOW IN MICROCHANNELS

In this section, the exact solutions to the average flow velocity and the flow distribution of a gas flow in a rectangular microchannel are sought. The difference between the exact solution and the simplified solutions is discussed. Compressibility, slip flow, and curvature effect are also discussed for a gas flow in a GC column.

3.1.1 POISEULLE FLOW

The motion for an incompressible Newtonian fluid can be described by 'Navier-Stokes equations' when the viscous effect is considered. For Cartesian coordinates, the equations are expressed as below for x, y, and z directions, respectively.

$$\rho\left(\frac{\partial u}{\partial t} + u\frac{\partial u}{\partial x} + v\frac{\partial u}{\partial y} + w\frac{\partial u}{\partial z}\right) = -\frac{\partial P}{\partial x} + \rho g_x + \mu\left(\frac{\partial^2 u}{\partial x^2} + \frac{\partial^2 u}{\partial y^2} + \frac{\partial^2 u}{\partial z^2}\right)$$

$$\rho\left(\frac{\partial v}{\partial t} + u\frac{\partial v}{\partial x} + v\frac{\partial v}{\partial y} + w\frac{\partial v}{\partial z}\right) = -\frac{\partial P}{\partial y} + \rho g_y + \mu\left(\frac{\partial^2 v}{\partial x^2} + \frac{\partial^2 v}{\partial y^2} + \frac{\partial^2 v}{\partial z^2}\right)$$

$$\rho\left(\frac{\partial w}{\partial t} + u\frac{\partial w}{\partial x} + v\frac{\partial w}{\partial y} + w\frac{\partial w}{\partial z}\right) = -\frac{\partial P}{\partial z} + \rho g_z + \mu\left(\frac{\partial^2 w}{\partial x^2} + \frac{\partial^2 w}{\partial y^2} + \frac{\partial^2 w}{\partial z^2}\right)$$

Equation 3-1

where ρ is density, P is pressure, μ is dynamic viscosity, g_x, g_y, and g_z, are the acceleration of gravity, and u, v, and w are the velocity components in the x, y, and z directions respectively.

The left sides of the equations represent the acceleration terms and the right sides represent the force terms. These equations provide a complete mathematical description of the flow of incompressible Newtonian fluids when combined with the conservation of mass equation shown below [49].

$$\frac{\partial \rho}{\partial t} + \frac{\partial(\rho u)}{\partial x} + \frac{\partial(\rho v)}{\partial y} + \frac{\partial(\rho w)}{\partial z} = 0$$

Equation 3-2

It is not easy in many cases to obtain the exact solution of the equations. A principal difficulty in solving 'Navier-Stokes equations' arises from the nonlinearity of the convective acceleration terms such as $u \cdot \partial u / \partial x$. For most practical flow problems,

fluid particles do have accelerated motion as they move in the flow field. However, there are a few cases for which the convective acceleration vanishes because of the nature of the geometry of the flow system. In these cases, exact solutions are possible. The geometries that are relevant to this study are parallel plate, circular tube, and rectangular tube (Figure 3-1).
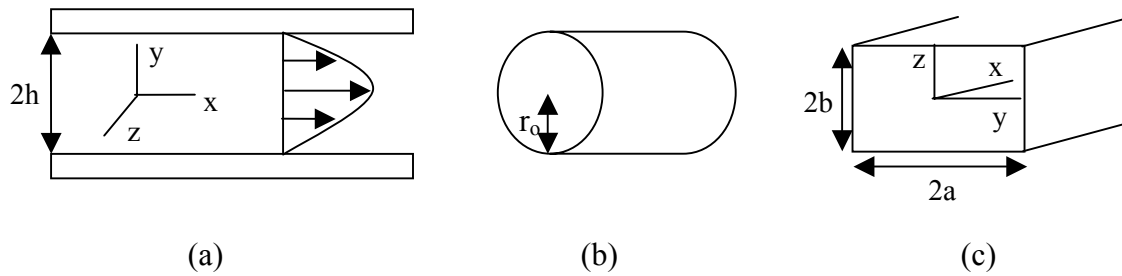
Figure 3-1. Three different geometries that are relevant to GC column, (a) parallel plate system, (b) circular column, (c) rectangular column.

Solving the Navier-Stokes equations for the fixed parallel plates and circular tube is relatively simple. The volumetric flow rate per unit length of width (Q), average flow velocity ($\bar{u}$), flow velocity distribution u of an incompressible, laminar, fully developed flow for the two case are shown in Table 3-1.

Table 3-1. Exact solutions of Navier-Stokes equations for fixed parallel plates and for circular tube.

Fixed parallel plates	Circular tube
$Q = \dfrac{2h^3}{3\mu}(-\dfrac{dP}{dx}) = \dfrac{2h^3}{3\mu} \cdot \dfrac{(P_o - P_i)}{L}$	$Q = \dfrac{\pi r_o^{\,4}}{8\mu}(-\dfrac{dP}{dx}) = \dfrac{\pi r_o^{\,4}}{8\mu} \cdot \dfrac{(P_o - P_i)}{L}$
$\bar{u} = \dfrac{h^2}{3\mu} \cdot \dfrac{(P_o - P_i)}{L} = \dfrac{3}{2} \cdot u_{max}$	$\bar{u} = \dfrac{r_o^2}{8\mu}(-\dfrac{dP}{dx}) = \dfrac{r_o^2}{8\mu} \cdot \dfrac{(P_o - P_i)}{L}$
$u(y) = \dfrac{(P_o - P_i)}{2\mu L} \cdot (y^2 - h^2)$	$u(r) = \dfrac{(r_o^2 - r^2)}{4\mu} \cdot \dfrac{(P_o - P_i)}{L}$

where μ is dynamic viscosity, $2h$ is the gap between the plates, r_o is the radius, L is the

length of the plates, and P_i, P_o are the inlet, outlet pressure.

The exact solutions for a rectangular tube are more complex. If we assume an

incompressible, laminar, fully developed flow through a rectangular tube as shown in

Figure 3-1 (c), the Navier-Stokes equations become

$$\frac{\partial^2 u}{\partial y^2} + \frac{\partial^2 u}{\partial z^2} = \frac{1}{\mu} \cdot \frac{\partial P}{\partial x}$$

Equation 3-3

By using nondimensional variables and the 'separation of variable' method, the

exact solutions can be obtained as below [50, 51].

$$Q = \frac{4ba^3}{3\mu}(-\frac{dP}{dx})[1 - \frac{192a}{\pi^5 b} \sum_{i=1,3,5...}^{\infty} \frac{\tanh(i\pi b/2a)}{i^5}]$$

Equation 3-4

$$\bar{u} = \frac{a^2}{3\mu}(-\frac{dP}{dx})[1 - \frac{192a}{\pi^5 b} \sum_{i=1,3,5...}^{\infty} \frac{\tanh(i\pi b/2a)}{i^5}]$$

Equation 3-5

$$u(y,z) = \frac{16a^2}{\mu\pi^3}(-\frac{dP}{dx}) \sum_{i=1,3,5...}^{\infty} (-1)^{(i-1)/2} \cdot [1 - \frac{\cosh(i\pi z/2a)}{\cosh(i\pi b/2a)}] \cdot \frac{\cos(i\pi y/2a)}{i^3}]$$

Equation 3-6

In order to quantify the column efficiency, the above equations need to be

combined with the diffusion equation. If we use the above exact solutions in the column

efficiency calculation without simplification, the computation will be extremely difficult.

Therefore, other simplified approaches have been used in GC theory. These include:

-

(1) Use the solution for a circular tube with the hydraulic diameter of the rectangular tube. The hydraulic diameter is defined as $D_h = \dfrac{4A}{p}$, where A and p are the area and the perimeter of the section, respectively.

(2) Use the solution for fixed parallel plates. This will be more reasonable for high aspect ratio rectangular columns (either a>>b or a<<b).

(3) Another simplified solution that satisfies the boundary condition of the problem was suggested in the literature [22]. The solutions are :

$$u(y,z) = \frac{1}{2\mu} \cdot \left[\frac{(y^2 - a^2)(z^2 - b^2)}{(y^2 - a^2) + (z^2 - b^2)} \right] \cdot \frac{dP}{dx}$$

Equation 3-7

$$\bar{u} \cong -\frac{1}{3} \frac{a^2 b^2}{a^2 + b^2} \frac{1}{\mu} \frac{dP}{dx}$$

Equation 3-8

$$Q \cong -\frac{4ab}{3} \frac{a^2 b^2}{a^2 + b^2} \frac{1}{\mu} \frac{dP}{dx}$$

Equation 3-9

It is worth comparing these solutions before advancing further to investigate theoretical column performance. Figure 3-2 shows the average velocity as a function of the aspect ratio (a/b). At low aspect ratio (a/b<3), the solution using hydraulic diameter was closer to the exact solution than other solution. Conversely, the parallel plate solution and Spangler solution were closer to the exact solution at a higher aspect ratio (a/b>5). Figure 3-3 shows the velocity distributions in a rectangular column (a/b = 4) by different

solutions. Figure 3-3 is the velocity distribution along the y-axis and z-axis. The parallel

plate solution is very close to the exact solution along z-axis. Spangler solution is close to

the exact solution along both axes; however, the hydraulic diameter solution shows a

fairly big deviation from the exact solution along both axes.
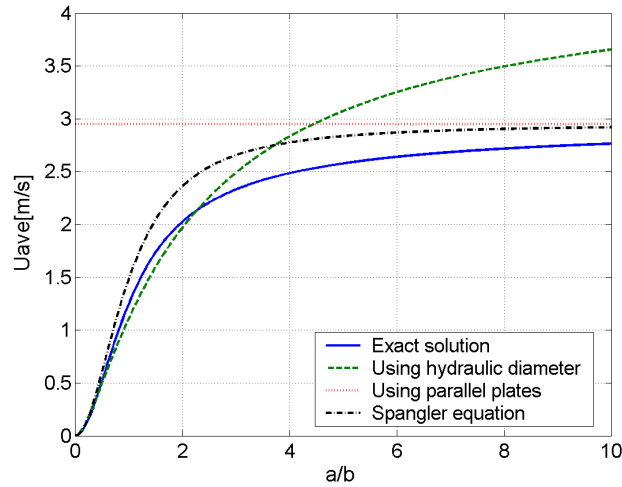
Figure 3-2. Comparison of different solutions for a gas flow in a rectangular channel
(a = 1 - 500 µm, b = 50 µm, L = 1 m, T = 20 °C, ΔP = 10 psi, helium flow).
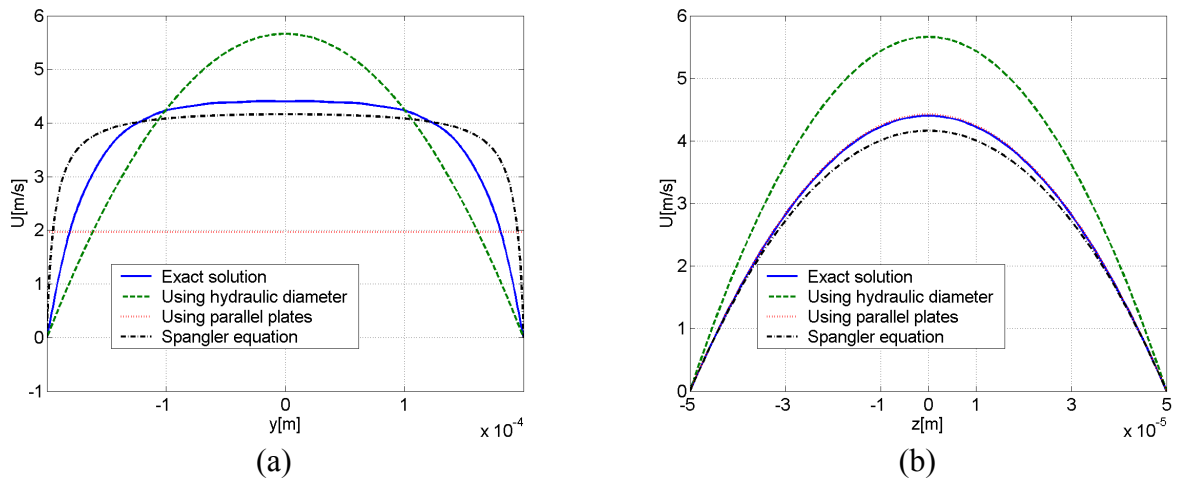
Figure 3-3. Flow velocity distribution in a rectangular channel (a = 200 µm, b = 50
µm) by different solutions; (a) along y axis, (b) along z axis.

58

3.1.2 Compressibility Effect

In the previous section, an incompressible flow in a rectangular tube was investigated. However, can we assume the gas flow in microchannel as an incompressible flow? Let's express the flow density as $\rho = \rho_o + \Delta\rho$, where ρ_o is a reference density; and $\Delta\rho$ is the local departure from this reference density. If $\Delta\rho/\rho_o \ll 1$, the term ρ can be assumed to be ρ_o and the flow can be considered to be incompressible.

The conventional criterion to determine whether a flow is compressible or incompressible is using Mach number (Ma), which is defined as flow velocity over the velocity of sound (a). Generally as the velocity of the fluid element increases, the density ρ of the fluid will change according to the following equation in case of isothermal or adiabatic gas flow.

$$\frac{\rho_o}{\rho} = \left(1 + \frac{\gamma-1}{2} \cdot Ma^2\right)^{1/(\gamma-1)}$$

Equation 3-10

where γ is c_p/c_v (=1.4 for air at standard conditions). If Ma is less than 0.3, the value ρ deviates from ρ_o by less than 5%, and for all practical purposes the flow can be treated as incompressible. On the other hand, if $Ma > 0.3$, the density variation becomes more pronounced and should be treated as compressible. Therefore the Mach number 0.3 is a convenient dividing line [52].

However, the well-known $Ma < 0.3$ criterion is only a necessary not a sufficient condition to consider the flow as incompressible. There are exceptional situations where the Mach number can be exceedingly small while the flow is compressible. One of the exceptional situations is a strong wall heating or cooling where the density is changed

sufficiently even at low flow velocity. Gas flow in a long and narrow microchannel is another example. In this case, viscous effect which was neglected in the derivation of the above density equation can become dominant and the pressure may strongly change along the channel. Thus as the size of channel decreases, it is necessary to consider the pressure term versus the viscous term. Wong *et al*. [53] performed a dimensional analysis considering the viscous effect and they derived the following expression for density variation:

$$\frac{\Delta\rho}{\rho_o} \sim \frac{\Delta P}{\rho a^2} \sim \frac{L}{d_o}\frac{Ma^2}{Re}$$

Equation 3-11

Therefore, when the viscous effect becomes dominant as in gas flow in a long and narrow capillary tube, it is necessary to consider a modified criterion, *(L/d₀)(Ma²/Re) <<1*, in order to determine whether the fluid can be treated as incompressible.

Table 3-2 compares the density variations according to the conventional and new criteria for microchannels having different dimensions. The fluid properties used in this calculation were those of Air at room temperature; the density (ρ) is 1.184 [kg/m^3] and viscosity (μ) is 1.85X10^{-5} [Ns/m^2]. In all cases Mach number was less than 0.3. In other word, all cases can be considered as incompressible by conventional criteria. However, in most of the cases, the actual density variation was more than 5% by new criteria. Therefore, the gas flow in a long and narrow microchannel cannot be treated as incompressible.

Table 3-2. Density variation by conventional and new criteria.

Variables	Case 1	Case 2	Case 3	Case 4	Case 5	Case 6
Column diameter, d [μm]	100	100	50	50	10	10
Column length, L [m]	1	1	1	1	1	1
Fluid velocity, u [m/s]	1	5	1	5	0.1	0.5
Reynolds number, ρud/μ	6.4	32	3.2	16	0.064	0.32
Mach number, u/c	0.0029	0.0147	0.0029	0.0147	0.0003	0.0015
Density variation [%] by - Conventional criteria - New Criteria	< 0.5 1.35	< 0.5 6.76	< 0.5 5.41	< 0.5 27.03	< 0.5 13.52	< 0.5 67.58

Assuming a fully developed laminar flow in a long capillary tube, if only considering the global density variation but not the local density variation within the infinitely small section, one can integrate the governing momentum equation to obtain the average flow rate as a function of pressure drop. Hence the relationship between the mass flow rate and the pressure drop across the capillary tube can easily be obtained. As a result, the relationships between the volumetric flow rate and the pressure drop for a circular and for a rectangular column can be expressed as follows.

$$Q = \frac{\pi \cdot d^4}{256 \mu L} \cdot \left(\frac{P_i^2 - P_o^2}{P_o} \right)$$

Equation 3-12

$$Q = \frac{h^3 d}{24} \cdot \frac{(P_i^2 - P_o^2)}{\mu L P_o} \cdot (1 - \frac{192}{\pi^5} \frac{h}{d} \sum_{i=1,3,5,...}^{\infty} \frac{\tanh(i\pi \cdot d / 2h)}{i^5})$$

Equation 3-13

Clearly these expressions imply a nonlinear relationship between the volumetric flow rate and pressure drop across the capillary tube. If the pressure drop is small when

compared with the outlet pressure, the expression can be simplified to show a linear relationship as in the analytical incompressible flow model. The following figures show the deviation between compressible and incompressible flow for circular and rectangular columns.

(a)   (b)
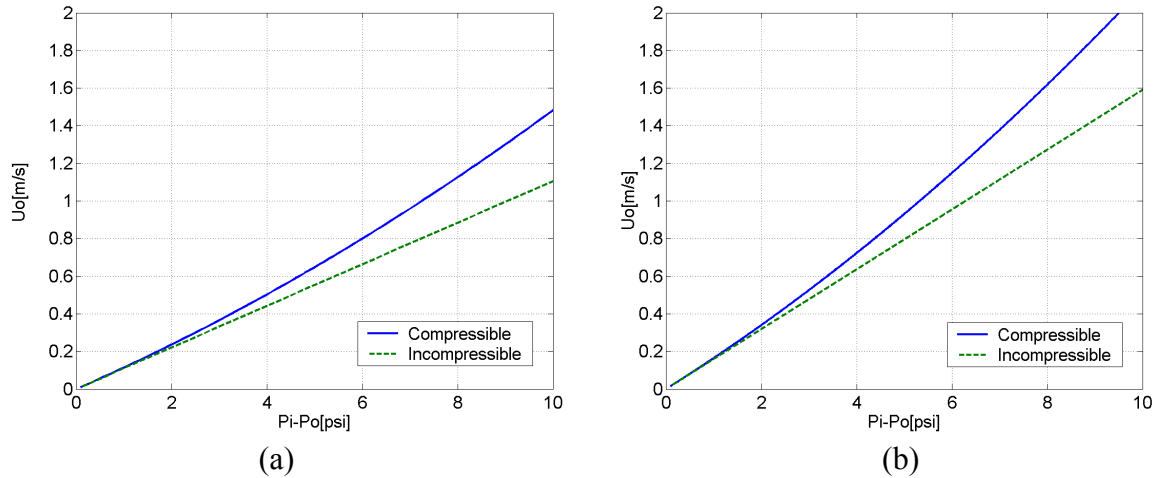
Figure 3-4. Comparison of compressible and incompressible flow, (a) circular column (diameter = 100 μm, length = 1 m), (b) a rectangular column (width = 80 μm, height = 320 μm, length = 1 m).

3.1.3 SLIP FLOW EFFECT

As the column size decreases into the micron scale, the effect of slip flow at the boundary needs to be considered. From the kinetic theory of gases, if the characteristic length of the physical domain (d) is small and compatible with the mean free path of the molecules (λ), the continuum hypothesis and no slip boundary condition become invalid. At the standard atmospheric conditions, the mean free path of air is about 0.065 μm. The deviation of the state of the gas from continuum is measured by the Knudsen number (*Kn*), which is defined as $Kn = \lambda/d$. As the value of Knudsen number increases, non-

continuum effects become more important. A typical way to determine the continuum

versus rarefied flow is as follows [54].

For Kn<0.001, continuum flow regime

For 0.001<Kn<0.1, slip flow regime

For 0.1<Kn<10, transition regime

For 10<Kn, free molecular flow regime

If gas compressibility and slip flow effects are considered, the relationship

between pressure drop and flow rate for a rectangular tube is modified as [19];

$$Q = \frac{2ba^3}{3} \cdot \frac{(P_i^2 - P_o^2 + 12Kn_o P_o(P_i - P_o))}{\mu L P_o} \cdot [1 - \frac{192a}{\pi^5 b} \sum_{i=1,3,5...}^{\infty} \frac{\tanh(i\pi b / 2a)}{i^5}]$$

Equation 3-14

If the column diameter is reduced below 65 μm, the gas flow will be in the slip

flow regime. However, the GC column dimension in this study does not go below 10 μm

and consequently we can consider that the flow is in the continuum flow regime.

Therefore Equation 3-13 will be used in this study for the relationship between flow rate

and pressure drop for the rectangular GC column.

3.1.4 CURVATURE EFFECT

So far, the gas flow in a rectangular channel has been discussed with an

assumption that the channel is straight. This is a reasonable assumption for the

conventional GC columns which have a curvature radius ($\geq$ 5cm) much bigger than

column diameter ($\leq$ 0.5 mm). However, micromachined silicon/glass columns have much

smaller curvature radius because they generally have a planar spiral design. The smallest

curvature radius may be less than several hundred micrometers. In this case, the

assumption of a straight channel is not true any more. How will this curvature affect the

gas flow and eventually GC column performance? Obviously, the analytes migrating at

the outer wall will be lagging behind the analyte migrating at the inner wall (Figure 3-5).

Also, the centrifugal force by the curvature will result in lateral diffusion in the flow.

This may lead to a broader band spreading. Therefore the curvature effect must be

considered when miniature column is designed.
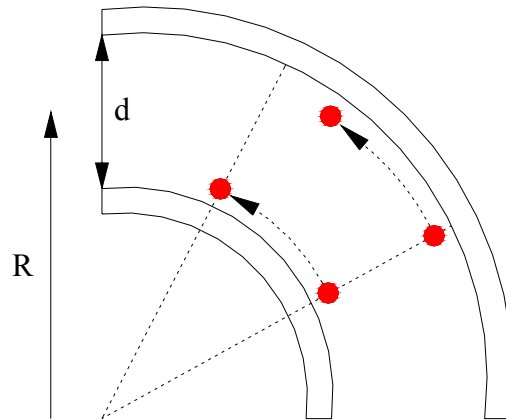
Figure 3-5. Curvature effect on analyte migration.

Then how can we quantify this curvature effect and estimate the proper curvature

radius to prevent considerable band broadening? The curvature effect can be described

using Dean number, which is the ratio of centrifugal force to viscous force (Equation

3-15). The higher the Dean number, the more influence the curvature effect will be. The

curvature effect becomes more significant as curvature radius (R) decreases or flow rate

increases or column diameter (d) increases. According to Sandia's simulation, the effect

of curvature becomes negligible when the Dean number as small as 0.2 {Wong, 1999

#58}.

$$De = \frac{\rho u d}{\mu} \cdot \sqrt{\frac{d}{2R}} = \mathrm{Re} \cdot \sqrt{\frac{d}{2R}}$$

Equation 3-15

3.2 RETENTION TIME

Figure 3-6 is a typical chromatogram for a two-component mixture. The time it

takes after a sample injection for the analyte peak to reach the detector is called the

retention time and is given the symbol t_R. The small peak on the left is for a species that

is not retained by the column. The time t_M is the time for the mobile phase and the

unretained species to reach the detector and is called the dead time. The rate of migration

of the unretained species is the same as the average velocity of the mobile phase. W is the

width of the peak and $W_{1/2}$ is the width of the peak at half its maximum height.
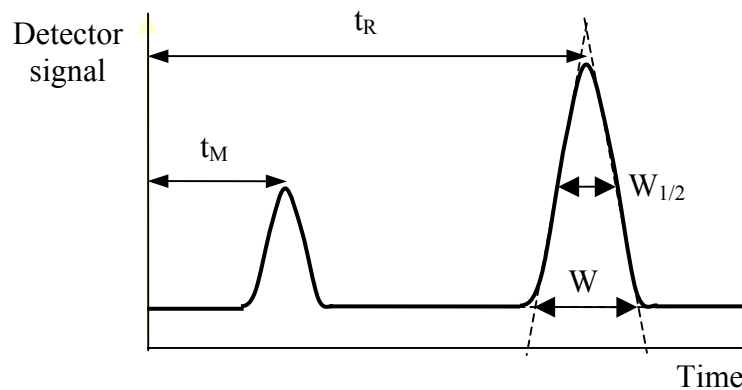
Figure 3-6. A typical chromatogram for two component mixture.

When the length of the column is L, the average linear rate of solute migration, $\bar{v}$ and the average linear rate of movement, u of the molecules of the mobile phase are:

$$\bar{v} = \frac{L}{t_R}$$

Equation 3-16

$$\bar{u} = \frac{L}{t_M}$$

Equation 3-17

In order to relate the retention time of a solute to its distribution constant, we express its migration rate as a fraction of the velocity of the mobile phase. Because solute movement can only occur in the mobile phase, the average rate at which a solute zone migrates down the column depends on the fraction of time it spends in that phase.

$$\bar{v} = \bar{u} \times \textit{fraction of time solute spends in mobile phase}$$

$$\bar{v} = \bar{u} \times \frac{\textit{Average mole of solute in mobile phase}}{\textit{Total mole of solute}}$$

$$\bar{v} = \bar{u} \times \frac{C_M \cdot V_M}{C_M \cdot V_M + C_S \cdot V_S}$$

$$\bar{v} = \bar{u} \times \frac{1}{1 + K \cdot V_S / V_M}$$

Equation 3-18

The retention factor, an important parameter that is widely used to describe the migration rates of solutes on columns is defined as

$$k = K \cdot \frac{V_S}{V_M}$$

Equation 3-19

Substitution of Equation 3-19 into Equation 3-18 yields:

$$\bar{v} = \bar{u} \times \frac{1}{1+k}$$

Equation 3-20

Substitution of Equation 3-16 and Equation 3-17 into Equation 3-20:

$$\frac{L}{t_R} = \frac{L}{t_M} \times \frac{1}{1+k}$$

Equation 3-21

This equation rearranges to:

$$k = \frac{t_R - t_M}{t_M}$$

Equation 3-22

$$t_R = t_M \cdot (1+k) = \frac{L \cdot (1+k)}{\bar{u}}$$

Equation 3-23

The retention factor and the average flow velocity for a circular column can be expressed as follows.

$$k = K \cdot \frac{V_S}{V_M} = K \cdot \frac{2\pi \cdot r \cdot w \cdot L}{\pi \cdot r^2 \cdot L} = K \cdot \frac{2w}{r}$$

$$\bar{u} = u_o \cdot j = \frac{d^2}{64\mu(T) \cdot L} \cdot \left(\frac{P_i^2 - P_o^2}{P_o} \right) \cdot \frac{3}{2} \cdot \frac{(P_i / P_o)^2 - 1}{(P_i / P_o)^3 - 1}$$

For a rectangular column these formula should be modified as follows.

$$k = K \cdot \frac{V_S}{V_M} = K \cdot \frac{2(d+h) \cdot w \cdot L}{d \cdot h \cdot L} = K \cdot \frac{2(d+h)w}{dh}$$

$$\bar{u} = u_o \cdot j = \frac{h^2}{24} \cdot \frac{(P_i^2 - P_o^2)}{\mu L P_o} \cdot (1 - \frac{192}{\pi^5} \frac{h}{d} \sum_{i=1,3,5,...}^{\infty} \frac{\tanh(i\pi \cdot d / 2h)}{i^5}) \cdot \frac{3}{2} \cdot \frac{(P_i / P_o)^2 - 1}{(P_i / P_o)^3 - 1}$$

The below graphs show the retention time of a solute (K = 1250) as a function of column diameter for different column lengths and pressure drops. When column diameter is 100 μm and pressure drop is 10 psi, the retention times are 5 sec for 1 m long column, 50 sec for 3 m, 500 sec for 10 m, and 5000 sec for 30 m. When column diameter is 200 μm and column length is 30 m, the retention times are 350 sec at 20 psi, 500 sec at 15 psi, 700 sec at 10 psi, and 1500 sec at 5 psi.
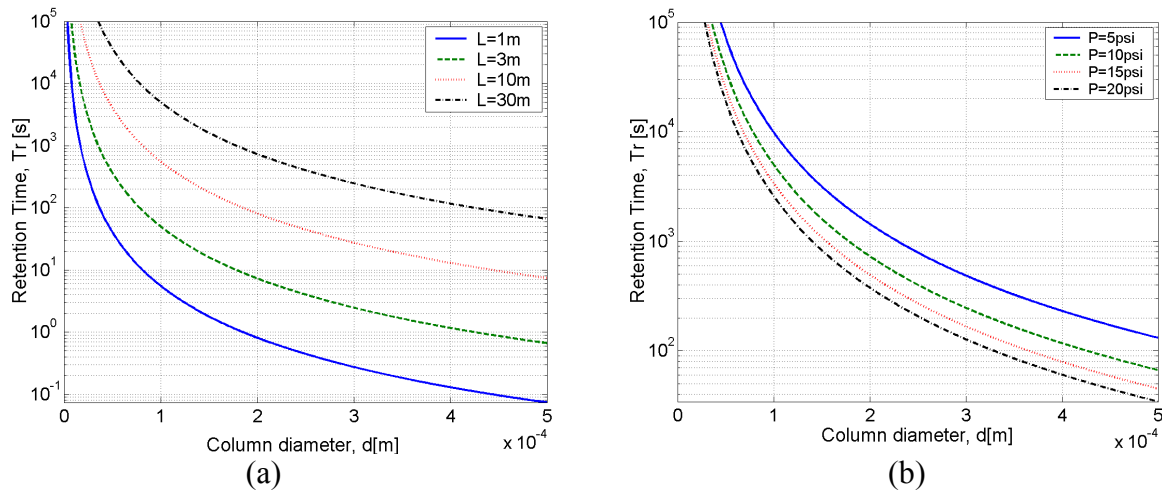
Figure 3-7. Retention time as a function of column diameter (K = 1250, w = 100 nm, T = 20 °C, helium gas), (a) ΔP fixed (10 psi), (b) L fixed (30 m).

3.3 COLUMN EFFICIENCY

3.3.1 PLATE HEIGHT AND PLATE NUMBER

If a sample in the form of a small band is injected into a circular column uniformly coated with a stationary phase, these injected molecules will be carried along

at an average speed, and will diffuse about the center of gravity of the band. Consequently, the sample band is broadened while it is traveling along the column. This is called 'band broadening' and is a measure of the efficiency of GC column [7, 55].

Two related terms are widely used as quantitative measures of chromatographic column efficiency: the height equivalent to theoretical plate (HETP) and the number of theoretical plates. These are often called plate height H and plate number N. The two are related by the equation

$$N = \frac{L}{H}$$

Equation 3-24

where L is the length of the column. The efficiency of chromatographic columns increases as the plate number becomes greater and as the plate height becomes smaller. The origin of the terms 'plate height' and 'plate number' is the theoretical study of Martin and Synge [56] in which they treated a chromatographic column as if it were similar to distillation column that is made up of numerous discrete but continuous layers called theoretical plates. This 'plate theory' successfully accounts for the Gaussian shape of chromatographic peaks and their rate of movement down a column. For example, plate height is defined as the variance per unit length and the standard deviation can be expressed by the retention time, column length and column width. As a result, plate height and plate number can be expressed as follows for Gaussian peaks.

$$H = \frac{\sigma^2}{L} = \frac{LW^2}{16t_R^2}$$

Equation 3-25

$$N = 16\left(\frac{t_R}{W}\right)^2 = 5.54\left(\frac{t_R}{W_{1/2}}\right)^2$$

Equation 3-26

3.3.2 GOLAY EQUATION AND ITS MODIFICATION

Although plate theory is a convenient way to quantify column efficiency, it fails to account for band broadening in a mechanistic way. The 'rate theory' has been proposed for this purpose. This theory describes the diffusion of a pulse of sample introduced into the carrier gas at the entrance of the column. Two diffusion mechanisms that cause band broadening are static and dynamic diffusion. Static diffusion takes place whether the gas is moving or not, and it is a function of elapsed time. Dynamic diffusion is due to the fluctuations in occupancy of the various portions of the column cross-section and of the fixed phase. The diffusion of a sample band is governed by the vectorial differential equation:

$$D_M \cdot \nabla^2 f = \frac{df}{dt} = \frac{\partial f}{\partial t} + \vec{u} \cdot grad\ f$$

Equation 3-27

where D_M is the diffusion coefficient of the sample in the mobile phase, carrier gas and f is the concentration of the sample and $\vec{u}$ is the velocity vector of the carrier gas.

Golay performed a 'moment analysis' with this equation to arrive at a simplified expression of the plate height for both circular and rectangular columns [57]. Let's first consider a circular column (radius = r_o) with uniform stationary phase coating thickness =

70

w. If we assume that the gas flow is Poiseulle flow in a circular column, Equation 3-27 can be expressed as below.

$$D_M \left(\frac{\partial^2}{\partial r^2} + \frac{1}{r} \frac{\partial}{\partial r} + \frac{\partial^2}{\partial x^2} \right) f = \frac{\partial f}{\partial t} + 2\bar{u} \left(1 - \frac{r^2}{r_o^2} \right) \frac{\partial f}{\partial x}$$

Equation 3-28

If we also assume that the diffusion within the stationary phase is instantaneous, the boundary condition at the tube wall is

$$2 \frac{D_M}{r_o} \left(\frac{\partial f}{\partial r} \right)_{r=r_o} = -k \left(\frac{\partial f}{\partial t} \right)_{r=r_o}$$

Equation 3-29

where k is retention factor, the ratio of the sample held in the retentive layer to the sample in vapour form when there is equilibrium between these two phases. Because of the retentive property of the stationary phase, the average velocity of the sample will be the fraction $1/(1+k)$ of the average velocity $\bar{u}$ of the carrier gas, and it will be expedient to change co-ordinates as:

$$x_1 = x - \frac{\bar{u}}{1+k} t$$

Equation 3-30

Now let the new variables $\bar{f}$, Δf be defined by $\bar{f} = \frac{2}{r_o^2} \int_0^{r_o} f r dr$ and $f = \bar{f} + \Delta f$

where Δf obeys the relation, $\int_0^{r_o} \Delta f r dr = 0$. If the above diffusion equation is rearranged by new variables, we get

$$\left(D_M + \frac{1+6k+11k^2}{48(1+k)^2} \cdot \frac{\bar{u}^2 r_o^2}{D_M}\right)\frac{\partial^2 \bar{f}}{\partial x_1^2} = (1+k)\frac{\partial \bar{f}}{\partial t} + \frac{k(1+k)}{24(1+k)} \cdot \frac{\bar{u} r_o^2}{D_M}\frac{\partial^2 \bar{f}}{\partial x_1 \partial t}$$

Equation 3-31

The chromatographic peaks can be characterized by their statistical moments. For example, the zeroth moment is the area under the peak, the first moment is the peak's center of mass related to the retention time, the second moment is a measure of peak width, and the higher central moments are further measures of peak shape. Golay's incremental second moment (du) of a normalized gas packet was

$$du = dt\int_{-\infty}^{+\infty} fx^2 dx = dt\int_{-\infty}^{+\infty}\frac{\partial f}{\partial t}x^2 dx = D_M \cdot dt\int_{-\infty}^{+\infty}\frac{\partial^2 f}{\partial x^2}x^2 dx$$

Equation 3-32

Combining Equation 3-31 and Equation 3-32,

$$du = \left(2\frac{D_M}{\bar{u}} + \frac{1+6k+11k^2}{24(1+k)^2} \cdot \frac{\bar{u} r_o^2}{D_M}\right)dx_1$$

Equation 3-33

The plate height is related to this incremental second moment by dividing it by the length of the column. Therefore the quantity within the parenthesis of the above equation, which has the dimension of a length, can be termed the plate height (H) of a circular column.

$$H = 2\frac{D_M}{\bar{u}} + \frac{1+6k+11k^2}{24(1+k)^2} \cdot \frac{\bar{u} r_o^2}{D_M}$$

Equation 3-34

If the diffusion within the stationary phase is not instantaneous, the boundary condition should be changed considering the dynamic diffusion of solute in the stationary

phase. Consequently, we obtain more complete expressions for the plate height of circular columns. This is called 'Golay equation.'

$$H = 2\frac{D_M}{\bar{u}} + \frac{1 + 6k + 11k^2}{24(1+k)^2} \cdot \frac{\bar{u}r_o^2}{D_M} + \frac{k^3}{6(1+k)^2} \cdot \frac{\bar{u}r_o^2}{F^2 K^2 D_S}$$

Equation 3-35

where $\bar{u}$ is the average carrier gas velocity, r_o is tube radius, D_M is diffusion coefficient of sample in gas phase, D_S is diffusion coefficient of sample in stationary phase, K is distribution constant, k is retention factor, and F is the effective to actual surface area of stationary phase.

Now let's consider a rectangular column. Golay derived the incremental second moment of a gas packet for a rectangular column in the same way as for a circular column [57]. However, this was only for high aspect ratio rectangular columns. In other words, he used the equation of a simple parallel plate flow in his derivation with an assumption that the width of the column is much bigger than height, $2z_o$. In that case, the governing diffusion equation and the boundary condition becomes

$$D\left(\frac{\partial^2}{\partial z^2} + \frac{\partial^2}{\partial x^2}\right)f = \frac{\partial f}{\partial t} + \frac{3}{2}\bar{u}\left(1 - \frac{z^2}{z_o^2}\right)\frac{\partial f}{\partial x}$$

Equation 3-36

$$\frac{D}{z_o}\left(\frac{\partial f}{\partial z}\right)_{z=z_o} = -k\left(\frac{\partial f}{\partial t}\right)_{z=z_o}$$

Equation 3-37

where $\bar{u}$ is average carrier gas velocity, z_o is half inside height of rectangular column, D is diffusion coefficient of sample in gas phase.

Rearranging the above equation with new variables as discussed in the case of circular column,

$$\left(D + \frac{2(1+9k+51k^2/2)}{105(1+k)^2} \cdot \frac{\bar{u}^2 z_o^2}{D}\right)\frac{\partial^2 \bar{f}}{\partial x_1^2} = (1+k)\frac{\partial \bar{f}}{\partial t} + \frac{k(1+6k)}{15(1+k)} \cdot \frac{\bar{u}z_o^2}{D}\frac{\partial^2 \bar{f}}{\partial x_1 \partial t}$$

Equation 3-38

The incremental second moment can be obtained from this equation as was done for the round tube.

$$du = \left(2\frac{D}{\bar{u}} + \frac{2(1+9k+51k^2/2}{105(1+k)^2} \cdot \frac{\bar{u}z_o^2}{D}\right)dx_1$$

Equation 3-39

Therefore, the plate height for the rectangular column can be expressed as

$$H = 2\frac{D}{\bar{u}} + \frac{2(1+9k+51k^2/2}{105(1+k)^2} \cdot \frac{\bar{u}z_o^2}{D}$$

Equation 3-40

If the diffusion within the stationary phase is not instantaneous, boundary condition should be changed considering the dynamic diffusion of solute in the stationary phase. Consequently, we obtain more complete expressions for the plate height of rectangular columns.

$$H = 2\frac{D}{\bar{u}} + \frac{4(1+9k+51k^2/2)}{105(1+k)^2} \cdot \frac{\bar{u}z_o^2}{D} + \frac{2k^3}{3(1+k)^2} \cdot \frac{\bar{u}z_o^2}{F^2 c^2 D_l}$$

Equation 3-41

where D_l is diffusion coefficient of sample in stationary phase, c is partition coefficient, k is retention factor, F is effective to actual surface area of stationary phase.

The above derivation was for the flat rectangular column where the column height is smaller than column width. The micromachined silicon/glass columns fabricated by wet etching technique have this type of cross section. But silicon/glass columns fabricated by deep RIE etching generally have a narrow rectangular cross section as shown below.
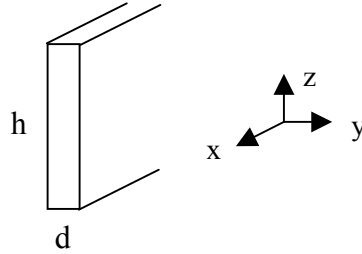
Figure 3-8. Schematic of a narrow rectangular column.

For this narrow rectangular column that has a width of d and a height of h, the Golay equation can be written as below.

$$H = \frac{2D_M}{u_o} + \frac{4(1+9k+\frac{51}{2}k^2)(\frac{d}{2})^2}{105(k+1)^2 D_M} \cdot u_o + \frac{2kw^2}{3(k+1)^2 F^2 D_s}(\frac{h+d}{h})^2 \cdot u_o$$

Equation 3-42

Later on, Giddings modified this equation considering varying pressure along the column as below [58, 59].

$$H = f_1 \cdot \frac{2D_M}{u_o} + f_1 \cdot \frac{4(1+9k+\frac{51}{2}k^2)(\frac{d}{2})^2}{105(k+1)^2 D_M} \cdot u_o + f_2 \cdot \frac{2kw^2}{3(k+1)^2 F^2 D_s}(\frac{h+d}{h})^2 \cdot u_o$$

Equation 3-43

where $f_1 = \dfrac{9(P_i^4 - P_o^4)(P_i^2 - P_o^2)}{8(P_i^3 - P_o^3)^2}$, $f_2 = \dfrac{3P_o(P_i^2 - P_o^2)}{2(P_i^3 - P_o^3)}$, D_M is diffusion coefficient of

analyte in carrier gas, D_s is diffusion coefficient of analyte in stationary layer, F is

effective to actual surface area of stationary layer, k is Retention factor, L is column

length, P_i is inlet pressure, P_o is outlet pressure, u_o is gas velocity at outlet, w is stationary

phase thickness.

3.3.3 SPANGLER EQUATION

Golay's fomula for the plate height of a rectangular column is valid for the

rectangular columns with high aspect ratio cross section because he used the simplified

flow equation for a fixed plate system in his derivation. Therefore this equation cannot be

used for low aspect ration rectangular columns. Spangler generated a new formula for the

plate height of a rectangular column that can be applied to any aspect ratio column. He

performed the same moment analysis as Golay did but employed different flow equation.

For a rectangular column with a width of 2b and a height of 2d, the velocity equation and

average velocity he used in his derivation are

$$u(x, y) = \frac{1}{2\mu} \cdot \left[\frac{(x^2 - b^2)(y^2 - d^2)}{(x^2 - b^2) + (y^2 - d^2)} \right] \cdot \frac{dP}{dz} = -\frac{K_u(x, y)}{\mu} \cdot \frac{dP}{dz}$$

Equation 3-44

$$\bar{u}(x, y) = \frac{1}{2\mu \cdot A_c \cdot L} \int_{-b}^{b} \int_{-d}^{d} K_u(x, y) dy dx \cdot \frac{P_i^2 - P_o^2}{\sqrt{P_i^2 - \frac{z}{L}[P_i^2 - P_o^2]}} = \frac{K_Q}{2\mu \cdot A_c \cdot L} \cdot \frac{P_i^2 - P_o^2}{\sqrt{P_i^2 - \frac{z}{L}[P_i^2 - P_o^2]}}$$

Equation 3-45

where A_c is the cross-sectional area. The HETP obtained by moment analysis is:

$$H = \frac{2D_M}{\bar{u}} + \frac{2kw^2}{3(k+1)^2 D_s} \cdot \bar{u}$$
$$+ \frac{2k}{1+k} \times \left\{ \begin{array}{l} \frac{1}{2dD_M} \int_0^d \left[\frac{4A_c\bar{u}}{K_Q(b^2+y^2)} \int\int\int K_u(x,y)dydydxdx \Big|_{x=b} - \frac{\bar{u}}{1+k} \cdot \frac{b^2y^2}{b^2+y^2} \right] dy \\ + \frac{1}{2bD_M} \int_0^b \left[\frac{4A_c\bar{u}}{K_Q(b^2+y^2)} \int\int\int K_u(x,y)dydydxdx \Big|_{y=d} - \frac{\bar{u}}{1+k} \cdot \frac{d^2x^2}{d^2+x^2} \right] dx \end{array} \right.$$
$$- \frac{1}{D_M} \left\{ \int_{-b}^b \int_{-d}^d \left(\frac{K_u(x,y)}{K_Q} - \frac{1}{(1+k)A_c} \right) \times \left[\frac{4A_c\bar{u}}{K_Q(b^2+y^2)} \int\int\int K_u(x,y)dydydxdx - \frac{\bar{u}}{1+k} \cdot \frac{x^2y^2}{x^2+y^2} \right] dydx \right\}$$

Equation 3-46

The Golay equation and the Spangler equation show common terms arising from longitudinal diffusion and resistance to mass transfer in the stationary phase. The difference lies in the resistance to mass transfer in the gas phase. The Golay equation for rectangular columns accurately responses for high aspect ratio columns but not for low aspect ratio columns. However, the Spangler equation does not have an aspect ratio limitation in its application, even though the velocity equation is not exact. Spangler claimed that his theory successfully predicts the performance of a fast GC, in the form of both short microbore and micromachined columns.

3.3.4 MAXIMUM COLUMN EFFICIENCY

The Golay equation describes how the plate height can be expressed as a function of the average velocity of a carrier gas and it can be simplified as below.

$$H = \frac{B}{\bar{u}} + C_M \cdot \bar{u} + C_s \cdot \bar{u}$$

Equation 3-47

This is called 'van Deemter equation'. The first term in this equation represents

static diffusion that is a function of elapsed time. The second and the third terms

represent dynamic diffusion in the mobile phase and stationary phase respectively. In

both the mobile and stationary phases, resistance (C_M and C_S) to dynamic diffusion tends

to reduce chromatographic efficiency in direct proportion to average carrier velocity. The

solutes dissolved in the bulk of either phase must depend on diffusion rate to reach the

interface at which their equilibrium concentrations in both phases can be continuously

reestablished. At a low average carrier velocity, the time it takes solute molecules to

diffuse to the surface is relatively short in comparison to the rate at which mobile phase is

being swept down the column. As a result, resistance to mass transport at low carrier

velocity poses very little impediment to efficient re-equilibration. Conversely, at higher

carrier velocities the time it takes molecules to diffuse to the interface becomes longer

and so the efficiency of re-equilibration is impeded.

Figure 3-9 shows the total effect of carrier gas velocity on plate height (H). As the

plate height decreases, the band broadening decreases and column efficiency increases.

Therefore the maximum column efficiency can be obtained at the minimum plate height

(H_{min}). The carrier gas velocity where H_{min} is obtained is called optimum carrier velocity,

u_{opt}. These values can be obtained by differentiating Equation 3-47 with respect to

average carrier velocity.

$$\overline{u}_{opt} = \sqrt{\frac{B}{(C_M + C_S)}}$$

Equation 3-48

$$H_{\min} = 2\sqrt{B(C_M + C_S)}$$

Equation 3-49
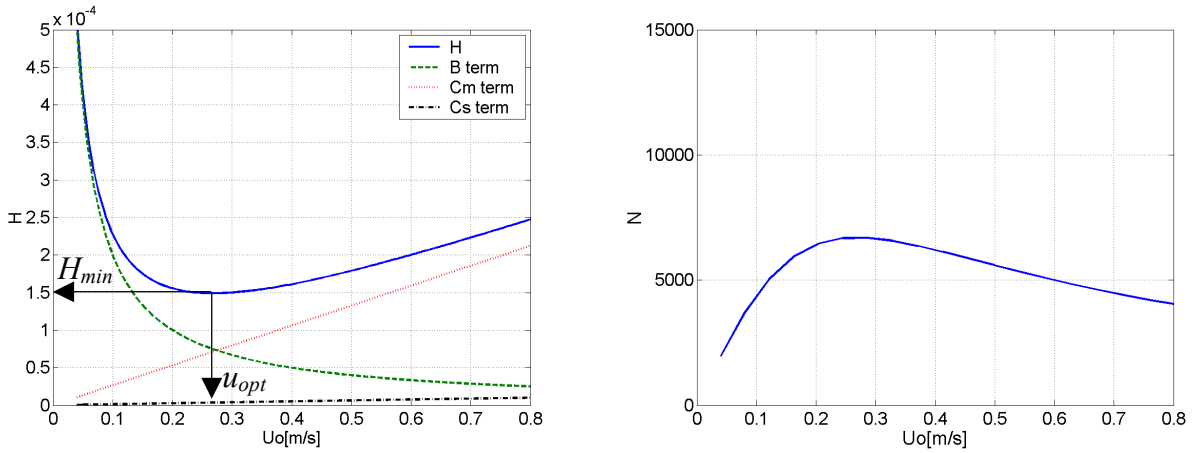
Figure 3-9 The total effect of carrier gas velocity on plate height (H) and plate number (N).

Here, H_{min}, u_{opt} can be calculated directly from either known or estimated values of B and C. Table 3-3 shows analytical expressions for the coefficients in the modified Golay equations for both circular and rectangular columns.

Table 3-3. Analytical expressions for the coefficients in the modified Golay equation.

	B	C_M	C_S
Circular column	$2D_M$	$\dfrac{1+6k+11k^2}{24(1+k)^2} \cdot \dfrac{r_o^2}{D_M}$	$\dfrac{k^3}{6(1+k)^2} \cdot \dfrac{r_o^2}{F^2K^2D_S}$
Rectangular column	$2D_M$	$\dfrac{4(1+9k+\frac{51}{2}k^2)(\frac{d}{2})^2}{105(k+1)^2 D_M}$	$\dfrac{2kw^2}{3(k+1)^2 F^2 D_s}(\dfrac{h+d}{h})^2$

H_{min} value obtained in the above calculation can be readily compared to the values measured from chromatogram. From Equation 3-26,

$$H = \frac{L}{\left[5.545\left(\frac{t_R}{W_h}\right)^2\right]}$$

Equation 3-50

H_{min} and u_{opt} are very useful concepts, but conditions that provide for maximum chromatographic efficiency almost always result in analysis times that are typically longer than necessary. Therefore, a new concept for optimum chromatographic efficiency needs to be introduced. It is calculating the number of theoretical plates (N) per second rather than per meter or total theoretical plates. In this case, the optimum average velocity (u_{opt}) no longer yields the best result. Generally the faster than u_{opt} delivers a higher number of theoretical plates per second. The best result is achieved at a velocity referred to as the 'optimum practical gas velocity (OPGV)'. The OPGV is found at a velocity for which N/t_R has been maximized.

3.4 RESOLUTION

Separation of a two-component mixture can be improved by altering the relative migration rate of the components and/or reducing zone broadening as shown in Figure 3-10. Zone broadening is decreased by those kinetic variables that decrease the plate height of a column. Migration rates are varied by changing those variables that affect

relative retention of the species. The selectivity factor α of a column for the two species

A and B is defined as

$$\alpha = \frac{K_B}{K_A}$$

Equation 3-51

where K_B is the distribution constant for the more strongly retained species B and K_A is

the distribution constant for the less strongly held, or more rapidly eluted, species A. By

this definition α is always greater than unity. Substitution of Equation 3-19 and Equation

3-22 into Equation 3-51 provides a relationship between the selectivity factor and

retention factors or retention times.

$$\alpha = \frac{k_B}{k_A} = \frac{(t_R)_B - t_M}{(t_R)_A - t_M}$$

Equation 3-52
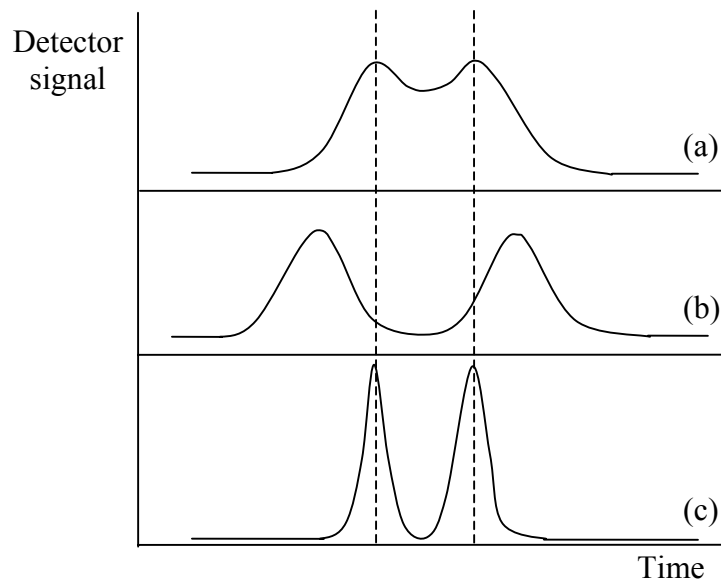
Figure 3-10. Two methods of improving separation of a two-component mixture; (a) original chromatogram with overlapping peaks, (b) improvement by an increase in band separation, (c) improvement by a decrease in band spread.

81

The resolution R_s of a column provides a quantitative measure of its ability to separate two analytes. Column resolution is defined as

$$R_s = \frac{\Delta Z}{W_A/2 + W_B/2} = \frac{2\Delta Z}{W_A + W_B} = \frac{2[(t_R)_B - (t_R)_A]}{W_A + W_B}$$

Equation 3-53

where ΔZ is the distance between the centers of two peaks, W_A and W_B are the peak width of species A and B at the bottom, and $(t_R)_A$ and $(t_R)_B$ are the retention times of species A and B. Figure 3-11 show the separations at three different resolutions ($R_s = 0.75$, 1.0, and 1.5).
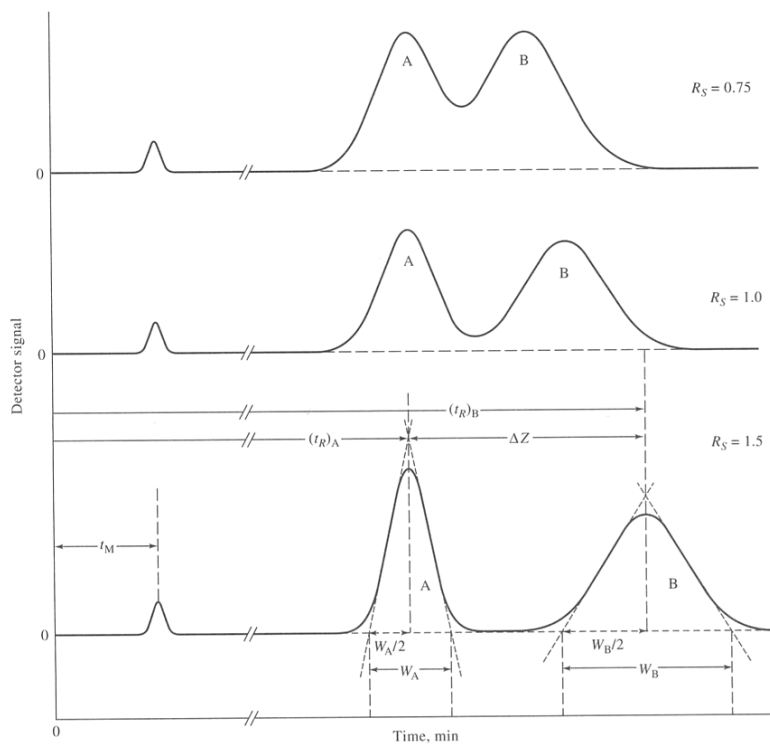
Figure 3-11. Separations at three different resolutions.

It is useful to develop a mathematical relationship between the resolution of a column and the retention factors, the selectivity factor, and the number of plates. If we assume

$$W_A = W_B \approx W$$

Equation 3-53 takes the form

$$R_s = \frac{(t_R)_B - (t_R)_A}{W} = \frac{(t_R)_B - (t_R)_A}{(t_R)_B} \times \frac{\sqrt{N}}{4}$$

Equation 3-54

By substituting Equation 3-22 and Equation 3-52,

$$R_s = \frac{\sqrt{N}}{4}\left(\frac{\alpha - 1}{\alpha}\right)\left(\frac{k_B}{1 + k_B}\right)$$

Equation 3-55

Often it is desirable to calculate the number of theoretical plates required to achieve a desired resolution. An expression for this quantity is obtained by rearranging Equation 3-55 to give

$$N = 16 R_s^2 \left(\frac{\alpha}{\alpha - 1}\right)^2 \left(\frac{1 + k_B}{k_B}\right)^2$$

Equation 3-56

3.5 EFFECTS OF PARAMETERS

There are many variables responsible for the chromatographic result. These can be classified into 'design parameters' and 'operational parameters'. Operational

parameters are under the control of the operator up to the time of sample injection but design parameters are no longer under operator control because they precede sample injection. The detail contents of both parameter groups can be listed in Table 3-4 [7]. Table 3-5 and Table 3-6 are diagrams that explain the effect of each parameter on retention time and column efficiency for a circular and a rectangular column, respectively. Many parameters are inter-related to each other resulting in the difficulties in understanding the effect of each parameter on column performance. For example, a change in column temperature results in changes in carrier gas viscosity, retention factor, and diffusion coefficients. The effect of each parameter on column efficiency is visualized in the following section by fixing all parameters except one interested parameter for a circular column.

Table 3-4. Parameters for column performance.

Design Parameters	Operational Parameters
Column Parameters - Length - Diameter (circular column) - Width and height (rectangular column) - Stationary phase type - Stationary phase thickness Non-column parameters - Choice of carrier gas - Choice of injection and detection modes - Design features of the injector and the detector	- Average velocity of the carrier gas - Column temperature: isothermal or temperature programming - Injection mode: split ratio (split injector), purge activation time (splitless injector) - Choice of sample solvent

Table 3-5. Effects of parameters on column performance in a circular column.

Retention time

$$t_R = t_M \cdot (1+k) = \frac{L \cdot (1+k)}{\bar{u}}$$

Design Parameters

- Choice of carrier gas
- Injection and detection modes
- Column variables
    - Column length
    - Column diameter
    - Stationary phase

Operation Parameters

- Carrier gas velocity
- Column temperature
- Injection control (split/splitless)
- Choice of solvent

$$\bar{u} = u_o \cdot j = \frac{d^2}{64\mu(T) \cdot L} \cdot \left(\frac{P_i^2 - P_o^2}{P_o}\right) \cdot \frac{3}{2} \cdot \frac{(P_i/P_o)^2 - 1}{(P_i/P_o)^3 - 1}$$

$$\mu(T) = A \cdot \left(\frac{T}{273.15}\right)^B$$

$$k = K \cdot \frac{V_S}{V_M} = K \cdot \frac{2w}{r} = E^{\Delta G/RT} \cdot \frac{2w}{r}$$

Column efficiency

$$H = f_1 \cdot \frac{2D_M}{u_o} + f_1 \cdot \frac{1+6k+11k^2}{96(1+k)^2} \cdot \frac{d^2}{D_M} \cdot u_o + f_2 \cdot \frac{2}{3} \cdot \frac{k}{(1+k)^2} \cdot \frac{w^2}{D_S} \cdot u_o$$

Design Parameters

- Choice of carrier gas
- Injection and detection modes
- Column variables
    - Column length
    - Column diameter
    - Stationary phase

Operation Parameters

- Carrier gas velocity
-
- Injection control (split/splitless)
- Choice of solvent

$$\bar{u} = u_o \cdot j = \frac{d^2}{64\mu(T) \cdot L} \cdot \left(\frac{P_i^2 - P_o^2}{P_o}\right) \cdot \frac{3}{2} \cdot \frac{(P_i/P_o)^2 - 1}{(P_i/P_o)^3 - 1}$$

$$f_1 = \frac{9(P_i^4 - P_o^4)(P_i^2 - P_o^2)}{8(P_i^3 - P_o^3)^2} \qquad f_2 = \frac{3P_o(P_i^2 - P_o^2)}{2(P_i^3 - P_o^3)}$$

$$\mu(T) = A \cdot \left(\frac{T}{273.15}\right)^B$$

$$D_M = \frac{0.001 \cdot T^{1.75} \left(1/M_S + 1/M_M\right)^{1/2}}{P(\Sigma V_S^{1/3} + \Sigma V_M^{1/3})^2}$$

$$\ln D_S = K_0 + K_1 \cdot C + \frac{(K_2 + K_3 \cdot C)}{RT}$$

$$k = K \cdot \frac{V_S}{V_M} = K \cdot \frac{2w}{r} = E^{\Delta G/RT} \cdot \frac{2w}{r}$$

Table 3-6. Effects of parameters on column performance in a rectangular column.

Retention time

$$t_R = t_M \cdot (1+k) = \frac{L \cdot (1+k)}{\overline{u}}$$

Design Parameters

- Choice of carrier gas
- Injection and detection modes
- Column variables
    - Column length
    - Column width
    - Column height
    - Suface roughness
    - Stationary phase

Operation Parameters

- Carrier gas velocity
- Column temperature
- Injection control (split/splitless)
- Choice of solvent

$$\overline{u} = u_o \cdot j = \frac{h^2}{24} \cdot \frac{(P_i^2 - P_o^2)}{\mu L P_o} \cdot (1 - \frac{192}{\pi^5} \frac{h}{d} \sum_{i=1,3,5,...}^{\infty} \frac{\tanh(i\pi \cdot d/2h)}{i^5}) \cdot \frac{3}{2} \cdot \frac{(P_i/P_o)^2 - 1}{(P_i/P_o)^3 - 1}$$

$$\mu(T) = A \cdot \left(\frac{T}{273.15}\right)^B$$

$$k = K \cdot \frac{V_S}{V_M} = K \cdot \frac{2w(d+h)}{dh} = E^{\Delta G/RT} \cdot \frac{2w(d+h)}{dh}$$

Column efficiency

$$H = f_1 \cdot \frac{2D_M}{u_o} + f_1 \cdot \frac{4(1 + 9k + \frac{51}{2}k^2)(\frac{d}{2})^2}{105(k+1)^2 D_M} \cdot u_o + f_2 \cdot \frac{2kw^2}{3(k+1)^2 F^2 D_S}(\frac{h+d}{h})^2 \cdot u_o$$

Design Parameters

- Choice of carrier gas
- Injection and detection modes
- Column variables
    - Column length
    - Column width
    - Column height
    - Suface roughness
    - Stationary phase

Operation Parameters

- Carrier gas velocity
-
- Injection control (split/splitless)
- Choice of solvent

$$\overline{u} = u_o \cdot j = \frac{h^2}{24} \cdot \frac{(P_i^2 - P_o^2)}{\mu L P_o} \cdot (1 - \frac{192}{\pi^5} \frac{h}{d} \sum_{i=1,3,5,...}^{\infty} \frac{\tanh(i\pi \cdot d/2h)}{i^5}) \cdot \frac{3}{2} \cdot \frac{(P_i/P_o)^2 - 1}{(P_i/P_o)^3 - 1}$$

$$f_1 = \frac{9(P_i^4 - P_o^4)(P_i^2 - P_o^2)}{8(P_i^3 - P_o^3)^2}$$

$$f_2 = \frac{3P_o(P_i^2 - P_o^2)}{2(P_i^3 - P_o^3)}$$

$$\mu(T) = A \cdot \left(\frac{T}{273.15}\right)^B$$

$$D_M = \frac{0.001 \cdot T^{1.75}\left(\frac{1}{M_S} + \frac{1}{M_M}\right)^{1/2}}{P(\Sigma V_S^{1/3} + \Sigma V_M^{1/3})^2}$$

$$\ln D_S = K_0 + K_1 \cdot C + \frac{(K_2 + K_3 \cdot C)}{RT}$$

$$k = K \cdot \frac{V_S}{V_M} = K \cdot \frac{2w(d+h)}{dh} = E^{\Delta G/RT} \cdot \frac{2w(d+h)}{dh}$$

3.5.1 DESIGN PARAMETERS

3.5.1.1 COLUMN LENGTH

Obviously, column length is a decisive parameter of plate number ($N = L/H$). In fact, it also affects plate height via flow velocity, although it is not included in Golay equation. Figure 3-12 shows the effect of column length on the number of plate height. When column diameter is fixed, the plate number increases as column length increases but u_{opt} does not change. If pressure is fixed ($\Delta P = 20$ psi), the column diameter required for the maximum plate number increases as the column length increase. In this section, the parameters are fixed at the following values unless the value is mentioned ($L = 30$ m, $d = 300$ μm, $D_M = 10^{-5}$ m^2/s, $D_S = 10^{-5}$ m^2/s, K = 1250, T = 20°C).

(a) (b)
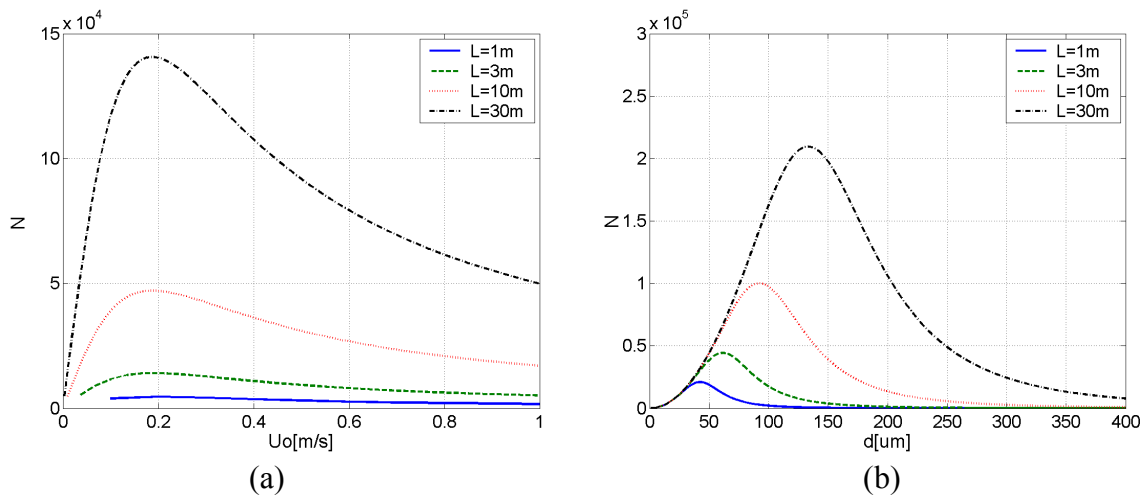
Figure 3-12. Effect of column length; (a) d = 300 μm, (b) ΔP = 20 psi.

3.5.1.2 COLUMN DIAMETER IN A CIRCULAR COLUMN

Column diameter is another important parameter. Figure 3-13(a) shows that H_{min} decreases and u_{opt} increases as column diameter decreases ($\Delta P = 0 \sim 40$ psi). Therefore, it is true that smaller diameter columns have better efficiency (smaller H_{min}). However, the absolute volume of stationary phase found in smaller ID columns will be considerably less. As a result, sample loading capacity will typically suffer and this may reduce sensitivity unless more concentrated samples can be used. Figure 3-13(b) shows that there is an optimum diameter that gives the best efficiency when pressure drop is fixed. As the pressure drop increases the optimum diameter value decreases and the best efficiency increases.

(a)   (b)
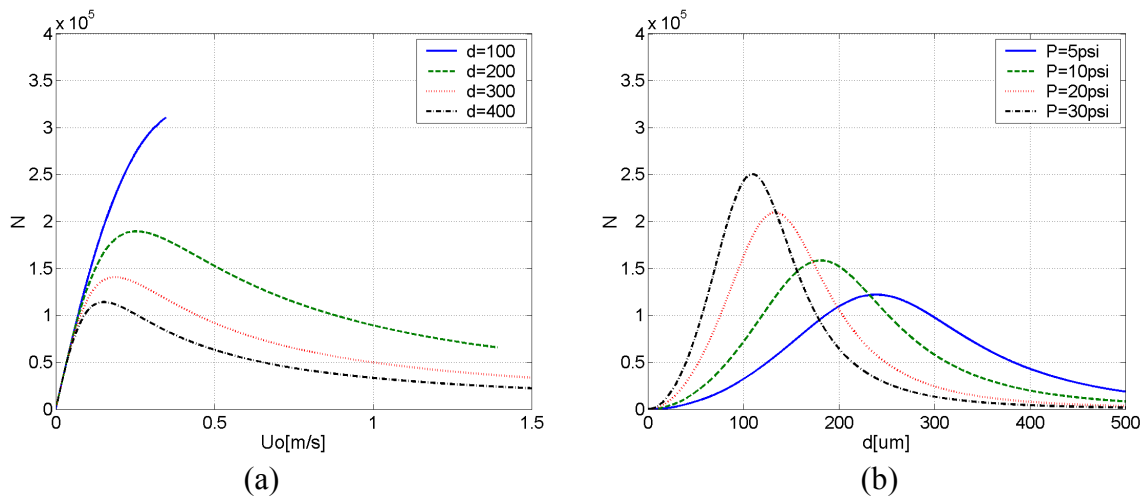
Figure 3-13. Effect of column diameter when L = 30 m.

3.5.1.3 COLUMN WIDTH AND HEIGHT IN A RECTANGULAR COLUMN

Column width and height influence chromatographic efficiency in two regards. First, they influence the velocity of the carrier gas that is an important parameter for retention time and column efficiency. Though column width and height are equally important to decide carrier velocity when the aspect ratio is low, the length of the narrow side becomes dominant factor when aspect ratio is high. In other words, column width is dominant factor in a narrow rectangular column (h>4d). Second, the column width and height affect phase ratio which, in turn, affects retention factor.

(a)   (b)
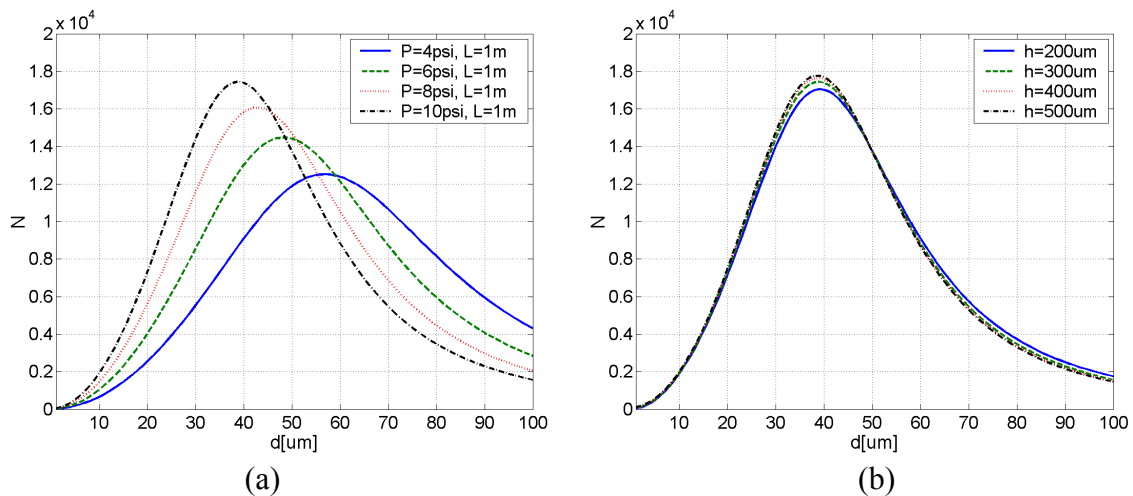
Figure 3-14. Effect of column width and height (L = 1 m, K = 1600).

As shown in Golay equation for a rectangular column, column width is very important parameter to determine the second term of the equation, consequently influencing H_{min} and u_{opt}. As column width decreases, H_{min} decreases (N increases) and u_{opt} increases as the effect of column diameter in a circular column. Figure 3-14 shows

the effect of column width and height on the number of plates. This graph shows us that there is an optimum column width to achieve the maximum column efficiency. However, column height does not affect the column efficiency much. Recall that column height is not included in the second term of Golay equation.

3.5.1.4 STATIONARY PHASE THICKNESS

Because the stationary phase thickness influences both the phase ratio and resistance to mass transport in the stationary phase (C_s term in Golay equation), thicker stationary phase films in otherwise identical columns will typically yield lower chromatographic efficiencies at u_{opt}. However the poor stability and sample loading capacity of thin stationary phase should be considered, too.
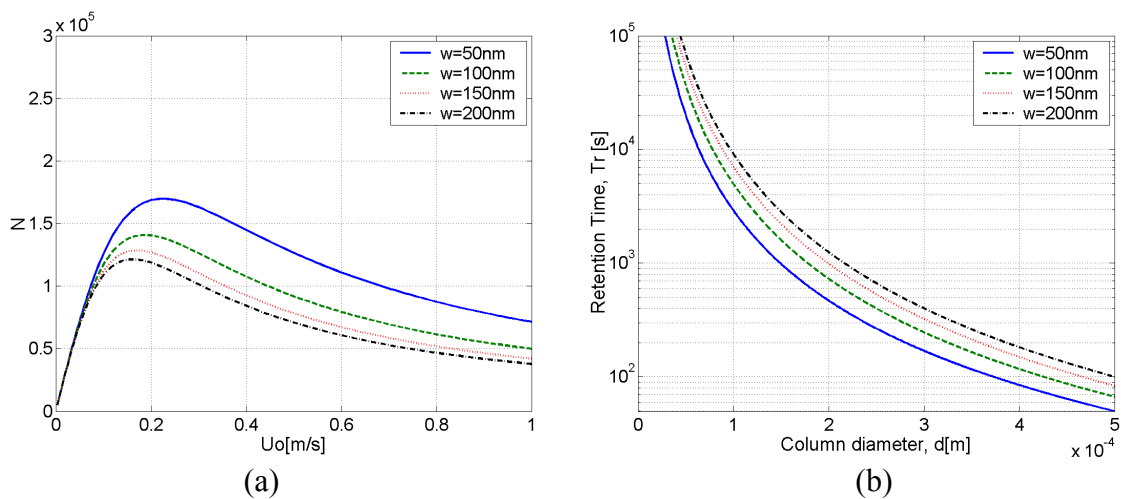
Figure 3-15. Effect of stationary phase thickness.

3.5.2 OPERATIONAL PARAMETERS

3.5.2.1 CARRIER GAS VELOCITY

Carrier gas velocity is the main variable of HETP in the Golay equation and it is a function of column diameter, length, inlet pressure, and carrier gas viscosity. Since the carrier gas is compressible, the relationship between flow rate and pressure drop is not linear as mentioned in the previous section. Pressure and velocity distribution along the column length and the average velocity of the carrier gas can be expressed as follows.

$$P(x) = P_o \cdot \sqrt{\left(\frac{P_i}{P_o}\right)^2 - \left(\frac{x}{L}\right) \cdot \left[\left(\frac{P_i}{P_o}\right)^2 - 1\right]}$$

Equation 3-57

$$u(x) = \frac{u_o}{\sqrt{\left(\frac{P_i}{P_o}\right)^2 - \left(\frac{x}{L}\right) \cdot \left[\left(\frac{P_i}{P_o}\right)^2 - 1\right]}}$$

Equation 3-58

$$\bar{u} = \frac{Q \cdot j}{\pi \cdot r^2}$$

Equation 3-59

where $j = \dfrac{3}{2} \cdot \dfrac{(P_i/P_o)^2 - 1}{(P_i/P_o)^3 - 1}$. Figure 3-16(a) shows the non-linear relationship between pressure drop and flow velocity at different column diameters. Figure 3-16(b) shows the pressure and flow velocity distribution along the column length.

91
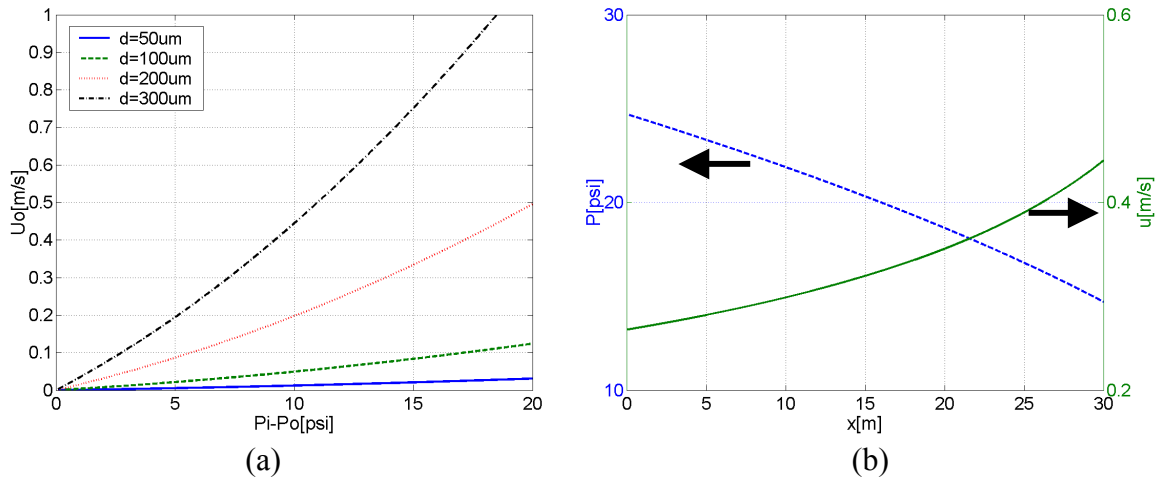
Figure 3-16. Pressure and flow velocity in a circular microcolumn.

3.5.2.2 TEMPERATURE

Much like column length, temperature never appears directly in either the retention time equation or the Golay equation. Nevertheless, temperature plays very important roles in determining the retention time and the column efficiency by virtue of its effect on carrier gas viscosity, distribution constant (K), and diffusion coefficients, D_M, and D_S. Therefore, during the temperature programmed analysis, the column efficiency keeps changing.

As temperature increases, u_{opt} appears to shift higher values, while H_{min} appears to shift to lower values. This reflects the fact that, at higher temperatures, k becomes smaller, while carrier gas viscosity and coefficients of solute diffusion in both the mobile phase and the stationary phase will increase. In general, decisions regarding column temperature should be made with the understanding that the effect temperature has on solute retention factors far outweighs the impact it has on chromatographic efficiency.

The viscosity of gas is a function of temperature as shown below.

$$\mu(T) = A \cdot \left(\frac{T}{273.15}\right)^{B}$$

Equation 3-60

where A and B are constants that are given empirically as follows.

Carrier gas	A	B
Hydrogen	8.35	0.68
Helium	18.6	0.646
Nitrogen	16.59	0.725
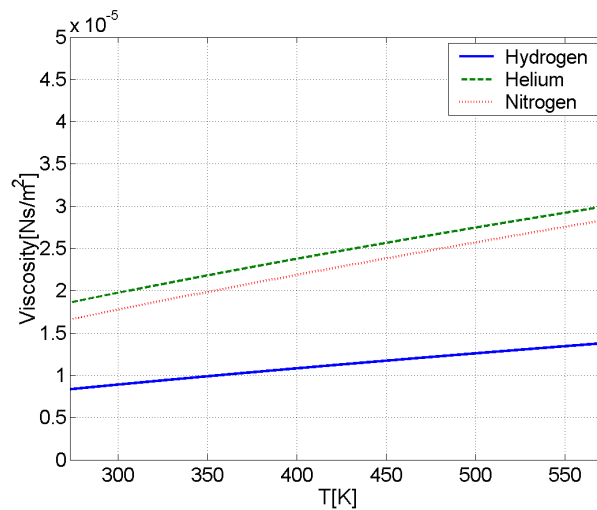
Figure 3-17. Carrier gas viscosity as a function of temperature.

As temperature of a gas system increases, so does the average speed of the molecules making up that system. As this occurs, the frequency with which such molecules collide increases and so the efficiency with which momentum is transported throughout the system increases. This results in an dynamic viscosity. As temperature increases, so does the dynamic viscosity of the mobile phase and a greater head pressure

is required to maintain the flow that was observed at lower temperatures. If the column pressure is held constant while temperature is increased, the average gas velocity will be decreased and consequently gas holdup time will be increased and column efficiency may be affected as well.

The temperature dependence of the diffusion coefficient of a solute in carrier gas is expressed by Fuller-Schettler-Giddings equation.

$$D_M = \frac{0.001 \cdot T^{1.75}\left(\frac{1}{M_S} + \frac{1}{M_M}\right)^{1/2}}{P(\sum V_S^{1/3} + \sum V_M^{1/3})^2}$$

Equation 3-61

where M_S, M_M are molecular masses of the solute and mobile phase respectively. For most organic chemicals, the values are $1 \sim 7 \times 10^{-5}$ [m^2/sec] at the temperature range of $20 \sim 80$ ^{o}C as shown in Table 3-7 [60].

The diffusion coefficient of a solute in stationary phase is also a function of temperature. Many cases, direct measurement and information of the coefficient are not available. It is usually estimated from the viscosity measurement.

$$D_s = \left(\frac{k}{2\pi}\right)\left(\frac{N}{V}\right)^{1/3}\left(\frac{T}{\mu}\right)$$

Equation 3-62

where D_s is the self diffusion coefficient in cm^2/sec, k Boltzman constant, N Avogadro's number, V molar volume in milliliters, T the absolute temperature, μ the viscosity of the liquid in poise (g/sec-cm). For large molecule diffusion, use 3π instead of 2π and for smaller molecule diffusion, use 1.4π. Value should be about $10^{-9} \sim 10^{-10}$ [m^2/sec].

Table 3-7. Diffusion coefficients of solvents in helium.

Analyte	Temp. [°C]	$D_M \times 10^5$ [m²/sec]	Temp. [°C]	$D_M \times 10^5$ [m²/sec]
Ethanol	20	4.76	70	6.71
Methanol	20	4.74	60	6.05
Isopropanol	20	3.14	80	4.76
Toluene	20	2.50	80	3.69
p-Xylene	20	2.26	80	3.28
Benzene	20	3.28	80	4.44
Pentane	20	2.86		
Hexane	20	2.27	60	2.73
Heptane	20	2.25	80	2.98
Octane	20	1.96	80	2.97

(a)   (b)
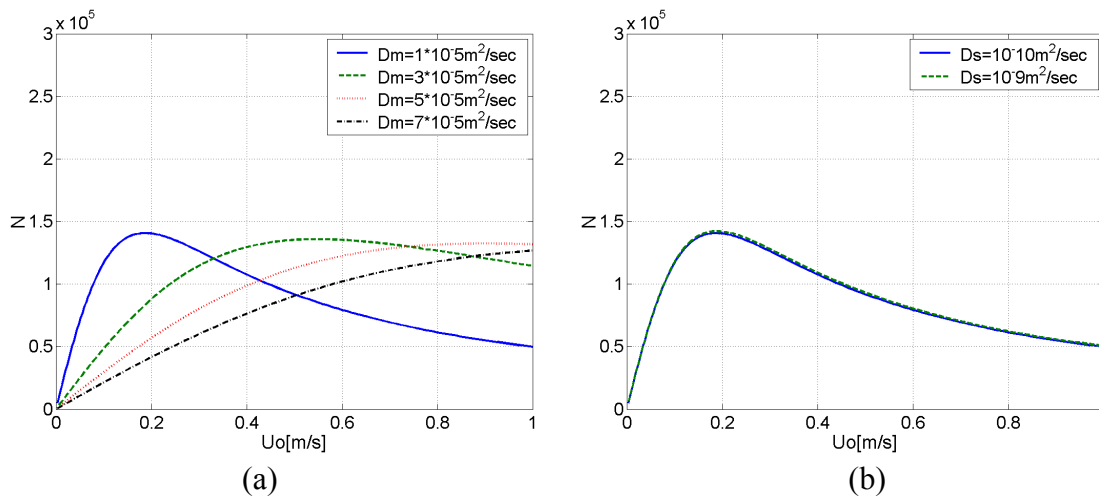
Figure 3-18. Effect of diffusion coefficients.

It is found from Figure 3-18 that H_{min} does not change much as D_M and D_S changes though u_{opt} increases significantly as D_M increases. The distribution constant (correspondingly retention factor) highly depends on temperature. Distribution constants (K) for many of the n-paraffin hydrocarbons on several stationary phases at specific temperatures are shown below. As K increases, both C_M and C_S increase. As a result H_{min} increases and u_{opt} decreases. Retention time increases as K increase.

Table 3-8. Distribution constants of hydrocarbons in commercial stationary phases.

Solute	Stationary Phase						
	SE-30		OV-210		OV-225	PEG 20M	
	51 ºC	100 ºC	48 ºC	97 ºC	97.5 ºC	98 C	148 ºC
Hexane	96						
Heptane	229		66				
Octane		87	139				
Nonane			302	45			
Decane			671	80	98		
Methanol						32	9
Etahnol						35	10
Propanol						64	15
Butanol						113	24
Pentanol						231	38
Benzene	161	37	117		42		
Chloroform	102		64		38		

(a)   (b)
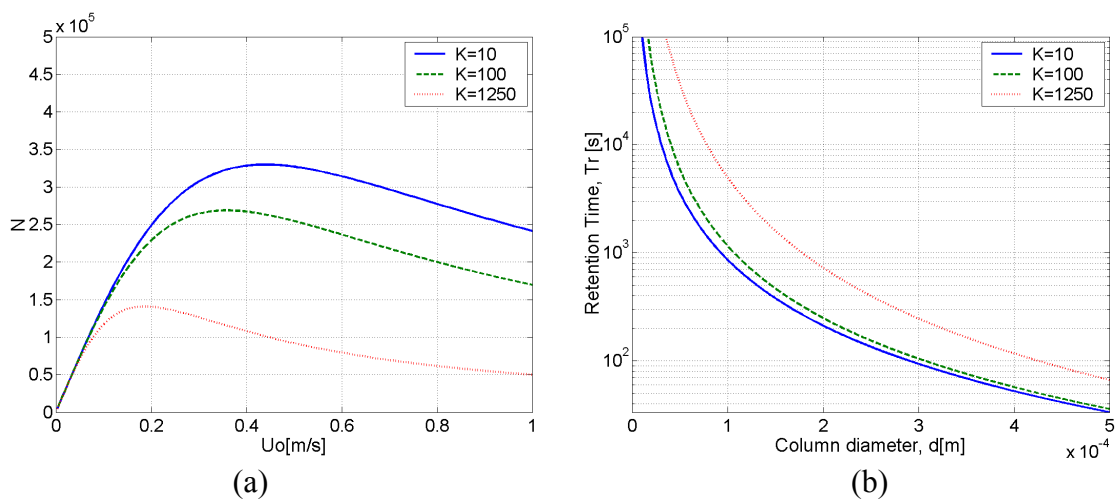
Figure 3-19. Effect of retention factor.

C H A P T E R 4

D E S I G N

The design of the parylene separation column comprises two elements; column

design and heating element design. Both design elements have several components that

need to be considered in the design of a GC column. The critical issues are listed in Table

4-1 with the related parameters and the methodology used in this research.

Table 4-1. Design strategy.

Design elements	Components	Related parameters	Methodology
Column design	Material selection	Column wall thickness	Manufacturability and material properties
	GC performance	Length, width, height, stationary phase type and thickness, and operation parameters	Analytic method (MatLab)
	Integration	Inlet/outlet	Manufacturability
	Deformation	Column wall thickness and effect of thin metal film	Finite element method (ANSYS)
	Gas permeation	Effect of thin metal film	Experiment
Heating element design	Entrance length	Inlet/outlet	Finite element method (ANSYS)
	Thermal cycling	Heating element location and dimension	Finite element method (ANSYS)
	Temperature distribution	Effect of thin metal film	Finite element method (ANSYS)

4.1 COLUMN GEOMETRY

4.1.1 COLUMN PERFORMANCE

The advantage of narrow rectangular column and the optimization of the parameters are discussed in this section.

4.1.1.1 ADVANTAGE OF NARROW RECTANGULAR COLUMN

For the conventional circular column, H_{min} decreases and u_{opt} increases as column diameter decreases. It is because the second term (C_M, dynamic diffusion in carrier gas) of the Golay equation becomes smaller as the diameter decreases. However, the trade-off for increasing the column efficiency by reducing its diameter is much higher pressure drop across the column, which is required to achieve the optimum carrier gas velocity. In addition, the volumetric flow rate often becomes too low for the detector.

When compared with standard capillary columns with radii greater than 200μm, the micromachined narrow rectangular columns (width d, height h, h>4d, d<100μm) are preferred due to its achievement of a large number of plates in a short column. As the channel becomes narrower, more gas is exposed to column walls and the diffusion distances become shorter. This increases the interaction with the stationary phase, decreases the required column length and leads to a shorter analysis time. In addition, the

higher volumetric flow rate can be provided by increasing column height, and this can be accomplished without affecting resolution.

Recall the modified Golay equation for a rectangular columns.

$$H = f_1 \cdot \frac{2D_M}{u_o} + f_1 \cdot \frac{4(1 + 9k + \frac{51}{2}k^2)(\frac{d}{2})^2}{105(k+1)^2 D_M} \cdot u_o + f_2 \cdot \frac{2kw^2}{3(k+1)^2 F^2 D_s} (\frac{h+d}{h})^2 \cdot u_o$$

where d and h are column width and height, respectively. The first (static diffusion) and third (dynamic diffusion in stationary phase) terms of the equation are basically the same as those of the original Golay equation for a circular column, although the third term slightly depends on the aspect ratio of the column. However, the second term depends highly on column width (Note that it depends on column diameter in the case of a round column). Therefore, H_{min} decreases and u_{opt} increases as column width decreases. Conversely, the change in column height does not affect H_{min} and u_{opt} much. However, volumetric flow rate increases as column height increases. This implies that we can have two control variables, column width and height, to control column efficiency and volumetric flow rate, respectively.

This can be clarified when a round column and a narrow rectangular column having the same cross-sectional area are compared. For example, a round column with a diameter of 190 μm and a rectangular with a width of 80 μm and a height of 350 μm have almost the same cross-sectional area. The narrow width of a rectangular column reduces the second term (dynamic diffusion in mobile phase) of the Golay equation and therefore the rectangular column has lower plate height and higher number of plates (~10,000) compared with a circular column ($N \sim 6500$) as shown in Figure 4-1 (a) and (b). In order that the round column may have as large number of theoretical plates as the rectangular

column, the diameter of the round column must be decreased to about 120 μm (Figure 4-1 (c)). In that case, however, the volumetric flow rate will be much less than that of the rectangular column. A good rule of thumb is that the efficiency can be adjusted by selecting the column width, and the volumetric flow rate can be adjusted by selecting the column height.
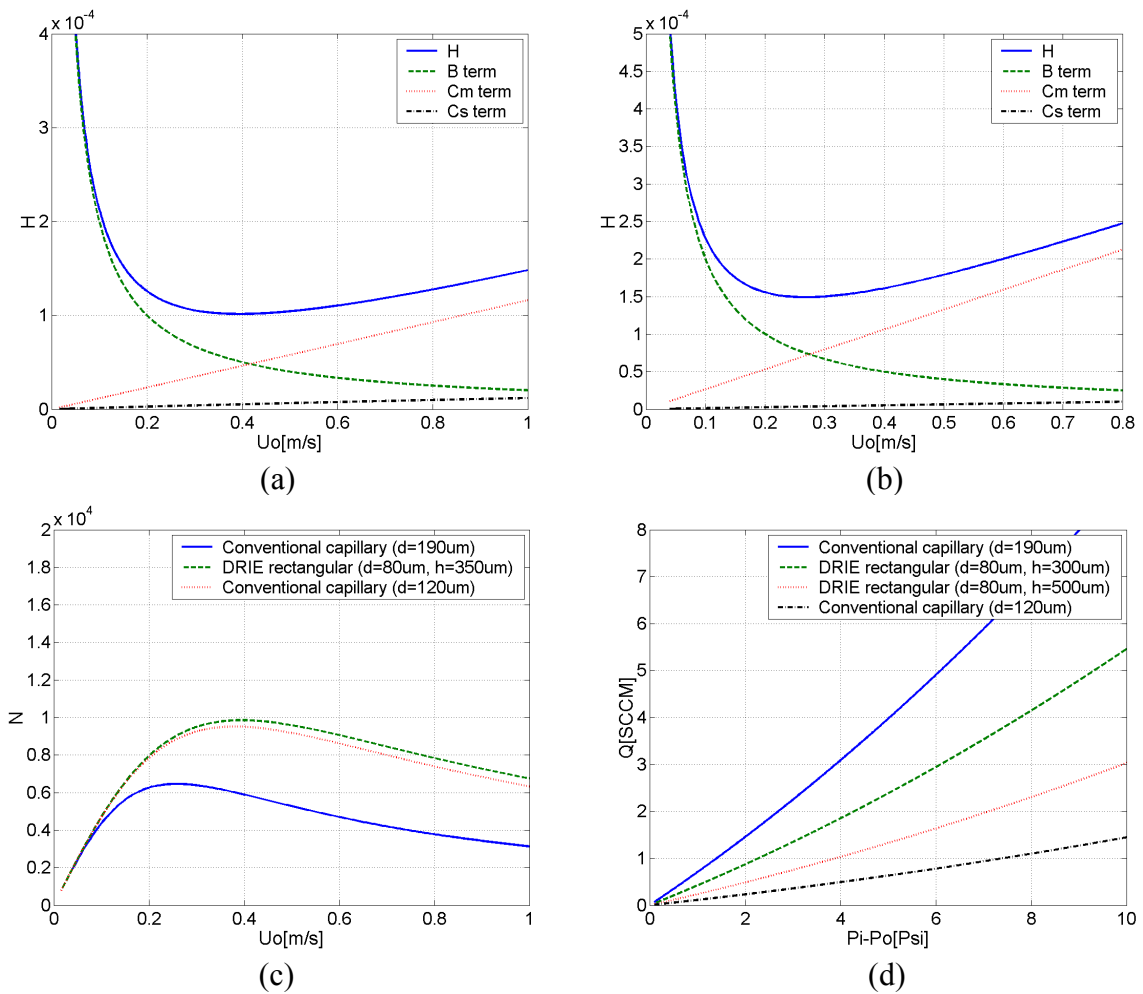
Figure 4-1. Comparison between a circular and a rectangular column having the same cross sectional area, (a) plate height of a rectangular column, (b) plate height of a circular column, (c) plate number of both columns, (d) volumetric flow rate.

4.1.1.2 COLUMN DESIGN OPTIMIZATION

For GC columns, good performance means short retention time and better efficiency (lower plate height or higher number of theoretical plates). However, satisfying the two components of good performance at the same time is almost impossible because they are contradictory. For example, the number of theoretical plates increases with column length but the retention time decreases with it. Therefore, the manufacturer's column design and user's column choice completely depend on type of analytes and demanded analysis time. In this research, our goal is developing a miniature GC column that can be used for a rapid, sensitive and selective hand-held GC system which could be used for the field detection of chemicals. Therefore, we suppose that the desirable retention time is less than 1 minute for the analytes having a retention factor of 5 at room temperature and the required number of theoretical plates is more than 10,000. Since both retention time and column efficiency can be enhanced using temperature cycling, these requirements are considered to be good enough for initial column design.

Even if specific performance requirements are given, the design of GC column is still very difficult due to the non-column parameters such as the material properties of carrier gas and analytes to be tested. As we discussed in the previous chapter, column efficiency and retention time are highly dependent on the distribution constant and diffusion coefficients of the analytes. In addition, operational variables such as pressure (flow rate) and column temperature play important roles in column efficiency. For instance, the distribution constant and diffusion coefficients are the function of temperature. Therefore, in order to optimize column design, all the detail information of non-column parameters and operational variables must be provided. However, many of

the material properties are not well known and usually many different analytes are used

in GC analysis resulting in broad ranges of material properties. Therefore many previous

researchers who have developed micro GC columns used general values for material

properties in order to optimize their column design. The values of non-column

parameters and operational variables they used are listed in Table 4-2. We also use some

general values of material properties to optimize our column design. The values are

retention factor k = 5, diffusion constants $D_M = 10^{-6}$ cm^2/sec, $D_S = 0.1$ cm^2/sec. These are

general values for organic samples. The inlet pressure is assumed to be less than 24.7 psi

($\Delta P \leq 10$ psi) and column temperature is 20 ^{o}C.

Table 4-2. Non-column parameters and operation parameters for column design.

	K	k	D_M [cm^2/sec]	D_S [cm^2/sec]	P_i, P_o	Temp.
Terry	-	-	-	-	~ 60 psi, 1 atm	
Reston	100	-	10^{-6}	-	~ 60 psi, 1 atm	50 ^{o}C
Wiranto	-	10	10^{-6}	0.1	~ 5, 1 atm	100 ^{o}C
Sandia	-	5	10^{-6}	0.1	14.7, 8.7 psi	
Michigan	-	10	-	-	1, 0.6 atm	
GT	1600	5	10^{-6}	0.1	~ 24.7 psi, 1atm	20 ^{o}C

Now since material properties and operational variables are chosen, column

design parameters can be optimized. Column parameters are length, width, height,

stationary phase type and thickness. Among these, column length and width, stationary

thickness are dominant parameters for column efficiency and retention time. Column

height (when h>4d) does not influence column performance much. Therefore, it is fixed

at 300 µm for the following calculations. But it should be noted that column height can

work as a knob to control volumetric flow rate though it does not affect flow velocity much. Stationary phase type is another important factor but is not considered here because the material constants are already assumed above.

Figure 4-2 shows how column efficiency changes with column width at different pressure drops (a) and column length respectively (b). The other parameters were fixed as follows: column height h = 300 μm, stationary phase thickness w = 100 nm, temperature T = 293.15 K. For pressure drop between 4–10 psi and column length 1 m, the required number of theoretical plates (≥ 10,000) can be obtained when column width is between 45–55 μm. These were calculated in MatLab using formulas in previous chapter. Of course, longer columns give higher number of plates but the cost is longer retention time and bigger size.

(a)   (b)
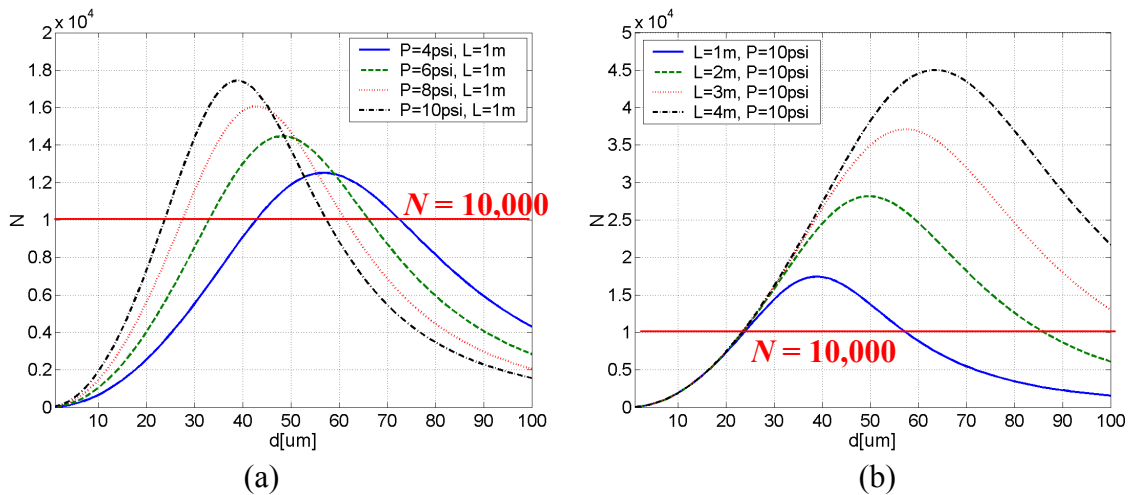
Figure 4-2. Change in column efficiency with column width (a) at different pressures, (b) at different lengths.

The retention time for the above conditions is shown below. For column width between 45-55 μm and pressure drop 4-10 psi, the retention time is always less than 1 min when column length is 1m but it ranges 2-8 min when column length is 3 m.
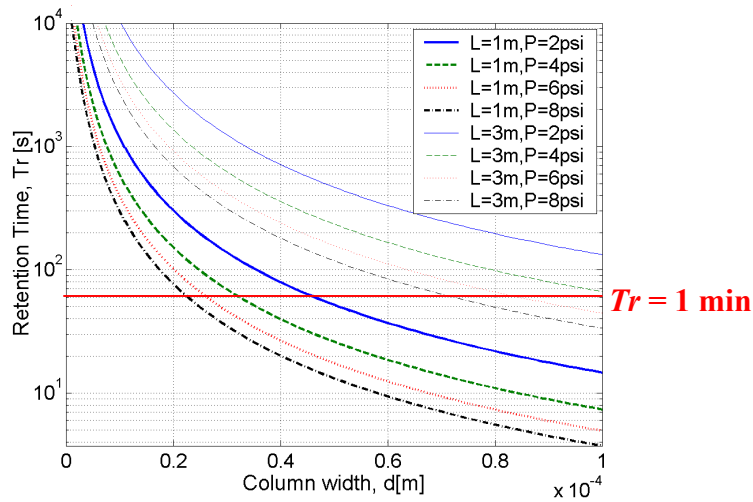
Figure 4-3. Retention time as a function of column width, length and pressure.

Now what will be H_{min} and u_{opt} for the above column dimensions? And also can u_{opt} be achieved with the given pressure drop? The following two graphs give the answers. When column width is 50 µm and length is 1 m, u_{opt} is about 0.6 m/s and maximum number of plates is about 14,600. However when column length is 3 m, u_{opt} cannot be achieved with pressure drop of 10 psi.
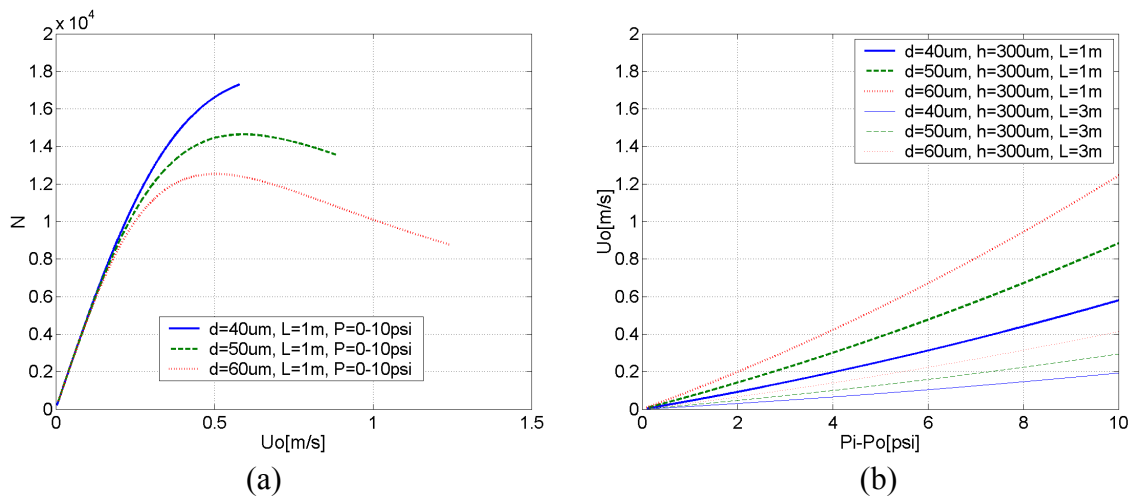
Figure 4-4. Maximum column efficiency and u_{opt} for different column dimension.

Lastly, Figure 4-5 show the effects of stationary phase thickness on column efficiency and retention time, respectively. The number of theoretical plates ranges 13,000-16,500 and the retention time ranges 10-30 sec according to stationary phase thickness when column width is 50 μm, height is 300 μm, and length is 1 m. Since both column efficiency and retention time highly depend on stationary phase thickness, uniform coating of stationary phase is very important. The non-uniformity in stationary phase thickness may cause significant change in column efficiency and retention time.

(a)   (b)
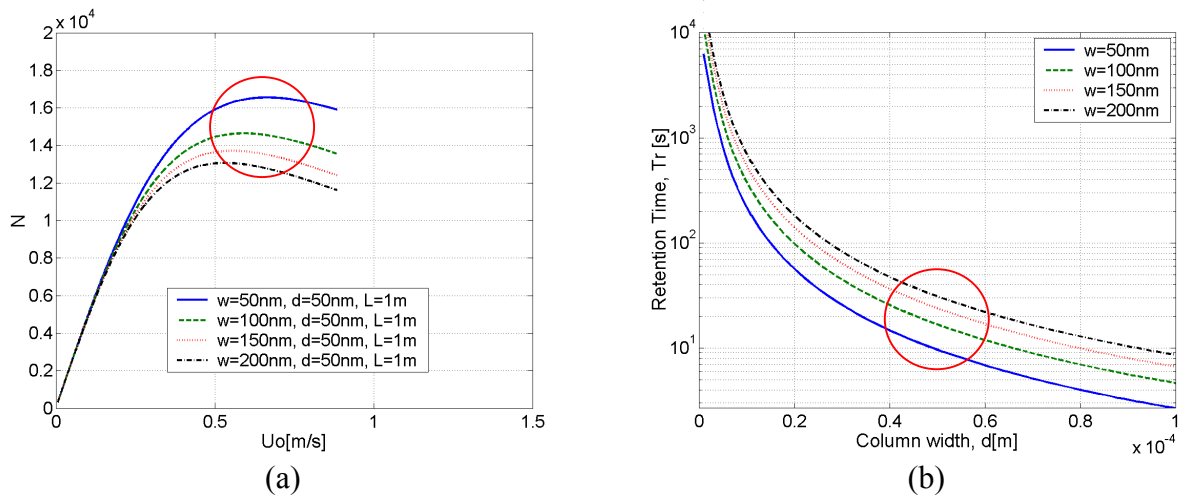
Figure 4-5. The effect of stationary phase thickness on column efficiency and retention time.

As a conclusion, the column parameters chosen to meet the given performance requirement (N ≥ 10,000, Retention time ≤ 1 min) are as follows.

Column length   = 1 m
Column width   = 50 μm
Column height   = 300 μm
Stationary phase thickness = 100 nm
Pressure drop   = 6 psi
Carrier gas velocity = 0.5 m/s

4.1.2 INTEGRATION

Micromachined silicon/glass columns generally have a spiral design in order to achieve a long column on a small area without creating sharp curvature (Figure 4-6 (a)). The most popular tubing methods for silicon/glass columns are top connection via etched hole in pyrex glass substrate (Figure 4-6 (b)) and bottom connection via etched hole in silicon substrate. However, these techniques cannot be applied to our parylene column because of parylene's nature as a thin film. Side tubing was devised for the parylene column as shown in Figure 4-7 (b). In both top and side tubing techniques, the flow path cannot remain constant, having some dead volume. However, while top connections have an abrupt change in the direction of flow path, side connections do not have such a change in flow direction. In order to realize side connections, both ends of the column must be located outside the spiral pattern. Therefore, a dual spiral design was selected for parylene column as shown in Figure 4-7 (a). Both the inlet and outlet have a bigger width (500 μm) than the main spiral part for the easy insertion of silica tubing.

(a)   (b)
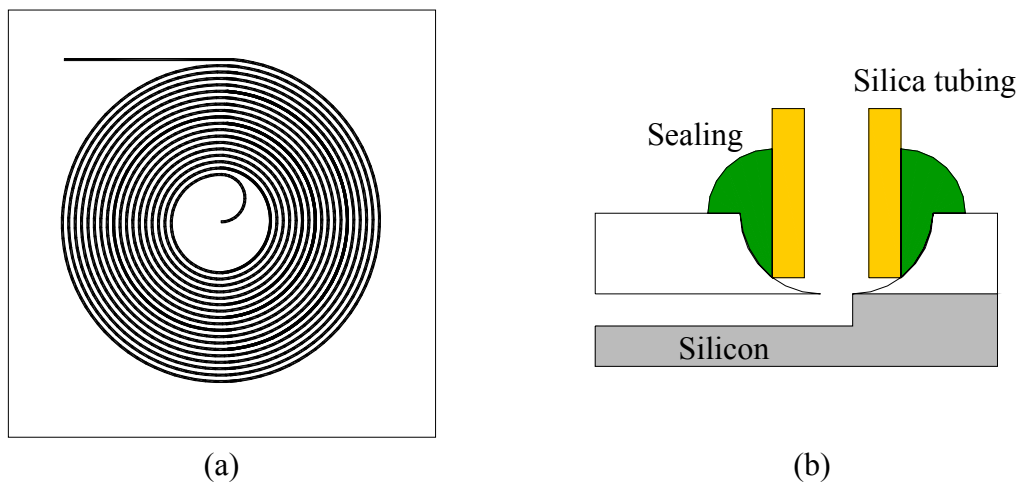
Figure 4-6. General design of silicon/glass column; (a) top view (spiral column), (b) side view of column end and tubing.

(a)   (b)
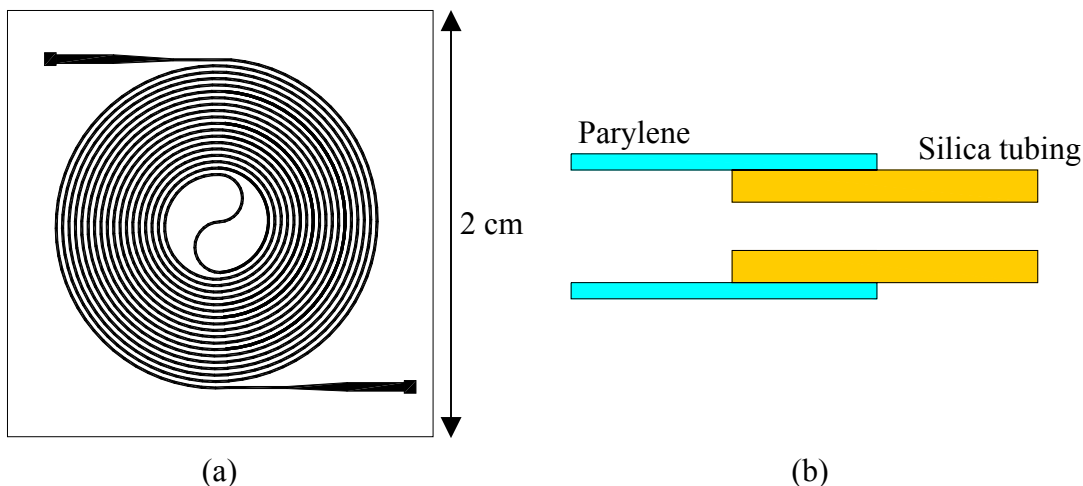
Figure 4-7. Design of parylene column; (a) top view (dual spiral column), (b) side view of column end and tubing.

As discussed in Chapter 3, we need to avoid a very small curvature radius because sharp curvature causes lateral diffusion due to centrifugal force, resulting in band broadening. Recall that this curvature effect can be quantified using the Dean number, the ratio of centrifugal force to viscous force. Sandia National Laboratories developed a time-dependent adsorption/desorption model and incorporated this model into a computational fluid dynamics (CFD) code to simulate analyte transport and separation process in GC columns [19]. According to Sandia, when the Dean number is low around 0.2, the flow behaves like a 2D flow with a minimal curvature effect. However, when the Dean number becomes big, around 13, the curvature effect becomes significant and the analyte migrating at the outer wall is lagging behind the analyte migrating at the inner wall. This leads to a band broadening. Hence, the curvature effect is more significant when flow rate increases or column size increases.

Now let's consider a dual spiral design as shown above. Gas goes in toward the center and then come out to the side of the die. In this design, the smallest curvature

radius exists in the center. For example, if the smallest curvature radius is 160 μm, column width is 80 μm, and the carrier gas velocity is 1 m/s, the Dean number becomes 1.34 but if the smallest curvature radius is increased to 800 μm, the Dean number becomes about 0.15, which is very low. So, the smallest curvature radius of 800 μm was used in this study.

The last thing we need to consider is the interchannel distance. The dimension of column itself was optimized by analytic tool for theoretical column performance. And a dual spiral design was selected considering tubing. However, the distance between channels in a dual spiral design has not been discussed. This is an important factor with column width and length to decide the chip size. The only limit regarding the interchannel distance was that it need to be enough for parylene/parylene bonding process. No literature was found regarding this issue nor any experiment was performed to answer the question. The interchannel distance was fixed at 100 μm for all designs in this study. As a result, the chip size was designed to have 2 cm by 2 cm square.

4.1.3 DEFORMATION AND GAS PERMEATION

4.1.3.1 DEFORMATION OF THE COLUMN BY INNER PRESSURE

Now the inner column dimension and the overall shape of column have been optimized. The only thing that was not discussed as to column design is the thickness of the column wall. As pointed out in the introduction chapter, the main advantage of the

parylene column is its low thermal mass. Therefore, the wall is preferred to be as thin as possible. However, if the wall is too thin, the column can be deformed or damaged by the high inner pressure required for both GC analysis and stationary phase coating. First, if any significant deformation occurs in the cross sectional shape of parylene column during GC analysis, it increases the length of dynamic diffusion of analytes, resulting in band broadening. As a result, the deformation if ever happens will bring about a big deviation between theoretical and empirical efficiency values because the theoretical column efficiency of a rectangular parylene column has been calculated based on the assumption that its cross-sectional shape does not change with inner pressure. Second, one of the most critical steps in GC column fabrication is stationary phase coating which is generally accomplished by injecting a solution containing polymeric material. The final coating thickness depends on the flow rate of the injected solution which is a function of cross-sectional dimensions. Therefore the deformation of the channel will change the coating thickness. Also it can affect the coating uniformity.

Finite element analysis was used to investigate the deformation of parylene column. 2D analysis was performed for a narrow rectangular column (80 μm width, 300 μm height) as shown below. The main parameters for the deflection are definitely the length and thickness of the wall. Since the length of the wall (height of the column) is fixed in this case, only the effect of wall thickness will be investigated. Another thing to be investigated is the effect of thin metal layer. A parylene/Pt/parylene sandwiched layer will be compared with a monolayer parylene column in terms of the deformation. The two structures of interest are shown in Figure 4-8.

There were some assumptions made for ANSYS 2D analysis. First, the top flat substrate was assumed to be fixed because it is supported by large bonded area and neighbor channels. Second, parylene/parylene bonded interface is assumed to be strong enough to remain unbroken for the deformation study. Third, parylene is assumed to have isotropic mechanical properties as shown in Table 4-3.

| | (a) | | (b) |
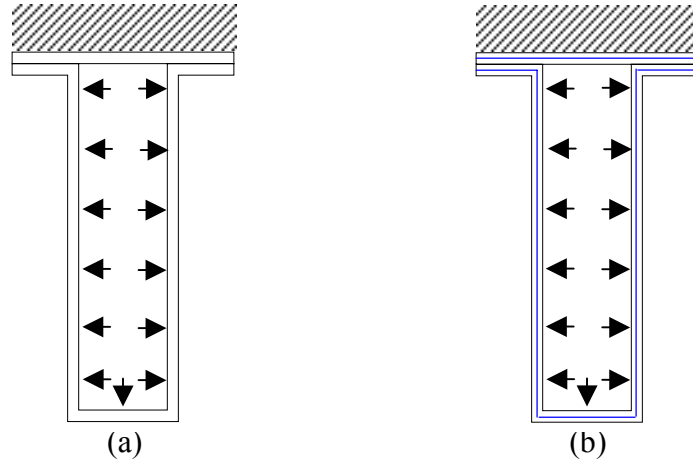
Figure 4-8. Two structures of interest for deformation study (a) parylene monolayer column, (b) parylene/Pt/parylene sandwiched layer column.

Table 4-3. Material properties of parylene and platinum.

Material	Density [g/cm^3]	Young's modulus	Poisson's ratio
Parylene C	1.289	3200 MPa	0.4
Platinum (Pt)	21.4	170 GPa	0.3

Figure 4-9 shows the stress distribution under a pressure difference of 60 psi in parylene monolayer columns. Obviously, thicker column has less deformation at the same pressure. Vertical wall has more deformation than horizontal wall because it is longer. The maximum deflection occurs around the center of each side and the value is plotted in Figure 4-10 as a function of pressure difference for different wall thicknesses.

When the wall thickness is 5 µm, the maximum deformation of the parylene monolayer column is as big as 58 µm (vertical wall) under the pressure difference of 10 psi. But if the wall thickness is increased to 10 µm or 20 µm, the maximum deformation is reduced to 7.5 µm or 1 µm, respectively. Since the pressure drop required for GC analysis ranges up to 10 psi, the wall thickness needs to be at least 10 µm.
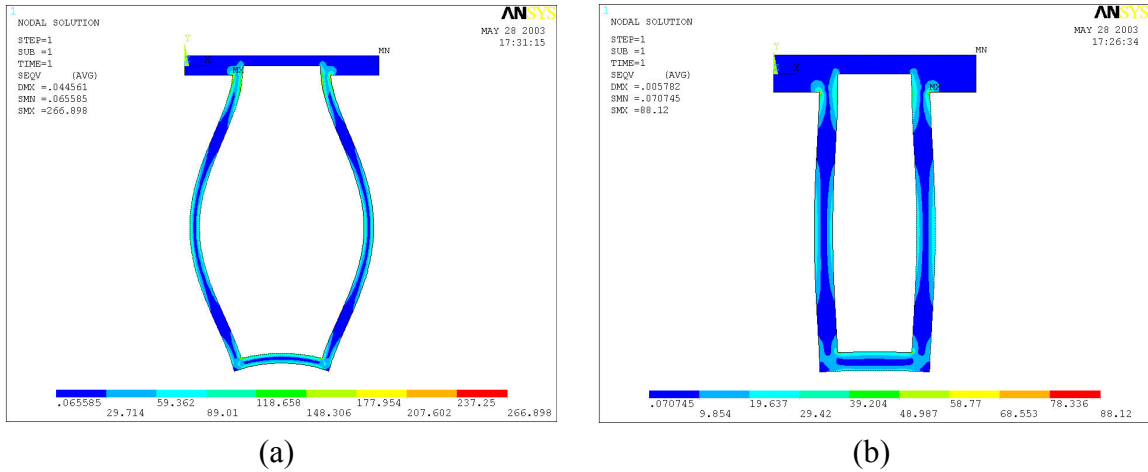
Figure 4-9. Stress distribution of parylene monolayer column; (a) 10 µm thick and 60 psi, (b) 20 µm thick and 60 psi.
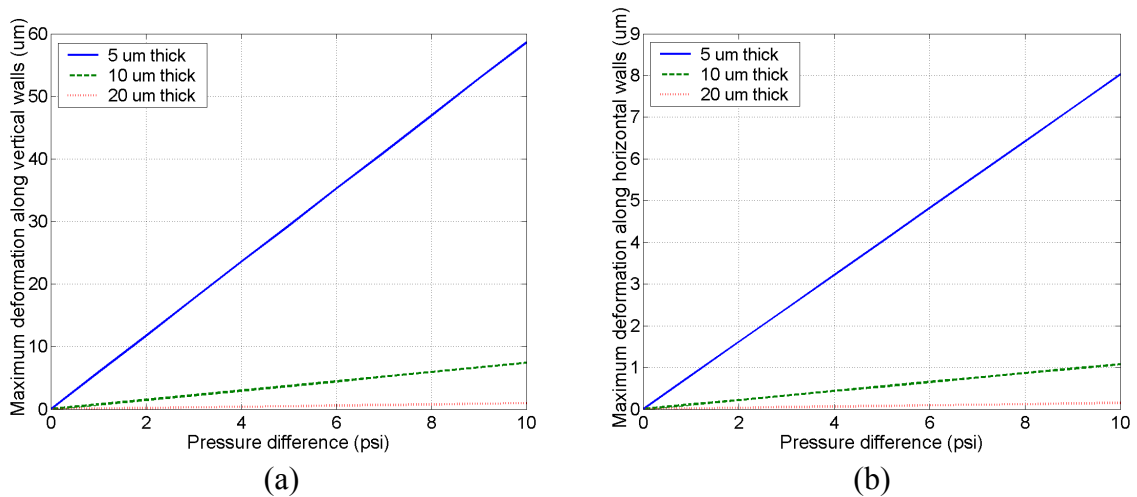
Figure 4-10. Maximum deformation of parylene monolayer column as a function of pressure difference at different thicknesses (a) vertical wall (b) horizontal wall.

111

What will be the effect of a thin metal layer on the deformation? Figure 4-11 shows the effect of metal layers on the maximum deflection. Three different thicknesses (0.1, 0.2, and 1 μm) were investigated. As the metal thickness increases, the maximum deformation decreases. In addition, the stress concentration effect at the corners was lowered by the insertion of the metal layer.

(a)   (b)
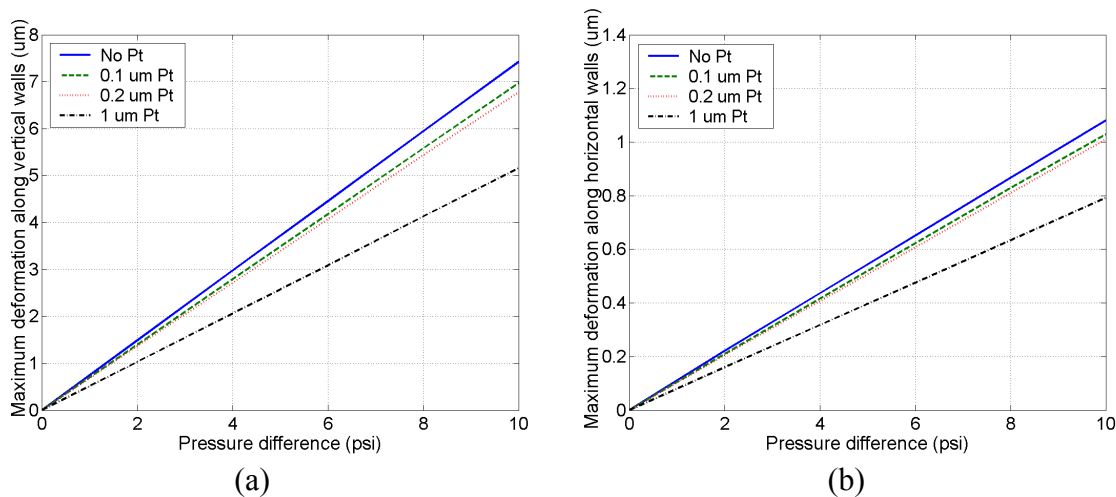
Figure 4-11. Effect of metal insertion on the maximum deflection for 10 μm thick parylene column (a) vertical wall, (b) horizontal wall.

4.1.3.2 GAS PERMEABILITY

Another thing that needs to be considered regarding column wall thickness is gas permeation. GC column must not allow gas molecules to permeate through the column wall. Especially, the permeation of oxygen should be lowered because it can degenerate the stationary phase of the column. In the previous section, we compared a parylene monolayer and a parylene/Pt/parylene sandwiched layer in terms of the deformation under inner pressure. The existence of a thin metal can also be a benefit to the permeation property of the membrane because the metal layer has lower permeability than polymers.

112

In order to measure the gas permeability of parylene layers, large membrane with an area of 100 in^2 were prepared. A 20 μm thick parylene monolayer and parylene/Al/parylene (10μm/0.1μm/10μm) sandwiched layer were prepared carefully. The measurement of gas permeation was done by *Polymer Diagnostics* (Minneapolis, MN 55428) and the average result is shown in Table 4-4. The triple structure showed much less permeation rate for both water vapour and oxygen. Therefore the sandwiched structure is desired to prevent gas permeation through the column.

Table 4-4. Gas permeation data of parylene membranes (test temperature was 50 ^{o}C and the unit of the data is cc/100 in^2·day)

Gas	Parylene (20μm)	Pary/Al/pary (10μm/0.1μm/10μm)
Water vapour	1.05	0.00770
Oxygen	27.85	Less than 0.0003

4.2 HEATING ELEMENT

It was emphasized in the previous chapters that thermal cycling of a GC column is very important for an efficient GC analysis. In conventional GC, the column is generally housed in a large convection oven for thermal cycling. What will be the alternative heating method for a miniature GC column? Joule heating can be the solution. Many MEMS devices have a thin metal layer as heating element. Where and how can we build the Joule heating element in the parylene column? A long gold film resistor can be formed by the evaporation of gold on the corrugated surface of the parylene column as

shown below. This method was chosen because we can create a heating element without further mask process by using the corrugated geometry of the parylene column.
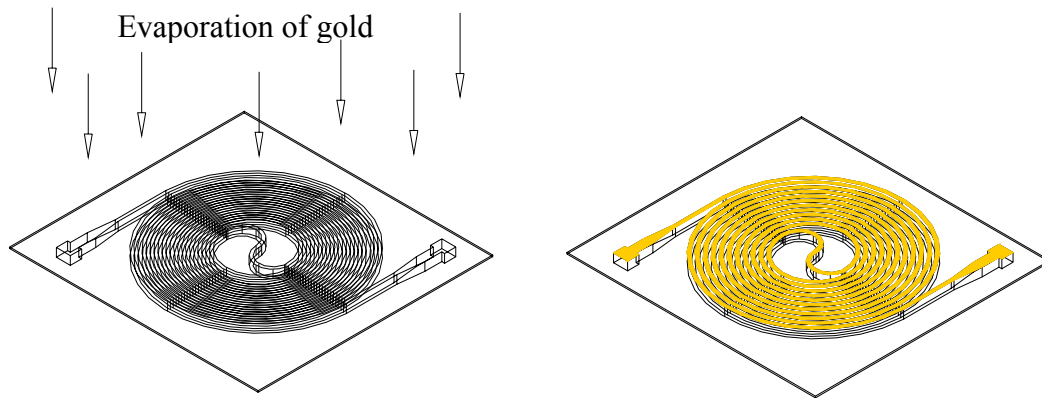
Figure 4-12. Formation of Joule heating element on parylene column.

Regarding the performance of heating element, there are two main questions that must be answered at the designing stage. First, how much advantage does low thermal mass parylene column have in the thermal cycling of the column and power consumption compared with silicon/glass column? Second, can a uniform temperature distribution be obtained in a parylene column? To answer these questions, the heat transfer in parylene column was investigated using finite element analysis.

To begin with, we need to simplify the geometry. The geometry that is being analyzed has two main simplifications that can be used on it. The first is in the z-direction. For our z-axis, we let it run down the center of the column. This means that we have a z-axis that is spiral in reality. We are able to eliminate the z-direction from analysis because analytic calculations and FEA showed that the length required to achieve fully developed temperature profile was very small compared to the overall length of the channel. These calculations will be shown in the following section. The second simplification that can

be made is more obvious, and is best demonstrated by Figure 4-13 below. This is the

SEM image of the cross-section of Si microchannel that is used as mold for parylene

column. This shows the repeating pattern of the channel in the x-direction. Since there is

a repeating pattern, it is possible to cut each channel wall in half and use symmetry (black

box in the figure).
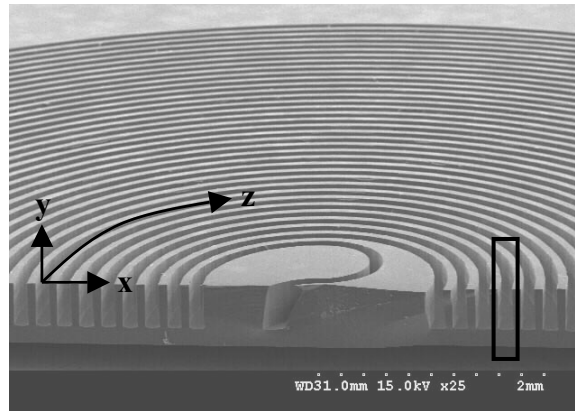
Figure 4-13. SEM image of the cross section of a microchannel.

4.2.1 ENTRANCE LENGTH

In an internal flow, flow velocity and temperature develops as the flow advance in

the channel. The length between the entrance and the location where the flow becomes

fully developed is called entrance length. One of the simplification made for FEA was

neglecting z-direction and performing 2D analysis. This simplification needs to be

justified by proving that the entrance length is negligible in this problem.

Analytic solutions for the entrance length are available. The hydrodynamic entry

length and the thermal entry length for laminar flow are expressed as below.

115

$$X_{fd,h} \approx 0.05 \cdot \text{Re} \cdot D_h$$

Equation 4-1

$$X_{fd,t} \approx 0.05 \cdot \text{Re} \cdot D_h \cdot \text{Pr}$$

Equation 4-2

When a helium gas flows through a rectangular parylene column (80 µm X 300 µm), the entrance length is only a few microns (Table 4-5) according to the above formula that is negligible compared with column length (1 m).

Table 4-5. Calculation for entrance length.

d [µm]	h [µm]	u [m/s]	ρ [kg/m^3]	μ [kg/m·s]	α [m^2/s]	Re	Pr	$X_{fd,h}$ [µm]	$X_{fd,t}$ [µm]
80	300	1	0.1625	1.99x10^{-5}	1.8x10^{-4}	0.653	0.678	2.6	1.8

(a)   (b)
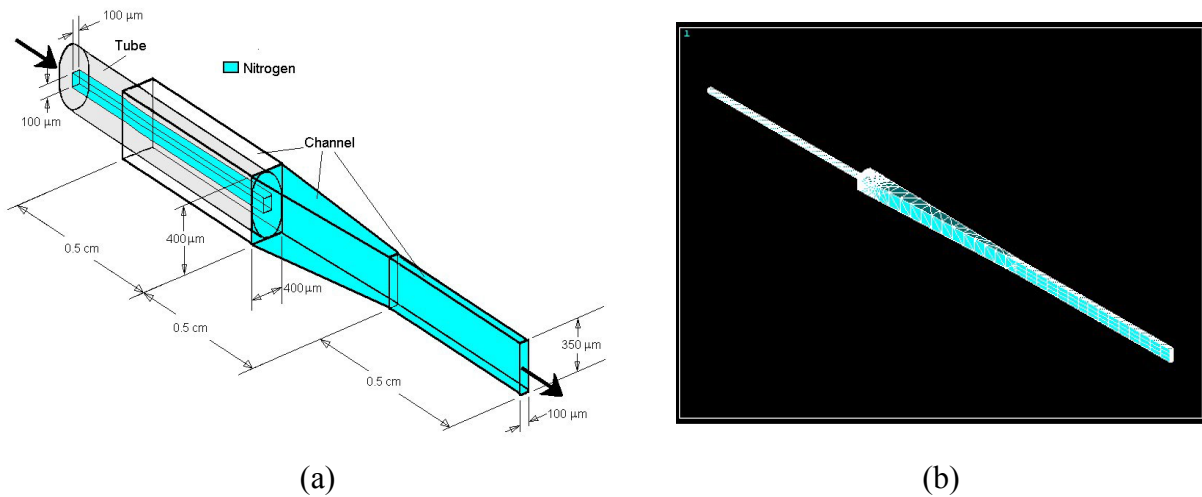
Figure 4-14. The geometry of the inlet of a parylene column with a microtube inserted; (a) schematic, (b) the meshed flow volume used in this analysis.

3D ANSYS analysis was also performed to find out the entrance length where the temperature and velocity of carrier gas are fully developed. The geometry of the inlet of

a parylene column is shown Figure 4-14 (a). the blue region in this figure shows the flow

volume for the fluid. To recreate this flow volume for ANSYS the blue area only was

used in fluidic analysis. Figure 4-14 (b) shows the volume and mesh used for ANSYS

computations. When the column temperature and flow rate are 80 ^{o}C and 1 ml/min, both

fluidic and thermal entrance length were less than 1 mm (Figure 4-15, Figure 4-16),

which is negligible comparing with column length (1m).

(a)   (b)
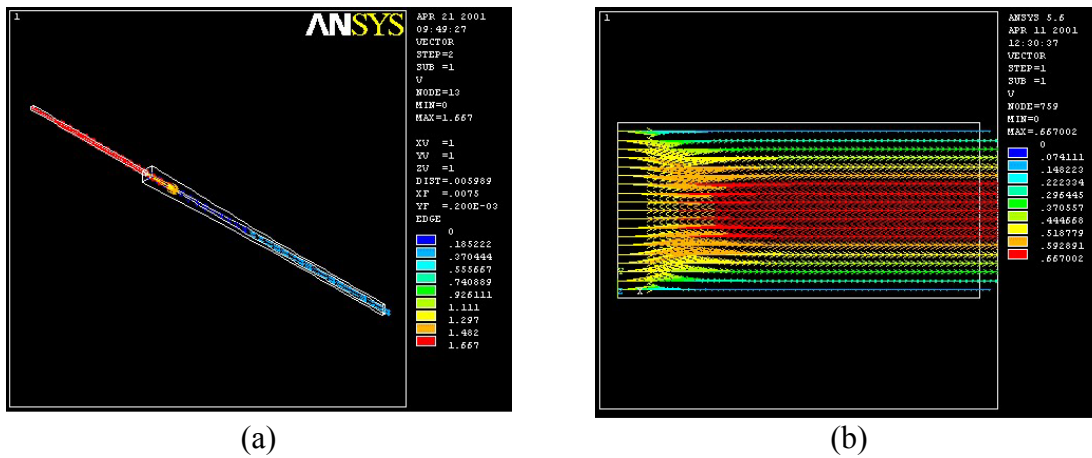
Figure 4-15. Fluidic entrance length; (a) velocity, (b) velocity vector distribution.
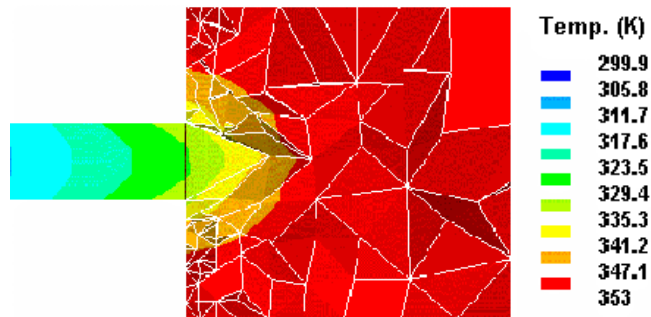
Figure 4-16. Thermal entrance length.

4.2.2 THERMAL CYCLING

Since the entrance length is negligible, simplified 2D geometry will be used for the further analysis. For the transient analysis for thermal cycling, simplified 2D geometries were used for three different columns as shown below.
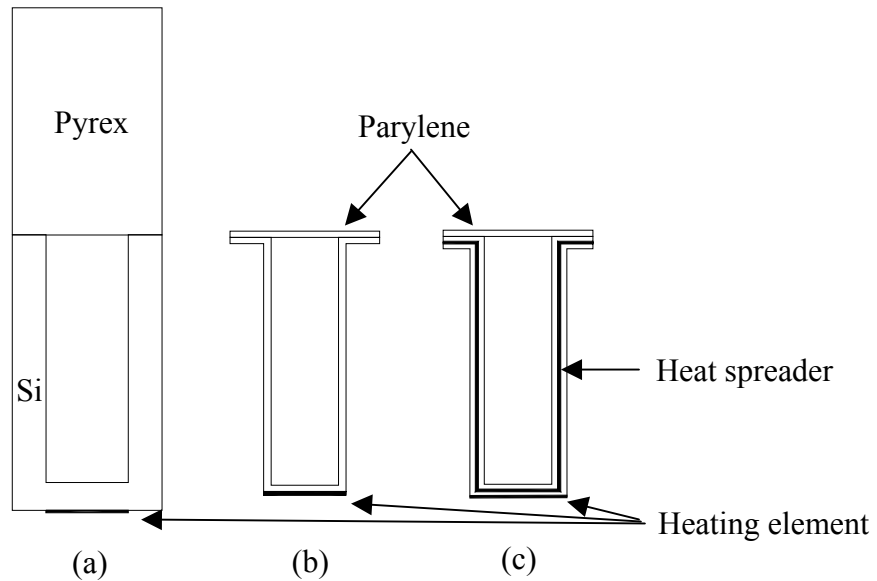
Figure 4-17. The 2D geometries of (a) the silicon/glass column, (b) monolayer parylene column, (c) sandwiched parylene column.

The material properties used in this analysis are listed in Table 4-6. For the following analysis, it was assumed that the column is filled with stagnant air to simulate the heating of column before the introduction of a carrier gas. Temperature-dependent properties of air was considered in this study by assuming that they change linearly with temperature between 27 $^{\circ}$C and 80 $^{\circ}$C. However, the materials have temperature-independent properties in the temperature below 100 $^{\circ}$C.

Table 4-6. Material properties used in ANSYS analysis.

Material	Density	Specific heat	Thermal conductivity	Resistivity	Melting point
	[kg/m³]	[J/kg·°C]	[W/m·°C]	[Ω·m]	[°C]
Pyrex glass	2225	835	1.4		
Silicon	2330	700	131		1412
Parylene	1289	714	0.084		290
Cu	8890	390	398	1.72E-8	1083
Au	19300	129	317	2.44E-8	1063
Air @ 300 K	1.1614	1007	0.0263		
Air @ 350 K	0.995	1009	0.0300		

In order to perform the transient heat transfer analysis with ANSYS, the natural heat convection coefficients for the column surfaces must be input as boundary conditions. The common method to calculate the free convection coefficients is as follows. For the upper, lower and side surfaces of a heated plate, the recommended correlations for the average Nusselt number are shown below respectively.

$$\overline{Nu}_L = 0.54 Ra_L^{1/4} \qquad (10^4 \leq Ra_L \leq 10^7)$$

$$\overline{Nu}_L = 0.27 Ra_L^{1/4} \qquad (10^5 \leq Ra_L \leq 10^{10})$$

$$\overline{Nu}_L = \left\{ 0.825 + \frac{0.387 Ra_L^{1/6}}{\left[1 + (0.492/Pr)^{9/16}\right]^{8/27}} \right\}^2$$

Equation 4-3

where $Ra_L = \dfrac{g\beta(T_s - T_\infty)L^3}{v\alpha}$, g = 9.81 m/s², and β = 1/T. The Nusselt numbers calculated from these correlation can be used for the heat transfer coefficient calculation using the following equation.

$$\bar{h} = \frac{\overline{Nu_L} \cdot k}{L}$$

Equation 4-4

However, the above general correlation cannot be used for microchannel heat transfer because the Rayleigh number of our case is far lower than the valid range. So, empirical approach was used to obtain the free convection coefficients for the column surfaces. Arbitrary values were used for ANSYS simulation and the steady state temperature of the column obtained from the simulation was compared with the measured value as shown in Figure 4-18. The steady-state temperatures of a parylene column were measured using an infrared camera (thermaCAM PM190, *Inframetrics,* Portland, OR) with different powers applied to the heating element.

0

(a)   (b)

Figure 4-18. Steady state temperature with applied power for different sets of free convection coefficients; (a) h(wall) and h(bottom) are fixed at 1 and 0.1 W/m^{2}K, respectively, (b) h(top) and h(bottom) are fixed at 2 and 0.1 W/m^{2}K, respectively.

The set of free convection coefficients that shows a good agreement with the measured data was h(top) = 2, h(wall) = 0.8 and h(bottom) = 0.1 W/m²C respectively. These values were used for the transient analysis. The transient analysis was based on the assumption that there was no gas flow in the column. Figure 4-19 shows the thermal cycling of silicon/glass column and parylene columns. Power was applied for the first 60 sec and then turned off for both columns. The parylene column is heated and cooled down much faster and soon reaches a steady state in a minute but silicon/glass column is heated linearly and does not reach a steady state until several minutes have elapsed. The time to reach a steady state is not dependent on the applied power for parylene column, but it does increase with the applied power for silicon/glass column. Also, only 50 mW is required for parylene column to heat up to 100 °C in 40 seconds while 500 mW is required for the silicon/glass column. These significant differences in the thermal cycling of the silicon/glass column and the parylene column can be ascribed to the different thermal mass (silcon/glass column ~ 2 g, parylene column ~ 0.4 g).

(a)   (b)
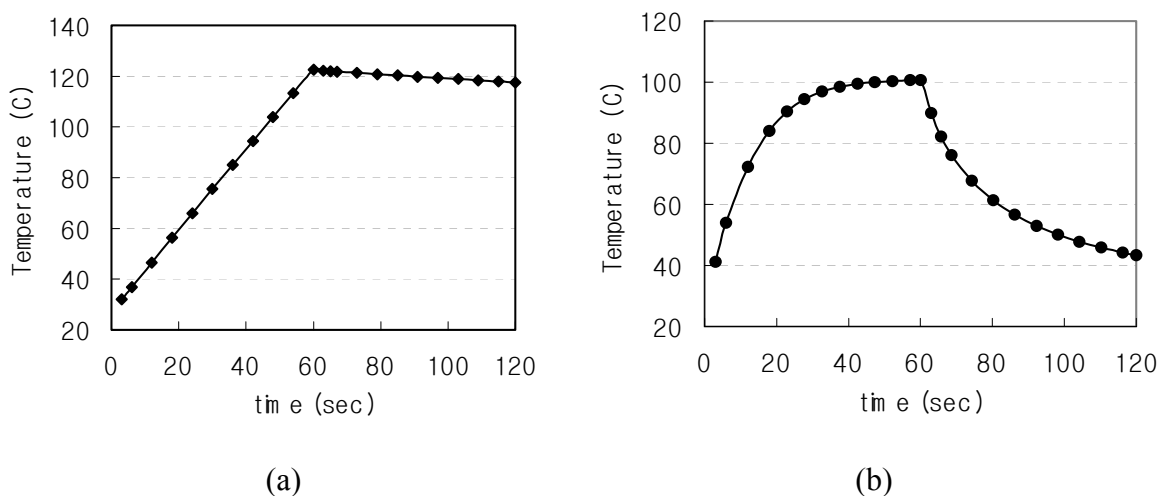
Figure 4-19. The thermal cycling of silicon/glass and parylene columns; (a) Silicon/glass column at 500 mW, (b) parylene column at 50 mW (power was applied for 60 sec and turned off for both columns).

121

4.2.3 TEMPERATURE DISTRIBUTION

Uniform temperature distribution is also important for good column performance. Non-uniform temperature distribution can result in peak broadening because the partition ratio is a function of column temperature. The temperature distribution is also closely related to the thermal conductivity of column material and the location of heating source. Figure 4-20 shows the temperature distributions of three different column geometries. While silicon/glass column shows a uniform temperature, a significant temperature difference (about 3°C) is observed in the parylene column. To solve this problem, a thin metal film can be inserted between parylene layers as a heat diffuser. The temperature difference in the parylene column is reduced to less than 0.1°C when the heat diffuser is used.

(a)   (b)   (c)
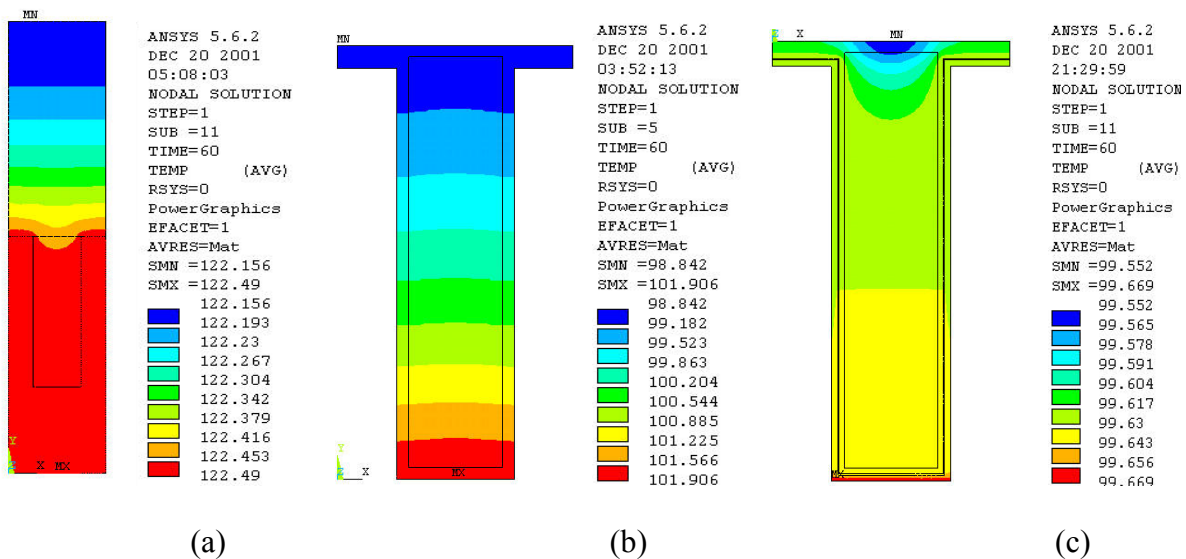
Figure 4-20. Temperature distribution in column cross sections (a) silicon/glass column after 1 min at 500 mW, (b) parylene column after 1 min at 50 mW, (c) parylene column that has heat diffuser after 1 min at 50 mW.

4.3 FINAL DESIGN

The goals and the final design parameters for the parylene separation column are
listed in Table 4-7. Figure 4-21 shows the final design for parylene GC column.

Table 4-7. The goals and the final design for the parylene separation column.

Goals	Final Design
- Retention time less than 1 min	- Low thermal mass parylene thin film column
- Plate number greater than 10,000	- Dual spiral design in an area of 2 cm by 2 cm
- Deflection at 10 psi less than 10 μm	- Side tubing via wide inlet/outlet
- Heating and cooling less than 1 min	- Sandwiched layer (parylene/Pt/parylene)
- Power consumption less than 50 mW	- Embedded heating element and heat spreader
- Temperature gradient less than 0.1 oC	- Column dimensions and operating parameters (L = 1 m, d = 50 μm, h = 300 μm, wall thickness > 10 μm, stationary phase thickness = 100 nm, Δp = 6 psi, u = 0.5 m/s)
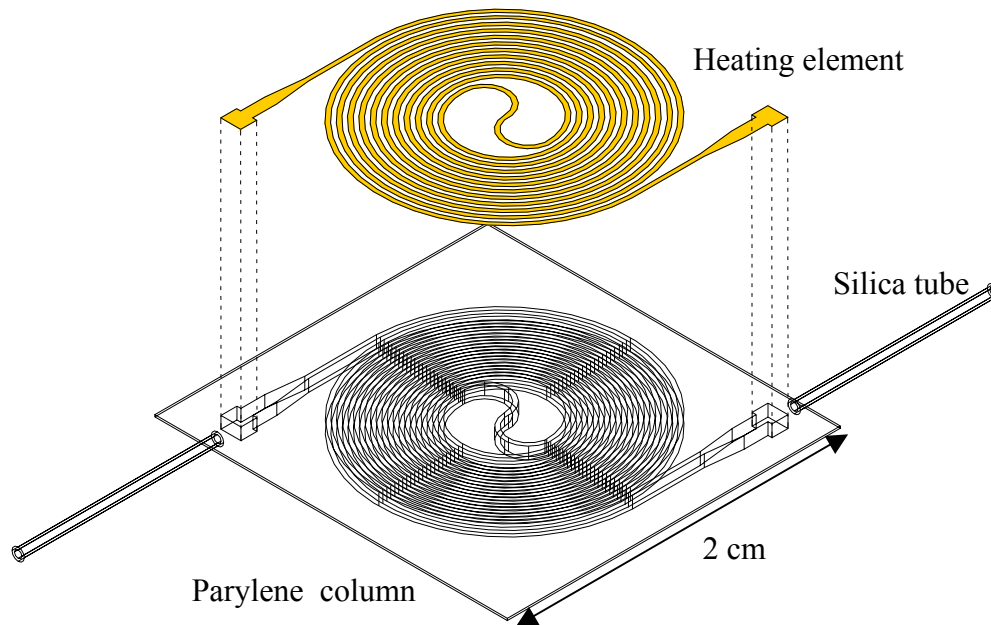
Figure 4-21. Final design for parylene GC column.

CHAPTER 5

PROCESS DEVELOPMENT

This chapter describes the development of two processes that are crucial in fabricating the parylene GC column. The first one is a new fabrication technique, so called 'parylene micromolding.' This technique was developed to build a long parylene microcolumn but can be widely used in many microfluidic devices. The second one is the stationary phase coating for parylene GC column. The fundamental investigations on new materials and the descriptions about different coating processes for the parylene GC column are included in this chapter.

5.1 PARYLENE MICROMOLDING

How can we make a long parylene microcolumn? The conventional method to fabricate an enclosed parylene microchannel is a surface micromachining technique as shown in Figure 5-1. In this technique, reactive ion etching (RIE) is used to pattern parylene layer and photoresist (PR) pattern is used as a sacrificial material. The detail process steps are first, parylene deposition, and photoresist patterning on parylene layer; second, another parylene deposition and oxygen RIE to pattern it; and third, the

dissolution of the sacrificial material, photoresist. The main drawback of this fabrication technique is that it is a considerably slow process because the dissolution of sacrificial photoresist is a diffusion-limited process at the restricted solute-solvent interface. It has been reported that the dissolution of sacrificial photoresist take about 30 minutes per 1 mm dissolution distance in acetone regardless of the cross-sectional dimensions of the channel [61]. In addition, post-releasing rinsing is always required to remove the photoresist residue remaining in the parylene channel. Consequently it may take several days to completely release several centimetre-long microchannels, not to mention a meter-long GC column. It must be also noted that this surface micromachining technique is relatively high cost process because it involves several lithography and oxygen plasma etching steps.

The new 'parylene micromolding' technique employs a molding concept [45, 46]. In this technique, Si microchannels fabricated by either wet or dry etching are used as molds for parylene deposition. Parylene is deposited both on a silicon microchannel mold and a flat substrate. Then these two parylene-deposited substrates are attached together and laminated by heat and pressure. After the lamination, the flat substrate is removed and the parylene microcolumn is released from the silicon mold. This method is much more rapid and less expensive fabrication method for parylene microchannels compared to the conventional method. This parylene micromolding technique can be applied for the fabrication of many microfluidic devices or disposable Micro Total Analytic Systems (µTAS). The information and issues about this technique will be discussed in detail in the following sections.
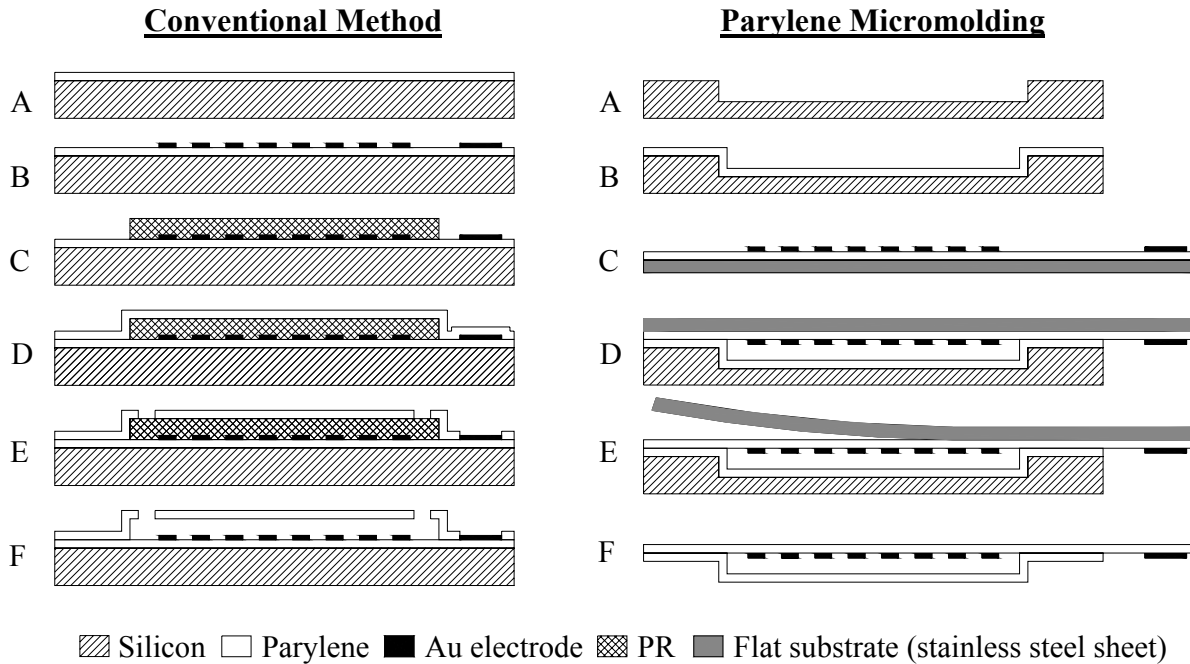
Figure 5-1. Conventional surface micromachining method and new 'parylene micromolding' method for parylene microchannel fabrication (Conventional method – A: parylene deposition, B: electrode patterning, C: sacrificial material (PR) patterning, D: parylene deposition, E: parylene patterning by oxygen RIE, F: dissolution of PR, Parylene micromolding method – A: silicon mold fabrication using deep RIE, B: parylene deposition, C: electrode patterning, D: thermal bonding, E: flat substrate removal, F: channel release)

5.1.1 Parylene/parylene Thermal Lamination

Parylene/parylene thermal lamination is the key process in the parylene micromolding technique. Parylene is a semi-crystalline thermoplastic polymer formed by chemical vapor deposition. After the deposition, the surface of a parylene layer has more low-molecular weight chains than the bulk. These polymer chains of parylene surface can inter-diffuse when two layers are laminated at high temperature and pressure. Such thermal lamination generally occurs at the temperature close to the melting temperature of the polymer.

Before trying the thermal lamination of two parylene layers, the thermal characteristics of parylene must be studied well. Several tools such as differential scanning calorimetry (DSC), thermal gravimetry (TGA), and FT-IR were used to investigate the thermal characteristics of parylene-C. The first graph of Figure 5-2 shows the DSC (DSC Q1000, *TA Instrument,* New Castle, DE) data of parylene-C. This experiment was performed with nitrogen gas purging into the chamber where the sample was. According to this graph, the melting temperature (T_m) of parylene-C was exactly 290 ^{o}C as reported in the literature but the glass transition temperature (T_g) was not clearly observed. This indicates that parylene-C is highly crystalline polymer. The second graph of Figure 5-2 is the TGA data of parylene-C. TGA provides an information about how a polymer is decomposed and turned into volatile molecules with temperature. Parylene was completely decomposed into volatile molecules at above 700 ^{o}C, which is higher than those of other insulating polymers (500 ~ 600 ^{o}C). However, it is known that the mechanical strength of parylene drops greatly at above 150 ^{o}C because it is oxidatively decomposed at the high temperature [27]. In order to investigate this phenomenon, FT-IR analysis (Magna IR560 spectrometer, *Thermo Nicolet Corporation,* Madison, WI) was performed at different temperatures as shown in the third graph of Figure 5-2. Two broad peaks appeared approximately at 3400 and 1700 cm^{-1} when the temperature was over 150 ^{o}C. These peaks are considered to be O-H and C=O absorption peaks respectively due to oxidative degradation. Therefore, parylene-C becomes easily decomposed at high temperature when it is exposed to oxygen. However, the degradation does not happen if the parylene is not exposed to oxygen.
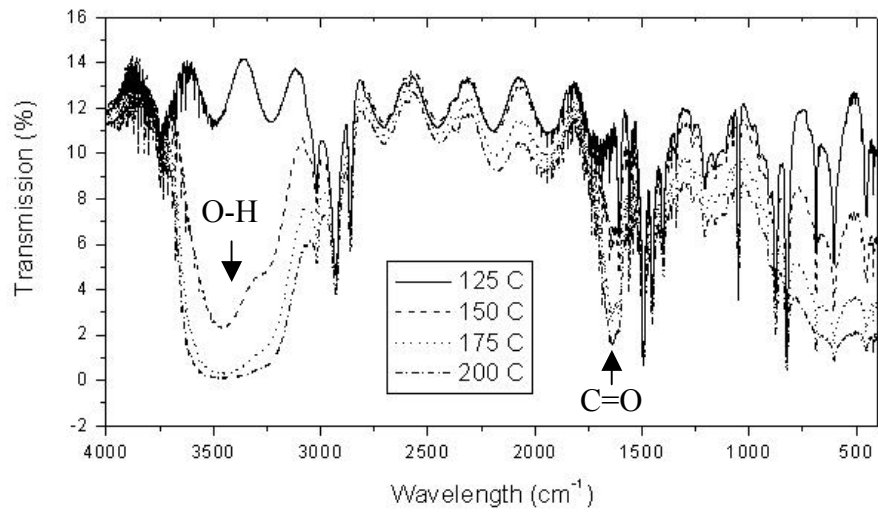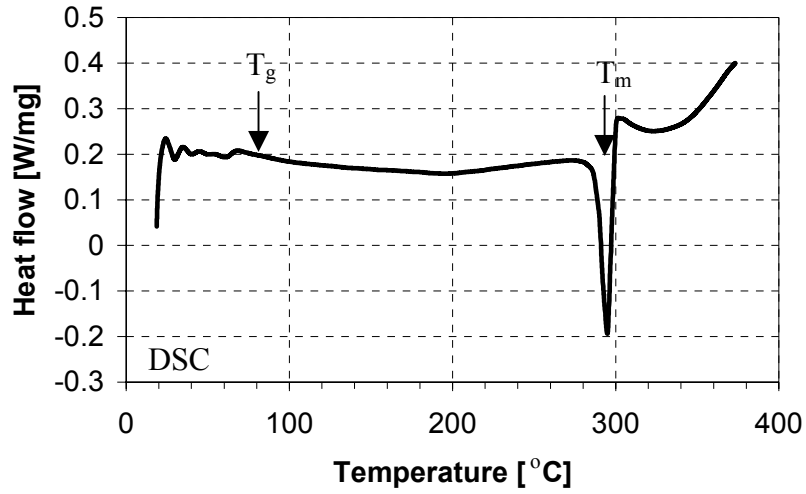
Figure 5-2. Differential scanning calorimetry (DSC), thermal gravimetry analysis (TGA) and FT-IR data of parylene C.

Knowing the thermal characteristics of parylene-C, the thermal lamination of two parylene layers was investigated. Thermal lamination of polymer layers is generally achieved by heat and pressure. Two different heating sources were investigated in this study: convection oven heating and microwave heating. Pressure was applied by a simple compression apparatus which consists of stainless steel blocks and screws as shown in Figure 5-3. Two parylene coated substrates are attached together and placed between two steel blocks. Screws are used to apply pressure and a torque wrench is used to control the applied pressure. The applied pressure can be calculated from the torque using the following equation.

$$F = \frac{T}{r\mu + \frac{d}{2}\tan(\alpha + \rho)}$$

Equation 5-1

where F is force, T is torque, r is the average radius of the screw head, μ is the friction constant (generally 0.15 ~ 0.25), d is the diameter of screw, α is the pitch angle of the screw, and ρ is $\tan^{-1}\mu$. Teflon sheets (0.7 mm thick) were inserted between substrates and steel blocks to prevent glass substrates from breaking during the lamination. As a result, the applied pressure was not constant due to the viscoelastic behavior of teflon sheets. The compression apparatus was then placed in a vacuum oven or a microwave oven and heated.
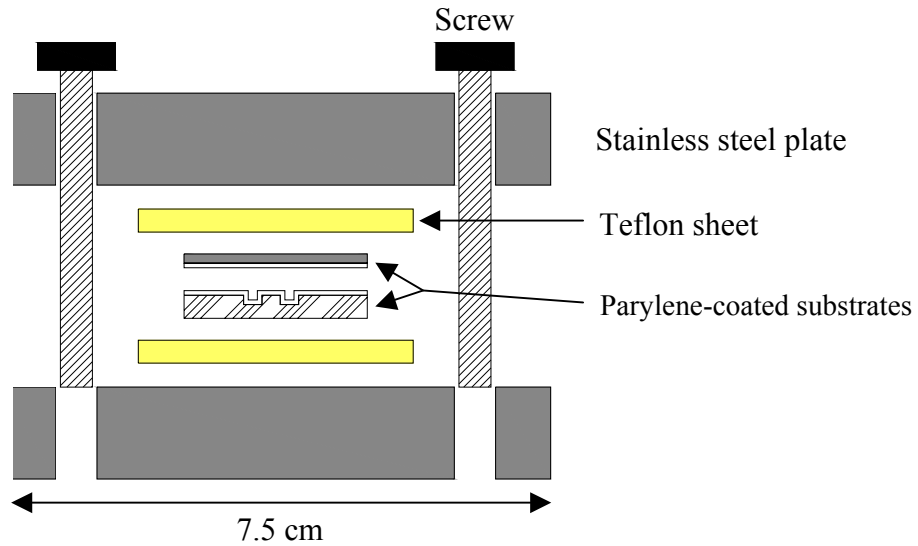
Figure 5-3. Compression apparatus for the thermal lamination of parylene.

5.1.1.1 CONVECTION OVEN HEATING

Preliminary bonding experiments were conducted using Pyrex glasses. Pyrex glass substrates (thickness: 2 mm, area:1x1 in^2 or 2x2 in^2) were coated with parylene-C using parylene deposition system (Labcoater II, *Specialty Coating System*, Indianapolis, IN). Then, the parylene-coated pyrex substrates were put together in the compression apparatus. The compression apparatus was then placed in a vacuum oven for heating. It must be noted that a vacuum oven is required to prevent oxidative degradation of parylene. Three different temperatures between T_g and T_m of parylene-C, 150, 200, and 250 ^{o}C were selected in this experiments. Temperature was increased from room temperature to the set temperature for an hour and then soaked for another hour followed by slow cooling.

Table 5-1 shows the bonding results. Initially 2x2 in^2 glass plates were used in the bonding tests but the bonding was not uniform even at high temperatures because the force was concentrated near the screws. The force concentration phenomena could be overcome by reducing sample area to 1x1 in^2. The bonding result was evaluated by visual inspection and by inserting a razor blade between two pyrex substrates and tilting it until they are separated. If fracture occurs at the interface between parylene and pyrex substrate instead of that of two parylene layers, the bonding was considered as a good bonding. The good bonding results were obtained at above 200 ^{o}C with a pressure more than 5 MPa.

Table 5-1. Bonding results by convection oven heating.

Area (in^2)	Temp (^{o}C)	Torque (N x m)	Pressure (MPa)	Result
2 x 2	150	6	3.86	Not bonded
2 x 2	150	7	4.51	Not bonded
2 x 2	150	8	5.15	Not bonded
2 x 2	200	5	3.22	Partially bonded
2 x 2	200	6	3.86	Partially bonded
2 x 2	250	5	3.22	Partially bonded
2 x 2	250	6	3.86	Partially bonded
2 x 2	250	7	4.51	Partially bonded
2 x 2	300	8	5.15	Partially bonded
1 x 1	250	3	7.71	Well bonded
1 x 1	250	2	5.14	Well bonded
1 x 1	200	3	7.71	Well bonded
1 x 1	200	2	5.14	Well bonded
1 x 1	150	2	5.14	Not bonded

5.1.1.2 MICROWAVE HEATING

Microwave heating of materials occurs due to dielectric loss mechanisms. The principal mechanism of coupling microwave radiation to polymer dielectrics is through dipole orientation by the electric field. The amount of microwave energy absorbed by a material is a function of the applied electric field and dielectric properties of the material as shown below [62].

$$P_{absorbed} = 2\pi f E_{rms}^2 \varepsilon_o \varepsilon^"$$

Equation 5-2

where $P_{absorbed}$ is the dissipated or absorbed power per unit volume, E_{rms} is the root mean square electric field strength, ε_o is the permittivity of free space, ε" is the relative loss factor and f is the frequency. It is also known that microwaves can accelerate chemical reaction rates. For example, the curing time of adhesives can be reduced as much as 10 to 20 times compared with convection heating [63].

The variable frequency microwave (VFM) is a modified microwave technology that allows uniform and selective heating. By rapidly sweeping through a bandwidth of frequencies, VFM not only provides a uniform energy distribution inside the chamber but also eliminates the problem of arcing that is usually observed in fixed frequency microwaves. This permits processing of samples with metal, electrical circuits, and high value semiconductor assemblies without any damage.

In this study, the VFM was investigated as a new heating technique of parylene/parylene thermal lamination. Parylene-C has a dielectric constant of 2.95 and a dielectric loss factor of 0.013 at the frequency of 1 MHz. It is noted that the dielectric loss factor of parylene is higher than other spin-coated polymers while dielectric

132

constants are similar. This suggests that parylene can be effectively heated by VFM. As a

preliminary test, silicon chips (2x2 cm^2) having thin parylene films (1~10 μm) were

heated to different set temperatures at different ramping rates. A commercially available

VFM oven (MicroCure 2100, *Lambda Technologies*, Morrisville, NC) was used in this

study. Air was constantly purged into the VFM chamber during the heating.

The actual temperature of parylene during the VFM heating was monitored using

an infrared sensor that is a part of the VFM oven. Figure 5-4 shows the heating profiles

for different set temperatures and ramping rates. When the set temperature was 160 ^{o}C,

parylene could be heated linearly with time at a ramping rate of 1 ^{o}C/sec (Figure 5-4 (a)).

However, when the set temperature was 200 ^{o}C, the ramp speed was reduced gradually

above 170 ^{o}C causing the delay in the time required to reach the set temperature.

Moreover, parylene could not be heated to the higher set temperature (> 230 ^{o}C) even

after 1 hour. This reduction in ramp speed occurred at a lower temperature when the ramp

speed was lowered (Figure 5-4(b)). Such heating characteristic of parylene is considered

to be due to its oxidative degradation. As mentioned in the previous section, parylene can

be oxidatively degraded above 150 ^{o}C in air. Once oxidative chain scission occurs,

material properties change abruptly. This can explain why the reduction of ramp speed

was observed in the VFM heating of parylene. With the lower ramp speed, parylene can

be degraded at lower temperatures because it has more reaction time. However it must be

noted that this heating characteristic is only for the parylene that is exposed to air during

the heating. In the actual lamination of parylene layers, they are not exposed to air

because they are sandwiched and compressed during the lamination. As a result, the

degradation was seldom observed in the parylene layers.
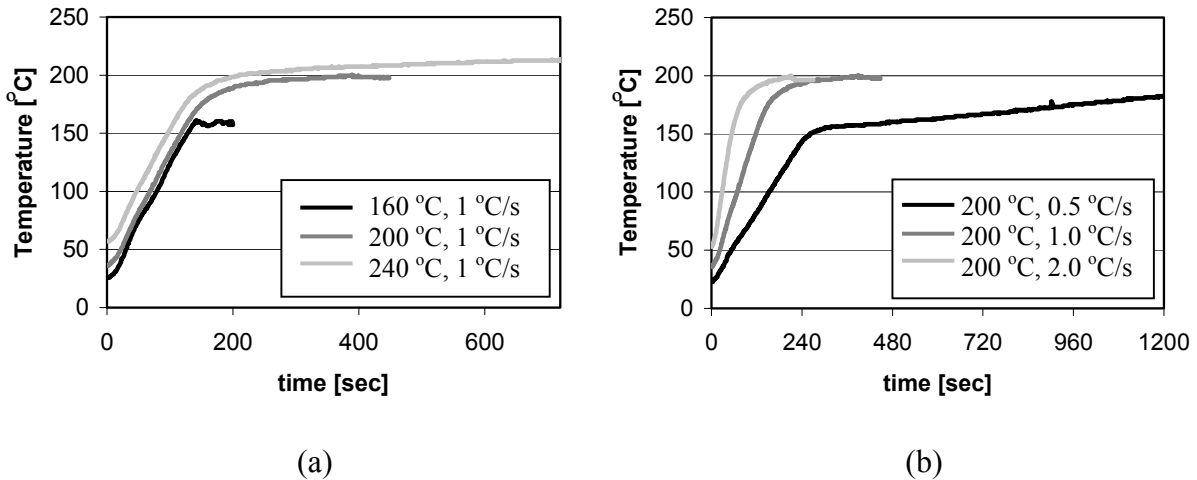
Figure 5-4. Variable frequency microwave (VFM) heating profile of parylene C (a) heating to different set temperatures at 1 $^{\circ}$C/sec, (b) heating to 200 $^{\circ}$C at different ramping rates.

VFM can provide uniform, fast and selective heating for parylene layers and this idea can be applied to the wafer bonding technique [47]. In other words, parylene can be used as intermediate layers for wafer-to-wafer bonding. In this bonding technique, the substrates are not heated significantly and thus stress due to differences in thermal expansion could be drastically decreased. Therefore, this technique will be specifically useful for bonding two substrates consisting of dissimilar materials and having different coefficients of thermal expansion. In addition, this new heating technique along with a new intermediate layer material, parylene, provides a rapid, low-temperature, uniform, chemically stable, and biocompatible wafer bonding. This technique can be used for bonding structured wafers as well.

For preliminary bonding tests, silicon wafers with a diameter of 7.5 cm were used. All wafers were cleaned with organic solvents and dried completely followed by parylene-C deposition. Then the parylene-coated wafers were put together in the compression apparatus followed by VFM heating. The bonding temperature and time

were programmed using the VFM software. In order to monitor the temperature of parylene, a reference parylene film coated on a silicon chip was always placed on top of the bonding sample so that the infrared camera might read the temperature.

The four major bonding parameters investigated in this study were temperature, pressure, time, and thickness. Three different bonding temperatures (120, 160, and 200 ^{o}C) were selected between T_g and T_m of parylene-C. Pressure was controlled by a torque wrench and the three different torque values used in this study were 1.2, 2.4, and 4.0 N·m, which is equivalent to 0.45, 0.9 and 1.5 MPa respectively. Bonding time was varied from 10 to 120 min and parylene thickness was varied from 1 to 10 μm. Another important parameter that needs to be considered is the pre-treatment of the silicon surface because fracture may occur at the parylene/silicon interface instead of the parylene/parylene interface during bond strength test. An adhesion promoter recommended by the parylene manufacturer has been used to see its effect. The adhesion promoter was a mixture (50:50:1) of Isopropyl alcohol, DI water, and A-174 (gamma-methacryloxytropyl trimethoxy silane, *Specialty Coating Systems*). The treatment procedure was as follows. Silicon wafers were immersed in isopropyl alcohol for 5 min. Then, wafers were immersed in the mixed adhesion promoter solution for 30 min. Then, the wafers were air dried. The wafers were then immersed in isopropyl alcohol again for 5 min. Finally, the wafers were dried with nitrogen gas and baked on a hot plate at 100 ^{o}C.

5.1.1.3 BOND STRENGTH : SHEAR AND TENSILE TESTS

The bonding strength was first evaluated qualitatively by a razor blade insertion test. For the samples that could not be separated by razor blade insertion, two quantitative tests, a die shear test and a tensile pull test, were performed. For the die shear test the bonded wafers were diced into 4x4 mm^2 pieces and mounted on a glass slide using a super glue (specific name of product?). The die shear tester used in this experiment was STM 100K (*Micro Systems Inc.*, Anyang, Korea). At least 10 samples were tested for each bonding condition, and the bonding strength values were averaged. For the pull test, the bonded wafers were diced into 9x9 mm^2 pieces and each piece was mounted to a cylindrical plastic holder fabricated using rapid prototyping. A strong epoxy resin (Epoxy 907, *Miller-Stephenson*, Sylmar, CA) was used for the mounting. Pull tests were performed using MicroTester 5548 (*Instron Corporation*, Canton, MA). At least five samples were tested for each bonding condition, and the bonding strength values were averaged. Figure 5-5 shows the samples prepared for the die shear test and the tensile pull test.

(a) (b)
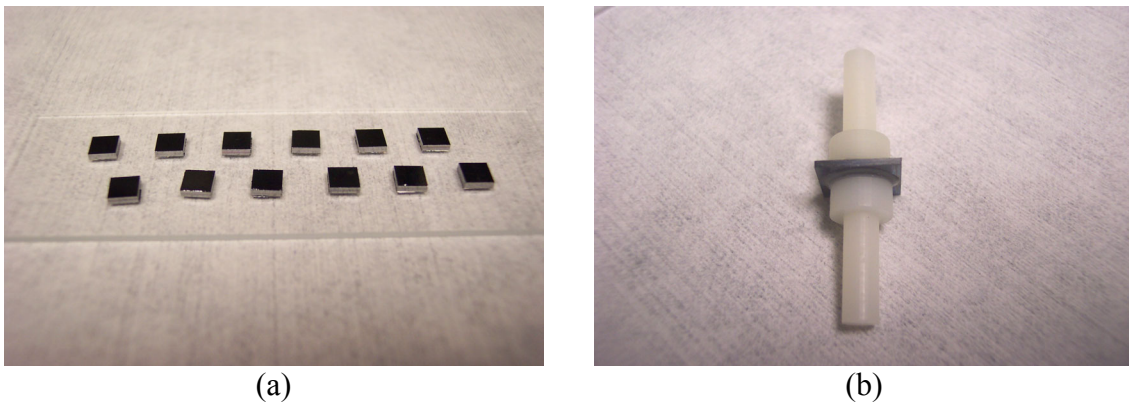
Figure 5-5. Samples for (a) die shear test and (b) tensile pull test.

Table 5-2 is the summary of the bonding strength test results. All values were averaged. For every sample, a razor blade insertion test was performed first just after the bonding experiment. The samples bonded at 120 $^{\circ}$C were separated by razor blade insertion regardless of other bonding parameters. The separated wafers still had parylene layers on the surface indicating that parylene layers had not been bonded with those bonding parameters. When the bonding temperature was 160 $^{\circ}$C, parylene/parylene bonding was achieved depending on pressures and time, and the bonded wafers were not separated by razor blade. However, the parylene thickness did not make any difference in the bonding strength. The shortest process condition for parylene/parylene bonding in our experiments was 10 min at 160 $^{\circ}$C and 1.5 MPa.

Table 5-2. Bond strength at different bonding conditions.

Bonding parameters					Bonding strength	
Temperature [$^{\circ}$C]	Pressure [MPa]	Time [min]	Thickness [µm]	Adhesion promoter	Die shear test [MPa]	Pull test [MPa]
120	0.9	60	2	No	N/A	N/A
120	1.5	120	2	No	N/A	N/A
160	0.9	30	2	No	N/A	N/A
160	0.9	120	2	No	7.94	-
160	0.9	90	1	No	7.07	-
160	0.9	90	5	No	5.78	-
160	0.45	60	2	No	7.09	-
160	1.5	10	2	No	7.75	3.45
160	1.5	30	2	No	5.97	5.38
160	1.5	30	1	No	6.76	-
160	1.5	30	5	No	6.22	-
160	**1.5**	**30**	**2**	**Yes**	**12.68**	**9.16**
200	0.9	90	1	No	6.64	-
200	1.5	30	2	No	5.33	-
200	1.5	10	2	No	4.92	-
N/A		Wafers were separated with razor blade (parylene layers were not bonded).				

The bonding strength measurement through the die shear test revealed that the bonding strength did not change much with the changes of bonding parameters. The bonding strength ranged from 5 to 7 MPa. The tensile pull test result also showed similar characteristics. The bonding strength ranged from 3.5 to 5.5 MPa regardless of the bonding parameters. However, the adhesion promoter-treated sample showed almost two times the strength both in shear (12.68 MPa) and tensile strength (9.16 MPa). All the tested samples were inspected visually to see where the fracture had occurred. This inspection provided a good interpretation of the above bonding strength result. The fracture mechanism in this experiment can be classified into three cases as shown in Figure 5-6. First, when the parylene intermediate layers were not bonded, the fracture occurred at the parylene/parylene interface. In this case, the samples were usually separated during the razor blade test. Second, when the parylene intermediate layers were bonded well, the fracture occurred at the parylene/silicon interface during the bonding strength test. In this case, the bonded parylene intermediate layers were observed to remain only on one wafer after the bonding test. This was because the parylene/parylene bond was stronger than the parylene/silicon bond. The adhesion strength of the parylene/silicon bond was not influenced much by the bonding parameters. Consequently, the bonding strength did not change much as the bonding parameters varied in this case. The third case is that the bonded parylene layers were torn during the bonding strength test. The adhesion promoter-treated sample belonged to this case. Both parylene/parylene bonding and parylene/silicon adhesion were so strong that the fracture generated damage in the parylene layers. But still the fracture mainly occurred at the parylene/silicon interface.

Silicon

Parylene

|Fracture at parylene/parylene interface|Fracture at parylene/silicon interface|Parylene layers torn|
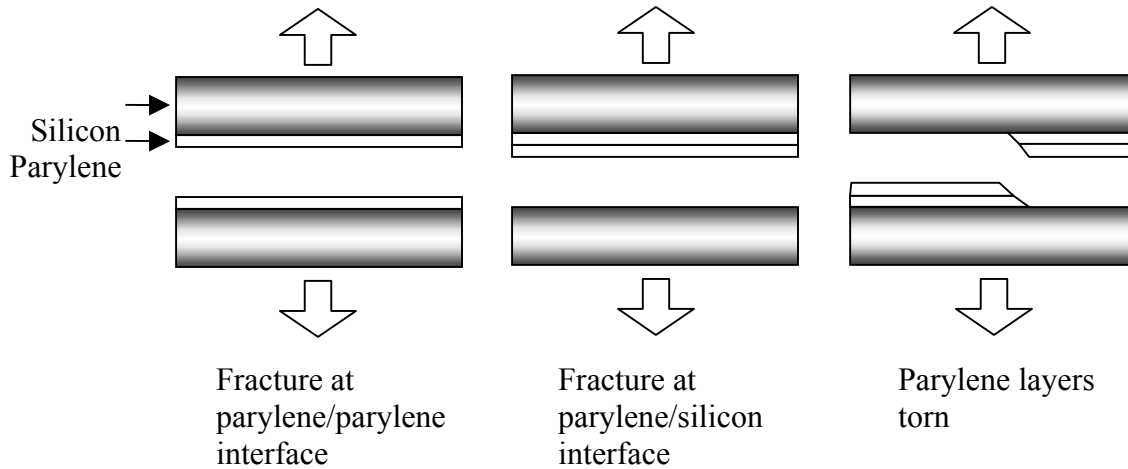
Figure 5-6. Different fracture mechanisms in bonding strength tests.

Another characteristic was that the bonding strength value often showed a large deviation (~ 50%) from the average value. This is considered to be mainly due to the existence of particles. This issue will be discussed more in the bonding uniformity section. However, the adhesion promoter-treated sample was quite different. It showed uniform bonding strength in both shear and tensile test. The deviation from the average value was less than 20%.

5.1.1.4 DEBOND ENERGY : BLISTER TEST

The die shear tests and the tensile pull tests revealed that a parylene/parylene bond is stronger than the adhesion between parylene and silicon substrate. Therefore the bond strength data obtained by those tests are in fact the adhesion strength between parylene and silicon substrate. Then how can we measure the debond energy of the parylene/parylene interface? The answer is a blister test. This test was originally devised to measure the adhesion strength of polymeric thin films on their substrates [64-66]. The

concept is very simple. Polymer film laminated on a substrate that has a through-hole is pressurized until debond occurs. By measuring the critical pressure and blister dimensions, debond energy can be calculated. The same concept can be applied to measure the bonding strength of two parylene layers. The only difference is that the substrate is conformally coated with parylene and then it is thermally laminated with flat parylene layer as shown below.
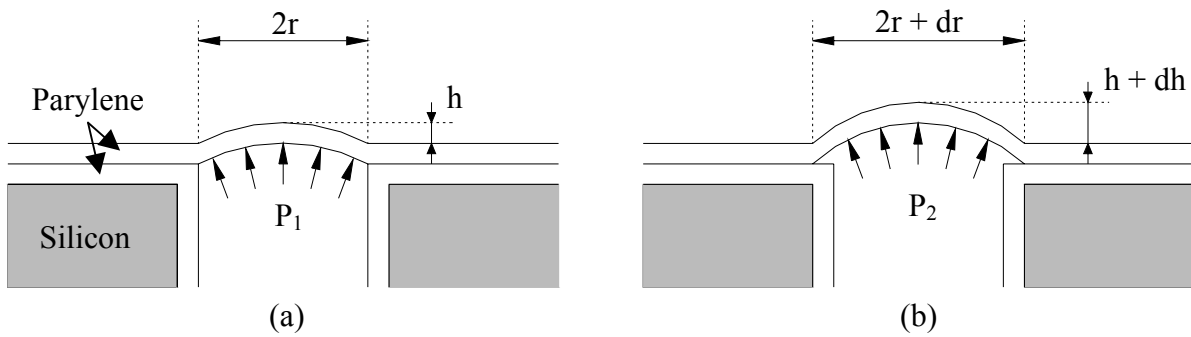
Figure 5-7. Schematic of the blister test for the measurement of parylene/parylene debond energy (a) before debonding, (b) after debonding.

The hole in a blister test can be square or round. Since the round hole can eliminate the stress concentration and is easily modeled to determine the debonding energy, it is commonly used. The blister test with a round hole is of interest in this study. When the unbounded area is progressively pressurized by the pressurizing medium, the top layer will form a blister if it is relatively thin compared with the hole radius. The pressure-deflection behavior prior to any debonding can be described as follows.

$$p = 3.56 \frac{Et}{r^4} h^3 + 4 \frac{\sigma_0 t}{r^2} h$$

Equation 5-3

The blister volume can be estimated as

140

$$V = C_3 \pi r^2 h$$

Equation 5-4

During this phase, the work done by the external pressure is converted into the elastic

energy of the bulged film. When the pressure inside the hole is continuously increased,

the interface will fail at a critical pressure and debonding propagates along the interface

as shown in Figure 5-7 (b). Under this condition, the work done by the external pressure

is converted into the elastic energy of the bulged film and the interface debonding energy

at the critical pressure, $p_{critical}$. To make the debonding happen, the following relationship

must be satisfied:

$$\Delta W_{external}\big|_{p_{critical}} \geq \left[\Delta W_{elastic}\big|_{p_{critical}} + \Delta W_{debonding}\big|_{p_{critical}} \right]$$

Equation 5-5

For the sample preparation, silicon wafers are machined to have holes using laser

ablation. These wafers are then diced into small dies (2x2 cm^2) which have a single hole

in the center. The diameter of the hole was either 1, 2, or 4 mm. Parylene is conformally

coated on this silicon dies and a flat steel sheet. This is followed by thermal lamination.

After the lamination, the steel sheet is removed.

Figure 5-8 shows the experimental setup for the blister test to measure the debond

energy of parylene/parylene interface. The sample prepared as described above is

clamped in a holder that was built by stereolithography. This holder has an inner channel

and its two ends are connected to a syringe pump (Sage^{TM} model 362, *Filtronic*,

Merrimack, NH) and a pressure sensor (PX302-050GV, *Omega Engineering Inc.*,

Stamford, CT) respectively using peek tubings. The probe of an optical sensor (MTI 2000

Fotonic Sensor, *MTI Instruments*, Latham, NY) is then placed above the hole of silicon

substrate to measure the deflection of the membrane. DI water was used as the pressurizing medium. Both pressure and membrane deflection data were monitored using a data acquisition system (HP 34970A, *Hewlett Packard*) and appropriate computer software (HP Benchlink Data Logger, *Hewlett Packard*).
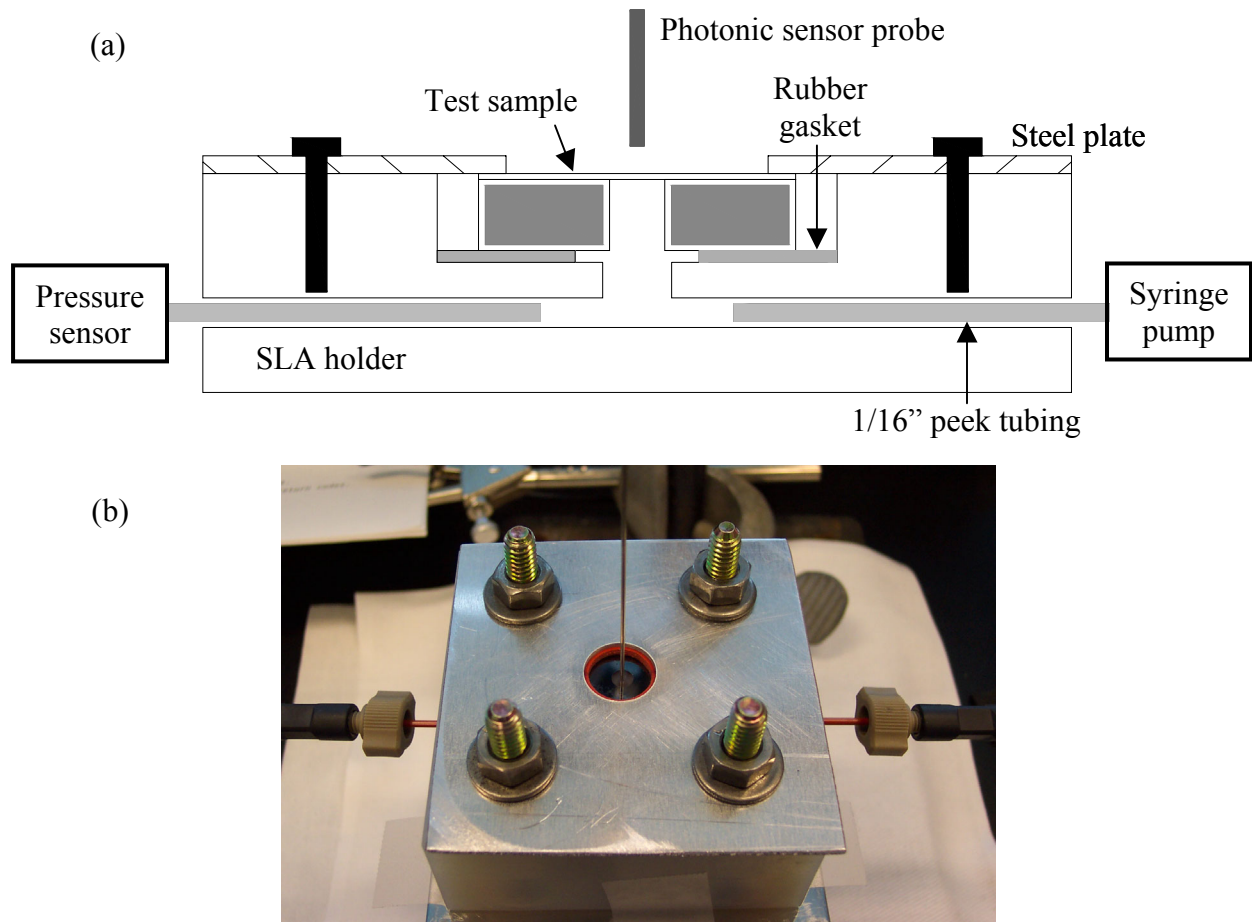
Figure 5-8. Blister test setup for the measurement of parylene/parylene debond energy (a) schematic of the cross section, (b) bird view of the setup.

It turned out that laser ablation is not a good way of preparing for the sample. Because of the sharp edges of the silicon die, parylene membranes were usually damaged during the thermal lamination. Some of the samples that had not been damaged during the lamination were used for preliminary tests. However, debonding was not observed within the pressure range for which the Fotonic sensor could be used. The hole diameter

of the sample was 2 mm and the parylene thickness was 10 μm. The maximum pressure applied was nearly 20 psi. Until that pressure, the parylene/parylene interface was not debonded. It is suggested to use samples that has smaller hole diameter or thicker parylene layers to avoid large deflection.

5.1.1.5 BOND UNIFORMITY AND INTERFACE

Bonding uniformity across the wafer was investigated using a c-mode scanning acoustic microscope, so called c-SAM (series D-9000, *Sonoscan.Inc*., Elk grove village, IL). This enabled the non-destructive visualization of the interface between bonded wafers. Figure 5-9 shows the c-SAM image of a bonded sample. The bonding condition for this sample was 160 ^{o}C, 1.5 MPa for 30 min and the intermediate parylene thickness was 2 μm. The bright parts indicate non-bonded areas in this image. The bonding uniformity was good in the center of the wafer but the edge was not as good. Although the overall bonding uniformity was good, a few local defects were observed. Most local defects were found to have tiny dirt particles in them as shown in the magnified image of Figure 5-9. Dirt particles can sit on parylene layers either during the venting process of the parylene coating procedure or during the preparation of the bonding. This existence of particles can also explain why some of the samples showed very weak bonding strength during the die shear test. Better bonding quality is expected if the bonding experiment is done in a cleanroom environment.

Local defect in
bonding due to
dirt particle
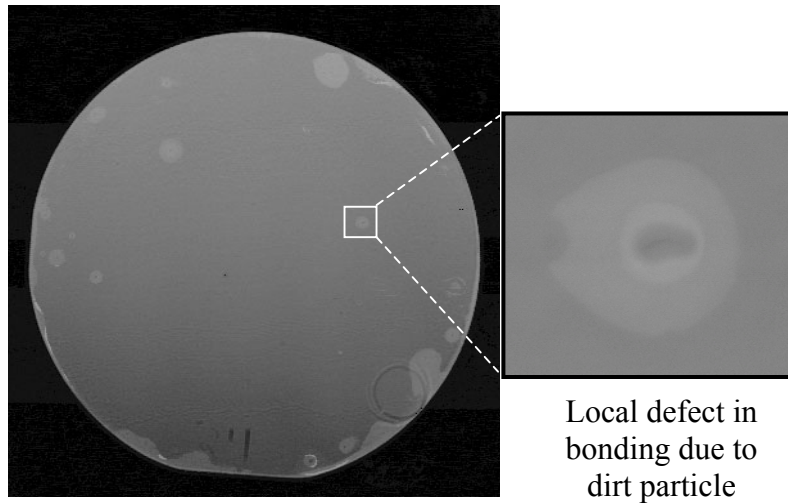
Figure 5-9. Scanning acoustic microscope image of a bonded wafer (7.5 cm in diameter).

(a)

(b)
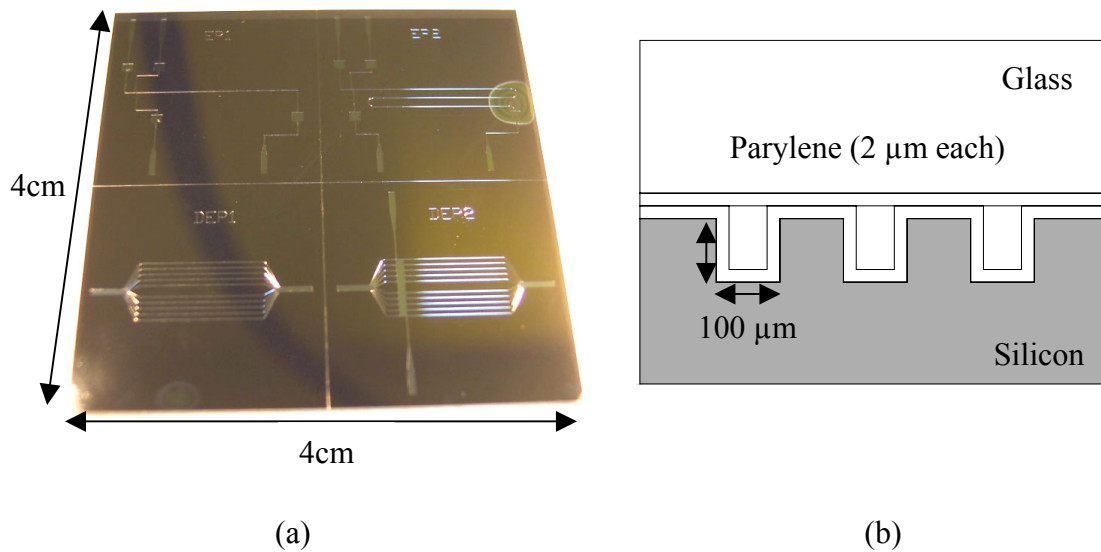
Figure 5-10. The bonding of a structured wafer (a) a bird view, (b) a schematic diagram of the cross-section.

A structured wafer that has microchannels was successfully bonded to a glass

substrate using parylene intermediate layers (Figure 5-10). Again, the bonding condition

for this sample was 160 $^{\circ}$C, 1.5 MPa for 30 min and the intermediate parylene thickness

was 2 μm. The overall bonding quality was good but still a few local defects due to the existence of particles were observed visually.

The microscopic bonded interface was also investigated using a scanning electron microscope (Hitachi S-800, *Hitachi High Technologies*, Pleasanton, CA). A bonded sample was broken in liquid nitrogen and coated with a thin gold coating for SEM imaging. Figure 5-11 shows the SEM image of the bonded interface. The bonding condition for this sample was 160 ^{o}C, 1.5 MPa for 30 min and the intermediate parylene thickness was 2 μm. The magnified view in Figure 5-11 clearly shows the two parylene layers (approximately 2 μm thick) and the interface. A uniform interface layer that is less than 200 nm was observed between two parylene layers. This thin interface layer is considered to be the inter-diffusion layer of the two parylene layers indicating a good bond. Many different spots were inspected in the SEM, and uniform bonding was observed between the two parylene layers.
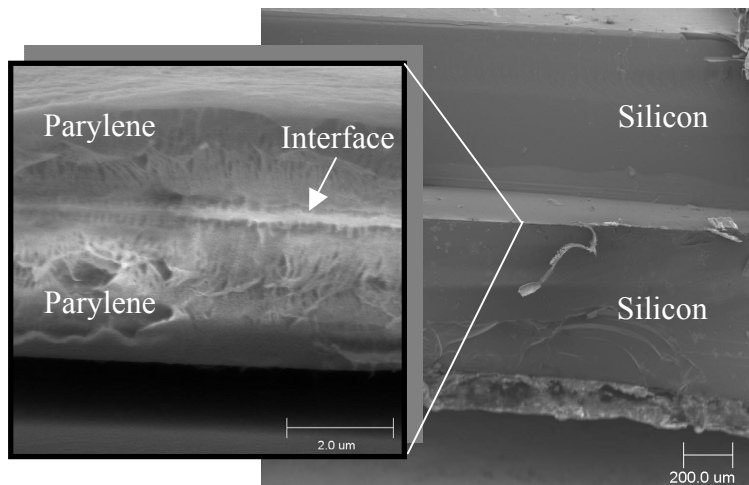
Figure 5-11. Scanning electron microscope image of the bonded interface.

5.1.2 Release of Parylene Microchannel

After the thermal lamination, the free-standing parylene column can be achieved by removing the silicon mold. For example, silicon mold can be dissolved in KOH solution because parylene is inert in it. However, if a silicon microchannel mold has to be sacrificed whenever we make a parylene column, the fabrication cost still remains high. Can we release the parylene column from the silicon mold without damaging the mold? In order to release parylene channel from silicon mold, the flat substrate must be removed first (Figure 5-1). If it is not removed easily after the thermal lamination, parylene channel cannot be released without any damage. Therefore the choice of the flat substrate is very important for a successful channel release. Several requirements for the flat substrate are flexibility, low thermal expansion coefficient, and poor adhesion of parylene. Four different substrates, pyrex glass plate, teflon sheet, PET (polyethylene-terephtalate) film, and stainless steel sheet were suggested for the purpose and tested.

Once the flat substrate is removed, the next step is releasing the parylene channel from the silicon mold. Regarding this release, several questions can arise. How does the aspect ratio of silicon microchannel mold affect parylene channel release? Can releasing agents help the release? Can Si mold be reused? Silicon molds having different aspect ratios were fabricated using deep RIE and used to investigate the effect of the aspect ratio on parylene channel release. In terms of the effect of releasing agents, two different type of releasing agents, Micro-90 (*Specialty Coating Systems*) and Camie 1080 (*Camie-Campbell Inc.,* St. Louis, MO) were used in this study. Since Micro-90 is a solution, the silicon mold was dipped in the diluted Micro-90 solution and then dried with nitrogen. However, Camie 1080, a spray type releasing agent, was sprayed on silicon mold before

parylene deposition. In order to investigate the reusability of the silicon mold, some channels were reused after being cleaned by oxygen plasma RIE and compared with others that had not cleaned by oxygen plasma RIE.

Among four flat substrate candidates (pyrex plate, teflon sheet, PET film, and stainless steel sheet), the stainless steel sheet turned out to be better than others for the parylene micromolding method. For the thermal laminaiton, a Pyrex plate worked better than others because of its uniform thickness and smooth surface. But it was very hard to remove the Pyrex plate after bonding. The Teflon sheet also worked well for bonding and it could be removed easily after bonding due to parylene's poor adhesion on Teflon, but a significant indentation ($\sim$ 30 µm) was observed on teflon after bonding process due to teflon's viscoelasticity. Consequently, the parylene channel was also deformed by this indentation. PET film did not work well even for the thermal lamination because of its high thermal expansion coefficient. The stainless steel sheet worked fine for both bonding and channel release, but when the device requires complex electrode patterns like in an interdigitated comb drive, parylene tends to stick on the substrate, making the release difficult. To address this problem, a thin layer of teflon (Teflon AF, *DuPont*, Wilmington, DE) was coated onto the stainless steel sheet through the dipping technique. This Teflon-coated stainless steel sheet was the best substrate for parylene micromolding because it had the combination of Teflon's surface property and stainless steel sheet's mechanical property.

Regarding the effect of releasing agents, Micro-90 was very effective while Camie 1080 was not. However, even with the help of a releasing agent, Micro-90, it was difficult to release parylene channel without damage from silicon molds that have an

147

aspect ratio higher than 1:1 (width:depth). Oxygen plasma cleaning of the silicon mold

was very effective in enhancing the reusability of the silicon mold. When the used silicon

molds were descummed completely by oxygen plasma etching (200 mTorr, 200 W, 30

min) and treated with Micro-90, they could be reused many times. Figure 5-12 shows the

detailed fabrication flow of parylene micromolding.

1. Deep RIE to build silicon microchannel mold
2. Oxygen RIE to descum
3. Soap solution treatment
4. Parylene deposition

5. Coat Teflon on stainless steel sheet
6. Parylene deposition
7. Electrode patterning if required

8. Thermal lamination

9. Peeling the steel sheet

10. Release the parylene microchannel

11. Go to step 2 for additional fabrication

⬚ Silicon ▢ Parylene ■ Au electrode ▨ PR ▬ Flat substrate (stainless steel sheet)

Figure 5-12. Detail process flow of parylene micromolding.

5.1.3 OTHER ASPECTS OF PARYLENE MICROMOLDING

Since parylene deposition copies substrate geometry, final parylene channels have

the same cross-sectional shape as silicon molds. Therefore round channels can be

obtained by using isotropically etched (HNA or XeF_2 etching) silicon molds and

triangular or rectangular channel can be obtained by using anisotropically etched (KOH

or DRIE etching) molds as shown in Figure 5-13 (a). Another very interesting aspect of

parylene micromolding is that the inner aspect ratio of the parylene channel can be controlled by simply varying the parylene thickness. In other words, parylene channels having different inner aspect ratios can be fabricated using the same silicon mold as shown in Figure 5-13 (b). Moreover, the channel wall can have multiple layer structures as shown in Figure 5-13 (c). If a thin metal layer is deposited between two parylene layers, the final form will be a parylene/metal/parylene triple structure and if two different parylenes are deposited in series, double parylene structure can be obtained. For example, if parylene A (diX A, *Daisankasei Co., Ltd*) is deposited on parylene C, the inner channel surface will be more hydrophilic and bioactive than parylene C because parylene A has amino functional group on its surface.
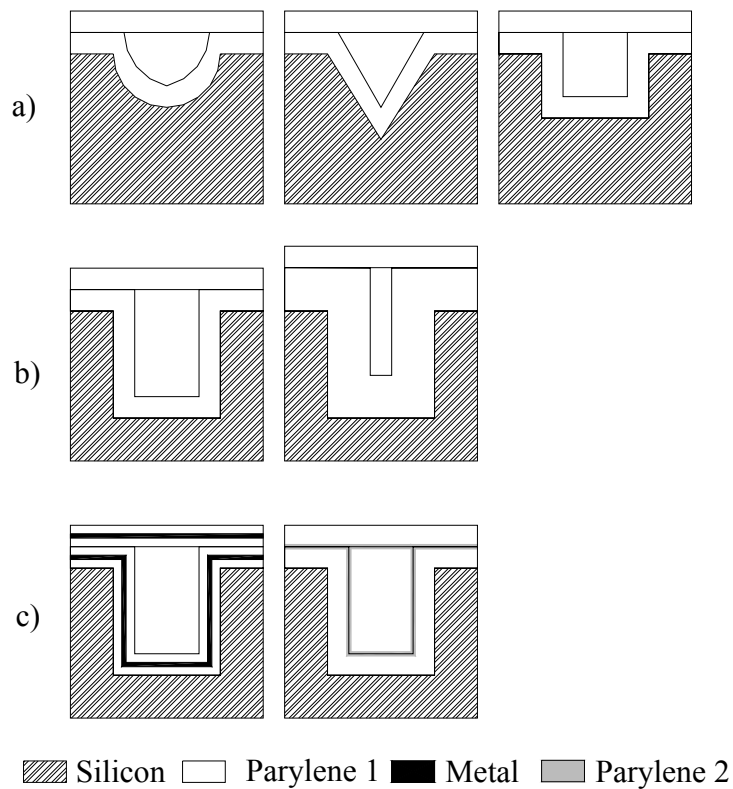
Figure 5-13. Cross-sectional geometries of parylene channels (a) different of silicon mold, (b) aspect ratio control via parylene thickness, (c) multiple layer channel.

149

In this study only deep RIE etched silicon molds have been used because it is more difficult and challenging to release parylene channels from rectangular Si mold than from round or triangular mold. Rectangular microchannels (both width and depth were 100µm) were fabricated on silicon wafers using deep reactive ion etching (RIE). The standard BOSCH process was used for the fabrication. The photoresist mask used for deep RIE was removed completely by both wet treatment and oxygen plasma etching. Figure 5-14 shows the SEM images of the silicon microchannels having diverse designs.

a) b)

c) d)
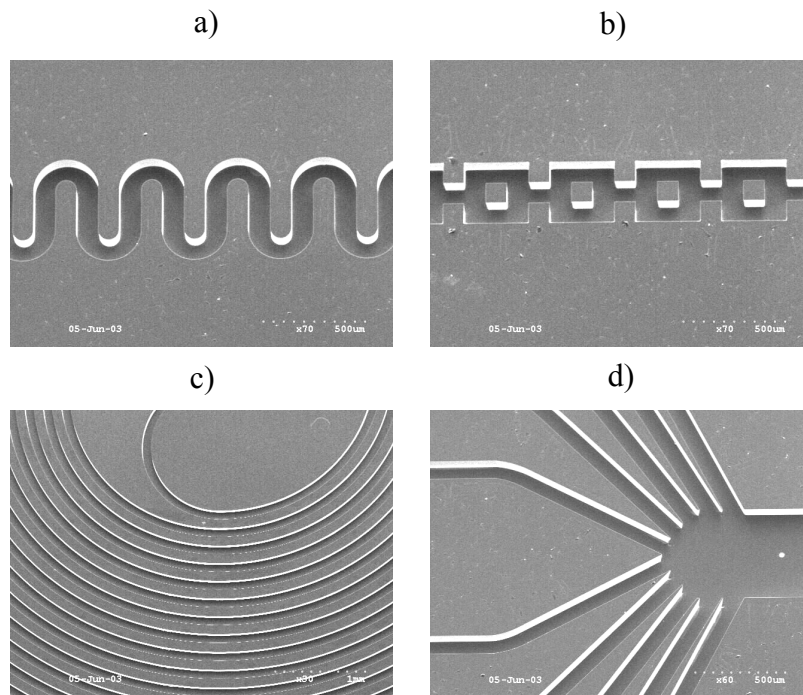
Figure 5-14. SEM images of silicon microchannel molds fabricated by deep RIE (a) and (b) meander type channels, (c) long spiral channel, (d) multiple channel (all channels have same width of 100 µm and depth of 50 µm).

Parylene microchannels have been fabricated using the silicon molds. Meandering channels, long spiral channels, electrophoretic channels, and dielectrophoretic channels are presented in Figure 5-15. All the channels have the same inner channel dimension (80 µm width, 50 µm height). Different cross-sectional geometries can be fabricated using

the same mold for all different types of channels as mentioned above. The fabrication time was basically identical regardless of the design and length of the channel. Microfluidic components often require embedded electrodes. In order to investigate the feasibility of electrode integration with parylene micromolding, electrophoretic and dielectrophoretic channels were designed and fabricated using the parylene micromolding technique (Figure 5-15 (c) and (d)). The electrophoretic channel has electrodes defined under each reservoir and the dielectrophoretic channel has complex interdigitated electrodes (finger width and gap are 20 µm) along the length of the channel. Ti/Au (0.03/0.1 µm) was deposited on the parylene-coated stainless steel sheet using an E-beam evaporator and then patterned by lift-off process with Futurrex NR5-8000 photoresist before bonding process. It must be noted that when a high melting temperature metal needs to be deposited, parylene may be degraded, causing cracks because of the high temperature during the evaporation process. The electrophoretic channel was single channel of 4 cm length and the dielectrophoretic channel was multiple channel of 1 cm length.
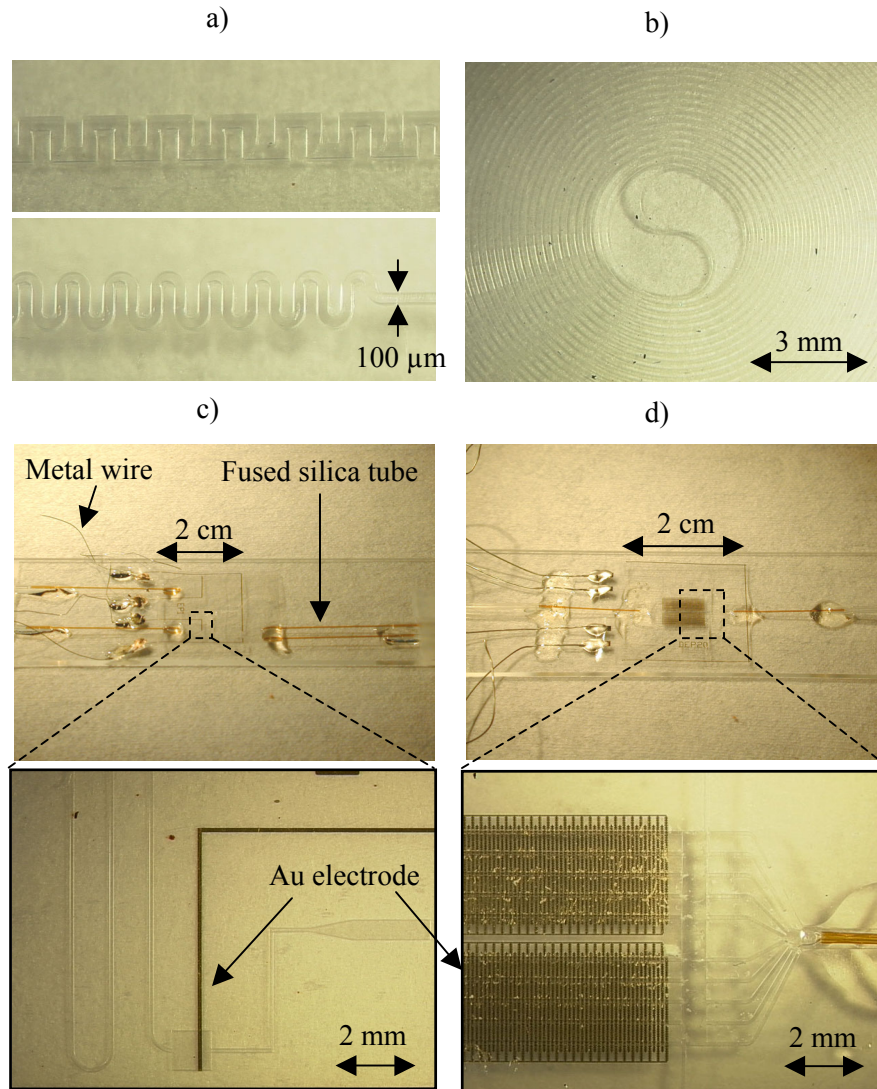
Figure 5-15. Diverse kinds of parylene microchannels fabricated by parylene micromolding technique (all channels have same inner dimension of 80 μm width, 50 μm depth, and 10 μm wall thickness) (a) meander type channels, (b) 1 m long spiral channel, (c) electrophoretic channel, (d) dielectrophoretic channel.

Tubing is not a trivial issue in many microfluidic devices. Since the final free-standing parylene microchannels is a flexible thin film structure, the conventional method of tubing is hard to apply. Therefore, both the inlet and outlet of the channel were punched from the side with a needle and then polyimide coated fused silica microtubes (OD ~ 250 μm, ID ~ 100 μm, *Polymicro*, Phoenix, AZ) were inserted and sealed with a

small amount of epoxy resin. For this purpose, all the parylene microchannels were designed to have wider (500 μm) inlets and outlets than the main channel (100 μm) part. After tubing, dyed water was introduced through the channel using syringe pump to see if there is any leakage. Figure 5-16 shows the tubing and leakage test for a long spiral channel. No leakage was found in most of the parylene microchannels under the volumetric flow rate of 0.2 SCCM. A higher flow rate was not able to be tried because soft tubing used in this experiment could not endure the increased flow rate.
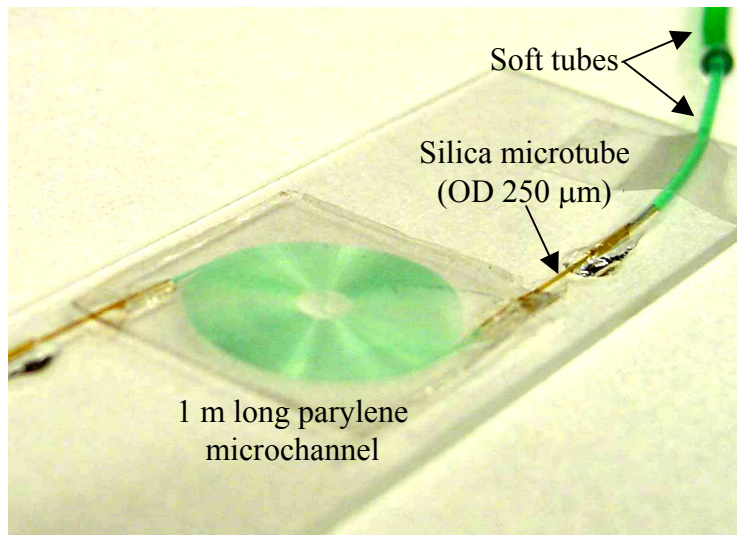
Figure 5-16. Tubing and leakage test of a long spiral parylene channel.

5.2 STATIONARY PHASE COATING

Stationary phase coating is the most important process in developing a GC

column. The actual column performance can be much worse than the theoretical

performance if the coating is not good. The most common methods for the stationary

phase coating of conventional fused-silica GC columns are dynamic (injection) and static

(withdrawal) coatings which can be classified as a wet coating method. The same coating

technique can be applied to micromachined GC columns as long as the columns endure

the high pressure required to inject the coating solution through them. However, unlike

fused-silica columns, micromachined channels have an open structure before they are

bonded to flat substrates. Can we take advantage of the open structure of the

micromachined channel for stationary phase coating?

Table 5-3. Stationary phase coating methods for micromachined GC columns.

Method	Material	Mechanism/Selectivity	References
Thermal evaporation	Copper Phthalocyanine (CuPc)	Good adsorption/ NO_2, NH_3	Kolesar et al. Kurosawa et al.
Plasma polymerization (RF sputtering)	Polychloro-trifluoethylene (PCTFE)	High concentration of interactive sites π-conjugated systems/ Nonpolar species	Sugimoto et al.
Plasma polymerization (RF sputtering)	Amino acid	Hydrophilic structure/ Polar solvent gases	Sugimoto et al.
Plasma polymerization (PECVD)	Siliconorganic film (PDMS-like polymer)	Nonpolar stationary phase	Lehmann et al.
Injection coating	Polydimethylsiloxane (PDMS)	Nonpolar stationary phase	

In order to take advantage of the open structure of the micromachined channel, we need to develop a dry coating method through which a uniform stationary phase can be achieved. Table 5-3 shows the previously reported stationary phase coating methods for micromachined silicon channels. Dry coating can provide a more uniform stationary phase and more precise thickness control compared to injection coating. In this study, two dry coating techniques and the injection coating technique (wet coating) were investigated for parylene GC column.

5.2.1 DRY COATING

One of the dry coating techniques used in this study was the plasma polymerization of fluorocarbon that is similar to the second method in Table 5-3. The other method is chemical vapor deposition of a functionalized parylene. Parylene A which has amino functional group was selected for this purpose. Since both materials are not commonly used stationary phases, their retention properties needed to be evaluated first. Quartz crystal microbalance (QCM) method was used here to investigate the absorption and the diffusion of organic chemicals in the materials. The distribution constants of representative volatile organic chemicals were also able to be calculated.

5.2.1.1 Film Deposition

A parallel plate radio frequency (RF) plasma reactor was used to deposit fluorocarbon films from precursor/argon mixtures as shown in Figure 5-17. The precursor used was pentafluoroethane (C_2F_5H). The distance between the electrodes was fixed at 2.9 cm and RF power at 13.56 MHz was used. The bottom electrode was electrically grounded and heated. The substrates were placed on the bottom electrode and maintained at a constant temperature of 70 ^{o}C. The base pressure in the chamber was < 7 mTorr, while the operating pressure was maintained at 1 Torr for all the depositions. The deposition time was 25 seconds. A commercial parylene deposition system was used to deposit parylene A. The furnace temperature and vaporizer temperature were adjusted to 690 ^{o}C and 190 ^{o}C, respectively. The parylene A dimer was provided by Uniglobe Kisco, Inc. With 0.5 g and 0.2 g of the dimer, the final coating thicknesses were 560 nm and 228 nm respectively. The thickness was measured using an ellipsometer.
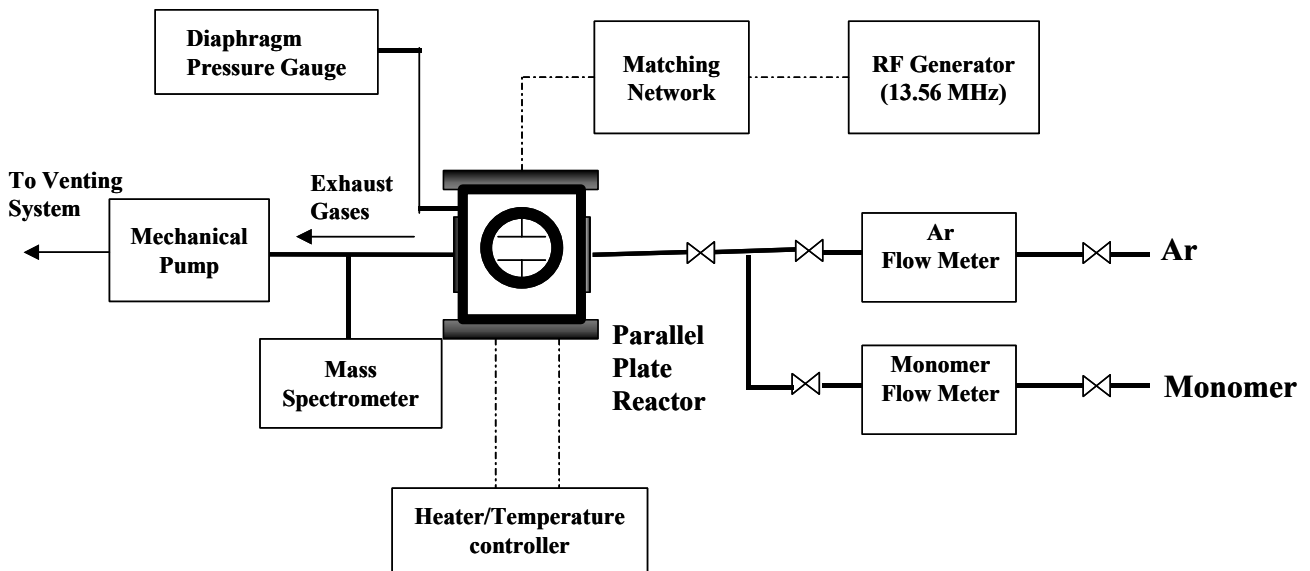
Figure 5-17. Schematic of the plasma reactor system [67].

5.2.1.2 QCM Tests

The absorption of gas into the films was studied using quartz-crystal microbalance (QCM) techniques. QCM crystals vibrate at precise and reproducible frequencies in the presence of an electric field. When a rigid load is deposited on a crystal, the resonant frequency decreases in response to the added mass. As long as the added mass is rigid and small compared to the crystal mass, the decrease in frequency is inversely proportional to the mass increase. This is the Sauerbrey relationship and is described below.

$$\Delta m = \frac{\Delta f}{C_f}$$

Equation 5-6

$$C_f = \frac{2 f_q}{\rho_q v_q}$$

Equation 5-7

where m is mass, f is measured frequency, C_f is the constant that is dependent on the crystal, f_q is the crystal resonant frequency on the unloaded crystal, ρ_q is the density of the quartz and v_q is the acoustic velocity. For the system used in these studies, f_q is 5.0 MHz, ρ_q is 2.65 g/cc and v_q is 3340 m/s. With less than 5 wt% absorption of organic vapors in the film, it is assumed that the films will remain rigid when becoming saturated, validating the Sauerbrey relationship.

The films investigated by this method were fluorocarbon, parylene-A, parylene-C, and PDMS. They were deposited on QCM crystals using PECVD (fluorocarbon), CVD (parylenes), and spin coating (PDMS). Parylene-C was investigated because it is the

structural material of the column and PDMS because it is the representative conventional stationary phase. To measure the absorption of the various organic chemicals, a dual-chamber system is used. First, the crystal and crystal holder are place in a dry plexiglass chamber that is continuously purged with house nitrogen. The frequency is monitored until it reaches a constant value for several minutes. A second chamber is purged with a saturated organic vapor from a bubbler. The flow rate of nitrogen into the bubbler is controlled. The temperature of the bubbler and chamber is also monitored. A minimum flow rate of 4.5 scfh into the bubbler ensures a consistent environment in the chamber. At this flow rate, an equivalent chamber volume is delivered in 36 seconds. Initially, this chamber is purged for 25 minutes prior to testing. The partial pressure of the absorbent in the chamber environment is assumed to be at the vapor pressure at the temperature of the bubbler. While evaporation causes the temperature in the bubbler to be less than ambient, the chamber temperature stays at ambient temperature within ± 2 °C.
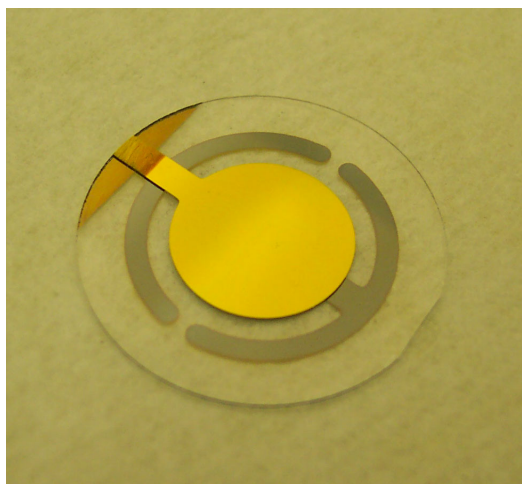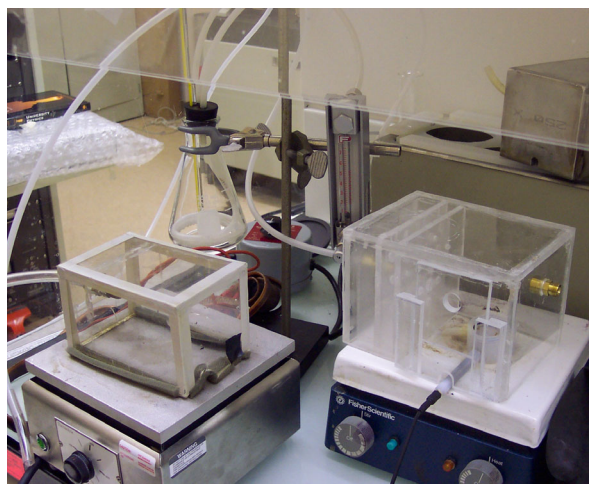
(a)   (b)

Figure 5-18. (a) QCM and (b) experimental setup.

After the frequency is constant in the dry atmosphere, the QCM crystal and holder are quickly transferred the second chamber. The QCM is exposed to ambient conditions during the transfer, however, the transfer takes less than half of a second which is slower than the timescale of the absorption. After the frequency is stable for several minutes in the organic atmosphere, the QCM is returned to the dry chamber. This cycle is repeated 2-3 times to ensure reproducible results and complete desorption of the vapor. A typical absorption/desorption cycle is shown in Figure 5-19.
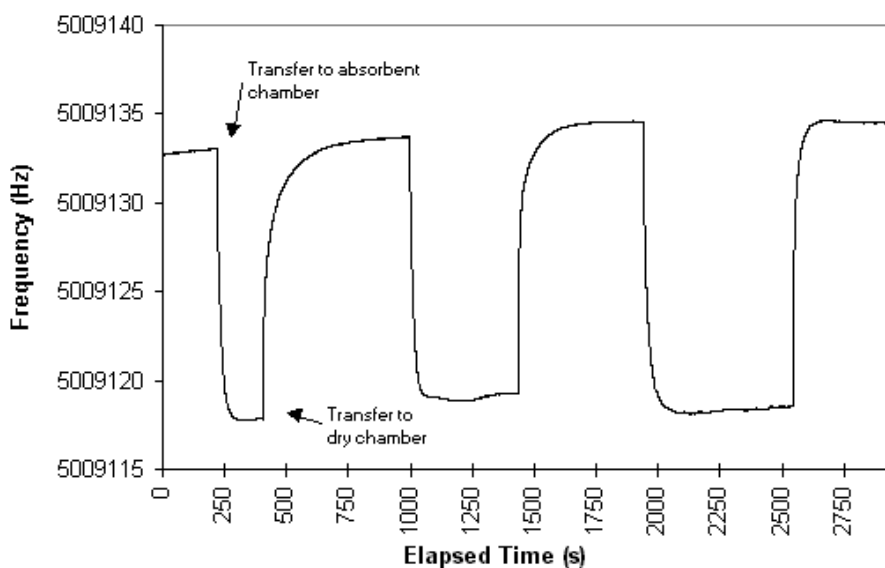
Figure 5-19. Typical absorption/desorption cycles. Shown is hexane/fluorocarbon system.

The absorption of seven chemicals representing a range of functional and structural groups were tested using the four films. The seven chemicals are water, ethanol, diethyl ether, tetrahydrofuran, acetonitrile, hexane, and benzene. The analysis includes the equilibrium mass uptake, diffusion coefficient, and distribution constant calculation. The total mass uptake is calculated using the frequency decrease upon exposure to the organic atmosphere. The equilibrium mass uptake for the four films is listed in Table 5-4.

159

The fluorocarbon film readily absorbed the non-polar and slightly polar molecules. While the carbon-fluorine bond is one of the most polar covalent bonds, the large fluorine molecules in CF_3 and CF_2 moieties shield the carbon backbone from absorbed species creating a more non-polar environment. Polar molecules may be able to interact with CF centers where the carbon is less shielded. This could explain the moderate absorption of the more polar molecules. The amine functional group in the parylene-A film seems to strongly interact with ethanol and acetonitrile allowing significant absorption. This can be explained by the strong dipole of the O-H and the CN in those respective molecules. It is surprising that the water absorption is not comparable. Parylene-c films absorbed vapor more than expected. Since the parylene-c is partially crystalline, vapor sorption was expected to be low. In areas that are not crystalline, the pi bonds on the benzene ring and the polarity of the carbon-chlorine bond will provide some interactions allowing polar vapor absorption. In addition the organic nature of the film provides for non-polar absorption. Exposure of the PDMS film to THF, hexane, and benzene resulted in a large increase in the QCM resonant frequency, implying a decrease of the mass onto the film. This is likely due to a large degree of swelling resulting in a significant change of the modulus of elasticity. This condition can be likened to the difference between vibrating a firm material and a gel-like material. For the same driving force, the more viscous material will vibrate at a higher frequency until the resonance matches the vibrations of the gel-like medium. The equipment currently used does not allow for independent measurement of both mass and modulus of elasticity.

Table 5-4. Vapor uptake for different films.

	Flourocarbon (wt%)	Parylene-A (wt%)	Parylene-C (wt%)	PDMS (wt%)
Water	0.31	0.56	0.31	0.01
Ethanol	0.80	2.88	1.22	0.45
Ether	1.90	0.13	1.38	0.73
Acetonitrile	2.22	5.16	0.99	0.63
Tetrahydrofuran (THF)	3.91	0.17	1.15	-6.70 *
Hexane	1.43	0.08	0.46	-48.06 *
Benzene	3.75	0.17	0.76	-20.39 *

About half of the film/absorbate systems exhibited typical Fickian-like diffusion behavior. Fickian behavior is illustrated in Figure 5-20. This behavior is obvious when the normalized mass uptake is plotted versus the square root of time as shown in Figure 5-20 (a). During the first 50-60% of mass uptake, the plot is linear if the diffusion is Fickian. The slope of this line can be used to determine the diffusion coefficient of the system. When this coefficient is used in the analytical model for Fickian diffusion, the model fits the experimental data well (Figure 5-20 (b)). This analysis is a common for determination of diffusion coefficients.

Some systems initially exhibited Fickian type diffusion until 50-60% of mass uptake. At that point, a noticeable change in the rate of absorption can be observed. This concentration-dependent diffusion behavior (Figure 5-21 (a)) is common in polymer absorption and may be explained by clustering. Clustering occurs when all of the absorption sites become saturated, molecules continue to absorb into the film and interact with already absorbed molecules. Clusters of absorbent molecules form around sites. The diffusion rates decreases because this is a slower process. Several systems initially

161

absorbed a higher than equilibrium and became super-saturated before equilibrating to a

lower concentration. This type of behavior is shown in Figure 5-21 (b). No good

explanation has been made for this behavior.

(a)   (b)
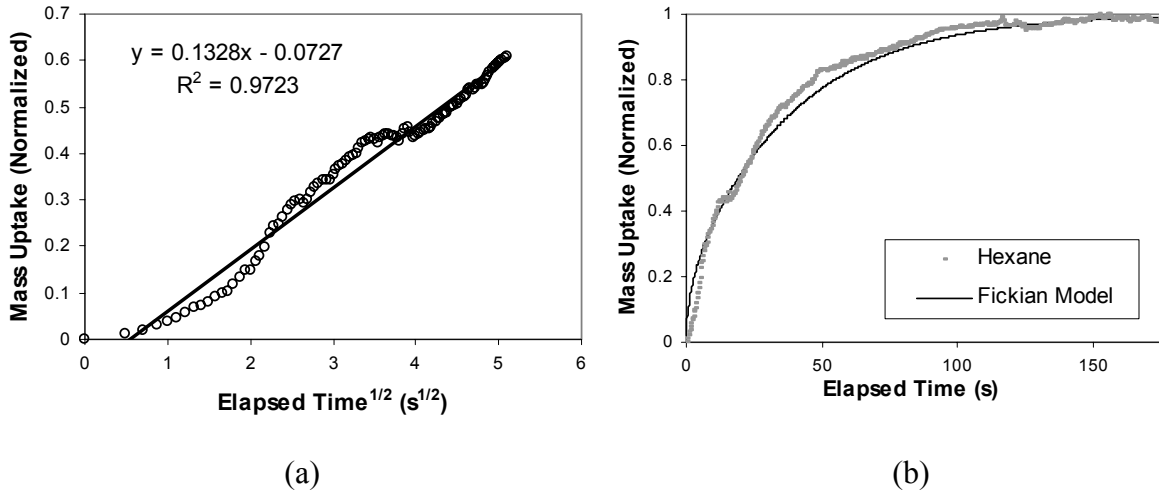
**Figure 5-20. Fickian behavior with hexane/fluorocarbon system; (a) normalized
mass uptake versus elapsed time1/2 (diffusion coefficient can be calculated from the
slope of this graph), (b) comparison of the measurement and the Fickian model.**

(a)   (b)
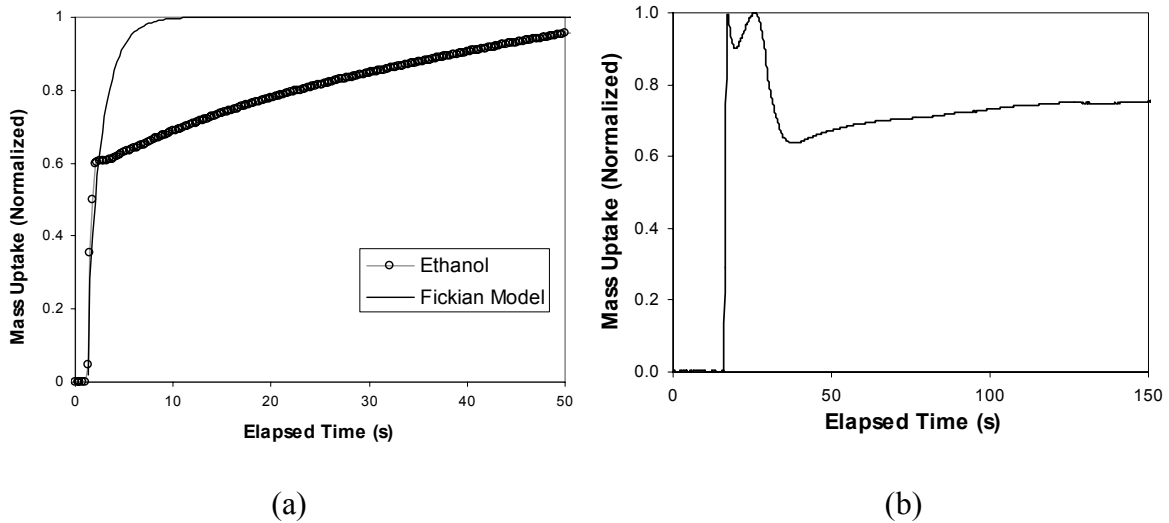
**Figure 5-21. Non-Fickian behaviors ; (a) concentration-dependent diffusion
behavior (ethanol/parylene A), (b) super-saturation behavior (THF/parylene A).**

Table 5-5 is a summary of the behaviors observed for each type of system. From the equilibrium absorption for each system, a distribution constant can be calculated. The distribution constant can be used as a predictor for solvent separation in a column. The concentration in both phases is required. The concentration in the vapor phase is calculated assuming saturation of the organic phase in the bubbler at the bubbler temperature and that the vapor behaves as an ideal gas at the temperature in the chamber. The vapor pressure is estimated using the Antoine equation and data from the DIPPR online thermodynamic database. The concentration in the solid phase is calculated using the molecular weight of the absorbent and the density of the solid polymer. There appears little correlation between the behavior of the system and the strength or type of film/absorbent or absorbent/absorbent interaction. For the systems which exhibited Fickian-like behavior, the estimated diffusion coefficient is listed, although the solubility, not the diffusion rate is generally more important for separation in a GC column.

Parylene-C films absorbed vapor more than expected. Since the parylene-C is crystalline, vapor sorption was expected to be low. In areas that are not crystalline, the pi bonds on the benzene ring and the polarity of the carbon-chlorine bond will provide some interactions allowing polar vapor absorption. In addition the organic nature of the film provides for non-polar absorption. As expected, the rate of absorption for the PDMS was faster than the measurement capability. With the thickest film possible spun on the QCM (1.1 micron), the absorption appears instantaneous with measurement interval of 0.1 seconds. This observation agrees with the model and literature values for the diffusion coefficient.

Table 5-5. Summary of observed behavior for each system.

Film	Absorbent	Behavior	Diffusion Coefficient [cm^2/s]	Conc. in film [mmol/l]	Conc. in vapor [mmol/l]	Distribution constant, K
Fluorocarbon	Water	Fickian	1×10^{-11}	327.2	0.814	402.19
	Ethanol	Super-sat.	over equil.	1030.4	3.565	288.99
	Ether	Fickian	7×10^{-11}	487.2	7.945	61.32
	Acetonitrile	Super-sat.	over equil.	329.7	1.459	226.03
	THF	Clustering		912.3	2.337	390.39
	Hexane	Fickian	1×10^{-12}	1026.3	2.534	404.95
	Benzene	Super-sat.	over equil.	315.2	3.118	101.08
Parylene - A	Water	Fickian	8×10^{-10}	405.3	0.894	453.30
	Ethanol	Clustering		29.8	3.752	7.93
	Ether	Fickian	2×10^{-9}	22.8	7.945	2.86
	Acetonitrile	Fickian	3×10^{-12}	813.2	1.765	460.78
	THF	Super-sat.	over equil.	27.5	2.463	11.15
	Hexane	Super-sat.	over equil.	1631.1	2.289	712.53
	Benzene	Super-sat.	over equil.	12.4	3.730	3.34
Parylene - C	Water	Fickian	3×10^{-9}	223.4	0.691	323.51
	Ethanol	Clustering		206.0	1.453	141.78
	Ether	Clustering		392.6	6.143	63.92
	Acetonitrile	Fickian	2×10^{-9}	318.0	1.664	191.13
	THF	Clustering		203.5	3.373	60.34
	Hexane	Fickian	2×10^{-9}	70	2.724	25.70
	Benzene	Clustering		139.5	1.877	74.28
PDMS	Water	Swelling	-	-6.4	0.785	
	Ethanol		$> 1 \times 10^{-8}$	60.7	1.277	47.55
	Ether		$> 1 \times 10^{-8}$	165.9	6.143	27.00
	Acetonitrile		$> 1 \times 10^{-8}$	160.0	2.028	78.90
	THF	Swelling	-	-949.3	2.734	
	Hexane	Swelling	-	-5854.2	3.188	
	Benzene	Swelling	-	-2969.3	2.149	

5.2.2 WET COATING

5.2.2.1 PRELIMINARY TESTS

In order to see the feasibility of coating conventional stationary phase on a parylene surface, some preliminary experiments have been done using spin coating. Parylene was deposited on 2 inch dia silicon wafers and its thickness was measured by ellipsometry. Parylene had very uniform thickness at about 0.8 μm. One of the most common non-polar stationary phase, OV-1 (PDMS, *Ohio Valley Specialty Chemical*, Marietta, OH) was selected for this study. Two different concentrations were prepared using toluene as a solvent. Both Si and parylene-coated Si substrates were then spin-coated with the solutions at 2000 rpm for 20 seconds. After spinning, the wafers were put in 120 $^{\circ}$C oven for solvent removal. OV-1 coating thickness was measured by ellipsometry. Table 5-6 shows the results. The samples coated with solution 1 did not show detectable thickness on either substrate. However, the samples coated with solution 2 showed similar coating thicknesses. Different substrate materials did not make a big difference in coating thickness (5% difference). OV-1 coating thickness seems to be able to be controlled by solution concentration and coating speed. The coatings on both substrates looked uniform like thermally grown SiO_2 layer.

Table 5-6. Spin coating of OV-1 on silicon and parylene surfaces.

	Solute	Solvent	Coating on silicon	Coating on parylene
Solution 1	0.1 g OV-1	40 mL Toluene	-	-
Solution 2	2.0 g OV-1	100 mL Toluene	287 nm	273 nm

Another preliminary test was parylene surface modification. The effect of wet treatment on the hydrophilicity was investigated. For this purpose, 1x1 cm^2 silicon pieces were treated with an adhesion promoter (A174:DI water:IPA=1:50:50) and then deposited with 1 μm thick parylene C.

First, the parylene-coated silicon pieces were exposed to 4 different oxidizing solutions: Piranha (H_2SO_4/H_2O_2, 3:1), Aqua regia (HNO_3/HCl, 1:3), RCA SC-1 ($NH_4OH/H_2O_2/H_2O$, 1:1:5, heated to 60 ^{o}C), RCA SC-2 ($HCl/ H_2O_2/H_2O$, 1:1:5, heated to 60 ^{o}C). The piranha and aqua regia seemed too aggressive and delaminated the film from the silicon after several minutes. Exposure to both the SC-1 and SC-2 solution modified the surface, however, the SC-2 solution was able to reduce the contact angle much more than the SC-1 solution as shown in Table 5-7. XPS also shows SC-2 oxidize the surface more than SC-1.

Table 5-7. Effect of oxidizing solutions on parylene surface.

Treatment	Contact angle	XPS – C (%)	XPS – Cl (%)	XPS – O (%)
None	90	89.9	10.1	0.0
SC-1 – 1.5 hrs	79	88.3	10.1	1.6
SC-2 – 1 min	83	85.0	9.0	6.1
SC-2 – 5 min	73	87.2	9.9	3.0
SC-2 – 10 min	54	84.2	10.2	5.7

Second, reduction and combination methods have been tried. The most common reductive method, and the one employed here is a sodium/naphthalene solution in THF. It is known that this acts to defluorinate the surface of Teflon to a depth dependent on the exposure time and concentration, but can range from tens of angstroms to microns. Literature reports indicated that these reductive treatments are not nearly as effective on

chlorine containing polymer films, however, the effective dechlorination in the parylene-C samples was observed. Samples were exposed to a reductive sodium/naphthalene solution for times ranging from 30 seconds to 30 minutes. XPS analysis indicated a complete removal of chlorine with the minimum treatment time. In addition, an increasing penetration depth is observed over the time range evidenced by the charge build-up during XPS analysis. For the minimum time, the dechlorinated film depth exceeds the penetration depth of the XPS analysis (~50-75 angstroms). After the treatment, aromaticity is still detected in the film, as well as trace amounts of oxygen. This treatment, however, did not significantly reduce the contact angle.

Third, combination treatments gave predictable results. Reductive treatments removed the chlorine and oxidative treatments incorporated a similar amount of oxygen as before (3-6%), however, contact angles did not seem to correlate to the addition of oxygen.

5.2.2.2 INJECTION COATING FOR CIRCULAR SILICA COLUMN

The conventional silica columns were used to find out an appropriate recipe for injection coating of parylene column. 1 m long silica columns having the inner diameter of 100 μm or 320 μm were used for this purpose. The final coating thickness is a function of many parameters and can be expressed by Fair-Brother equation shown below.

$$d = \frac{rc}{200} \cdot \left(\frac{u\eta}{\gamma} \right)^{1/2}$$

Equation 5-8

167

where d is coating thickness, r is radius, c is concentration, u is velocity, η is viscosity, and γ is surface tension.

Three solutions having different concentrations were prepared. 0.5, 2, and 5 g of OV-1 were dissolved in 100ml toluene, respectively. The viscosity of the solutions was measured by a rheometer (AR1000-N, *TA instruments*). The dynamic viscosity data of the solutions are shown in Figure 5-22. Compared to 0.5g/100ml solution, 5g/100ml solution was much more viscous and showed shear thinning property. The dynamic viscosity of the solution (5g/100ml) at the shear rate of 100 [1/sec] was about 0.25 Pa·s. The surface tensions of the two solutions were measured by a goniometer (NRL.C.A, *Rame-Hart, Inc.*, Mountain Lakes, NJ) and the values were 18.2 and 17 dyne/cm, respectively.
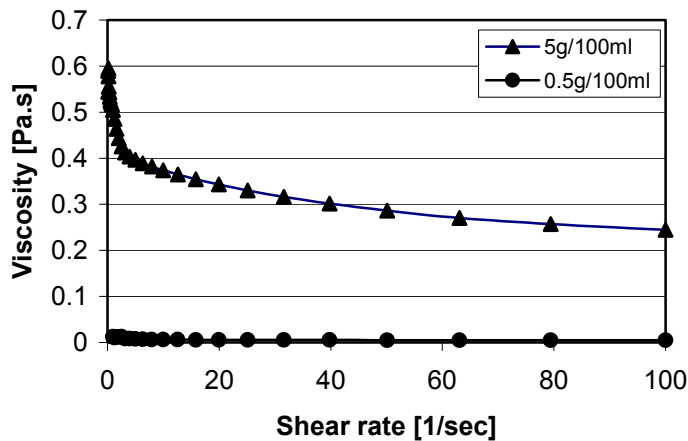

Figure 5-22. Dynamic viscosity of OV-1 solutions having different concentrations.

Knowing the viscosity and surface tension of the solution, the velocity and pressure drop required for a certain coating thickness can be calculated using the Fair-Brother equation. Table 5-8 shows the calculation results for 100 and 320 μm diameter columns (1m long). For 100 μm column, very high velocity and pressure drop are

required for the desired coating thickness (50 ~ 100 µm) when 0.5g/100ml solution is

used. However, the same coating thickness can be obtained by low velocity (< 0.5 mm/s)

and comparatively low pressure drop (< 3 atm) when 5g/100ml solution is used. For 320

µm column, approximately 10 times less velocity and 100 times less pressure drop are

required for the same coating thickness when the same solution is used.

Table 5-8. Coating thickness and flow rate.

r [µm]	A [m^2]	L [m]	C [%]	η [Pa.s]	γ [N/m]	d [nm]	u [m/s]	Q [SCCM]	ΔP [psi]
50	7.85E-09	1	0.5	4.90E-03	1.82E-02	100	2.38E+00	1.12E+00	5410
50	7.85E-09	1	0.5	4.90E-03	1.82E-02	50	5.94E-01	2.80E-01	1352
50	7.85E-09	1	0.5	4.90E-03	1.82E-02	30	2.14E-01	1.01E-01	487
50	7.85E-09	1	0.5	4.90E-03	1.82E-02	10	2.38E-02	1.12E-02	54
50	7.85E-09	1	5	0.25	0.017	100	4.35E-04	2.05E-04	51
50	7.85E-09	1	5	0.25	0.017	50	1.09E-04	5.12E-05	13
50	7.85E-09	1	5	0.25	0.017	10	4.35E-06	2.05E-06	0.5
160	8.04E-08	1	5	0.25	0.017	100	4.25E-05	2.05E-04	0.5
160	8.04E-08	1	5	0.25	0.017	200	1.70E-04	8.20E-04	1.9

(r: radius, A: cross sectional area, L: length, C: concentration, η: dynamic viscosity, γ:
surface energy, d: coating thickness, u: velocity, Q: volumetric flow rate, ΔP: pressure
drop)

A syringe pump was used to inject the solution through the column and

volumetric flow rate was controlled. However, the required velocity could not be

achieved at the calculated volumetric flow rate. When the volumetric flow rate was

increased to 0.1 SCCM, the reasonable velocity (~ 0.1-1 mm/s) could be achieved. But

the syringe needed to be held down tightly during the injection because the syringe pump

could not endure the high pressure. After flowing the solution through the column for 5

min, the solution filled in the column was pushed out using the injection module of the

conventional GC system. Helium gas was used for this and the inlet pressure was set 50 –
80 psi.

Figure 5-23 shows the SEM images of the cross section of OV-1 coated silica
column. The concentration of the solution was 5 g/100 ml and the volumetric flow rate
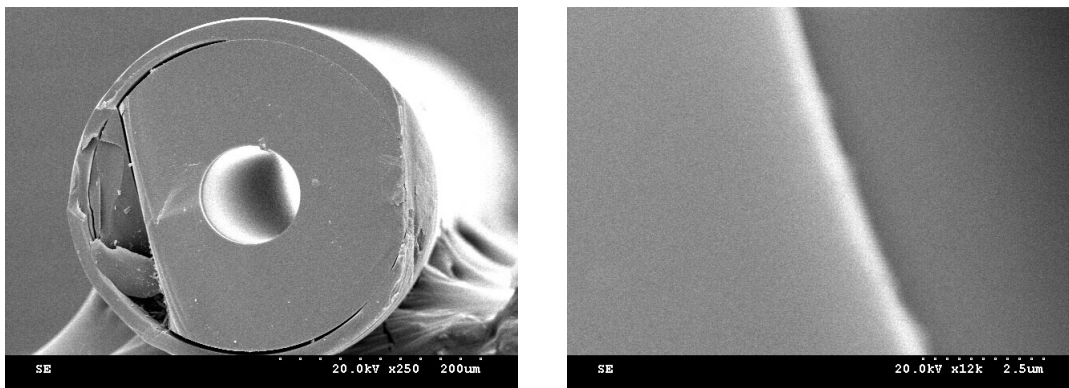was 0.01 SCCM. However, it was very hard to observe the thin coating lined in the
column.

Figure 5-23. SEM image of OV-1 coated silica column.

Since the direct measurement of the stationary phase thickness was failed, the
only means left is calculating the thickness through actual GC analysis. This method is
very simple. What we need to know from a chromatogram are the dead time (t_M) and the
retention time (t_R) of a solute whose distribution constant is known. Then the following
two equations are used to calculate the stationary phase thickness.

$$t_R = t_M \cdot (1 + k)$$

$$k = K \cdot \frac{V_S}{V_M} = K \cdot \frac{2\pi \cdot r \cdot w \cdot L}{\pi \cdot r^2 \cdot L} = K \cdot \frac{2w}{r}$$

The following graph is the chromatogram for hydrocarbon mixtures obtained with
a silica column (ID 100μm, 1m, stationary phase: injection coated OV-1 at 0.01 SCCM

with 5 g/100 ml solution). The sample was pentane, hexane, and heptane dissolved in methanol. The unretained peak and the peak for heptane appeared at 0.190 and 0.255 min respectively. The distribution constant of heptane for PDMS was obtained from literature. This data was used in the calculation of stationary phase thickness and the calculated stationary thickness was 37 nm.
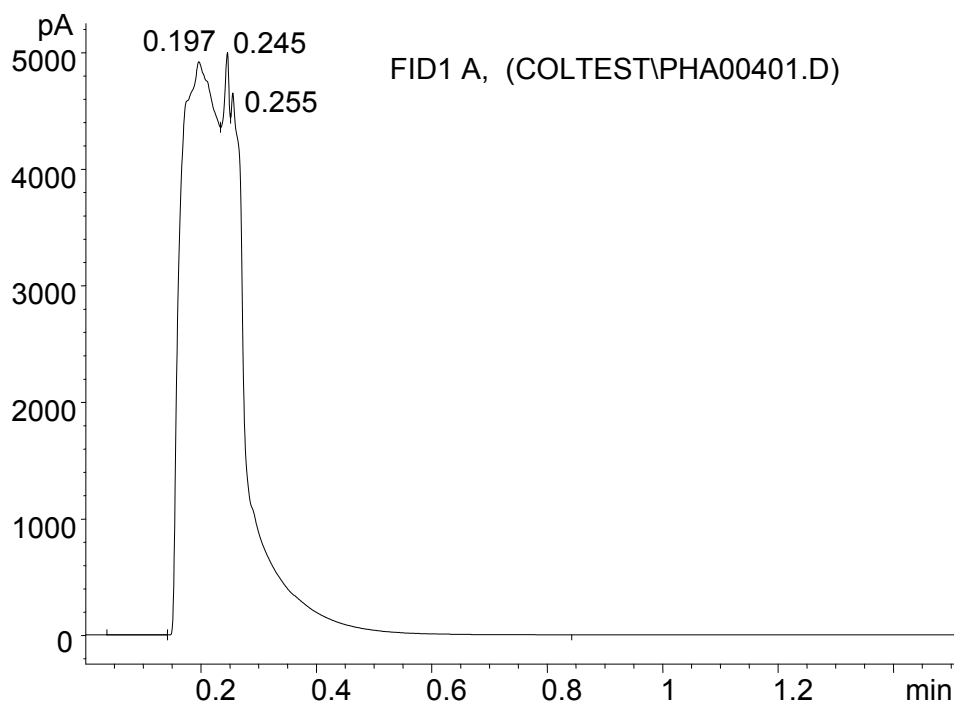

Figure 5-24. Chromatogram for hydrocarbon mixture obtained with a silica column that has injection-coated OV-1.

5.2.2.3 INJECTION COATING FOR PARYLENE COLUMN

In order to avoid the high pressure drop in a parylene column and the stationary phase coating in side tubings, a clamping method was tried. A parylene-coated silicon

171

microchannel was attached to a glass substrate having holes and tubings as shown in Figure 5-25. Then these were clamped together and the solution was injected using syringe pump. This method was not successful. There was a leakage observed during the injection of the solution. So the conventional injection coating method was tried after completing thermal lamination and tubing. Figure 5-26 shows the injection coating setup. However, the recipe obtained from the experiments with silica columns did not work well. The high concentration solution (5 g OV-1 / 100 ml toluene) used for silica columns built up too much pressure in a parylene column and did not advance. So the lower concentration (2.0 g OV-1 / 100 ml toluene) and lower volumetric flow rate (0.001 SCCM) were used for parylene columns. This recipe produced a reasonable speed of the solution and the solution was purged out using GC injection module. GC analysis was performed using this column and the results will be discussed in Chapter 7.
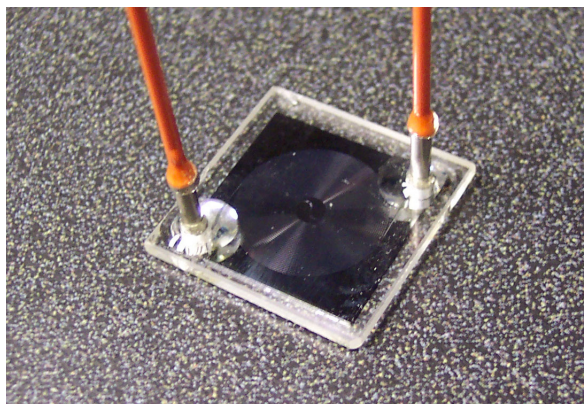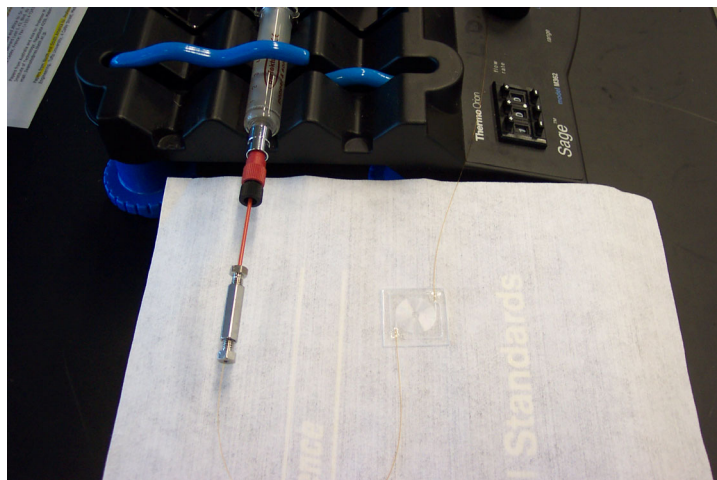

Figure 5-25. Assembly for injection coating.

Figure 5-26. Setup for injection coating of stationary phase.

CHAPTER 6

FABRICATION

This chapter describes the fabrication of a parylene GC column. Since the development of the key processes used in the fabrication was fully described in the previous chapter, this chapter will cover the other aspects related to the fabrication of parylene GC column. The detail recipes and the problem shooting of each fabrication process will also be provided in this chapter.

6.1 Overview

Figure 6-1 shows the overall fabrication flow for parylene GC column. This is one mask process and semi-batch process. Silicon microchannel molds are fabricated using deep RIE etching technique. The silicon mold is then deposited with parylene, platinum and parylene in series. A pyrex glass substrate is also deposited with parylene. These two substrates are then laminated with heat and pressure. After thermal lamination, parylene column is released by etching silicon mold away with KOH solution. The free-standing parylene column is then deposited with gold to form a heating element. Then, silica microtubes are inserted into parylene column and stationary phase is lined in the column by injection method. Finally, electrical wiring is made and parylene column is packaged.
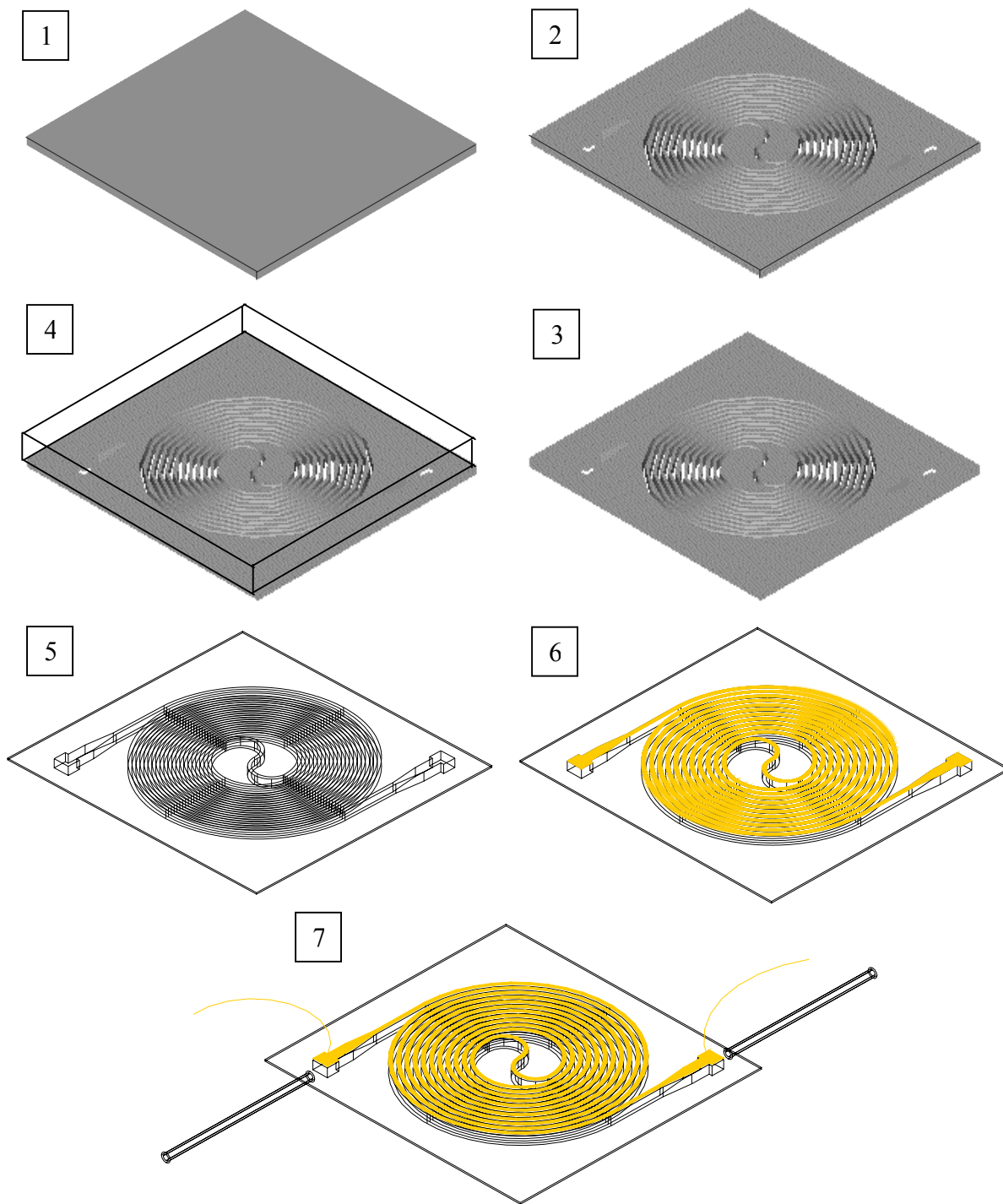
Figure 6-1. Fabrication process flow (1) silicon wafer, (2) deep RIE, (3) parylene/Pt/parylene deposition, (4) thermal lamination, (5) release of parylene column, (6) Au deposition, (7) tubing, stationary phase coating and packaging.

Lithography, deep RIE etching, KOH etching, and metallization were performed in cleanroom facilities and the other processes such as parylene deposition, thermal lamination, and stationary phase coating were conducted in non-cleanroom facilities.

6.2 SILICON MICROCHANNEL

Silicon microchannels were fabricated by deep RIE technique. The standard Bosch process that consists of one deposition and two etch steps was used to fabricate deep rectangular channels on silicon substrates. An inductively-coupled plasma etching system (Plasma-Therm ICP) was used for the Bosch process. Arrays of spiral microchannels were etched on 4-inch diameter silicon substrates. Nine 1 m long channels or four 3 m long channels were built on one wafer. Figure 6-2 is a part of the mask layout for 1 m long channel.
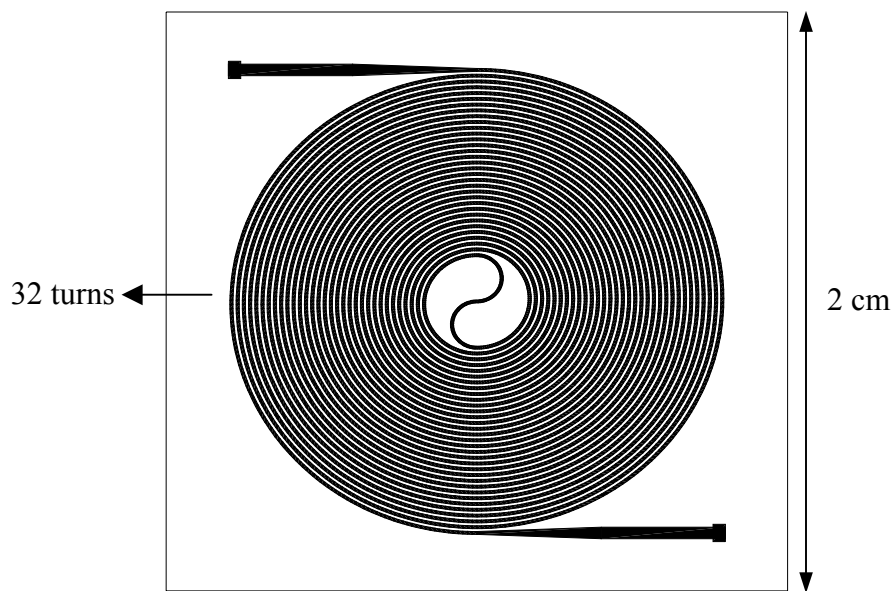

Figure 6-2. Mast layout for silicon microchannel (1 m long, 100 μm wide).

Four different channels were designed and fabricated. Their dimensions are as follows. For each channel design, silicon channel having different channel depth were fabricated by controlling the number of Bosch cycles.

Table 6-1. Four different dimensions of silicon microchannels.

	Length [m]	Width [μm]	Inter-channel distance [μm]
Channel 1	1	60	100
Channel 2	1	100	100
Channel 3	3	60	100
Channel 4	3	100	100

Table 6-2 is the detail description of the fabrication of silicon microchannel. AZ 4620 was used as the mask material for deep RIE of silicon. An adhesion promoter was required because the channel pattern is a long thin line. Hexamethyldisilazane (HMDS) was used for the purpose in this process. The existence of HMDS made developing much slower, so that higher concentration (AZ 400K:DI water = 1:1) solution was used for developing. Also pipetting over the pattern during developing was very effective. Figure 6-3 is the SEM images of the cross-section of a silicon microchannel that has a dual spiral design. Figure 6-3 (a) is a overall bird view and Figure 6-3 (b) is a magnified view. It is observed from Figure 6-3 (b) that the wall angle is slightly bigger than 90 $^{\circ}$. Most silicon microchannel fabricated in this study by standard Bosch technique showed such 're-entrant' shape. Figure 6-3 (c) is a magnified image of the channel bottom. The channel bottom did not have flat surface but a curved one. The difference in height between the edge and the center of the channel bottom was less than 20 μm for a 300 μm deep channel. Figure 6-3 (d) shows one end of the channel. As shown in the mask layout, the inlet and outlet of the channel have bigger dimension than the main channel. During

the deep RIE, the larger area is etched slightly faster than the small area because the etching species can reach the bottom of the channel more easily. As a result, the inlet and outlet have slightly deeper channel than the main channel.

Table 6-2. Detail description of the fabrication of silicon microchannel.

	Process step	Details			
1	Dehydration bake	Hot plate, 120 ^{o}C, 5 min			
2	Primer coating	HMDS, 3000 rpm – 1000 rpm/s – 10 s			
3	PR coating	AZ 4620 (15 μm) 1000 rpm – 500 rpm/s – 20 s – 3000 rpm – 10000 rpm/s -3 sec			
4	Soft bake	Hot plate, 95 ^{o}C, 20 min			
5	Exposure	365 nm, 1000 mJ			
6	Develop	AZ 400K:DI water = 1:1, pipetting			
7	Hard bake	Hot plate, 95 ^{o}C, 20 min			
8	Deep RIE	Standard Bosch process			
			Gas (C_4F_8:SF_6:Ar)	Power [W]	Time [sec]	Pressure [mTorr]
		Deposition	70:0.5:40	825	4	15
		Etch A	0.5:50:40	825	2	16
		Etch B	0.5:100:40	825	6	16
9	PR strip	AZ 400T, Hot plate, 80 ^{o}C, 10 min			

As a mold for parylene GC column, silicon microchannel needs to be free of defect. The fabrication technique used here was the standard Bosch process that is a widely used etching technique. However, it was not easy to fabricate such a clean silicon microchannel as the one shown in Figure 6-3. The most common problem was so called 'micrograss' or 'black silicon'. During deep RIE etching of silicon, tiny particles of polymers or oxide can behave as masks, creating tiny needles or grass in a silicon channel as shown in Figure 6-4. Since this kind of submicron structure absorbs light, it is often called 'black silicon'. It was observed that the formation of black silicon depended on the cleanness of the etcher chamber and the substrate to be etched. Although the amount of

black silicon changed wafer to wafer, almost all wafers was observed to have certain amount of black silicon. They could be localized or spread out over the wafer. SiO_2 mask was also tried but black silicon was still formed. In addition to black silicon problem, imperfect PR patterning was another common problem that caused defects in silicon microchannel. These defects include island shape, peninsular shape, and dam shape as shown in Figure 6-5.
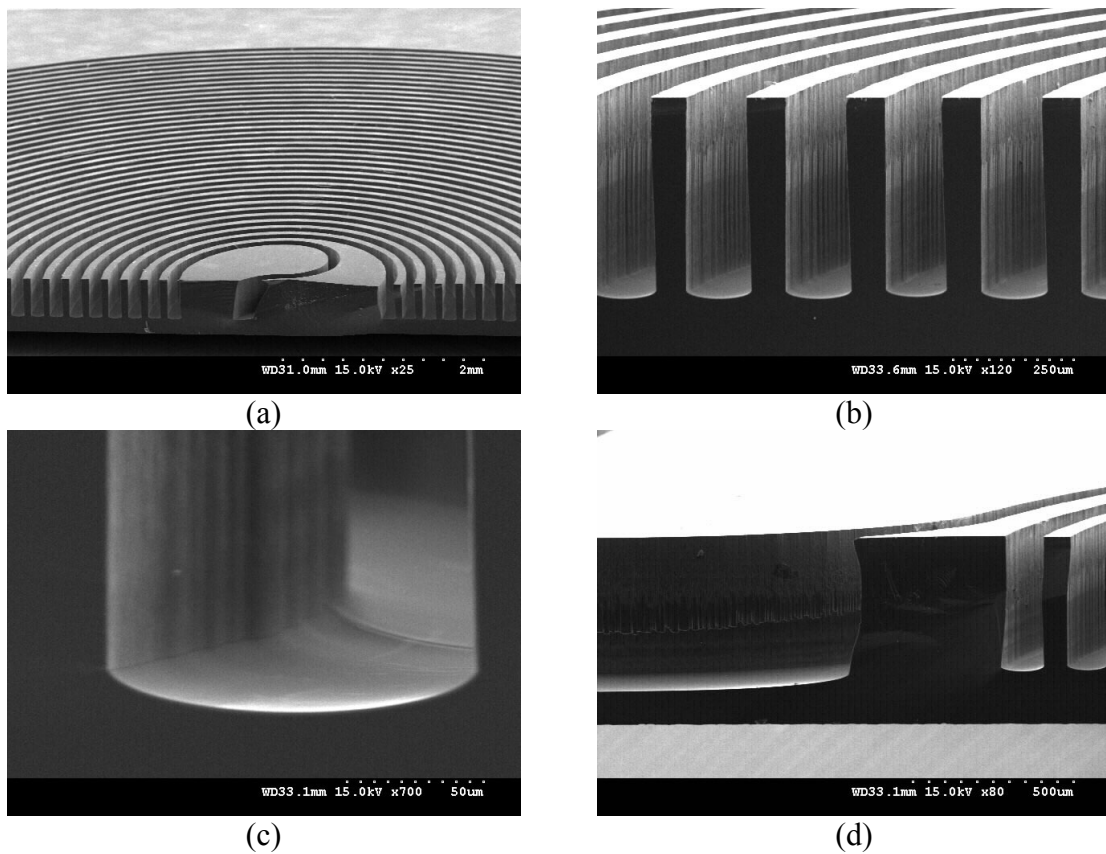

(a)   (b)

(c)   (d)

Figure 6-3. SEM images of a silicon microchannel; (a) overall view, (b) wall angle, (c) channel bottom, (d) channel end.

(a)   (b)
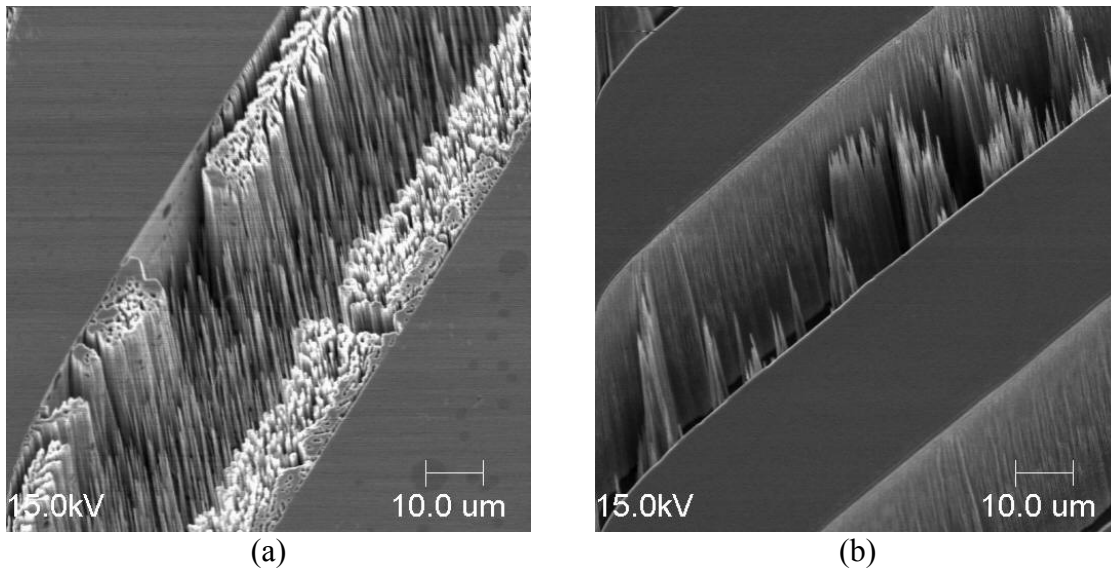
Figure 6-4. SEM images of black silicon formed in a microchannel (a) dense black silicon, (b) sparse black silicon.

(a)   (b)
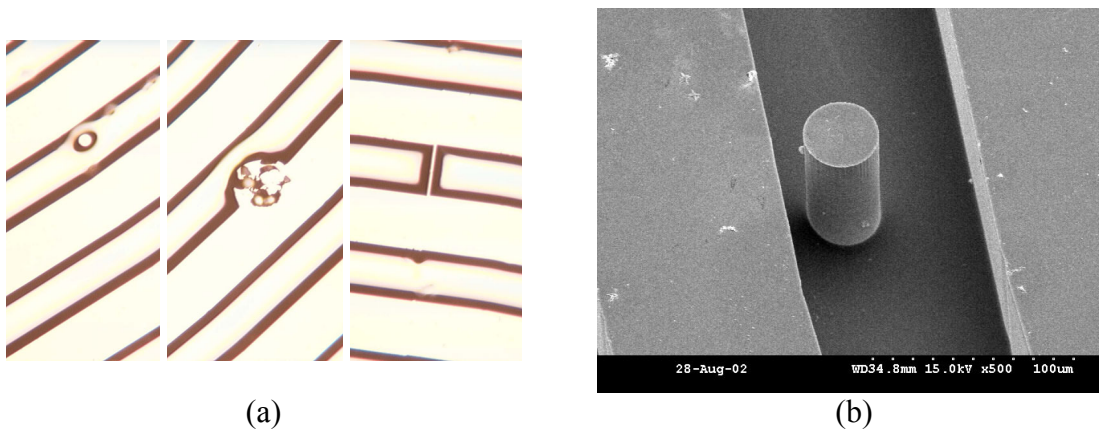
Figure 6-5. Defect in silicon microchannels due to imperfect PR patterning; (a) microscope image of three different defects, island, peninsula, and dam, (b) SEM image of an island-shape defect.

Another very important issue is the surface roughness of silicon microchannels. The surface roughness of GC column is very important because it affects the uniformity of stationary phase coating. Deep RIE silicon microchannels generally have a considerable roughness on the vertical walls while the bottom surface is comparatively smooth. There are two kinds of roughness on the wall surface of a deep RIE silicon

channel as shown in Figure 6-6. One is regularly repetitive horizontal scallop pattern (~

0.5 µm) due to repeating Bosch cycles. The other is irregular vertical groves (1-2 µm) the

cause of which has not been clearly known yet. These are unavoidable roughness
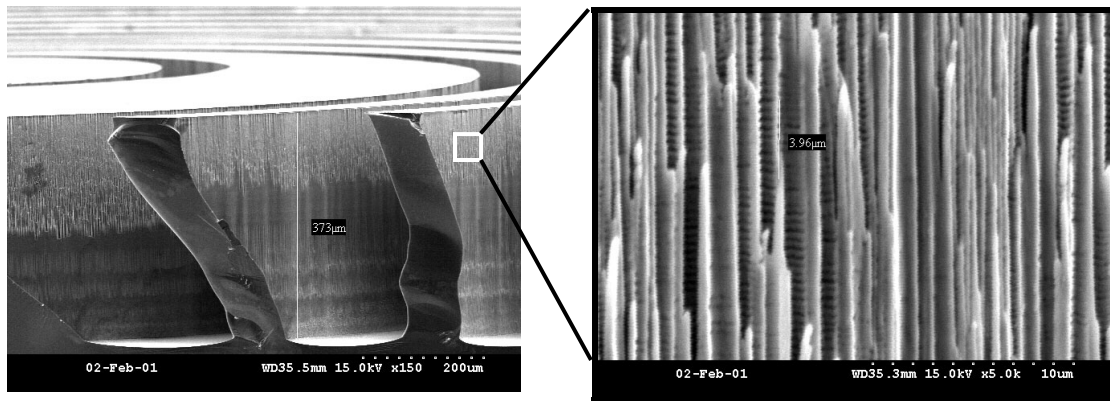
resulting from deep RIE process.

Figure 6-6. Surface roughness of a deep RIE silicon channel.

Can we reduce this surface roughness using wet treatment? Generally wet etching

produces smoother surface than dry etching. So, a short treatment with wet etchant may

reduce the surface roughness of a deep RIE silicon channel. Two most common wet

etchants for silicon were used for this purpose. One was 50% KOH solution. This is an

anisotropic etchant and known to have an etch rate of approximately 0.5 µm/min at 80°C.

The other was HNA solution (20% HF + 45% HNO3 + 35% CH3COOH). This is an

isotropic etchant and known to have an etch rate of approximately 4 µm/min at room

temperature.

Figure 6-7 shows the effect of a short KOH etching on the surface roughness of a

deep RIE silicon microchannel. A short KOH etching seemed to make sharp grooves

smooth initially but soon it started roughening even clean surfaces. The time control was

not easy and the smoothening effect was not considerable. HNA solution was no different. In addition, wet etching affected top surfaces as well as the channel walls.
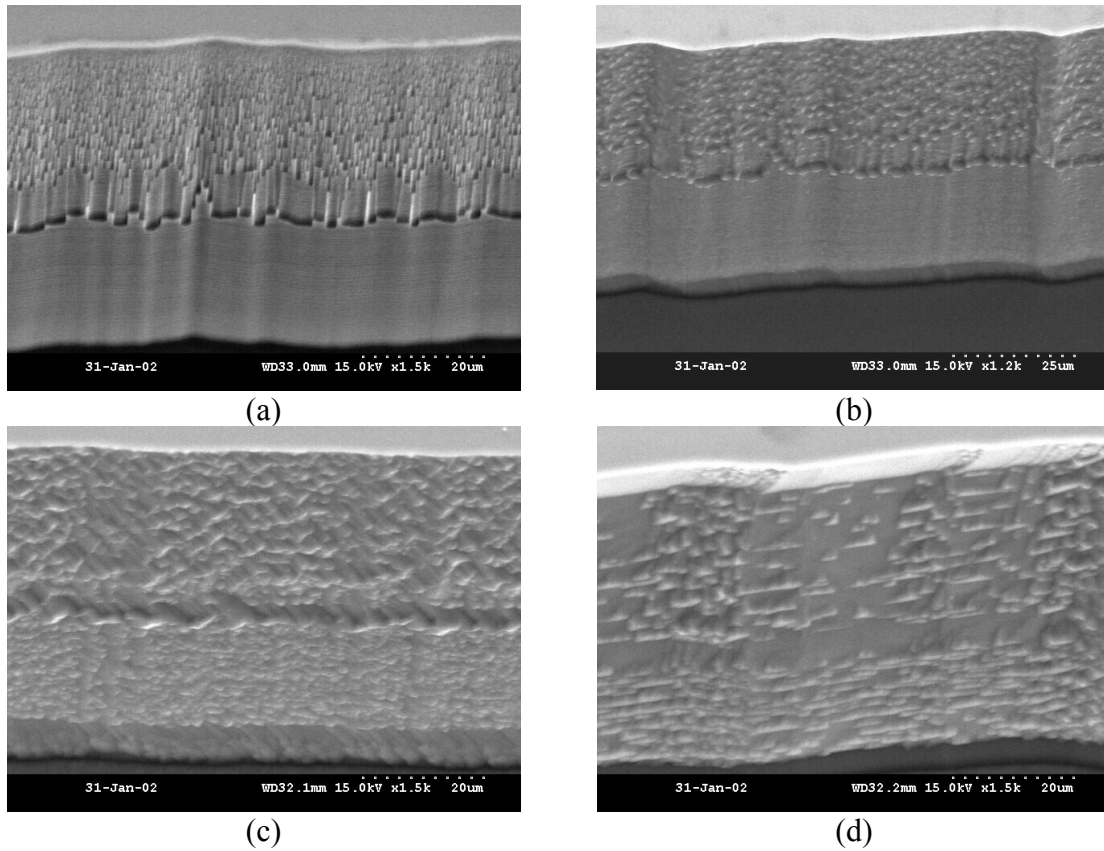

(a)

(b)

(c)

(d)

Figure 6-7. The effect of a short KOH etching (50% KOH, 80 $^{\circ}$C) on the surface roughness of a deep RIE silicon microchannel; (a) before etching, (b) after 1 min, (c) after 2 min, (d) after 5 min.

6.3 PARYLENE DEPOSITION

A 5 μm Parylene-C (*Specialty Coating Systems*, Indianapolis, IN) was deposited on silicon microchannel mold using a commercial system (Labcoater2, *Special Coating System*). One of the samples was diced after the parylene deposition to observe the coating uniformity. Figure 6-8 shows SEM images of the cross-section of a parylene-

coated silicon microchannel. Although the parylene coating at the diced plane was delaminated and deformed by the shear force, the overall parylene coating on silicon channel was uniform. After the first parylene deposition, a 1 μm thick platinum film was sputtered on the parylene layer using CVC DC sputterer (pressure ~ 8.7×10^{-4} Pa, power ~ 25% of 1500 W supply max.). Platinum was chosen because it is KOH compatible. Finally another 5 μm thick parylene layer is deposited on the platinum layer.
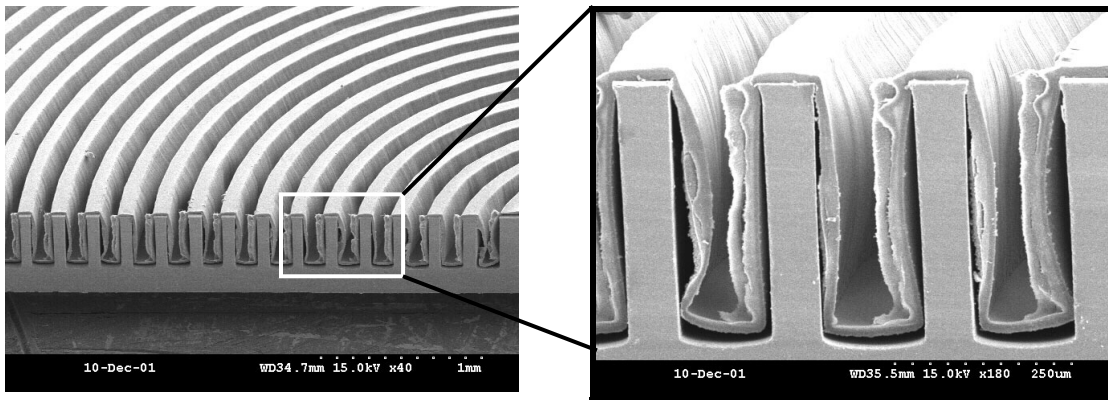

Figure 6-8 SEM images of a parylene-coated silicon microchannel.

Will the parylene coating reduce the surface roughness of a deep RIE silicon microchannel? Figure 6-9 shows the surface roughness change by parylene deposition. Two different surface patterns (Figure 6-9 (b) and (c)) were observed on the parylene surface. According to Figure 6-9 (b), parylene deposition basically copied the roughness of its mold but at least the horizontal scallop pattern was not observed anymore. In other words, the overall roughness could be reduced because parylene coating (~ 10 μm) was much thicker than the roughness of silicon channel. However, according to Figure 6-9 (c), parylene does not seem to just copy the silicon surface. The surface pattern was convex and smooth while the surface of silicon channel was concave and sharp. The exact reason for this change was not investigated thoroughly but the surface roughness seems to affect

the polymerization process of parylene. Again, horizontal scallop pattern was not observed, either.
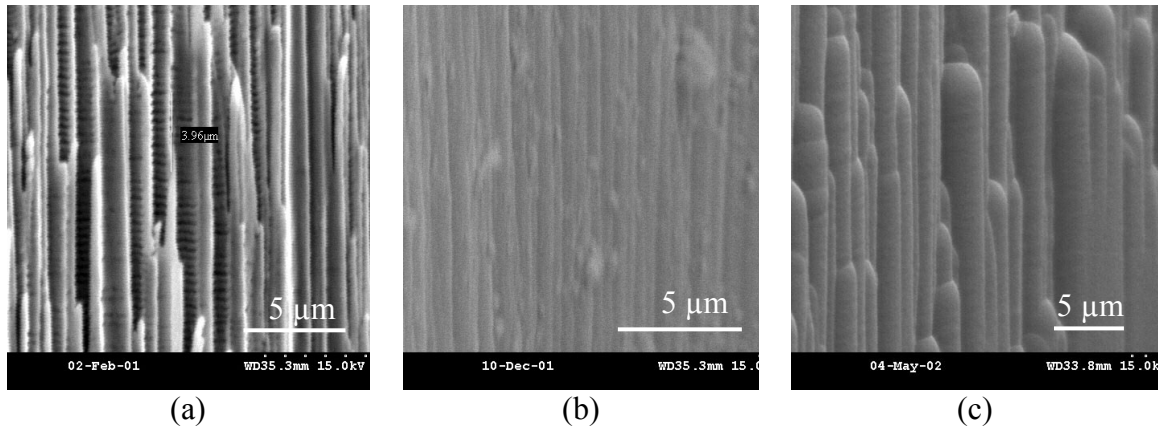

Figure 6-9. Surface roughness change by parylene deposition (a) the roughness of deep RIE silicon channel, (b) and (c) two different surface patterns on parylene coating.

In order to investigate the planarization effect of parylene deposition, simple grid patterns were generated by photoresist as shown below. Surface profile was scanned by a profilometer before and after parylene deposition (10 µm). The PR pattern width (d) and gap (g) were varied from 10 to 20 µm and the PR thickness (t) was fixed at approximately 1 µm.
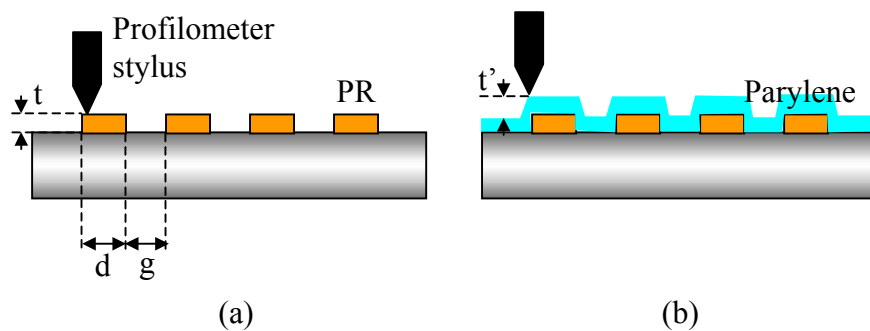

Figure 6-10. Test for the planarization effect of parylene deposition; (a) before parylene deposition, (b) after parylene deposition.

Figure 6-11 shows the results of the planarization test. When the pattern width

and gap were bigger than 15 μm, the profile of parylene-coated surface was almost same

as that of PR pattern and t' was also same as t. But when the pattern width and gap were

10 μm each, the profile of parylene-coated surface was changed and t' was smaller than t

indicating the reduced surface roughness. Since the surface roughness of silicon channel

is smaller than 10 μm, it is considered that some amount of surface planarization occurs.

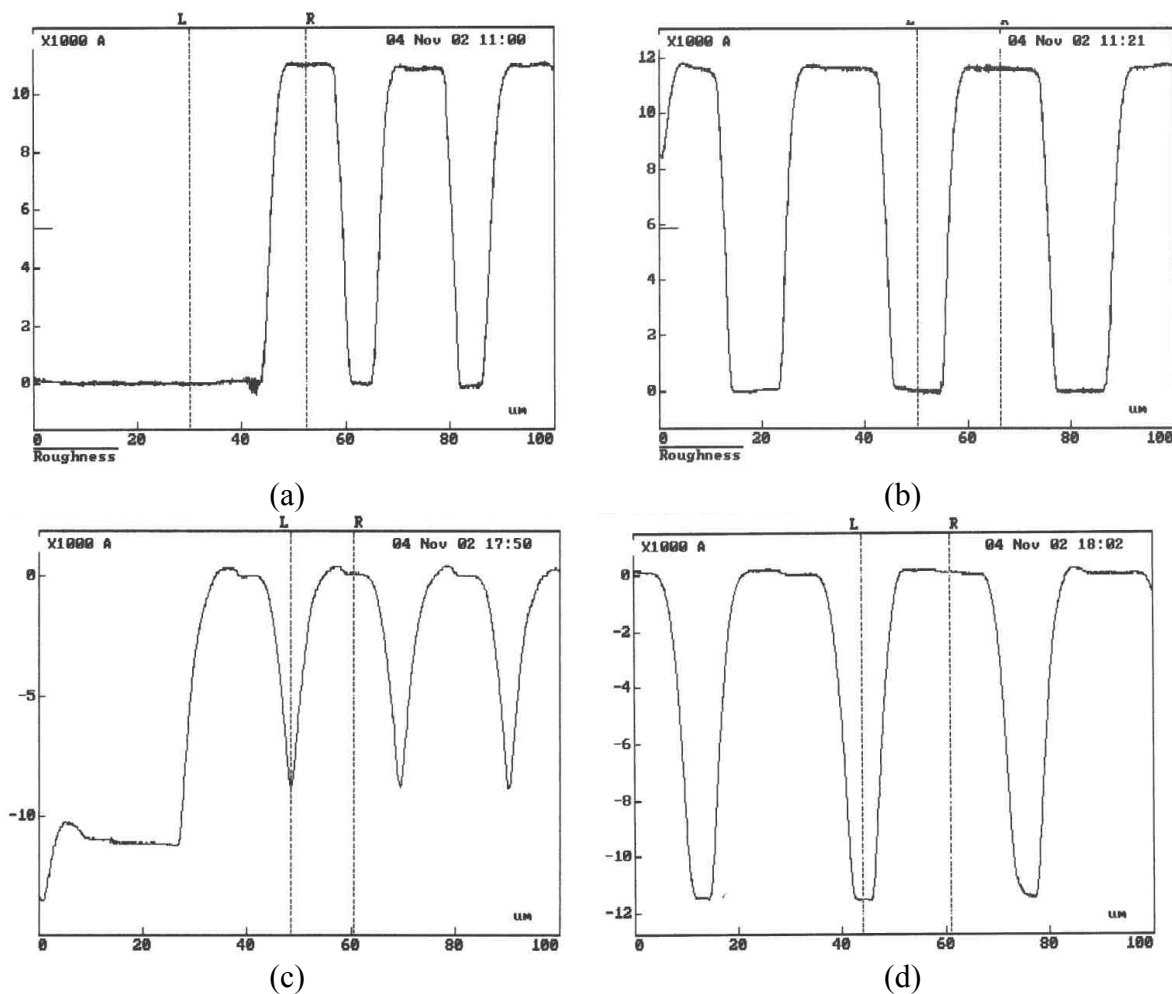**Figure 6-11. Surface profile before and after parylene deposition (a) before parylene deposition (d = g = 10 μm), (b) before parylene deposition (d = g = 15 μm), (c) after parylene deposition (d = g = 10 μm), (d) after parylene deposition (d = g = 15 μm).**

Another thing that needed to be investigated was the uniformity of platinum layer deposited by DC sputtering. A silicon microchannel was deposited with approximately 1 µm platinum layer using DC sputter. This is then diced to see the cross section of the channel. Figure 6-12 is the SEM images of the cross section of a Pt-deposited silicon channel. There was a quite big deviation in the Pt thickness. The minimum thickness observed at the bottom of the channel was 0.5 µm and the maximum thickness observed at the top corner of the channel was about 2.1 µm.
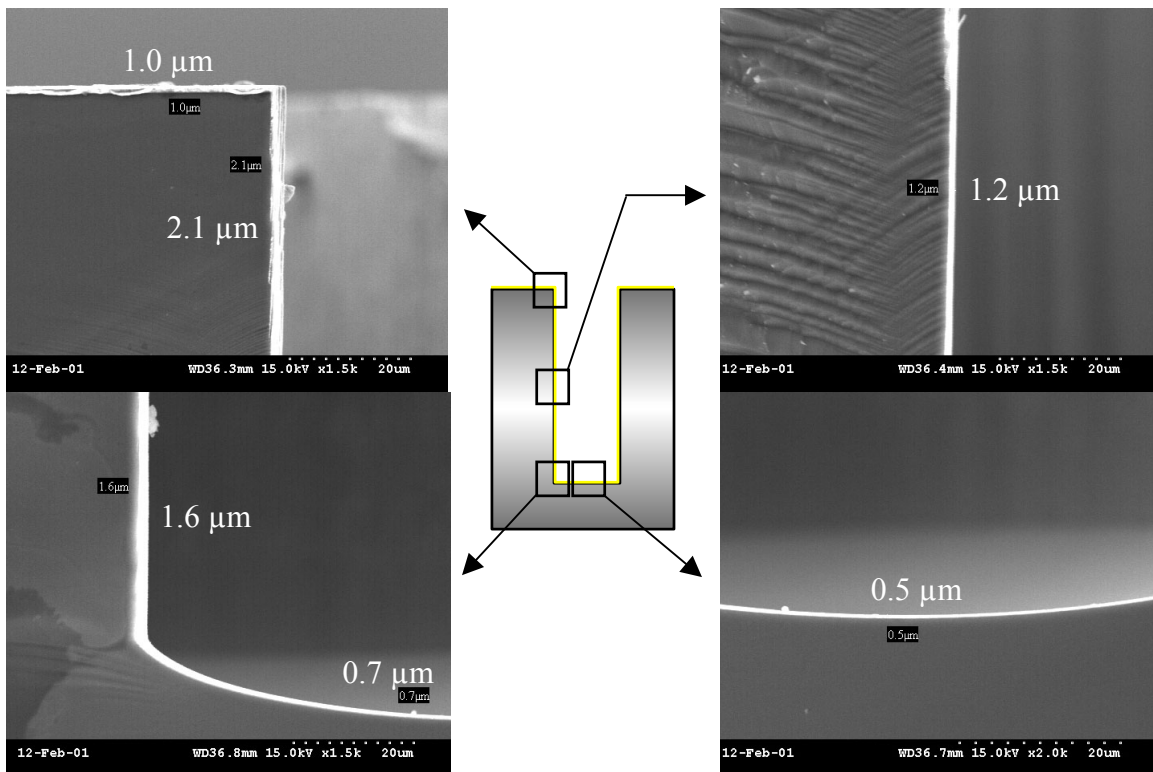

Figure 6-12. The uniformity of a sputtered platinum layer on a rectangular silicon channel (100 µm wide, 300 µm deep).

6.4 THERMAL LAMINATION AND RELEASE

After parylene deposition, the next step is parylene/parylene thermal lamination. The parylene-coated silicon channel was put together with a parylene-coated pyrex glass substrate in a compression apparatus as discussed in chapter 5. The torque used for each screw was 2.4 N·m and this is equivalent to a pressure of 6.2 MPa. Either vacuum oven or microwave oven was used for heating. For both ovens, the samples were heated to 200 ^{o}C for 2 hrs followed by slow cooling. Once the bonding is achieved, the silicon microchannel is dissolved in a KOH solution. Since the silicon microchannels used here had a high aspect ratio, parylene column could not be released without sacrificing the silicon channel. The wet etching condition was 20% KOH, 5 hrs at 80 ^{o}C. Parylene column was usually released before the silicon channel was completely dissolved. And the pyrex substrate was separated during the KOH etching. Figure 6-13 shows a free-standing parylene column .
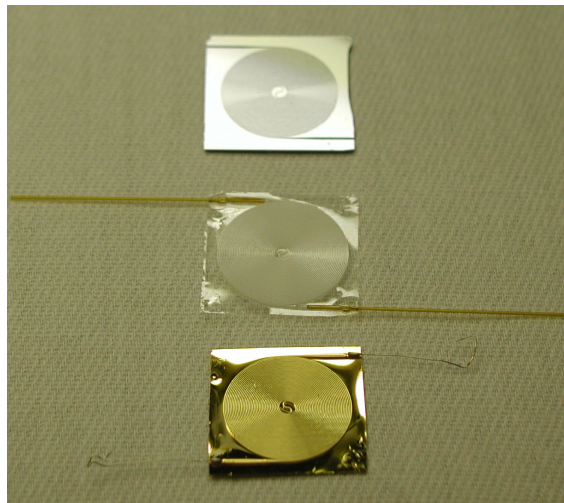

Figure 6-13. Silicon microchannel mold and parylene GC columns.

6.5 HEATING ELEMENT

After a parylene column is released from the silicon channel, a thin gold film is evaporated on the corrugated surface of the free-standing parylene column using a CVC electron beam evaporator. The gold thin film coated on top of a parylene column is the heating element of a parylene column. The resistance of the 1 m long gold film depends on its thickness. However, it was found that if more than a 0.2 μm thickness of gold is deposited, the wall of the parylene column can also be slightly coated with gold, resulting in a short circuit. In order to avoid this problem, 0.15 μm of gold was deposited. The deposition rate and thickness were measured with a quartz crystal microbalance that is installed in the evaporator.
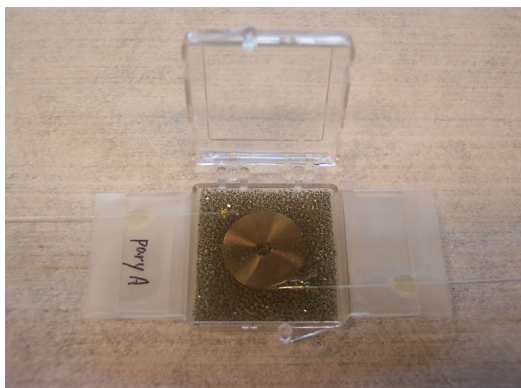
6.6 STATIONARY PHASE COATING

Three different methods were tried for stationary phase coating. Two of them were dry coating techniques and the other was conventional injection coating technique. The first method was depositing fluorocarbon using PECVD technique. The deposition technique was described in detail in the previous chapter. The film deposition on parylene was good but the problem was with the following thermal lamination. The thermal lamination of two fluorocarbon-coated parylene layers was tried with both vacuum oven and microwave oven. Vacuum oven heating did not work very well so that the sample was delaminated easily. On the contrary the sample laminated by microwave oven

heating showed good bonding quality. Three prototypes have been made but unfortunately all of them showed leakage when water was injected through them. The second method was parylene-A deposition. This was the easiest way of depositing stationary phase. Thermal lamination was also successful. Parylene GC columns with parylene-A coating (228 nm thick) were successfully fabricated. GC analysis was performed with the columns and the results will be discussed in the next chapter. The last method was conventional injection coating technique. The solution that consists of 2 g OV-1 and 100 ml toluene was used and the injection flow rate was 0.01 SCCM. During the injection some leaking points were found around the tubing area. This was mended by applying more epoxy resin on them. The solution was purged out using GC injection module.

6.7 Tubing and Packaging

Both ends of a parylene GC columns are punched by a sharpened metal needle and polyimide-coated silica microtubes (OD ~ 350 μm, ID ~ 100 μm square, *Polymicro*, Phoenix, AZ) are inserted into the ends of the parylene column. These areas are then sealed with an epoxy adhesive. To supply power to the heating element, gold wires are attached to both column ends using conductive epoxy resin (Loctite 3880, *Loctite*, Rocky Hill, CT). A plastic box was used to package the completed parylene columns. Polystyrene foams were put in the plastic box and then a parylene column is placed on it as shown in Figure 6-14.
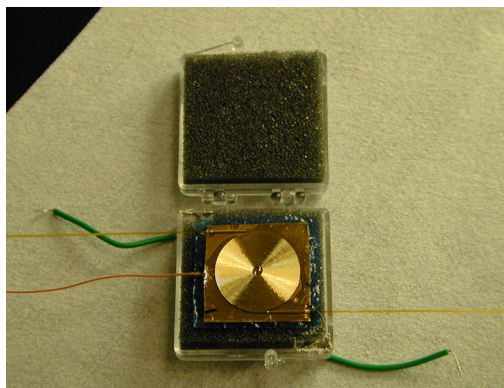
(a)   (b)

Figure 6-14. Packaged parylene columns (a) parylene column with parylene-A stationary phase, (b) parylene column with integrated heater.

CHAPTER 7

TESTING AND EVALUATION

This chapter describes testing and evaluation of the parylene GC column prototypes. The pressure drop versus flow rate relationship for nitrogen was measured and compared with the analytical result. The thermal cycling of a parylene column by an embedded heater was investigated and compared with ANSYS lump model. Most of all, the GC performance of the parylene columns was thoroughly investigated and compared with theoretical performance. The separation of some chemical mixtures is demonstrated.

7.1 PRESSURE DROP VERSUS FLOW RATE

The pressure drop versus volumetric flow rate relationship for a rectangular channel (width = d, height = h, and length = L) is expressed as below if the flow is incompressible.

$$Q = \frac{h^3 d}{12\mu L} \cdot (1 - \frac{192}{\pi^5} \frac{h}{d} \sum_{i=1,3,5,\ldots}^{\infty} \frac{\tanh(i\pi \cdot d / 2h)}{i^5}) \cdot \Delta P$$

Equation 7-1

If the flow is compressible, the formula can be modified as below.

$$Q = \frac{h^3 d}{24\mu L} \cdot (1 - \frac{192}{\pi^5} \frac{h}{d} \sum_{i=1,3,5,...}^{\infty} \frac{\tanh(i\pi \cdot d/2h)}{i^5}) \cdot \frac{(P_i^2 - P_o^2)}{P_o}$$

Equation 7-2

The pressure drop across a parylene microcolumn was measured at different flow

rates using dry nitrogen gas. A differential pressure sensor (max. ~ 133.32 GPa, *MKS*

Instruments, MA) and a flow controller (max. ~ 1 SCCM, *MKS Instruments*, MA) were

used for this measurement. Insulin syringe needles (ID = 165 μm) were inserted into the

inlet and outlet of a parylene column and sealed with epoxy as shown in Figure 7-1 (a).

This sample was connected to a pressure sensor and a flow controller as shown in Figure

7-1 (b).

(a)   (b)

Figure 7-1. Experimental setup for the flow test of a parylene column (a) prepared sample, (b) flow test setup.

Figure 7-2 shows the flow test result for a parylene column (width = 90 μm, heigh

= 350 μm , length = 1 m). The measured values showed a better agreement with the

analytical model for a compressible flow. In this experiment, the pressure range was

comparatively low because of the limitation of the flow controller. If the same

experiment is performed for higher pressure range the deviation of the result from the incompressible model will become larger.
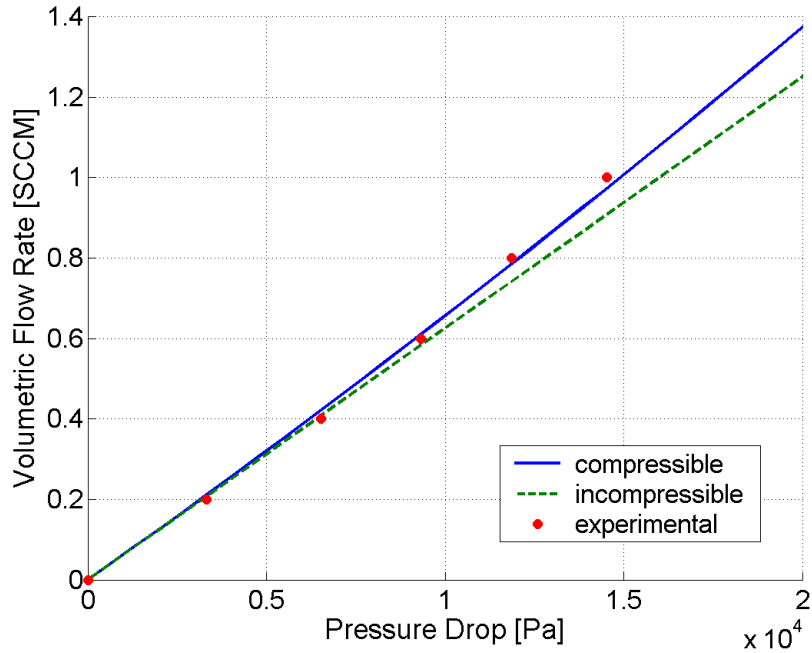

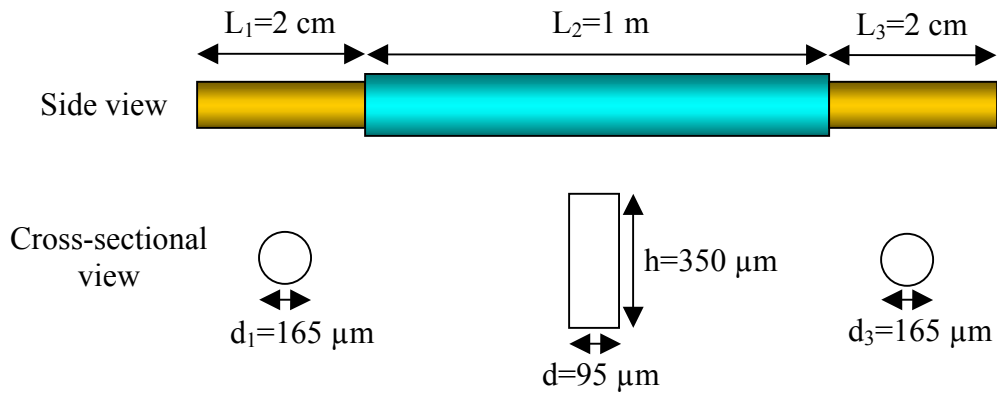**Figure 7-2. The calculated and measured pressure drop versus volumetric flow rate relation.**

Figure 7-3. Schematic of a parylene column with side tubing.

Can we neglect the effect of the side tubing on the above result? The sample used in the flow test had side tubing as shown in Figure 7-3. While the parylene column was a rectangular column, the syringe needles that were inserted into the inlet/outlet of a

193

parylene column were circular. All the dimensions are shown in Figure 7-3. How can we express the pressure drop versus flow rate relation for the sample that consists of three channels in series? The volumetric flow rate should be constant if the flow is assumed to be incompressible. Therefore the volumetric flow rate can be written as below if the local pressure drops at each tube is expressed as ΔP_1, ΔP_2, and ΔP_3. If we consider compressibility, solving this problem becomes extremely difficult.

$$Q = \frac{\pi d_1^4}{128 \mu L_1} \cdot \Delta P_1 = \frac{h^3 d}{12 \mu L_2} \cdot (1 - \frac{192}{\pi^5} \frac{h}{d} \sum_{i=1,3,5,...}^{\infty} \frac{\tanh(i\pi \cdot d/2h)}{i^5}) \cdot \Delta P_2 = \frac{\pi d_3^4}{128 \mu L_3} \cdot \Delta P_3$$

Equation 7-3

Since the total pressure drop (ΔP) is the sum of the local pressure drops, Equation 7-3 can be rearranged as below.

$$\Delta P = \left(\frac{128 \mu L_1}{\pi d_1^4} + \frac{12 \mu L_2}{h^3 d \cdot (1 - \frac{192}{\pi^5} \frac{h}{d} \sum_{i=1,3,5,...}^{\infty} \frac{\tanh(i\pi \cdot d/2h)}{i^5})} + \frac{128 \mu L_3}{\pi d_3^4} \right) \cdot Q$$

Equation 7-4

For the given dimensions, the first and third term in the right side is about 2% of the second term, respectively. Therefore, the pressure drop due to side tubing can be neglected in this case.

7.2 THERMAL CYCLING

The steady-state temperatures of a parylene column were measured varying the voltage applied to the heating element. A power supply (PS2520G, *Tektronics*, Beaverton, OR) was used to apply voltage to the gold heating element of a parylene column. The gold heating element was approximately 110 μm wide, 0.15 μm thick, and 1 m long. An infrared (IR) camera (thermaCAM PM190, *Inframetrics*, Portland, OR) was used to measure the surface temperature of a parylene column. Figure 7-4 shows the IR camera images of a parylene column with 30 V DC applied. The total hemispherical emissivity of parylene C is known as 0.34 (http://www.electro-optical.com/bb_rad/emissivity/matlemisivty.htm). The steady-state temperature with 30 V was 133.9 ^{o}C. The measured current at 30 V was 3 mA. Therefore, the actual power applied to the heater was about 90 mW. Figure 7-5 is the temperature profile across the column and Figure 7-6 shows the steady-state temperatures with different applied powers measured with IR camera. At each voltage, it was observed that parylene column reached the steady-state temperature within 30 sec. The cooling time was also within 30 sec when the power was turned off. This suggested that the parylene column has a rapid thermal cycling characteristic as designed.
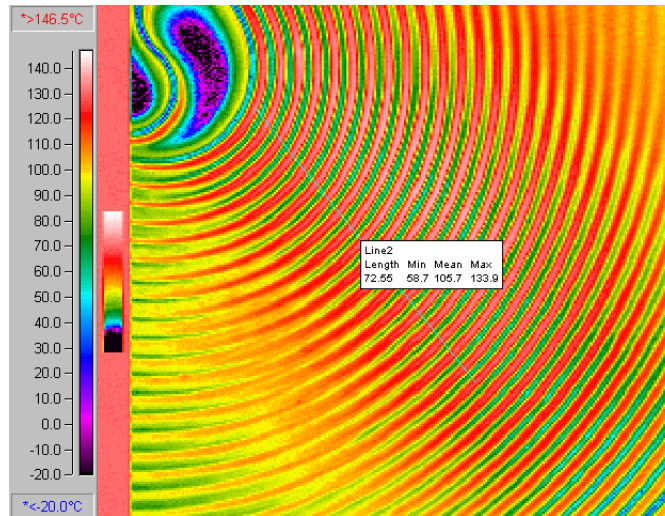
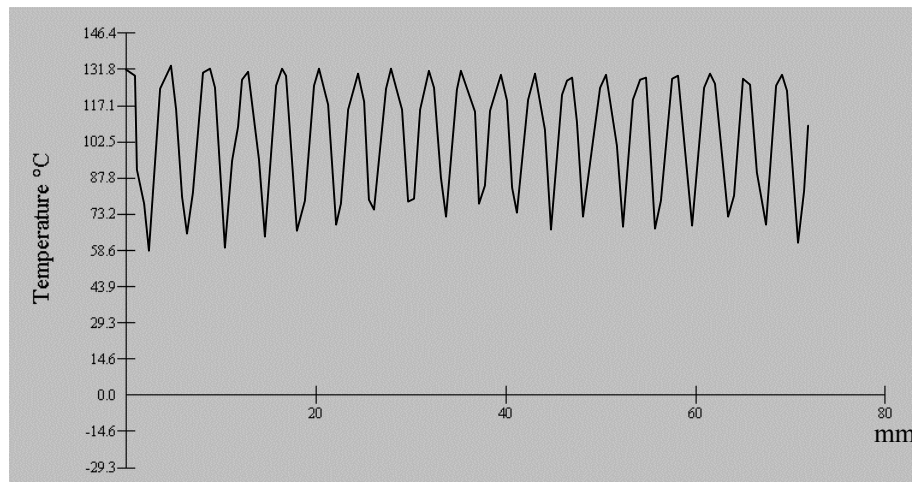**Figure 7-4 IR image of a parylene column with 90 mW applied.**

Figure 7-5 temperature profile across a parylene column with 90 mW.
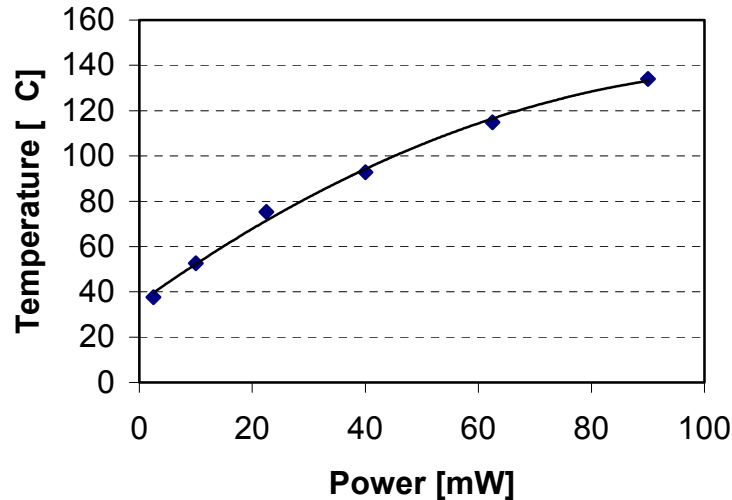
Figure 7-6 Steady-state temperatures with different applied power.

A lump type analysis was performed for the heating of a parylene column. Figure 7-7 shows a parylene column with embedded heating element, a cross section of a channel, and a lump composite model equivalent to the parylene column. The density and specific heat of the composite model were assumed to be same as those of parylene because the masses of air and gold were negligible compared to parylene. Conduction coefficient was calculated using area ratio. The thickness of the composite was also calculated using the given density and mass data. The geometry and material properties of the composite model are listed in Table 7-1.

This lump composite model was used in ANSYS heat transfer analysis. The natural convection coefficient for the top surface was assumed to be in the range of $1 \sim 4$ W/m^2·K. The convection coefficient for the bottom surface was fixed at 0.1 W/m^2·K and the convection coefficient for the side was neglected in this analysis. Figure 7-8 compares the result of ANSYS lump model with the measured temperature of the parylene column.
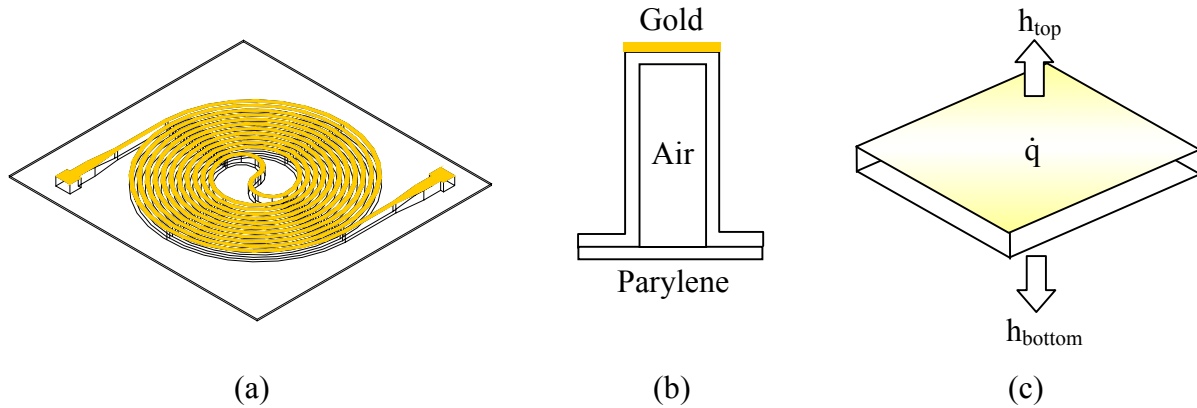
Figure 7-7. A lump composite model for a parylene column, (a) parylene column with embedded heater, (b) cross section of the parylene column, (c) a lump composite model.

Table 7-1. Geometry and material properties for a lump composite model.

Dimension	Density	Specific heat	Cond. Coeff.	Conv. coeff. (top)	Conv. coeff. (bottom)	Conv. coeff. (side)
2 cm x 2 cm x 78 µm	1289 kg/m3	714 J/kg·K	19.0 W/m·K	$1 \sim 4$ W/m^2·K	0.1 W/m^2·K	Negligible

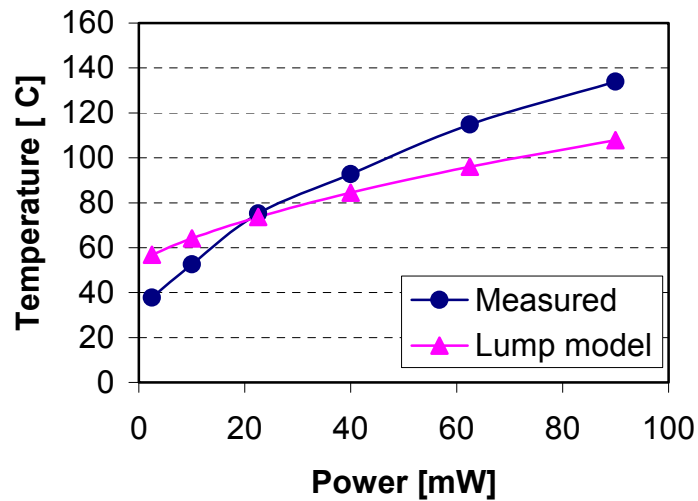**Figure 7-8. Measured temperature and the result from a lump model for h = 4 W/m^2·K.**

198

7.3 GC ANALYSIS

A conventional GC system (HP6850, *Agilent Technologies*, Palo Alto, CA) was used to investigate the GC performance of parylene columns. The GC system had a split/splitless injector and flame ionization detector (FID). Helium was used as a carrier gas. Compressed air and hydrogen were used as a fuel gas for FID detector. The GC system is shown in Figure 7-9 (a) and (b). Figure 7-9 (c) and (d) show how a fused-silica columns and a parylene column were installed in the GC system for analysis. Initially, the GC system had a 30 m long fused-silica column (HP-1, *Agilent Technologies*, Palo Alto, CA). The conventional column was cut into short columns (3 m and 1 m) and installed in the GC system for GC analysis. The GC data obtained by the short conventional columns were later compared to parylene column data.

Figure 7-10 compares a conventional column and a parylene column. The columns tested in this research are listed in Table 7-2. These include conventional columns with different lengths (30, 15, 3, 1 m), silica tubes with and without stationary phase, and three parylene column prototypes. Three parylene column prototypes have the same dimension but different stationary phase. Prototype 1 has no stationary phase. Prototype 2 has uniform parylene-A coating in the column. Prototype 3 has OV-1 (PDMS) coating in the column. OV-1 was coated by injection method.
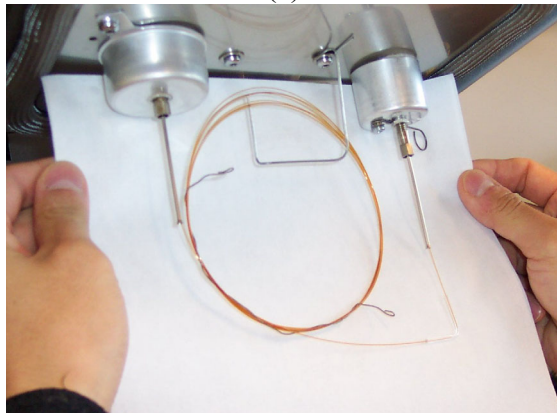
The organic chemicals used in this research are listed in Table 7-3. These include aliphatic and aromatic chemicals, solvents, and hydrocarbons. Table 7-3 includes the structural formula, distribution constant, and boiling point of the chemicals.
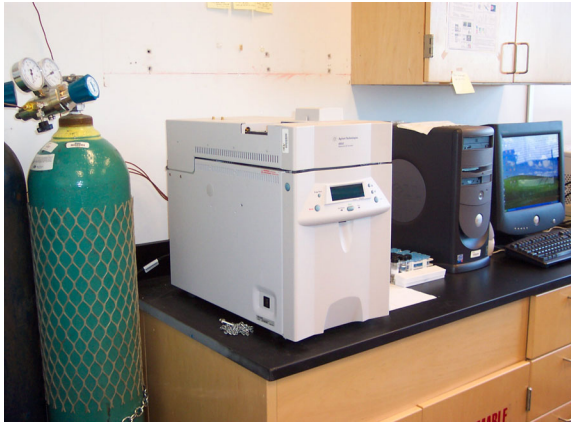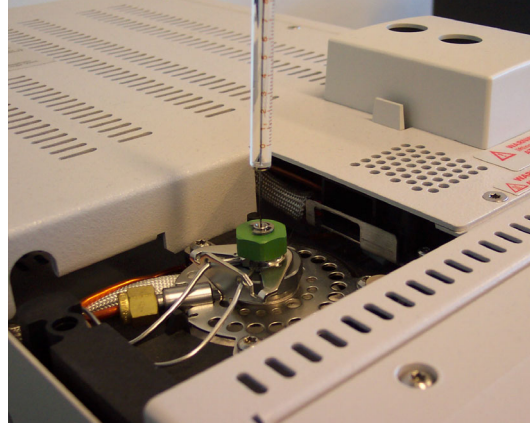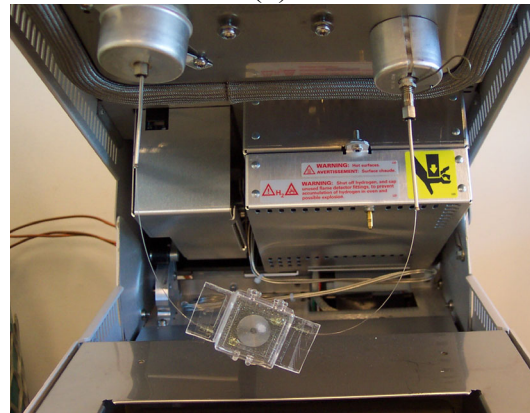
Figure 7-9. GC setup for column performance test; (a) HP6850, (b) inlet and detector, (c) installed fused silica column, (d) installed parylene column.
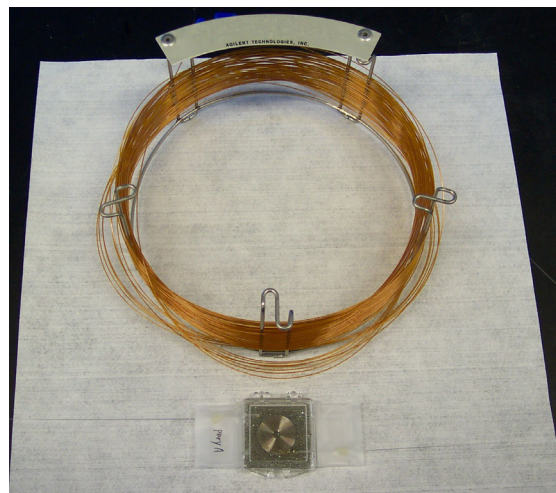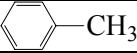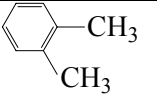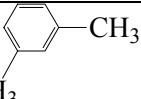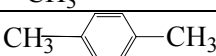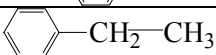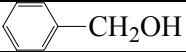

Figure 7-10. Conventional fused-silica column and parylene column.

200

Table 7-2. Columns tested in GC system.

Column Type	Dimension	Stationary Phase	Additional Tubing
Commercial fused-silica columns			
HP-1 (30 m)	ID 320 μm x 30 m	Polydimethylsiloxane, 250 nm	No
HP-1 (15 m)	ID 320 μm x 15 m	Polydimethylsiloxane, 250 nm	No
HP-1 (3 m)	ID 320 μm x 3 m	Polydimethylsiloxane, 250 nm	Yes/No
HP-1 (1 m)	ID 320 μm x 1 m	Polydimethylsiloxane, 250 nm	Yes/No
Fused-silica tubing, 1 m	ID 100 μm x 1 m	OV-1 (PDMS), 37 nm	No
Parylene column			
Prototype1	86 μm x 260 μm x 1 m	No stationary phase	Yes
Prototype2	86 μm x 260 μm x 1 m	Parylene A, 228 nm	Yes
Prototype3	86 μm x 260 μm x 1 m	OV-1 (PDMS), thickness unknown	Yes

Table 7-3. Chemicals used in GC analysis.

| Name	Formula	K (@ 50 °C)	Bp (°C)
Pentane	$CH_3-(CH_3)_3-CH_3$		36.1
hexane	$CH_3-(CH_3)_4-CH_3$	96	69
heptane	$CH_3-(CH_3)_5-CH_3$	229	98
octane	$CH_3-(CH_3)_6-CH_3$		126
Nonane	$CH_3-(CH_3)_7-CH_3$		150.8
decane	$CH_3-(CH_3)_8-CH_3$		174.1
dodecane	$CH_3-(CH_3)_{10}-CH_3$		216.3
Tetradecane	$CH_3-(CH_3)_{12}-CH_3$		253.7
Pentadecane	$CH_3-(CH_3)_{13}-CH_3$		270.63
hexadecane	$CH_3-(CH_3)_{14}-CH_3$		287
benzene		161	80
toluene	$-CH_3$		111
o-xylene	$-CH_3$ CH_3		144
m-xylene	$-CH_3$ CH_3		139
p-xylene	CH_3- $-CH_3$		138
ethylbenzene	$-CH_2-CH_3$		135
acetone	$CH_3-\overset{\overset{O}{\|\|}}{C}-CH_3$		57
Methanol	CH_3-OH		65
Ethanol	C_2H_5-OH		79
2-propanol	$CH_3-CH3OH-CH_3$		82
2-butanol	$CH_3-CH-CH_2OH$ CH_3		100
2-methoxy ethanol	$H_3C-O-CH_2CH_2OH$		124.6
Benzyl alcohol	$-CH_2OH$		205
Dimethylformamide (DMF)	$HC-N(CH_3)_2$ $\overset{O}{\|\|}$		153
Acetonitrile	$CH_3-C\equiv N$		81.6
Diethyl ether	$C_2H_5-O-C_2H_5$		34.6
Tetrahydrofuran (THF)			66

7.3.1 COMMERCIAL FUSED-SILICA COLUMN

It is important to know the performance of the commercial GC column before testing and evaluating the parylene columns. Figure 7-11 and Figure 7-12 shows the chromatograms of hydrocarbon mixture and solvent mixture obtained by 30 m long HP-1 and 1 m long HP-1 columns, respectively. For 30 m long column, the injected sample amount was 1µl and the split ratio was 50:1. The inlet pressure was fixed at 10 psi and the analysis temperature was 50 °C isothermal. For 1 m long column, the injected sample amount was 0.5µl and the split raio was 50:1. The inlet pressure was fixed at 0.5 psi and the analysis temperature was 50 °C isothermal.

The hydrocarbon mixture (C5-C7) was completely separated with a 30 m long column but with a 1 m long column, the peaks for pentane and hexane were not completely separated from the methanol peak. Almost all solvents were nicely separated with the 30 m long column, but with the 1 m long column, most solvent was not separated. This poor separation performance can be quantified by considering retention time and column efficiency. In Chapter 3, the formulas to calculate the theoretical retention time and column efficiency were introduced. Using the formulas, the theoretical performance of the 30 m long and 1 m long HP-1 column was calculated. Also, using the chromatogram obtained from GC analysis, the actual retention time and column efficiency were calculated (Table 7-4). Heptane peak was used for this calculation.

Table 7-4. Theoretical and actual performance of commercial columns.

Column	Theoretical Performance		Actual Performance	
30 m HP-1	t_R = 86.5 sec	N = 135,140	t_R = 91.0 sec	N = 107,000
1 m HP-1	t_R = 3.23 sec	N = 4,293	t_R = 4.63 sec	N = 181
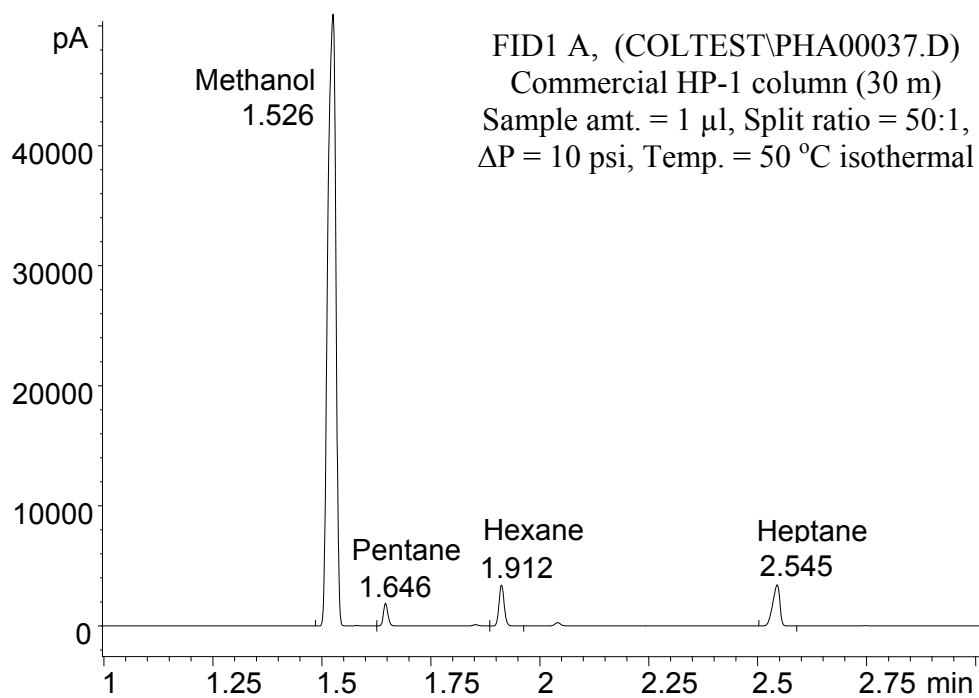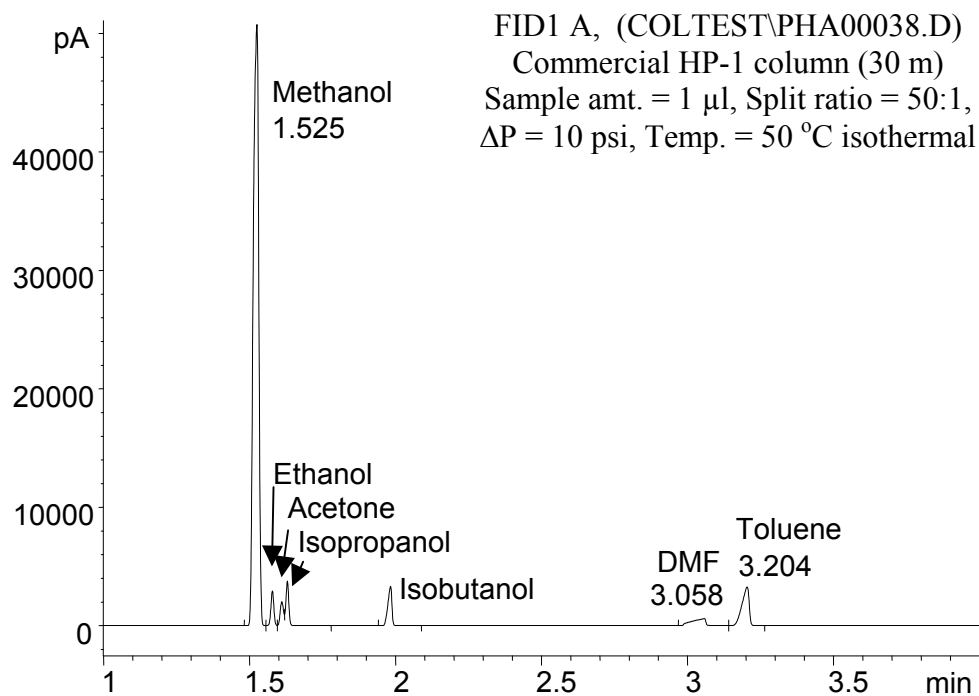
Figure 7-11. Chromatograms by 30 m long HP-1 column; (a) hydrocarbon mixture (C5-C7), (b) solvent mixture (methanol, ethanol, acetone, propanol, butanol, DMF, toluene).

Figure 7-12. Chromatograms by 1 m long HP-1 column; (a) hydrocarbon mixture (C5-C7), (b) solvent mixture (methanol, ethanol, acetone, propanol, butanol, DMF, toluene).

205

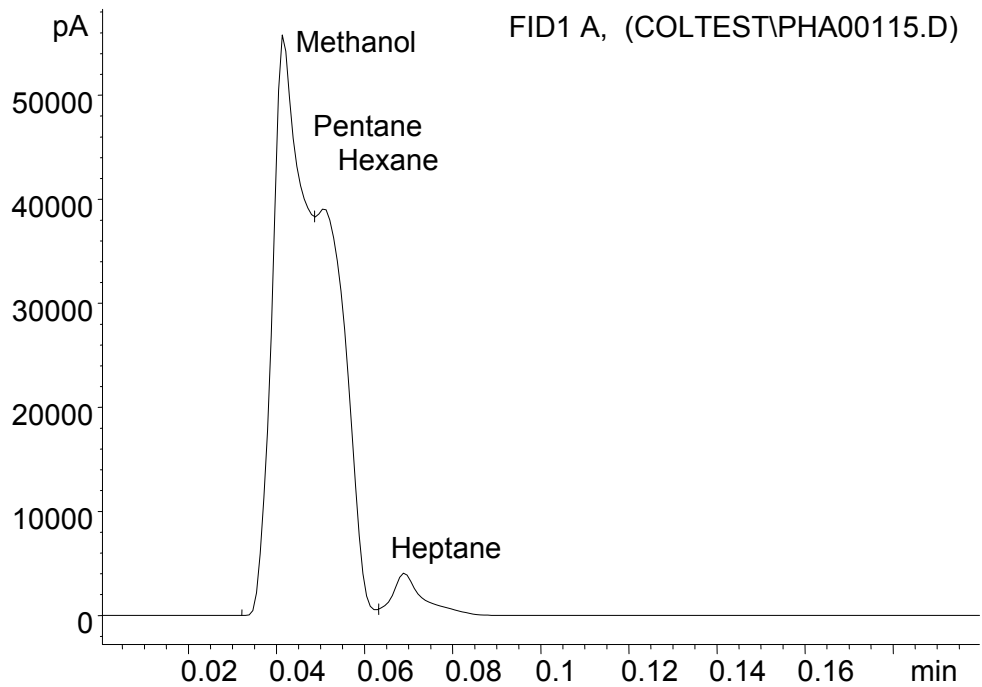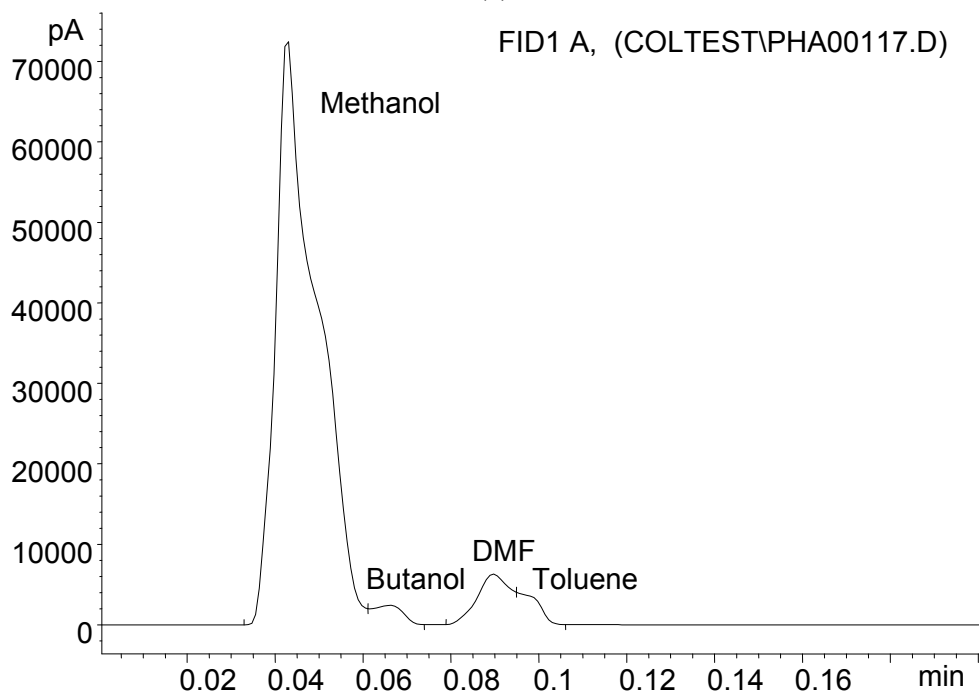## 7.3.2 PARYLENE COLUMN

7.3.2.1 RETENTION TIME

In the flow test described in the previous section, syringe needles were used as interfacing media and their effect on pressure-drop and flow rate relation was found to be negligible. In GC analysis, silica microtubes had to be used instead to interface the parylene column with a conventional GC. Because the inner dimension (ID = 100 μm) of the side tubing is smaller than parylene column and the length is fairly long (L_1 = 15.5 cm, L_3 = 19.5 cm), the pressure drop at the side tubing is not negligible any longer. From Equation 7-4, the volumetric flow rate can be expressed as below.

$$Q = \left(\frac{128\mu L_1}{\pi d_1^4} + \frac{12\mu L_2}{h^3 d \cdot (1 - \frac{192}{\pi^5}\frac{h}{d} \sum_{i=1,3,5,...}^{\infty} \frac{\tanh(i\pi \cdot d/2h)}{i^5})} + \frac{128\mu L_3}{\pi d_3^4} \right)^{-1} \cdot \Delta P$$

Equation 7-5

Although the volumetric flow rate is constant at any location if the flow is assumed to be incompressible, the flow velocity will change depending on column dimension. These local flow velocities can be calculated using the following equation.

$$Q = V_1 \cdot A_1 = V_2 \cdot A_2 = V_3 \cdot A_3$$

Equation 7-6

where V_1, V_2, V_3 are local velocities at each tubes (side tubing 1, parylene column, and side tubing 2) and A_1, A_2, A_3 are the cross sectional areas of each tubes. Using the local

velocities, the retention time (t_R) of GC analysis can be calculated according to the equation below.

$$t_R = \frac{L_1}{V_1} + \frac{L_2}{V_2} \cdot (1+k) + \frac{L_3}{V_3}$$

Equation 7-7

where the retention factor (k) is a function of distribution constant (K) and the dimension of the column discussed in Chapter 3. This equation is valid when the side tubing does not have stationary phase coating. If the side tubing also has stationary phase, this equation must be modified into:

$$t_R = \frac{L_1}{V_1} \cdot (1+k_1) + \frac{L_2}{V_2} \cdot (1+k_2) + \frac{L_3}{V_3} \cdot (1+k_3)$$

Equation 7-8

where k_1, k_2, and k_3 are the retention factor of an analyte in each tube. If there is no stationary phase in the column and side tubing, k value becomes zero and the dead time (t_M) is obtained using the above equation. This is the time required for a non-retained analyte to travel through the column.

$$t_M = \frac{L_1}{V_1} + \frac{L_2}{V_2} + \frac{L_3}{V_3}$$

Equation 7-9

The retention time of hexane was measured using the three parylene column prototypes listed in Table 7-2. Hexane was selected because its distribution constant in PDMS stationary phase (K = 69) is known. The sample amount was 0.2 μl and the pressure-drop was 5 psi. The split ratio was 1000:1.

Figure 7-13 and Figure 7-14 show the chromatogram obtained using the three

prototypes. The measured retention time was 0.074 min (4.44 sec), 0.077 min (4.62 sec)

and 0.110 min (6.6 sec). Table 7-5 compares the calculated and measured retention time

of hexane for the three prototypes. For the parylene column without stationary phase

(Prototype 1), the calculated retention time was 3.4 sec and the measured retention time

was 4.44 sec. The difference between these two values may be due to the errors in

column dimension (especially column height and length) and/or the minor head losses by

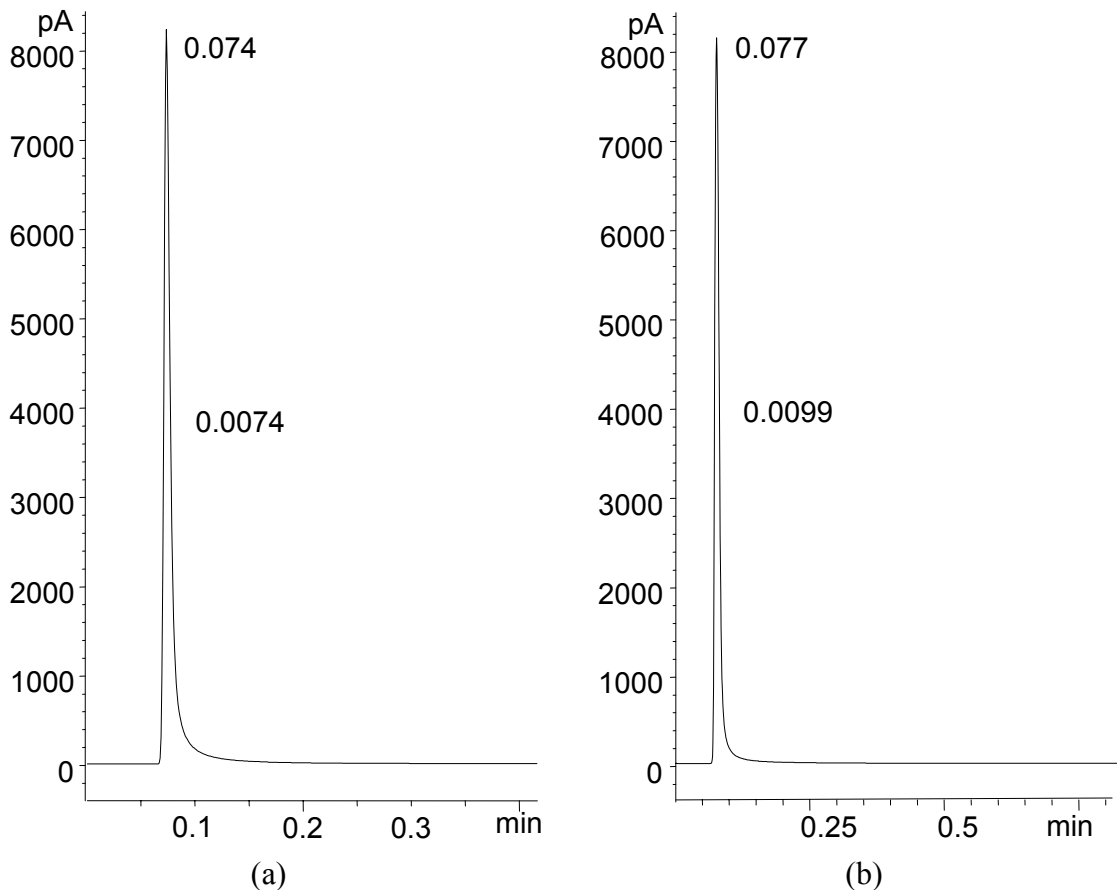the joint area between the parylene column and silica tube.

Figure 7-13 Chromatogram of hexane using (a) parylene column without stationary phase, (b) parylene column with parylene-A coating.

Table 7-5 Retention time of hexane using parylene columns.

Parylene Column	Stationary Phase	Calculated t_R	Measured t_R
Prototype 1	None	3.40 sec	4.44 sec
Prototype 2	Parylene A	18.59 sec	4.62 sec
Prototype 3	PDMS	N/A	6.60 sec

For the parylene column with parylene-A stationary phase (prototype 2), there was a large difference between the calculated and the measured retention time. Since there was no distribution constant (K) found in the literature for parylene-A and hexane system, the distribution constant (K = 713) calculated from the QCM test result was used for this calculation. According to this calculation, hexane was supposed to have a large retention time but the measured value was almost same as the value obtained from prototype 1. This means that parylene-A does not retain hexane effectively. In other words, the distribution constant for parylene-A and hexane system is very small. Then why did we obtain a large distribution constant from the QCM test? This can be understood when we consider the difference in experimental conditions between QCM and GC analysis. In QCM, we allowed 25 min for the absorption of solute vapors but in GC analysis, solute vapors are swiftly swept by carrier gas and does not have enough time to be absorbed. Therefore, the transient characteristic of a solute is more important than steady-state characteristic. As a result, the distribution constant calculated from QCM result cannot predict directly the retention behavior of the analyte.

For the parylene column with PDMS stationary phase (prototype 3), the retention time could not be calculated using the above equations because the exact thickness of the stationary phase was not known. Both the thickness and the uniformity of the stationary phase were questionable and there was no way to measure them. However, the existence

of the stationary phase was verified through the GC test. The measured retention time value (6.6 sec) for hexane was larger than the values (4.4 - 4.6 sec) for the other prototypes, indicating that hexane was retained by the stationary phase. This difference in retention time value became more clear when the chemicals having higher distribution constants were used. Although the retention time could not be calculated with the given information, inversely, the stationary phase thickness could be calculated using the measured retention time value. The difficulty in this calculation is in the fact that silica tubing also has the stationary phase whose thickness will be different from that of the main parylene column. To solve this problem, the flow velocity at the tube and column was investigated because the coating thickness is proportional to the flow velocity of the coating solution as explained in Chapter 5. Since the local flow velocity at the side tubing was approximately 3 times of the velocity at the parylene column, the stationary phase thickness in main parylene column was assumed to have one thirds of the coating thickness at the tubes. According to this calculation, the stationary phase thickness in the parylene column is about 240 nm.

Table 7-6 listed the retention times of some chemicals measured by a parylene column with OV-1 stationary phase. Most chemicals showed retention times less than 1 minute while some chemicals such as DMF, dodecane, and benzyl alcohol showed much longer retention times and broadened peak. These chemicals that showed long retention time and broadened peak were the ones that have higher boiling temperatures.

Table 7-6. Measured retention times of chemicals

Chemical	t_R [min]	Chemical	t_R [min]
Methanol	0.095	Benzene	0.148
Ethanol	0.100	2-methoxyethanol	0.154
Propanol	0.105	heptane	0.185
Acetone	0.105	Octane	0.358
Ether	0.105	Nonane	0.817
Acetonitrile	0.107	Decane	1.045
Hexane	0.123	Dimethylformamide (DMF)	-
Butanol	0.132	Dodecane	-
Tetrahydrofuran (THF)	0.138	Benzyl alcohol	-

7.3.2.2 COLUMN EFFICIENCY

Column efficiency can be expressed by the number of theoretical plates (N) or the height equivalent to theoretical plate (H) as explained in chapter 3. Analytical calculation of the number of theoretical plates for a circular or a rectangular column was described in Chapter 3. The formulas for the number of theoretical plates (N) of a circular and a rectangular column are as below:

$$N = \frac{L}{H} = \frac{L}{2\dfrac{D_M}{\bar{u}} + \dfrac{1+6k+11k^2}{24(1+k)^2}\cdot\dfrac{\bar{u}r_o^2}{D_M} + \dfrac{k^3}{6(1+k)^2}\cdot\dfrac{\bar{u}r_o^2}{F^2K^2D_S}}$$

Equation 7-10

$$N = \frac{L}{H} = \frac{L}{\dfrac{2D_M}{\bar{u}} + \dfrac{4(1+9k+\frac{51}{2}k^2)(\frac{d}{2})^2}{105(k+1)^2 D_M}\cdot\bar{u} + \dfrac{2kw^2}{3(k+1)^2 F^2 D_s}(\dfrac{h+d}{h})^2\cdot\bar{u}}$$

Equation 7-11

211

However, in reality, the parylene column cannot be considered as a single column because silica microtubes are always attached to it for the GC test. How does the side tubing affect the column efficiency? When three columns are connected in series, the total number of theoretical plates can be expressed as a sum of the plate number of each tube and column as shown in Equation 7-12.

$$N = N_1 + N_2 + N_3 = \frac{L_1}{H_1} + \frac{L_2}{H_2} + \frac{L_3}{H_3}$$

Equation 7-12

The number of theoretical plates can also be calculated empirically from GC analysis data using the below equation.

$$N = 5.545 \left(\frac{t_R}{W_h} \right)^2$$

Equation 7-13

where t_R is retention time and W_h is the peak width at the half height of the peak. Again, the hexane peak was used for this calculation. Figure 7-14 shows the chromatograms of hexane using parylene column with OV-1 stationary phase (prototype 3). The number of theoretical plates of the parylene column prototypes was calculated using Equation 7-13 and the chromatograms. The results are listed in Table 7-7 with the values from the analytical model.
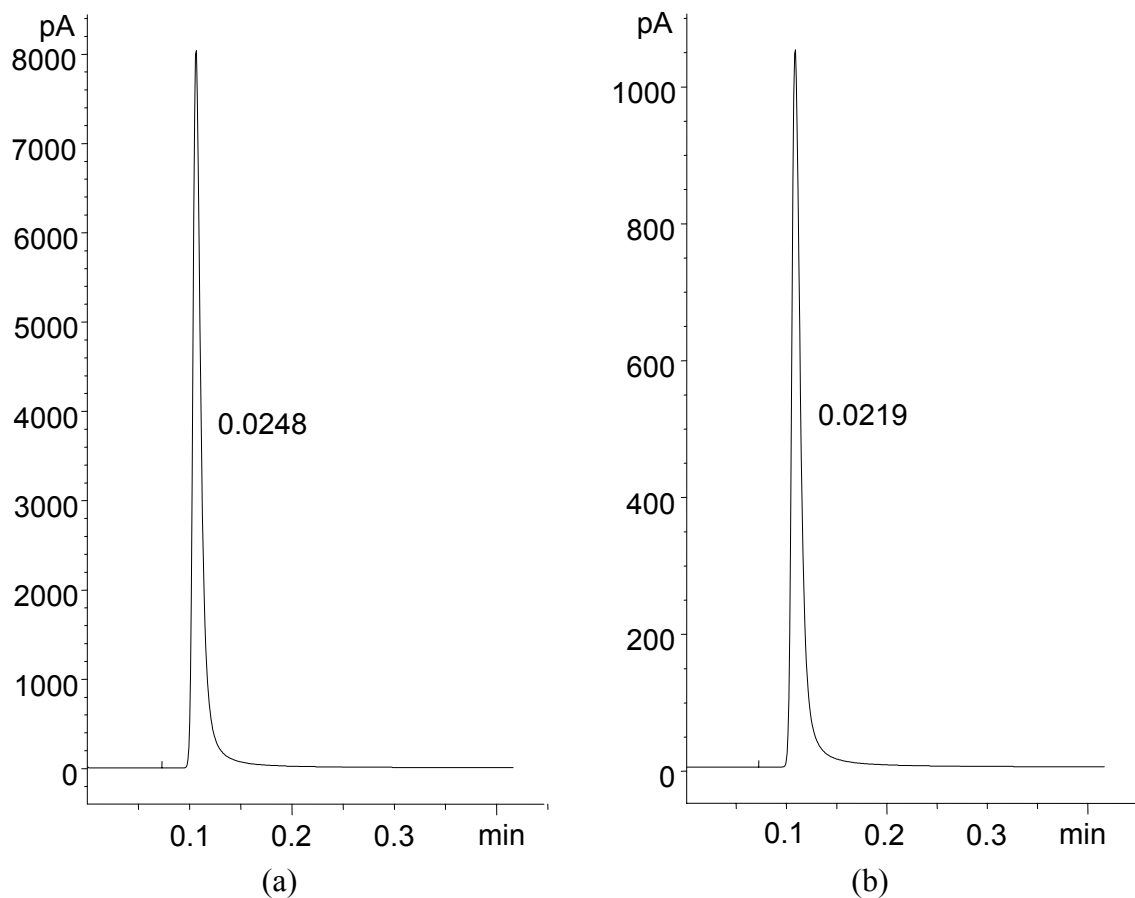
Figure 7-14 Chromatogram of hexane using parylene column with OV-1 coating (a) sample amount ~ 0.2 μl, (b) sample amount ~ 0.02 μl.

Table 7-7 Plate numbers of parylene columns.

Parylene Column	Stationary Phase	N (Analytic Model)	N (Chromatogram)
Prototype 1	None	11,599	554.5
Prototype 2	Parylene A	10,212	335.4
Prototype 3	PDMS	5,024	109.1
Prototype 3	PDMS	5,024	145.3

For all prototypes, the plate numbers calculated from actual chromatograms were much lower (less than 5%) than the values obtained from the analytic models. It is general that the plate number calculated from the actual chromatogram is less than 60%

213

of the value obtained from the analytic model because of imperfect injection skill. However, the actual plate numbers of the parylene column prototypes were lower than expected. Initially, the existence of side tubing was doubted as the main cause for the difference in the plate numbers. However, the contribution of the side tubing for the plate number turned out to be less than 5 % of that of parylene column according to calculation. In addition, the GC test with conventional silica columns revealed that the column efficiency could be enhanced by using smaller size of side tubing. Therefore, the existence of the side tubing should be excluded from the causes for the difference in plate numbers. The possible causes for the big difference in the plate numbers are as follow:

(1) The abrupt dimension change at the joint area between parylene column and silica tubes may cause considerable band broadening.

(2) The analytic model was for a high aspect ratio (>1:4) column but the actual parylene column had a comparatively low aspect ratio (~ 1:3). As a result, the retention effect of the narrower sides could be considerable. In addition, the errors in column dimension (especially column height and length) used in analytic model can be the cause of the difference.

(3) For the prototypes with stationary phase coating (especially, prototype 3), non-uniformity in stationary phase coating could be the cause for the difference. Generally, the corners of a rectangular column have thicker stationary phase than other parts, resulting in band broadening.

7.3.2.3 SEPARATION PERFORMANCE

Separation of two components (A and B) depends on their retention times and the column efficiency. It was explained in Chapter 3 that the resolution of a column could be expressed as below when the peak widths ($W_A = W_B = W$) are assumed to be equal.

$$R_s = \frac{(t_R)_B - (t_R)_A}{W} = \frac{(t_R)_B - (t_R)_A}{(t_R)_B} \times \frac{\sqrt{N}}{4}$$

Equation 7-14

The retention time of each chemicals through parylene column was investigated in the previous section and the retention times through prototype 3 are listed in Table 7-6. The number of theoretical plates was also investigated in the previous section. Using these retention time and plate number values, the resolution can be calculated for any two different components. Some example values for the parylene column with OV-1 stationary phase are listed in Table 7-8. Good separation is achieved when the resolution (R_s) is larger than 1. The chemicals whose retention times are close from each other are difficult to be separated. On the contrary, the chemicals whose retention times are not very close to each other showed a resolution larger than 1.

Table 7-8. Examples of resolutions of two components in parylene column.

Components and Retention Times [min]	Resolution
Methanol ($t_R = 0.095$), propanol ($t_R = 0.105$)	0.29
Methanol ($t_R = 0.095$), hexane ($t_R = 0.123$)	0.69
Methanol ($t_R = 0.095$), benzene ($t_R = 0.148$)	1.08
Methanol ($t_R = 0.095$), heptane ($t_R = 0.185$)	1.47
Methanol ($t_R = 0.095$), octane ($t_R = 0.358$)	2.21
Methanol ($t_R = 0.095$), nonane ($t_R = 0.817$)	2.66

Prototype 1 (no stationary phase)

Most chemicals were not retained by the parylene column without stationary phase. These include pentane, hexane, heptane, methanol, ethanol, propanol, ether, THF, benzene, acetone, and acetonitrile. However, some chemicals such as isobutanol, DMF, 2-methoxyethanol, benzyl alcohol, and dodecane were observed to be retained by the column. Two mixtures of chemicals were prepared. One is the mixture of the unretained chemicals and the other is the mixture of retained chemicals. Figure 7-15 and Figure 7-16 are the chromatograms for the mixtures, respectively. The sample amount was 0.2 μl and the split ratio was 100:1. The inlet pressure was fixed at 5 psi and temperature condition was 50 ^{o}C isothermal. Unretained chemicals were not separated and a single peak was observed. But retained chemicals showed some separation although the peaks were very broad and the resolution was poor. Figure 7-17 shows a chromatogram of a mixture of retained chemicals with temperature programming. The analysis temperature was ramped from 40 ^{o}C to 80 ^{o}C at a ramping speed of 120 ^{o}C/min. The retention time of dodecane was shortened and the resolution was enhanced by using temperature programming. In order to see whether these chemicals show any retention in a silica column, a silica tube (ID = 320 μm, L = 1 m) without stationary phase was installed in the GC system. Figure 7-18 shows the result. Similar retention and band broadening were observed in a silica column. Therefore, the retention is not by the reaction between parylene and the chemicals but the characteristic of the chemicals. They all have high boiling temperature. As a result, they repeat condense and evaporation continually while they are passing through low temperature column. This is the cause of the retention and separation that occurred even without any stationary phase.
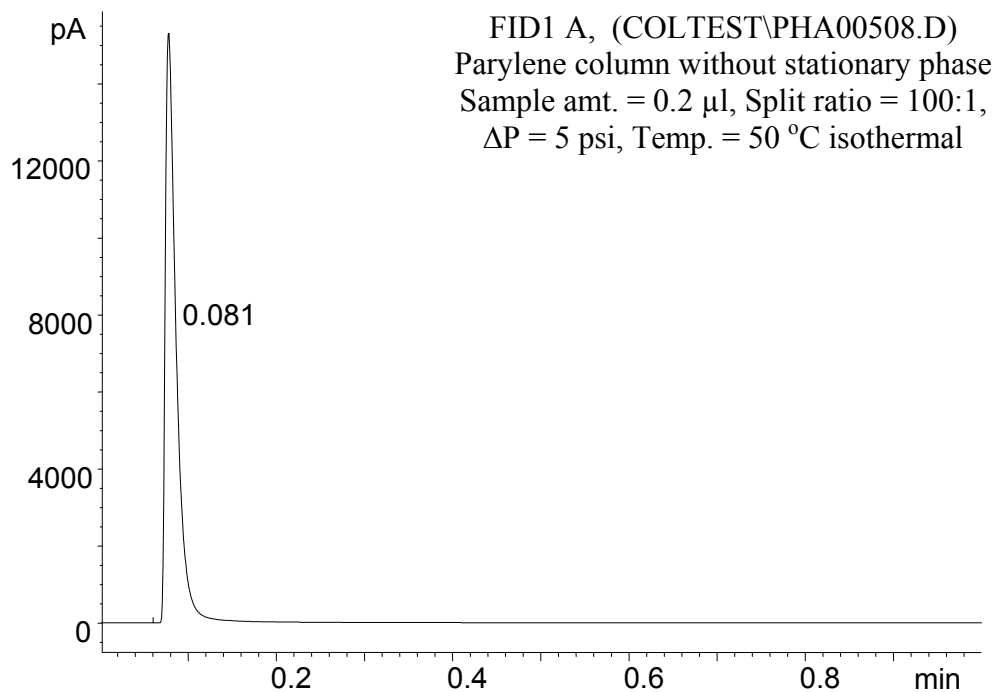
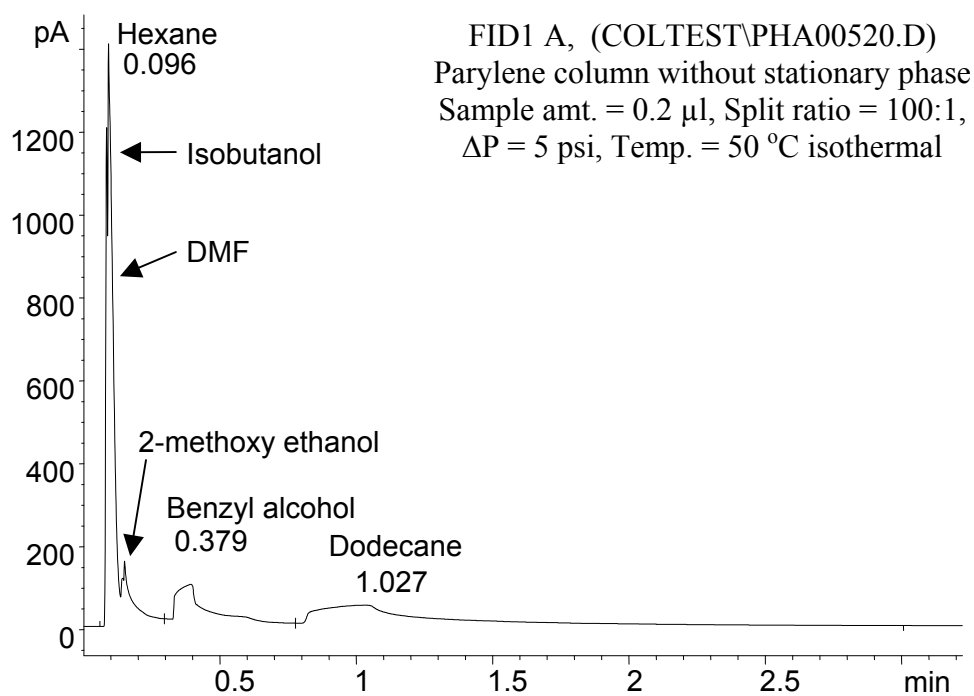**Figure 7-15. Chromatogram of a mixture of unretained chemicals.**

Figure 7-16. Chromatogram of a mixture of retained chemicals.
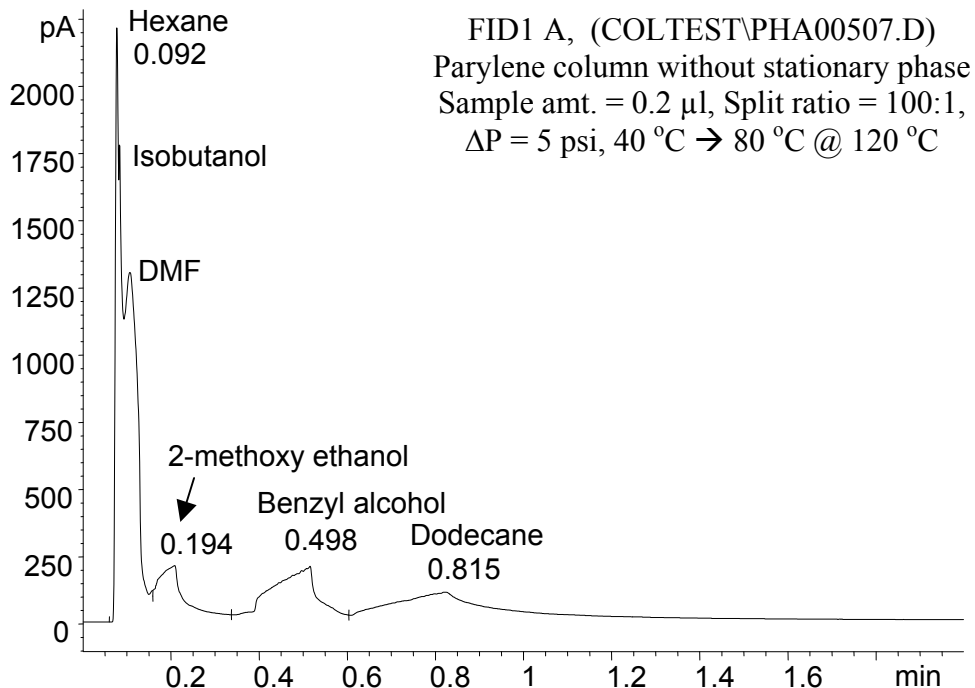
217

Figure 7-17. Chromatogram of a mixture of retained chemicals with temperature programming.
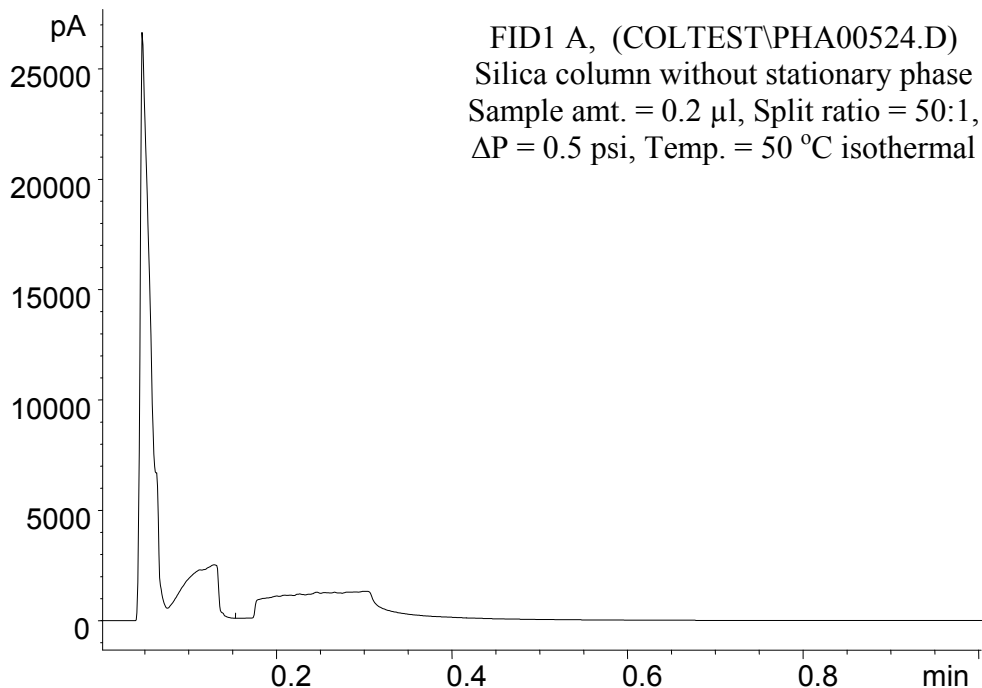

Figure 7-18. Chromatogram using silica column without stationary phase.

Prototype 2 (parylene-A stationary phase)

218

Parylene-A stationary phase was not an effective stationary phase for GC column. This column behaved like the prototype 1 which had no stationary phase. Figure 7-19 shows the chromatograms obtained by this column. The chromatograms are very similar to those obtained with prototype 1 column. This result reveals that retention process is mainly a physical process that highly depends on the solubility characteristics between the analytes and the stationary phase. The existence of the amine functional group in parylene-A stationary phase did not make significant difference in the GC analysis.
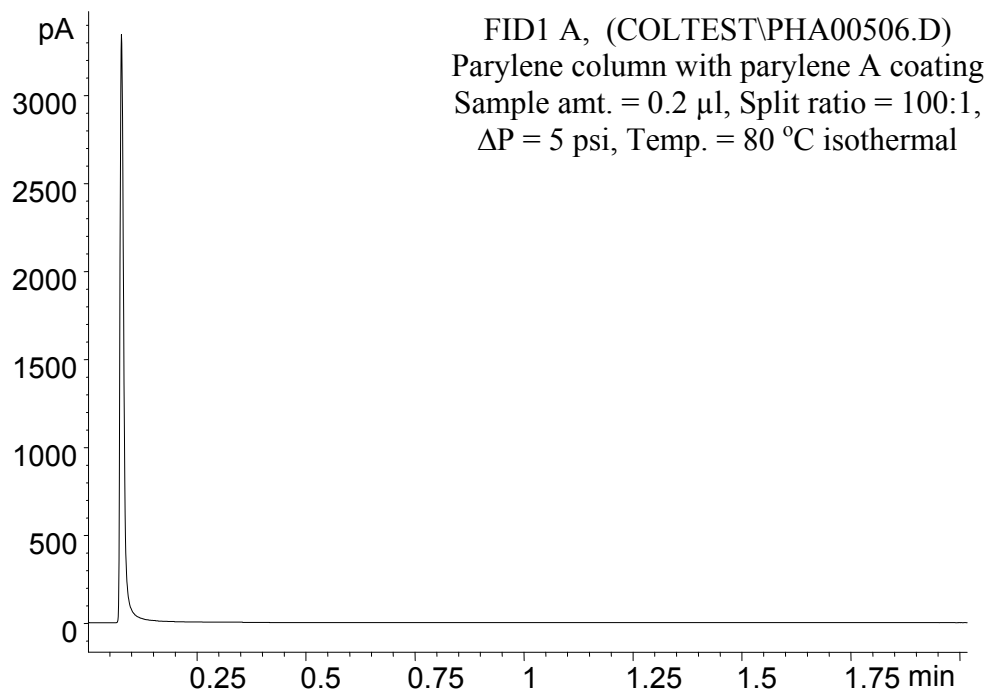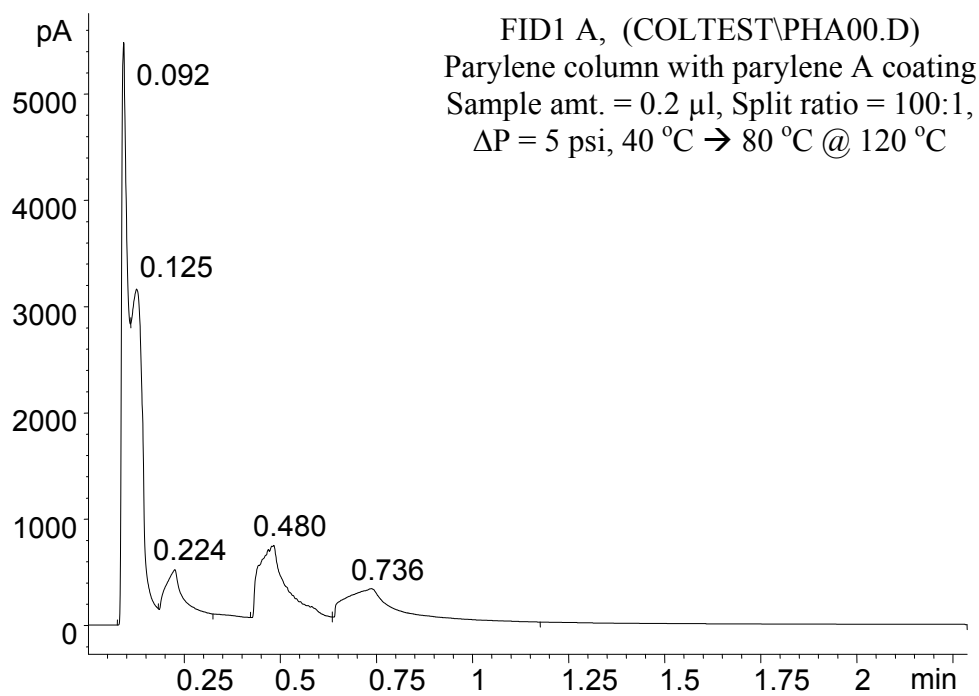
Figure 7-19. Chromatograms obtained by parylene column with parylene-A stationary phase, (a) a mixture of unretained chemicals, (b) a mixture of retained chemicals.

220

<u>Prototype 3 (OV-1 coating)</u>

Figure 7-20 shows the chromatograms of obtained by parylene column with OV-1 stationary phase. There was some separation observed for the unretained chemicals. Also, the retention times of the retained chemicals were longer than other prototypes. These results are very similar to the chromatogram obtained using commercial HP-1 column shown in Figure 7-21.

Some other chemical mixtures were tested using this prototype. The first one was hydrocarbon mixture (C7-C10). Figure 7-22 and Figure 7-23 shows the chromatogram of the mixture. Figure 7-22 (a) is the chromatogram of the mixture diluted in hexane. The concentration was 1%. Injected sample amount was 0.2 μl and the split ratio was 1000:1. The inlet pressure was fixed at 5 psi and analysis temperature was 50 ^{o}C isothermal. In this case, the large solvent peak affected the peaks of other chemicals so that the peaks for the analytes were not able to appear clearly. So, another test was performed without the solvent. Figure 7-22 (b) is the chromatogram of the mixture of 4 hydrocarbons under the same analysis condition. The retention times of the chemicals remained same. But four different hydrocarbons were well separated although the peaks for higher number hydrocarbons are diminishing and broadened because of band broadening effect.

Figure 7-23 is the chromatogram of the same mixture when the analysis temperature was ramped from 30 ^{o}C to 100 ^{o}C at a ramp speed of 120 ^{o}C/min. An excellent separation was achieved in one minute and the peaks for higher number hydrocarbons remained as sharp as that of the lower number hydrocarbon. This indicates that temperature programming is very efficient tool to achieve a nice separation in a GC analysis.
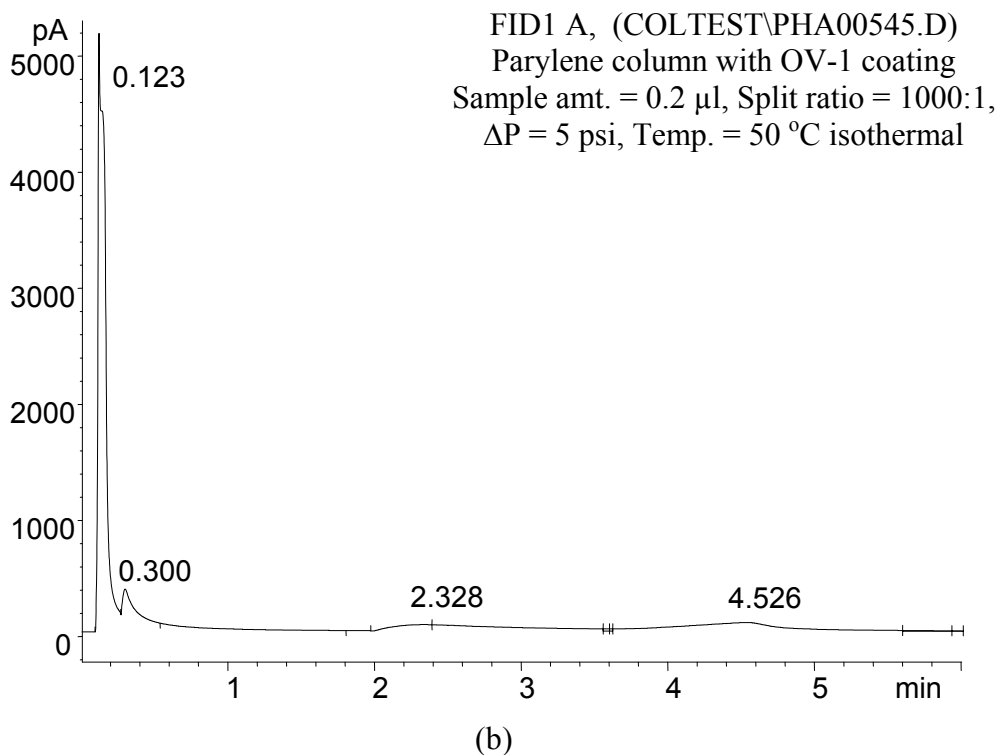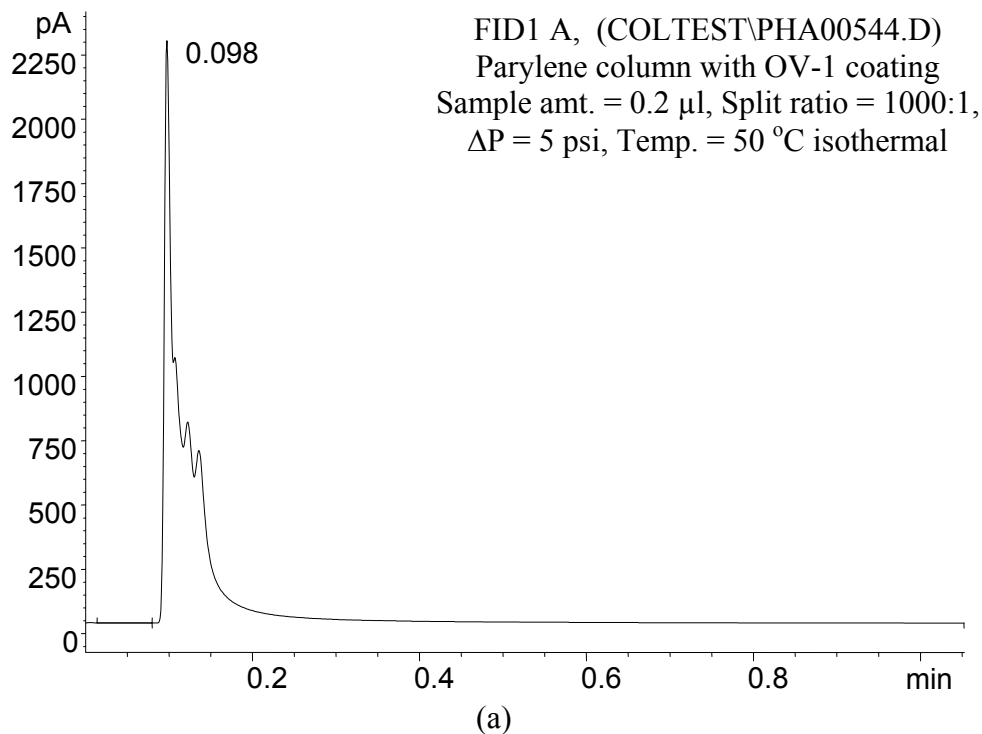
Figure 7-20. Chromatograms obtained by parylene column with OV-1 stationary phase, (a) a mixture of unretained chemicals, (b) a mixture of retained chemicals.
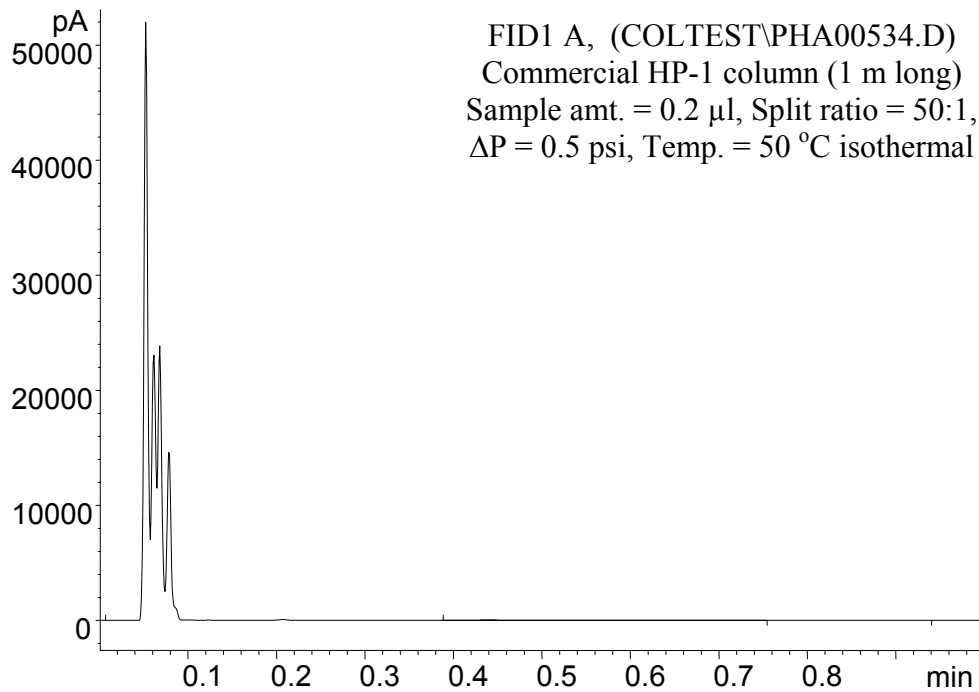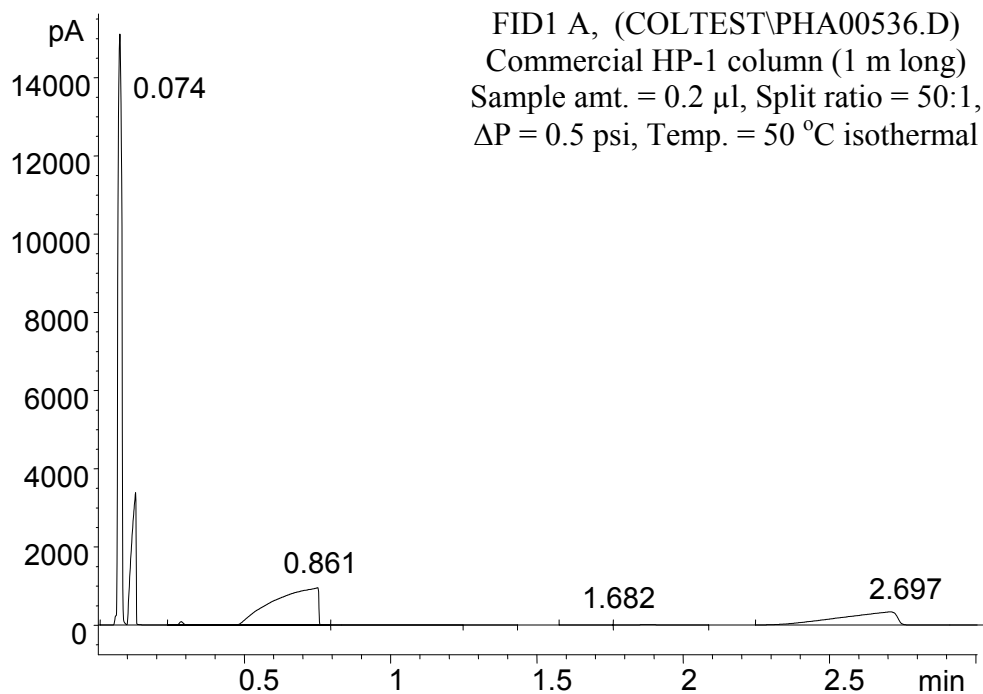
Figure 7-21 Chromatograms obtained by commercial HP-1 column (1 m long), (a) a mixture of unretained chemicals, (b) a mixture of retained chemicals

223
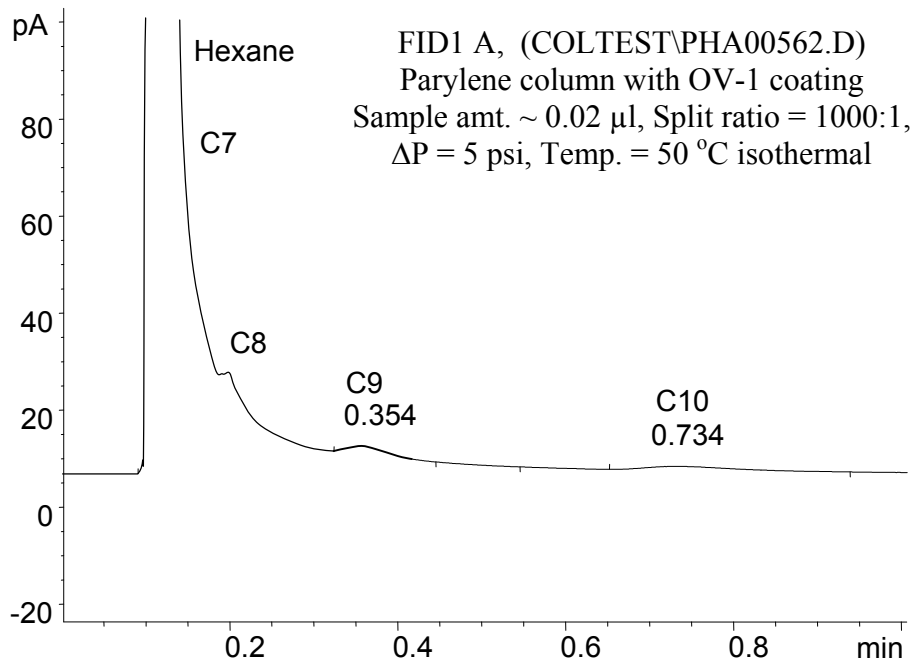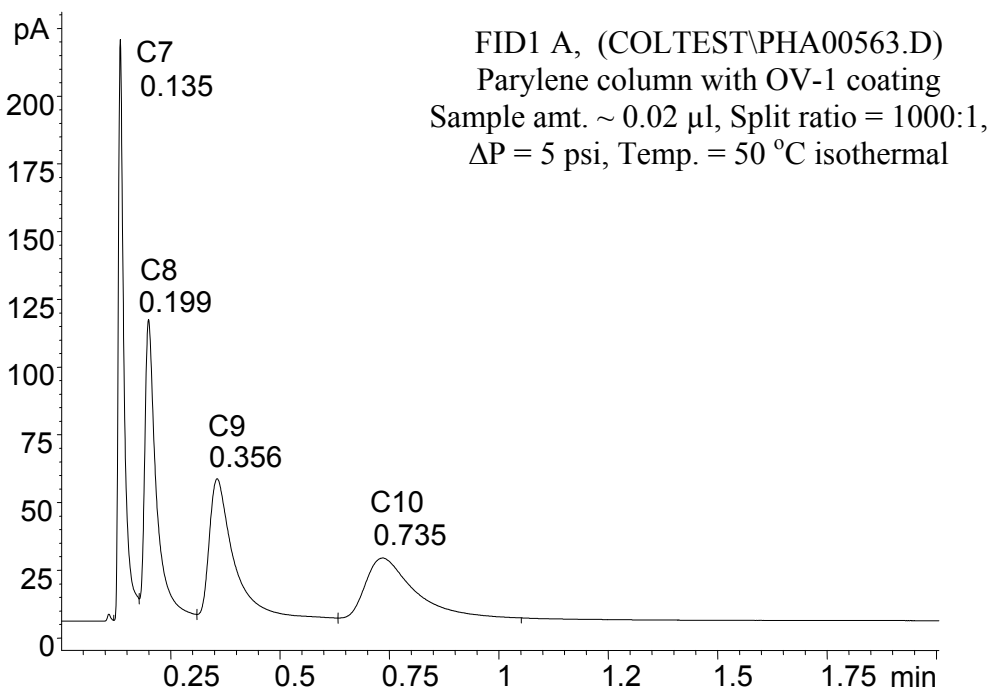
Figure 7-22 Chromatograms of hydrocarbon mixture (C7-C10), (a) diluted mixture (1% in hexane), (b) non-diluted mixture.

224
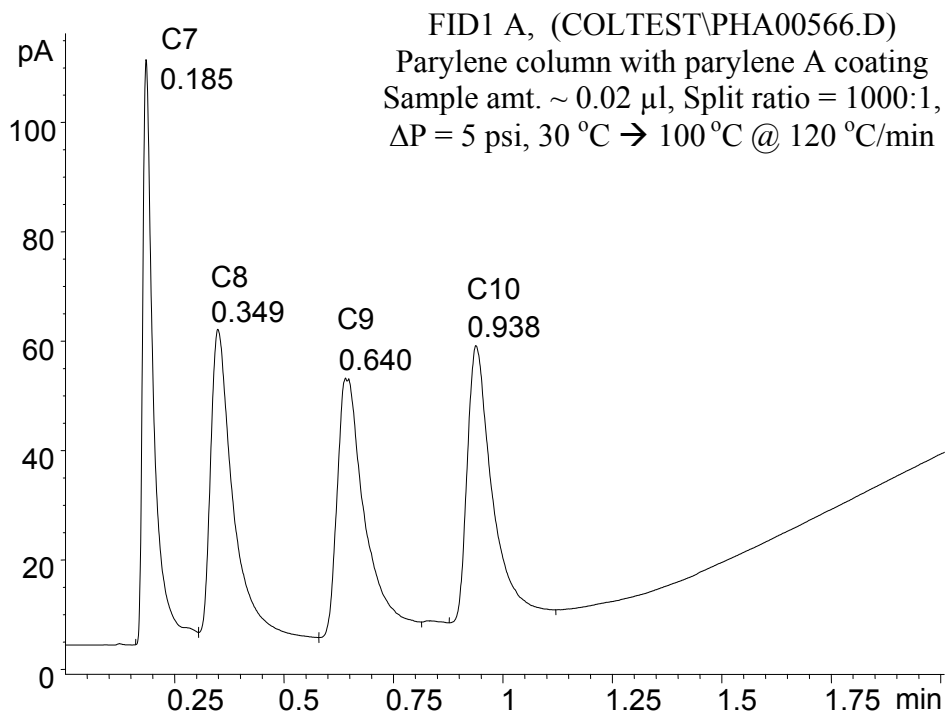
Figure 7-23 Chromatograms of hydrocarbon mixture (C7-C10) with temperature programming.

How much amount of the solutes produced the peaks in the chromatogram? For the chromatogram in Figure 7-23, total 0.02 μl of sample was used. Since the sample was a mixture of 4 chemicals, each chemical was about 5 nl. The first peak of the chromatogram (area = 190.2) is for heptane. The density of heptane is 0.684 g/cm^3. Therefore, approximately 3.6 x 10^{-5} g of heptane was injected from the syringe. This solute was evaporated immediately and only a thousandth of the sample was introduced to the column. As a result, the sample amount that was transferred to the FID detector was about 3.6 x 10^{-8} g. In other words, 36 ng of heptane resulted in the first sharp peak of the chromatogram. Generally, it is said that FID detector requires 5 ng of sample to generate nice sharp peak.

Another mixture tested was a mixture of 8 chemicals (Methanol, hexane, butanol, benzene, C7-C10). The first four chemicals were the ones that could not be separated with other prototype columns. However, they were able to be separated with this prototype at 30 $^{\circ}$C isothermal condition as shown in Figure 7-24 (a). The samples were not diluted and the injected sample amount was approximately 0.02 μl. The split ratio was 1000:1 and the inlet pressure was fixed at 5 psi. Figure 7-24 (b) shows the effect of temperature programming. The analysis temperature was kept at 30 $^{\circ}$C for 0.2 min and then ramped to 100 $^{\circ}$C at a ramp speed of 120 $^{\circ}$C/min. A nice separation was obtained within 1 min using the temperature programming.

A mixture of aromatic carbons (benzene, toluene, ethylbenzene, σ-xylene) was also tested. Three different analysis temperatures were tried (80, 50, and 30 $^{\circ}$C isothermal). The mixture was not diluted and the injected sample amount was 0.2 μl. The split ratio was 100:1 and the inlet pressure was fixed at 5 psi. The result is shown in Figure 7-25. At 80 $^{\circ}$C, three peaks were observed. The benzene peak and toluene peak were too close from each other and the other four component generated a big single peak. However at lower temperature (50 and 30 $^{\circ}$C), benzene peak and toluene peak were completely separated and the other big peak was also little bit splited. This split is considered as the separation between ethylbenzene and xylenes. However, even at 30 $^{\circ}$C, the 3 different xylenez were not able to be separated. Smaller amount (~ 0.02 μl and split ratio of 1000:1) of sample was tried as shown Figure 7-26 but still the xylenes were not separated.
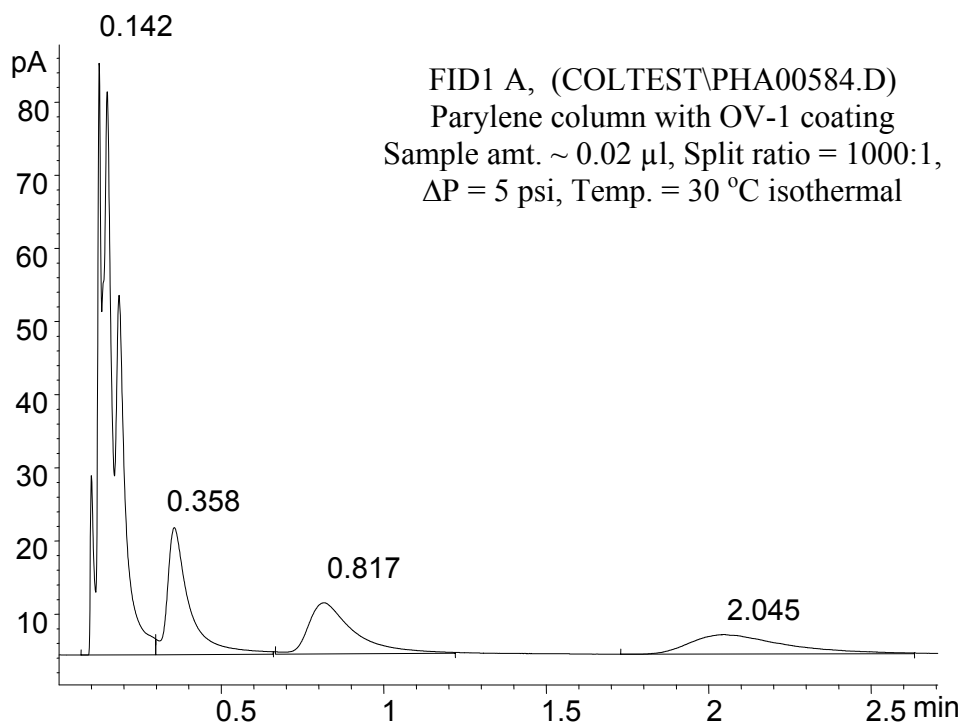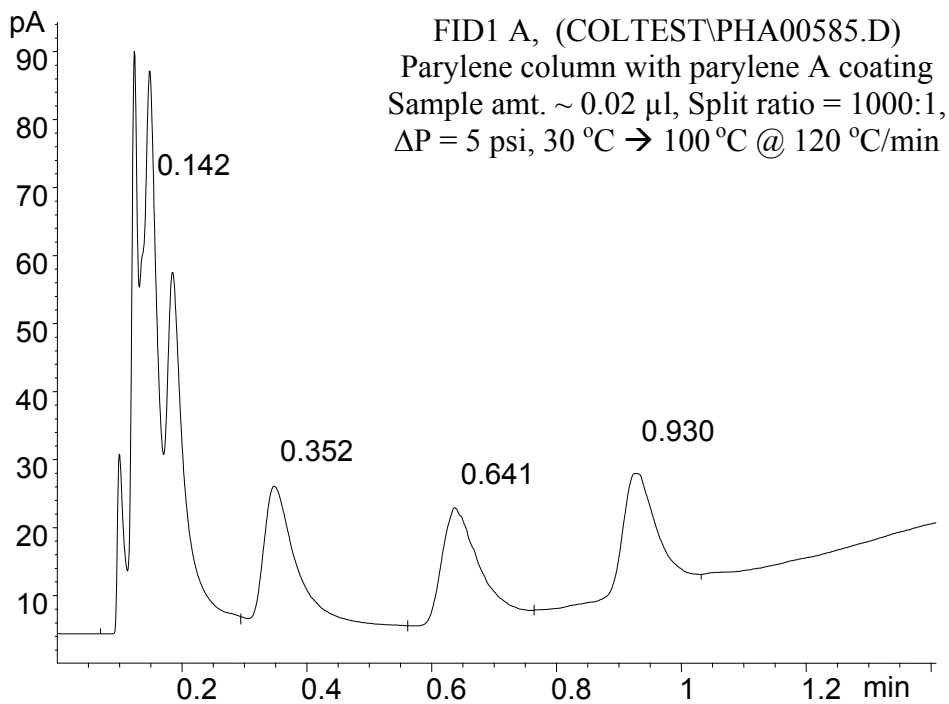
Figure 7-24 Chromatograms of a mixture of 8 chemicals (methanol, hexane, butanol, benzene, C7-C10), (a) isothermal, (b) temperature programming.
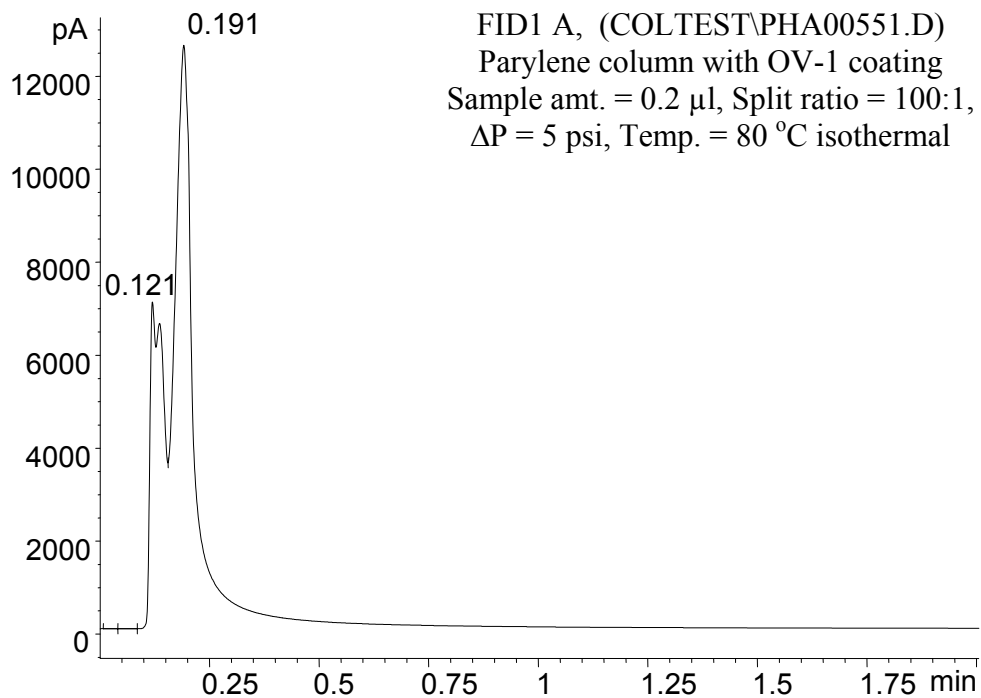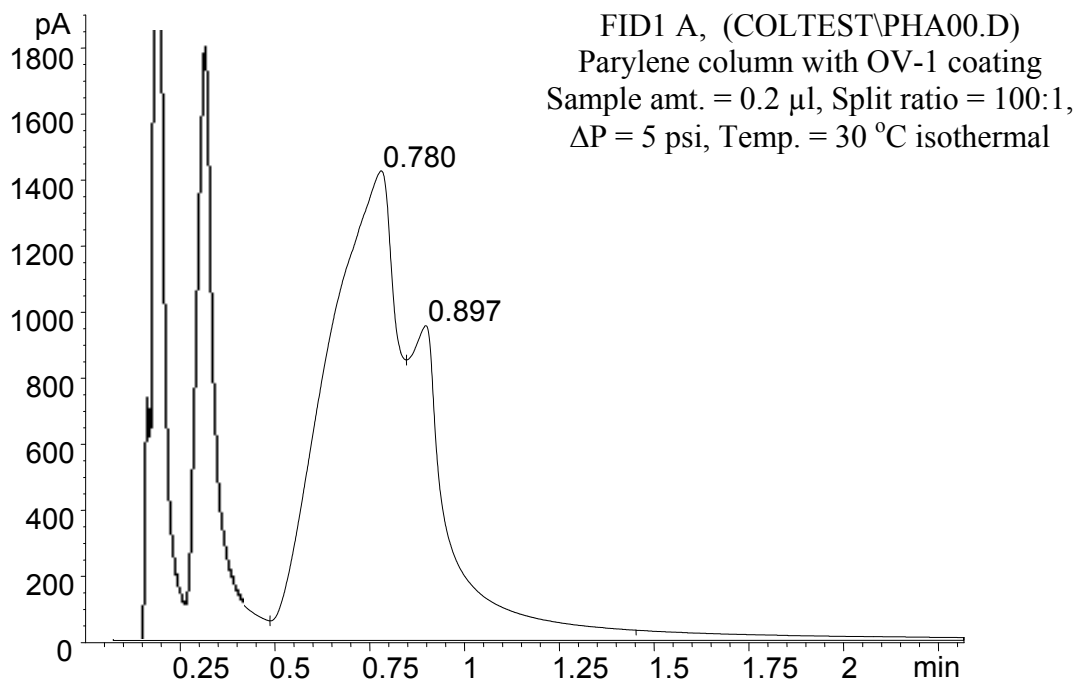
Figure 7-25 Chromatograms of a mixture of aromatic carbons (benzene, toluene, ethylbenzene, -xylenes), (a) 80 °C isothermal, (b) 30 °C isothermal.
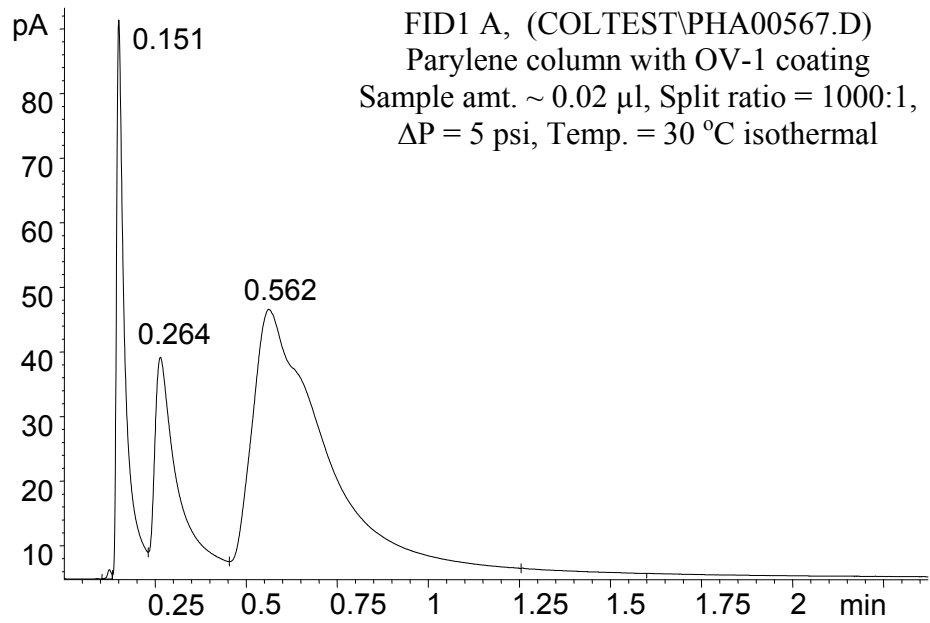
Figure 7-26 Chromatograms of a mixture of aromatic carbons (small amount of sample).

C H A P T E R 8

CONCLUSIONS AND FUTURE WORK

In this chapter, the conclusions of the research and the recommendations for future work are presented. This include the accomplishments and the contributions made by the research. The limitations and shortcomings of the research are also discussed as well as topics for future work.

8.1 CONTRIBUTIONS AND CONCLUSIONS

The goal of this research was to develop a miniature separation column that has low thermal mass and an embedded heating element for rapid thermal cycling. The new column material chosen for the goal was thin film polymer, parylene. It was a great challenge to build a parylene GC column because it was a completely new approach. The goal was successfully accomplished, although there were many hurdles. This work included new process development for parylene microcolumn structural fabrication, a study of theoretical column performance, design and fabrication of a parylene GC column with an embedded heating element, and the evaluation of the GC column. The contributions and the achievements of the research are as follows.

■ Theoretical Analysis of Column Performance and Design

(1) Investigated gas flow in a rectangular microchannel. The exact solutions to the average flow velocity and the flow distribution of a gas flow in a rectangular microchannel were compared with simplified solutions. Compressibility, slip flow, and curvature effect were also investigated for a gas flow in a rectangular microchannel.

(2) Performed an analysis of column performance for a micromachined rectangular GC column. The formula for column efficiency (Golay equation) has many parameters that influence each other. This results in difficulty in predicting the effects of parameters on retention time and column efficiency. The effects of design and operation parameters on the column performance have been thoroughly investigated using Matlab. Based on this information, the design of a parylene GC column has been optimized for the recommended column performance (the retention time should be less than 1 minute and the number of theoretical plates should be more than 10,000).

(3) Investigated the deformation, gas permeation, and integration of the parylene GC column. The effect of wall thickness and structure on the deformation due to inner pressure was investigated using ANSYS. For the inner pressure up to 10 psi, a parylene layer thicker than 10 μm was recommended. Gas permeation test result showed that parylene/metal/parylene triple layer was much less permeable than the parylene monolayer. A side tubing method was devised because conventional top/bottom connections are not appropriate for the thin film parylene column. The

inlet and outlet of the parylene column were designed to have a wider dimension for this purpose.

(4) Investigated the thermal cycling of parylene GC column. A gold thin film evaporated on the corrugated surface of parylene column was selected as a heating element for parylene column because it can be achieved without additional lithography. ANSYS heat transfer modeling has been performed to investigate the heating and cooling rate, power consumption, the entrance length and temperature distribution of the parylene column with an embedded heating element. Parylene column could be heated to 100 $^{\circ}$C within 1 min with only 50 mW while silicon/glass column required almost 500 mW for the same heating. Also, the cooling of the column was much faster in parylene column because of its lower thermal mass. The temperature gradient existing across the cross section of a parylene column was reduced to less than 0.1 $^{\circ}$C by adding a thin metal layer in the parylene wall as a heat diffuser.

■ Process Development and Fabrication

(1) Investigated parylene/parylene thermal bonding. Two heating techniques, convection oven heating and microwave heating, were investigated for parylene/parylene bonding. The bonding was achieved at above 200 $^{\circ}$C by convection oven heating and at above 160 $^{\circ}$C for microwave heating. The process parameters such as temperature, pressure, time, and parylene thickness were thoroughly examined and the bonding quality was evaluated through die shear

tests, tensile pull tests, blister tests, scanning acoustic microscopy (SAM), and scanning electron microscopy (SEM). The SEM image showed approximately 200 nm thick inter-diffusion layer at the bonded interface and the overall bonding uniformity was good according to the SAM image. The maximum shear stress and tensile stress were 12.68 MPa and 9.16 MPa, respectively. This technique was applied to wafer level bonding and demonstrated a successful bonding result.

(2) Developed a new fabrication method, 'parylene micromolding.' The conventional fabrication method for parylene devices, surface micromachining, is not appropriate for fabricating a long parylene GC column because it is a diffusion-limited process. A new concept for using a molding technique was proposed in this research. This new method consists of silicon mold fabrication, parylene deposition, parylene/parylene thermal bonding, and parylene column release from the mold. When the aspect ratio of the channel is lower than 1:1, parylene column was able to be released from the mold without any damage. However, the columns with high aspect ratio such as GC column could not be released successfully. In this case, silicon mold needs to be etched away to obtain parylene column. This new fabrication method was further explored to fabricate other microfluidic components such as meander type channels, electrophoretic, and dielectrophoretic microchannels.

(3) Investigated the stationary phase coating methods for a parylene GC column. Both conventional injection coating method and dry coating method have been investigated. A commercial stationary phase, OV-1 was coated using an injection

coating method and the average thickness was calculated through GC data although it was not be directly measured. For dry coating, PECVD fluorocarbon and parylene-A have been investigated. Film deposition was successful, but the coating made parylene/parylene bonding difficult. Microwave bonding was more effective than convection oven bonding in this case.

(4) Fabicated parylene GC columns with embedded heating element. The completed parylene GC columns include stationary phase, proper tubing and packaging, and are literally 'ready for use' (Figure 8-1).
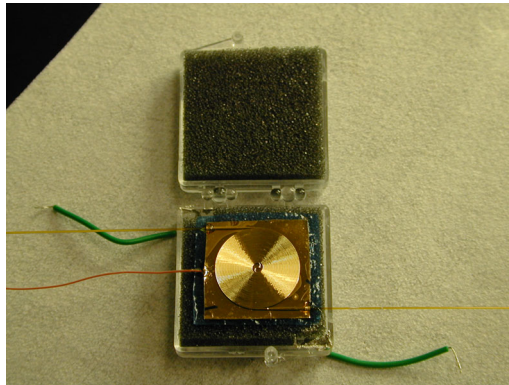
Figure 8-1. The final parylene column with an embedded heating element.

■ Testing and Evaluation

(1) Measured the pressure drop versus flow rate relationship. The measured data shows a good agreement with the compressible model.

(2) Measured the thermal cycling of a parylene column. The actual temperature of the parylene column was monitored during heating and cooling. The steady-state temperature of the parylene column was also measured varying the voltage

applied to the heating element. This data was compared with the lumped model developed in ANSYS.

(3) Performed GC analysis with parylene columns. Three prototype columns having different stationary phases were tested. The parylene columns were installed in a conventional GC (HP6850) replacing conventional fused-silica column. Retention time and the number of theoretical plates have been measured and compared with theoretically calculated values. Separation performance was also demonstrated using volatile chemical mixtures.

(4) Retention time: The measured retention time was compared with theoretically calculated value for each prototype. Side tubing was taken into account in the theoretical calculation. For the column with parylene-A stationary phase, there was a large difference between the calculated and the measured value. The retention time was close to the value obtained by the column without stationary phase. This indicated that parylene-A does not retain analytes as expected. The distribution constant obtained from QCM test cannot predict the retention behavior of the analyte in GC column. The column with PDMS stationary phase showed longer retention time than the other columns for the same analytes. This indicates that the analytes are retained effectively by the stationary phase. The retention times of many volatile organic chemicals have been measured. However, the theoretical retention time could not be calculated because the stationary phase thickness was unknown. Conversely, the stationary phase thickness was calculated from the measured retention time.

(5) Column efficiency: The actual number of theoretical plates was calculated from the GC data and compared with the theoretical value. Again, the side tubing was taken into account. For all prototypes, the actual plate numbers were much lower (less than 5%) than the values obtained from the analytic models. The possible causes for the big difference are: first, the abrupt change in flow path due to tubing; second, errors in the analytical model such as the error in column dimension and the error due to inappropriate assumption; and third, non-uniformity in stationary phase coating.

(6) Separation performance: The column without stationary phase and the column with parylene-A stationary phase showed basically similar chromatograms because parylene-A was not functioning effectively as a stationary phase. However, some chemicals such as isobutanol, DMF, 2-methoxyethanol, benzyl alcohol and dodecane were retained in those columns, resulting in some separation. The similar retention was observed in silica tubing. The chemicals having high boiling points seemed to be retained by the column without stationary phase. More GC analysis was performed with the column with PDMS stationary phase. The separation of hydrocarbon mixture (C7-C10) was successfully demonstrated. The separation was improved greatly through temperature programming. The separations of organic solvents and aromatic chemical mixtures were also performed, but the separation was not complete because of the short retention time and low column efficiency.

8.2 RECOMMENDATIONS FOR FUTURE WORK

The world's first parylene GC column with an embedded heating element has been developed. However, there are many things to be improved. The recommendations for future work can be made for several areas such as: process, column performance, heating element and integration with other components of a GC system.

■ Process

Making a defectless silicon microchannel is very critical in the fabrication of parylene column. However, the general deep RIE process often produces black silicon in the silicon channel. This was why longer columns (3 m long) could not be successfully built. Improvement needs to be made in this process to increase the yield.

Parylene/parylene bonding has been shown successful for a single die. Wafer level bonding needs to be accomplished to have the advantage of using batch processes.

■ Column performance

Column efficiency needs to be improved to provide powerful separation of chemicals. Uniform stationary phase coating is crucial to achieve better column efficiency. A dry coating technique is preferred for this purpose. PECVD deposition of PEG and PDMS needs to be investigated.

■ Heating element:

A Parylene column requires lower power consumption for heating. However, the current heating element is not suitable for the commercial battery because it has high resistance.

In order to generate the required power with commercial batteries, the heating element needs to have lower resistance. One of the methods to achieve this involves making it thicker. Electroplaing seems to be the best choice for this purpose.

■ Integration

The fabricated parylene columns have been tested in a conventional GC system. In order to construct a miniature GC system, the column needs to be integrated with other components such as a micropump, microvalve, and sensor. Interfacing components and constructing a complete system must be investigated in the future. Multiple columns can be used in a single GC system.

Another interesting approach is building hyphenated system such as GC-MS, GC-IR, and GC-IMS. A miniature GC column can be a powerful tool for the separation of analytes in many hyphenated systems.

BIBLIOGRAPHY

[1]S. C. Terry, "A Gas Chromatography System Fabricated on a Silicon Wafer Using Integrated Circuit Technology," Stanford University, 1975.

[2]S. C. Terry, J. H. Jerman, and J. B. Angell, "Gas chromatographic air analyzer fabricated on a silicon wafer," *IEEE Transaction on Electronic Devices*, vol. 26, pp. 1880-1979, 1979.

[3]C. M. Matzke, R. J. Kottenstette, S. A. Casalnuovo, G. C. Frye-Mason, M. L. Hudson, D. Y. Sasaki, R. P. Manginell, and C. C. Wong, "Microfabricated silicon gas chromatographic micro-channels: fabrication and performance," presented at SPIE Conference on Micromachining and Microfabrication Process Technology IV, 1998.

[4]G. Wiranto, M. R. Haskard, D. E. Mulcahy, D. E. Davey, and E. F. Dawes, "Microengineered open tubular columns for GC anaylsis," presented at SPIE Conference on Electronics and Structures for MEMS, 1999.

[5]L. Nieradko and K. Malecki, "Silicon components for gas chromatograph," 2000.

[6]C. K. Ho, M. T. Itamura, M. Kelley, and R. C. Hughes, "Review of chemical sensors for in-situ monitoring of volatile contaminants," Sandia National Laboratories 2001.

[7]W. Jennings, *Analytical Gas Chromatography*. San Diego: Academic Press, 1987.

[8]W. E. Harris and H. W. Habgood, *Programmed Temperature Gas Chromatography*. New York: Wiley, 1966.

[9]D. A. Skoog, F. J. Holler, and T. A. Nieman, *Principles of Instrumental Analysis*. Toronto: Brooks/Cole, 1998.

[10] M. W. Bruns, "Silicon micromachining and high speed gas chromatography," presented at Internation Conference on Electronics, Control, Instrumentation, and Automation, 1992.

[11] M. Madou, *Fundamentals of Microfabrication*. New York: CRC Press, 1997.

[12] R. R. Reston and E. S. Kolesar, "Silicon micro-machined gas chromatography system used to separate and detect ammonia and nitrogen dioxide-part I: design, fabrication, and integration, of the gas chromatography system," *Journal of Microelectromechanical Systems*, vol. 3, pp. 134-146, 1994.

[13] R. R. Reston and E. S. Kolesar, "Silicon micro-machined gas chromatography system used to separate and detect ammonia and nitrogen dioxide-part II: evaluation, analysis, and theoretical modeling of the gas chromatography system," *Journal of Microelectromechanical Systems*, vol. 3, pp. 147-154, 1994.

[14] S. Hannoe, I. Sugimoto, K. Yanagisawa, and H. Kuwano, "Enhanced chromatographic performance of silicon-micromachined capillary column with clean structure and interactive plasma organic films," presented at The 9th International Conference on Solid State Sensors, Actuators and Microsystems, 1997.

[15] G. Frishman and A. Amirav, "Fast GC-PFPD system for field analysis of chemical warfare agents," *Field Analytical Chemistry and Technology*, vol. 4, pp. 170-194, 2000.

[16] U. Lehmann, A. Feustel, and J. Muller, "A micro gas chromatograph based on a plasma polymerized siliconorganic stationary phase," presented at Sensors, 1997.

[17] U. Lehmann, M. Mahnke, O. Glampe, A. Behrends, H. Schliffke, T. Schmidt, and B. Bollapragada, "A miniature gas chromatograpic module on a credit card sized motherboard," presented at Sensors, 2003.

[18] G. C. Frye-Mason, R. J. Kottenstette, E. J. Heller, C. M. Matzke, S. A. Casalnuovo, P. R. Lewis, R. P. Manginell, W. K. Schubert, V. M. Hietala, and R. J. Shul, "Integrated chemical analysis systems for gas phase CW agent detection," presented at The 2nd International Conference on Miniaturized Chemical and Biochemical Analysis Systems (microTAS), 1998.

[19] C. C. Wong, D. R. Adkins, G. C. Frye-Mason, M. L. Hudson, R. J. Kottenstette, C. M. Matzke, J. N. Shadid, and A. G. Salinger, "Modelling transport in gas chromatography columns for the micro-ChemLab," presented at SPIE Conference on Microfluidic Devices and Systems II, 1999.

[20] R. C. Hughes, R. P. Manginell, and R. J. Kottenstette, "Chemical sensing with an integrated preconcentrator/chemiresistor array," presented at Electrochemical Society Meeting, 2001.

[21] J. A. Potkay, J. A. Driscoll, M. Agah, R. D. Sacks, and K. D. Wise, "A high-performance microfabricated gas chromatography column," presented at IEEE Microelectro Mechanical Systems Conference, 2003.

[22] G. E. Spangler, "Height equivalent to a theoretical plate theory for rectangular GC columns," *Analytical Chemistry*, vol. 70, pp. 4805-4816, 1998.

[23] G. E. Spangler, "Theoretical approximations for the linear flow of carrier gas through a rectangular GC column," 1999?

[24] G. E. Spangler, "Relationships for modeling the performance of rectangular gas chromatographic columns," *Journal of Microcolumn Separations*, vol. 13, pp. 285-292, 2001.

[25] I. Sugimoto, M. Nakamura, and H. Kuwano, "Organic gas sorption characteristics of plasma-deposited amino acid films," *Analytical Chemistry*, vol. 66, pp. 4316-4323, 1994.

[26] Kirk-Othmer, *Encyclopedia of Chemical Technology*: John Wiley & Sons, 1998.

[27] W. F. Gorham and W. D. Niegisch, "Xylene Polymers," in *Encyclopedia of Polymer Science and Technology*, vol. 15: Interscience Publishers, 1989, pp. 98-124.

[28] T. A. Harder, T.-J. Yao, Q. He, C.-Y. Shih, and Y.-C. Tai, "Residual stress in thin-film parylene-C," presented at IEEE Microelectro Mechanical Systems Conference, 2002.

[29] S. Dabral, J. Van Etten, X. Zhang, C. Apblett, G.-R. Yang, P. Ficalora, and J. F. McDonald, "Stress in thermally annealed parylene films," *Journal of Electronic Materials*, vol. 21, pp. 989-994, 1992.

[30] J. T. C. Yeh and K. R. Grebe, "Patterning of poly-para-xylylenes by reactive ion etching," *Journal of Vacuum Science and Technology A*, vol. 1, pp. 604-608, 1983.

[31] R. R. A. Callahan, G. B. Raupp, and S. P. Beaudoin, "Effects of gas pressure and substrate temperature on the etching of parylene N using a remote microwave oxygen plasma," *Journal of Vacuum Science and Technology B*, vol. 19, pp. 725-731, 2001.

[32] X.-Q. Wang, L. Qiao, and Y.-C. Tai, "A parylene micro check valve," presented at IEEE Microelectro Mechanical Systems Conference, 1999.

[33] C. Grosjean, X. Yang, and Y.-C. Tai, "A practical thermopneumatic valve," presented at IEEE Microelectro Mechanical Systems Conference, 1999.

[34] X.-Q. Wang, A. Desai, Y.-C. Tai, L. Licklider, and T. D. Lee, "Polymer-based electrospray chips for mass spectrometry," presented at IEEE Microelectro Mechanical Systems Conference, 1999.

[35] S. Wu, J. Mai, Y.-C. Tai, and C. M. Ho, "Micro heat exchanger by using MEMS impinging jets," presented at IEEE Microelectro Mechanical Systems Conference, 1999.

[36] T. N. Pornsin-Sirirak, S. W. Lee, H. Nassef, J. Grasmeyer, Y.-C. Tai, C. M. Ho, and M. Keennon, "MEMS wing technology for a battery-powered ornithopter," presented at IEEE Microelectro Mechanical Systems Conference, 2000.

[37] T. N. Pornsin-Sirirak, Y.-C. Tai, H. Nassef, and C. M. Ho, "Flexible parylene actuator for micro adaptive flow control," presented at IEEE Microelectro Mechanical Systems Conference, 2001.

[38] Q. He, E. Meng, Y.-C. Tai, C. M. Rutherglen, J. Erickson, and J. Pine, "Parylene neuro-cages for live neural networks study," presented at The 12th International Coference on Solid State Sensors, Actuators, and Microsystems, 2003.

[39] J. Wu, R. T. Pike, C. P. Wong, N. P. Kim, and M. H. Tanielian, "Evaluation and characterization of reliable non-hermatic conformal coatings for MEMS device encapsulation," *IEEE Transaction on Components, Packaging, and Manufacturing Technology B*, vol. 23, pp. 721-728, 2000.

[40] C.-H. Han and E. S. Kim, "Parylene-diaphragm piezoelectric acoustic transducers," presented at IEEE Microelectro Mechanical Systems Conference, 2000.

[41] T. Stanczyk, B. Ilic, P. J. Hesketh, and J. G. Boyd, "A microfabricated electrochemical actuator for large displacements," *Journal of Microelectromechanical Systems*, vol. 9, pp. 314-319, 2000.

[42] H.-S. Noh, S. Kim, P. J. Hesketh, M. Hua, and L. Wong, "Miniature corrugated diaphragm for fiber-optic-linked pressure sensing (FOLPS)," presented at ASME International Mechanical Engineering Congress (IMECE), 2003.

[43] H.-S. Noh, P. J. Hesketh, and G. C. Frye-Mason, "Heating element embedded parylene microcolumn for miniature gas chromatograph," presented at IEEE Microelectro Mechanical Systems Conference, 2002.

[44] H.-S. Noh, P. J. Hesketh, and G. C. Frye-Mason, "Parylene gas chromatographic column for rapid thermal cycling," *Journal of Micromechanics and Microengineering*, vol. 11, pp. 718-725, 2002.

[45] H.-S. Noh, Y. Huang, and P. J. Hesketh, "Parylene micromolding, a rapid and low-cost fabrication method of parylene microchannel," *Sensors and Actuators B*, vol. In review, 2003.

[46] H.-S. Noh, Y. Choi, C.-F. Wu, P. J. Hesketh, and M. G. Allen, "Rapid, low-cost fabrication method of parylene microchannel for microfluidic applications," presented at The 12th International Coference on Solid State Sensors, Actuators, and Microsystems, 2003.

[47] H.-S. Noh, K.-S. Moon, A. Cannon, P. J. Hesketh, and C. P. Wong, "Wafer bonding using microwave heating of parylene intermediate layers," *Journal of Micromechanics and Microengineering*, vol. 14, pp. 625-631, 2004.

[48] H.-S. Noh, K.-S. Moon, A. Cannon, P. J. Hesketh, and C. P. Wong, "Wafer bonding using microwave heating of parylene for MEMS packaging," presented at The 54th Electronic Components and Technology Conference (ECTC), 2004.

[49] B. R. Munson, *Fundamentals of Fluid Mechanics*. New York: John Wiley & Sons, 1998.

[50] F. M. White, *Viscous Fluid Flow*. Boston: McGraw-Hill, 1991.

[51] R. L. Panton, *Incompressible Flow*. New York: John Wiley & Sons, 1995.

[52] J. D. Anderson, *Fundamentals of Aerodynamics*. Boston: McGraw-Hill, 2001.

[53] C. C. Wong, T. L. Zoeller, D. R. Adkins, and J. N. Shadid, "Investigation of gas flow in long and narrow channels," presented at ASME Fluid Engineering Division Summer Meeting (FEDSM), 2000.

[54] G. A. Bird, Molecular Gas Dynamics and Direct Simulation of Gas Flows: Clarendon Press, 1994.

[55] A. B. Littlewood, *Gas Chromatography*. London: Academic Press, 1970.

[56] A. T. James and A. J. P. Martin, *Biochemistry Journal*, vol. 50, pp. 697, 1952.

[57] M. J. Golay, "Theory of chromatography in open and coated tubular columns with roung and rectangular corss sections," *Gas Chromatography*, pp. 36-55, 1958.

[58] J. C. Giddings, S. L. Seager, L. R. Stucki, and G. H. Stewart, "Plate Height in Gas Chromatography," *Analytical Chemistry*, vol. 32, pp. 867-870, 1960.

[59] J. C. Giddings, *Dynamics of Chromatography*. New York: Marcel Dekker, 1965.

[60] A. N. Berezhnoi and A. V. Semenov, *Binary Diffusion Coefficients of Liquid Vapors in Gases*. New York: Begell House, 1997.

[61] K. Walsh, J. Norville, and Y.-C. Tai, "Photoresist as a sacrificial layer by dissolution in acetone," presented at IEEE Microelectro Mechanical Systems Conference, 2001.

[62] D. M. Pozar, *Microwave Engineering*. NewYork: Wiley, 1997.

[63] K. D. Farnsworth, "Variable frequency microwave curing of 3, 3, 4, 4 - Biphenyltetracarboxylic acid dianhydride/p-phenylenediamine (BPDA/PPD)," *International Journal of Microcircuit and Electronic Package*, vol. 23, pp. 162-171, 2000.

[64] N. Taheri, N. Mohammadi, and N. Shahidi, "An automatic instrument for measurement of interfacial adhesion of polymeric coatings," *Polymer Testing*, vol. 19, pp. 959-966, 2000.

[65] H.-S. Jeong, Y. Z. Chu, C. J. Durning, and R. C. White, "Adhesion study of polyimide to si surfaces," *Surface and Interface Analysis*, vol. 18, pp. 289-292, 1992.

[66] M. G. Allen and S. D. Senturia, "Application of the island blister test for thin film adhesion measurement," *Journal of Adhesion*, vol. 29, pp. 219-231, 1989.

[67] S. Vaswani, J. Koskinen, S. Zauscher, and D. W. Hess, "Barrier films on paper and cellulose using fluorocarbon plasmas," presented at The 203rd Electrochemical Society Meeting, 2003.